Fakultät für
Mathematik, Informatik
und Naturwissenschaften

RWTHAACHEN
UNIVERSITY

Interplay of proximity effects in superconductor/ferromagnet heterostructures

Von der Fakultät für Mathematik, Informatik und Naturwissenschaften der RWTH Aachen
University zur Erlangung des akademischen Grades einer
Doktorin der Naturwissenschaften genehmigte Dissertation

vorgelegt von

Master of Science

Annika Stellhorn

aus

Paderborn, Germany

Berichter: *Professor Dr. Thomas Brückel*

Professor Dr. Matthias Wuttig

Tag der mündlichen Prüfung: *22.03.2021*

Diese Dissertation ist auf den Internetseiten der Universitätsbibliothek verfügbar.

Zusammenfassung

Proximity Effekte in Supraleiter(S)/Ferromagnet(F)-Heterostrukturen erfahren eine immer größer werdende Aufmerksamkeit sowohl in der Grundlagenforschung im Bereich neuer, exotischer Quantenzustände als auch in der Anwendung in Form von supraleitenden Spin-Valve-Strukturen und fluxonischen Elementen in Quantencomputern. Die inhomogene Magnetisierung des Ferromagneten führt zur Modifikation der supraleitenden Zustände, die sich in Streufeld-induzierter Domänensupraleitung oder direkter Austauschwechselwirkung manifestiert. In der vorliegenden Arbeit werden beide bisher separat betrachtete Phänomene – die Domänensupraleitung und die Erzeugung von Spin-Triplet Zuständen durch Austauschwechselwirkung – in Zusammenhang gebracht und deren Interaktion mit einem externen Magnetfeld präsentiert.

Systematische Untersuchungen an Nb(S)/FePd(F) mit senkrecht-magnetischer Anisotropie (PMA) und lateraler Domänenstruktur werden im Hinblick auf drei Ziele durchgeführt: (i) Die Herstellung von Nb/FePd Schichtsystemen mit reproduzierbarer und kontrollierbarer Domänenkonfiguration mittels Molekularstrahlepitaxie. (ii) Der Vergleich von Streufeld-generierten und durch Austauschwechselwirkung vermittelten Proximity Effekten mit Hilfe von Magnetotransportmessungen. In Abhängigkeit von der Stärke und Orientierung eines extern angelegten Magnetfeldes können diese differenziert und für Systeme unterschiedlich starker PMA zugeordnet werden. (iii) Der Nachweis des inversen Effektes – ein Einfluss des supraleitenden Zustandes auf das magnetische Tiefenprofil von FePd – mittels Neutronenstreuung. Kleinwinkelstreuung unter streifendem Einfall (GISANS) gibt dabei Aufschluss über eine Änderung des lateralen-, sowie des Tiefenprofils der Magnetisierung.

Die Anordnung der magnetischen Domänen kann über eine Variation der Wachstumsparameter reproduzierbar eingestellt werden. GISANS-Messungen bestätigen die Formierung von Abschlussdomänen an den Oberflächen der FePd-Schicht. Tieftemperaturmessungen im Bereich der supraleitenden kritischen Temperatur weisen eine Abhängigkeit der auftretenden Proximity Effekte von der Stärke der PMA und der Orientierung des externen Magnetfeldes auf. In Systemen mit hoher PMA wird eine streufeldgenerierte Domänenwandsupraleitung nachgewiesen. Ein Vergleich der Messergebnisse mit dem Ginzburg-Landau-Modell ergibt, dass diese analog zur Oberflächensupraleitung behandelt werden kann. Die Domänenwandsupraleitung wird begleitet von einem Anstieg der Domänenwandbreite im FePd, was mittels temperaturabhängiger polarisierter Neutronenstreuung nachgewiesen wird. Die Verwendung von GISANS mit Polarisationsanalyse eröffnet neue Möglichkeiten zur Bestimmung magnetischer Reorientierungen beim Übergang in die Supraleitung. In Systemen mit geringer magnetischer Anisotropie dagegen wird durch eine nicht-kollineare Magnetisierung im FePd die Bildung von Spin-Triplet Cooperpaaren begünstigt. Dadurch wird die Sprungtemperatur um $\Delta T_c = 100\,\mathrm{mK}$ abgesenkt. Durch eine Erweiterung des Zweischichtsystems auf F/S/F'-Schichten kann dieser Wert zusätzlich erhöht werden und bietet somit das Potenzial zur Anwendung in supraleitenden Spin-Valve-Systemen. Winkelabhängige Magnetotransportmessungen weisen auf die Erzeugung von Spin-Triplet Cooperpaaren auch in Schichten mit hoher magnetischer Anisotropie hin.

Abstract

Proximity effects in superconductor(S)/ferromagnet(F) thin film heterostructures are gaining tremendous interest in fundamental studies scrutinizing exotic new quantum states as well as in the application of superconducting spin valves or fluxonic devices for quantum computing. In particular, an inhomogeneous magnetization of the neighboring ferromagnet enables modifications of the superconducting state, which emerges as stray-field generated domain-superconductivity or direct exchange related proximity effects such as spin-triplet superconducting correlations.

In this thesis, a combination of both phenomena in one heterostructure system, and their interplay and controllability by an external magnetic field, is studied. A systematic study on thin film heterostructures of Nb(S)/FePd(F) with Perpendicular Magnetic Anisotropy (PMA) and a lateral magnetic domain pattern is performed addressing three main objectives: (i) growing the Nb/FePd bilayers reproducibly with varying strength of PMA and a controllable domain configuration, (ii) characterizing macroscopic magnetotransport measurements of stray-field generated and direct exchange proximity effects which reveal their interplay and tunability by an external magnetic field, and (iii) characterizing the inverse phenomenon where the superconducting state affects the lateral magnetic depth-profile of FePd. Grazing-Incidence Small-Angle Neutron Scattering (GISANS) is the method of choice for such inverse proximity effects that appear in S/F heterostructures with a lateral domain pattern on the mesoscopic length scale.

Room-temperature characterizations reveal a successfully reproducible growth of thin film FePd with an adjustable strength of PMA and a controllable domain configuration. GISANS measurements confirm triangular shaped closure domains at the layer surfaces of stripe-patterned FePd. Results at low temperatures demonstrate isolated, stray-field generated domain-wall- and reverse-domain-superconductivity in samples of high PMA.

This is consistent with theoretical models based on the Ginzburg- Landau approach. These confinement effects are accompanied by a change of magnetic fluctuations inside the FePd domain pattern and an increase of the domain wall width probed by neutron scattering in an out-of-plane applied guiding field. Polarized GISANS studies on S/F heterostructure systems exhibiting PMA are an entirely new research field and are demonstrated to reveal small changes in the magnetic orientation by the onset of superconductivity. Results on Nb/FePd with low PMA and a non-collinear magnetization promote spin-triplet Cooper pair generation with spin alignment along the F-layer magnetization in an in-plane applied field. The variation of the S critical temperature due to spin-triplet Cooper pairs (ΔT_c) of 100 mK is a promising large value for a bilayer system with capability for higher ΔT_c in corresponding trilayer systems. In-plane measurements on samples with higher magnetocrystalline anisotropy and an angle-dependent study on the low-PMA Nb/FePd suggest a spin-triplet Cooper pair generation also in high-PMA Nb/FePd bilayers.

Contents

1 Introduction **1**

2 Superconductor-Ferromagnet Interactions **5**

- 2.1 Ferromagnetism . . . 5
  - 2.1.1 Basics of ferromagnetism . . . 5
  - 2.1.2 Magnetic anisotropy . . . 6
  - 2.1.3 Domain formation and closure domains in FePd thin films . . . 10
- 2.2 Superconductivity . . . 11
  - 2.2.1 Microscopic theory . . . 11
  - 2.2.2 Ginzburg-Landau theory . . . 14
  - 2.2.3 Dirty superconductors . . . 17
  - 2.2.4 Small superconductors . . . 18
  - 2.2.5 Magnetization of type-II superconductors . . . 22
  - 2.2.6 Nb thin films . . . 23
- 2.3 Proximity effects in S/N structures . . . 26
- 2.4 Proximity effects in S/F structures . . . 27
  - 2.4.1 Domain-superconductivity . . . 32
  - 2.4.2 Long-range proximity effects . . . 36
    - 2.4.2.1 Applications . . . 39

3 Neutron scattering theory **43**

- 3.1 Basics on scattering theory . . . 43
- 3.2 Reflectometry on thin film heterostructures . . . 48
  - 3.2.1 Specular reflectometry . . . 50
  - 3.2.2 Off-specular scattering . . . 53
  - 3.2.3 Magnetic reflectometry and off-specular scattering . . . 56

3.2.4 Simulation of GISANS measurements on thin film FePd 58

4 Experimental methods 61

4.1 Molecular Beam Epitaxy 61

4.1.1 Basic growth mechanisms 62

4.1.2 MBE-Setup 63

4.2 In-situ characterization methods 65

4.2.1 Reflection High-Energy Electron Diffraction 65

4.2.2 Low-Energy Electron Diffraction 67

4.3 Ex-situ characterization methods 68

4.3.1 X-Ray Reflectometry and Diffractometry 69

4.3.2 Scanning Transmission Electron Microscopy 69

4.3.3 Rutherford Backscattering Spectrometry 71

4.3.4 Atomic and Magnetic Force Microscopy 71

4.3.5 Magnetic Properties Measurement System 73

4.3.6 Physical Properties Measurement System 74

4.3.7 Large scale facility instruments 74

4.3.7.1 GALAXI 75

4.3.7.2 KWS-3 75

4.3.7.3 vSANS 76

5 Growth and room temperature characterization 79

5.1 FePd in the $L1_0$-phase 79

5.2 FePd with varying PMA 81

5.3 Sample growth 82

5.3.1 Growth procedure 84

5.3.2 Growth of FePd with high, low, and medium PMA 86

5.3.3 In-situ characterization 86

5.4 Ex-situ characterization 90

5.4.1 X-ray reflectometry and diffractometry 90

5.4.2 Surface analysis 94

5.4.3 Magnetic domain structure and macroscopic magnetization . . . 96

5.4.4 GISANS at room temperature 100

5.5 Conclusions 104

6 Low-temperature characterization 107

6.1 Coexistance of superconductivity and ferromagnetism 108

6.2 Magnetotransport with out-of-plane magnetic field 110

6.2.1 High PMA 111
6.2.2 Comparison of PMA 118
6.3 Magnetotransport with in-plane magnetic field 123
6.3.1 Low PMA 123
6.3.2 Comparison of PMA 128
6.4 Conclusions 128

7 Neutron scattering results of high-PMA Nb/FePd 131
7.1 Temperature dependence 131
7.2 Vector magnetization 134
7.2.1 Results at $T > T_\mathrm{c}$ 142
7.2.2 Results at $T < T_\mathrm{c}$ 144
7.3 Conclusions 147

8 Conclusion and outlook 149
8.1 Summary of room- and low-temperature results 149
8.2 Scope of future work 151

9 Supplementary information 155

Bibliography 181

List of Figures 199

List of Tables 213

List of Symbols 215

Acknowledgements 217

Declaration 219

Chapter 1

Introduction

The interplay between proximity effects of different origins arising in superconductor(S)/ferromagnet(F) heterostructures has an enormous impact on the performance and controllability of S/F based device structures. Recent developments in superconducting spintronics and fluxonic devices raise interest in further understanding fundamental processes and proximity effects in magnetically coupled S/F heterostructure systems [1–3]. Tailoring the superconducting parameters by external factors like a small applied magnetic field is desired [4, 5]. This can be reached by a field-dependent superconducting critical temperature T_c either by confinement of the superconducting state on the nanometer scale or by magnetic exchange processes.

Both phenomena arise in S/F systems with F being a lateral domain structured ferromagnet if the respective characteristic superconducting and ferromagnetic length scales are compatible [6]. The confinement of superconductivity by stray fields of the neighboring F layer takes place either on the domain walls (Domain-Wall-Superconductivity, DWS) or on top of magnetic domains in reverse direction to an external applied magnetic field (Reverse-Domain-Superconductivity, RDS) [7]. Magnetic exchange fields from the F layer affect the superconducting state via Pauli pair breaking [8–11]. Current progress in unconventional exchange mechanisms reveals a generation of spin-triplet Cooper pairs by a non-collinear magnetic arrangement [12].

The inverse effect, a change of the magnetic structure in S/F bilayers by the onset of superconductivity, is less examined experimentally because of relatively small variations in the ferromagnetic state with much higher Curie temperature compared to the S critical temperature arising in low-temperature superconductors like Nb [6]. High sensitivity and a depth-resolved probe are required to determine slight changes in the

magnetic orientations.
This work combines a macroscopic analysis on field-dependent domain-superconductivity and spin-triplet Cooper pair generation with a microscopic study of the lateral depth-resolved magnetization. By neutron scattering techniques, an inverse proximity effect near the S/F interface is probed. The Distorted-Wave Born Approximation (DWBA) extended by a serpentine domain structure and the paracrystal theory proves to be a powerful tool in determining the lateral magnetic depth-profile.

Outline of this thesis

The main principles of proximity and inverse proximity effects in thin film S/F heterostructures (with F being a domain structured ferromagnet) are introduced at the beginning of this thesis in **chapter 2**. First, general information on ferromagnetism, magnetic anisotropy, and FePd thin films in detail are presented, followed by the theory of superconductivity with a focus on the type-II superconductor Nb and its properties in a defected, thin film form. These antagonistic phenomena, ferromagnetism and superconductivity, are brought together in the sections on proximity effects, first introduced by the more easy example of superconductor/normal-metal (S/N) structures, and secondly expanded to proximity and inverse proximity effects in S/F heterostructures.

An inherent part for the characterization of S/F samples on a mesoscopic length scale is the Grazing-Incidence Small-Angle Neutron Scattering (GISANS) method. **Chapter 3** describes the essential elements of neutron scattering employed in this thesis. It concludes with a model of maze domain structured ferromagnetic samples with PMA, including triangular shaped closure domains and Bloch domain walls, in the framework of the DWBA and considering the paracrystal theory. This model was designed within the context of this thesis by Dr. Emmanuel Kentzinger.

The S/F thin film heterostructures were grown by Molecular Beam Epitaxy (MBE) and studied in-situ and ex-situ using in-house, macroscopic measurement methods presented in **chapter 4**. This chapter also outlines the instrument setups of the applied large-scale facility instruments GALAXI (Forschungszentrum Jülich, Germany), KWS-3 (MLZ in Garching, Germany), and vSANS (NCNR at NIST in Gaithersburg, USA).

The discussion is divided into three main parts: (i) a description of the growth methods of FePd with controllable strength of PMA and domain configuration, and the characterization of samples at room temperature in **chapter 5**, (ii) a comprehensive study of proximity effects at low temperatures by magnetization and magnetotransport measurements with respect to the strength of PMA and the orientation of an external magnetic field in **chapter 6**, and (iii) polarized and unpolarized GISANS measurements on S/F samples with high PMA in **chapter 7**, which were shown to allow an investigation of inverse proximity effects and a reorganization of magnetic moments inside the FePd layer due to the onset of superconductivity.

A comprehensive conclusion summarizing all main results is given in the **Summary 8**, a more detailed résumé can be found at the end of chapters 5-7.

Chapter 2

Superconductor-Ferromagnet Interactions

2.1 Ferromagnetism

In this section, the basics of ferromagnetism, magnetocrystalline anisotropy and magnetic domain formation in $L1_0$-ordered FePd thin films are discussed.

2.1.1 Basics of ferromagnetism

Ferromagnetic materials exhibit a spontaneous magnetization, originating from exchange interactions between the electrons. This exchange mechanism is based on the Pauli principle and the Coulomb interaction between two electrons on sites i an j with their respective spin orientations $\vec{S}_i$ and $\vec{S}_j$. It is formulated using the Heisenberg Hamiltonian $\mathcal{H}_{\text{Heisenberg}}$. Together with an external applied magnetic field $\mu_0\vec{H}_{\text{ext}}$ which acts on the sample via the Zeeman interaction term $\mathcal{H}_{\text{Zeeman}}$, the Hamiltonian is written as in (2.1) [13]:

$$\mathcal{H} = \mathcal{H}_{\text{Heisenberg}} + \mathcal{H}_{\text{Zeeman}}, \tag{2.1a}$$

$$\mathcal{H} = -\sum_{i,j} J_{i,j}\vec{S}_i \cdot \vec{S}_j + g\mu_B \sum_{j} \vec{S}_j \cdot \mu_0\vec{H}_{\text{ext}}, \tag{2.1b}$$

with the exchange constant $J_{i,j}$ between the i^{th} and j^{th} electrons, the g-value of electrons, and the Bohr magneton μ_B. In case of a ferromagnetic exchange interaction, $J_{i,j}$ has to be positive. To simplify and solve 2.1, the Heisenberg Hamiltonian can be rewritten in terms of the effective molecular field approximation (“Weiss model of ferromagnetism”), in which a fictive molecular field B_{mf} of all surrounding electrons acts on one electron on site i. In this model, the exchange interaction is replaced by B_{mf}, and hence in ferromagnetic materials B_{mf} aligns electrons also in the absence of an applied field below the Curie temperature T_{Curie} [13]. As ferromagnetic exchange interactions favor a parallel alignment of the electron spins, the density of states $D(E)$ is shifted for spin-up spins (i.e. parallel to B_{mf}, majority spins) and spin-down spins (i.e. antiparallel to B_{mf}, minority spins), as depicted in Fig. 2.1 [14] for ferromagnetic metals.

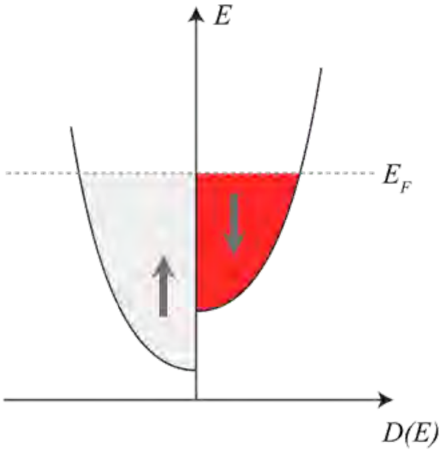

Figure 2.1: Density of states $D(E)$ for a metallic ferromagnet with majority spin up and minority spin down bands filled up to the Fermi energy E_{F}.

The increase in $D(E)$ for the majority spins as compared to the minority spins correlates with an increase in the kinetic energy, which has to be compensated by lowering the potential energy in terms of Coulomb interactions. The so called "Stoner-criterion" describes the conditions for an occurrence of ferromagnetism by comparing the Coulomb energy U and $D(E_F)$ and is in detail described in ref. [15].

2.1.2 Magnetic anisotropy

Pure exchange interactions as described above can explain basic principles of metallic ferromagnetism, but they cannot account for the existence of a spontaneous formation of domains and domain walls as they exist in $L1_0$-ordered FePd thin films. Each domain wall increases the energy state of the electrons and is unfavorable in the sole presence of exchange interactions with energy E_{ex} in an applied field with an energy E_{Zeeman} [13]. Further contributions to the total energy which can describe the domain formation in a thin film are the magnetic anisotropy energy E_{ma} and the demagnetizing energy E_{d} (includes stray fields/ shape effects), leading to $E_{\mathrm{tot}} = E_{\mathrm{ex}} + E_{\mathrm{Zeeman}} + E_{\mathrm{ma}} + E_{\mathrm{d}}$ [15]. The magnetic anisotropy energy again needs to be divided into parts originating from crystal anisotropies (like the uniaxial anisotropy in tetragonal crystals) and induced anisotropies (from lattice defects or applied strain) [16]. Here, additionally the shape anisotropy acting via stray fields is attributed to the magnetic anisotropy effects as in ref. [15]. Due to magnetic anisotropy, the magnetization $\vec{M}$ along a given anisotropy axis is favored and any deviation from this orientation is related to an increase in energy by E_{ma}:

$$E_{\mathrm{ma}} = K \sin^2(\theta), \tag{2.2}$$

with K being the anisotropy constant and θ as angle between the anisotropy axis and $\vec{M}$ [15]. For tetragonal systems like FePd in the L1_0-ordered phase, the important contributions to the magnetic anisotropy are (i) the uniaxial magnetocrystalline anisotropy with constant K_{u} and (ii) the shape anisotropy with constant K_{sh}, and are explained in detail in the following.

The magnetocrystalline anisotropy energy E_{a} originates from spin-orbit coupling, which depends strongly on the crystallographic axes. In uniaxial systems, only one easy axis direction exists [16]. A magnetic field H_{a} needed to align electron spins along the hard axis of an uniaxial system is given by (2.3a) and its uniaxial anisotropy constant K_{u} by (2.3b) [17].

$$H_{\mathrm{a}} = \frac{2K_{\mathrm{u}}}{\mu_0 M_{\mathrm{S}}}, \tag{2.3a}$$

$$K_{\mathrm{u}} = \frac{1}{2} M_{\mathrm{S}} \mu_0 H_{\mathrm{sat}}, \tag{2.3b}$$

with H_{sat} being the saturation field along the hard axis, and M_{S} the saturation magnetization.

The shape anisotropy with energy E_{d} is governed by the form and size of the sample and is caused by the internal magnetization distribution, which creates a demagnetizing field $\vec{H}_{\mathrm{d}}$. $\vec{H}_{\mathrm{d}}$ is given by (2.4a) with a shape-related demagnetizing tensor $\mathcal{N}$, and its anisotropy constant K_{sh} complies (2.4b). With $\vec{H}_{\mathrm{d}}$, also the stray fields outside the sample are generated.

$$\vec{H}_{\mathrm{d}} = -\mathcal{N}\vec{M}, \tag{2.4a}$$

$$K_{\mathrm{sh}} = \frac{1}{4}\mu_0 M_{\mathrm{S}}^2 (1 - 3N), \tag{2.4b}$$

with N being the component in the easy magnetization direction. In a thin film, $\mathcal{N}$ can be diagonalized and obtains a non-zero factor only in direction of the film normal [13]. The absolute value $|\vec{H}_{\mathrm{d}}| = H_d$ is minimized by non-zero components parallel to the surface plane. The internal magnetic field is approximately the sum of an applied field H_{ext} and H_{d} [15] and the shape anisotropy increases with decreasing layer thickness.

A formation of magnetic domains (with domain walls seperating the domains) increases the exchange energy, but reduces the stray field energy, especially via an insertion of closure domains [13]. Inside each domain, the magnetization direction is approximately homogeneous along the easy axis. Between domains, the magnetization rotates from one domain orientation to the other. In films with strong Perpendicular Magnetic Anisotropy (PMA), domain walls typically are of Bloch-type with the rotation axis perpendicular to the wall plane [16]. To reduce stray fields, closure domains are formed at the sample surfaces [13]. These closure domains are illustrated together with the out-of-plane domains and their respective domain walls in fig. 2.2. The two Bloch wall orientations shown above the domain structure depict the rotation of magnetic moments from closure domains on top of the thin film to the bottom of the thin film (left) and from out-of-plane domains in $+z$-direction to $-z$-direction (right). Here, the z-direction denotes the easy magnetization axis perpendicular to the surface plane. This model is similar to a model proposed from Navas et al. for thin film FePd [18]. In contrast to the model proposed in [18], here a continuous helical propagation vector is assumed, i.e. with a magnetization in $+\vec{x}$ and -$\vec{x}$ alternating from domain wall to domain wall. Such a domain wall magnetization is proposed due to results in the analysis part of the present thesis (see chapter 7).

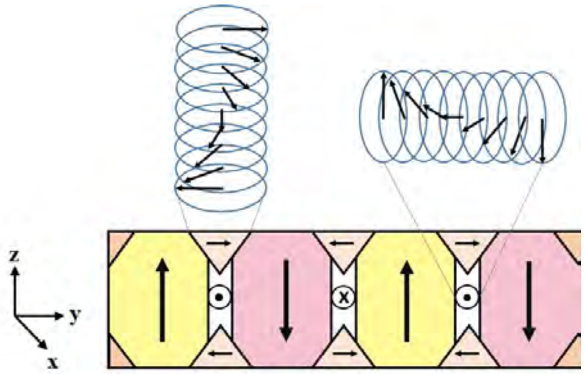

Figure 2.2: Sketch of a thin film with magnetic domains in out-of-plane direction, separated by Bloch domain walls and with closure domains at the sample surfaces.

In the case of uniaxial anisotropy, the energy density of the Bloch domain wall per unit area σ_{DW} is calculated by (2.5a), with a domain wall width w_{DW} of (2.5b), both determined by the exchange constant A and the anisotropy constant K_{u} [13].

$$\sigma_{\mathrm{DW}} = \pi\sqrt{AK_{\mathrm{u}}}, \tag{2.5a}$$

$$w_{\mathrm{DW}} = \pi\sqrt{\frac{A}{K_{\mathrm{u}}}}. \tag{2.5b}$$

Summarizing, thin films with a tetragonal crystal symmetry and with $\mathrm{L1_0}$-ordering lead to an easy axis in c-direction, i.e. along <001> (see for details chapter 5) [19]. Due to their relevance for magnetic recording media, thin films exhibiting $\mathrm{L1_0}$-ordering are grown with their c-axis parallel to the surface normal to increase the uniaxial anisotropy [17], which in this case leads to strong PMA and periodically arranged magnetic domains of alternating up and down magnetization perpendicular to the film plane [20]. The strength of PMA can be expressed in a quality factor Q, given by the ratio of K_{u} and K_{sh} [16]. For $Q>1$ the thin film has a strong PMA, whereas $Q<1$ denotes an in-plane easy axis of magnetization [17].

2.1.3 Domain formation and closure domains in FePd thin films

For the case of FePd thin films with $L1_0$ structural ordering and the easy magnetization axis in <001>-direction, a formation of closure domains on the sample surface to reduce the stray field energy has been proposed and investigated by Duerr et al. [21]. Further studies using soft x-ray resonant magnetic scattering improved the understanding of magnetization orientation in FePd with respect to the degree of PMA by inserting Bloch domain walls in between the out-of-plane domains [20, 22]. For weak PMA, the in-plane magnetization components inside the walls and closure domains are strong and a slight preferential magnetization direction in the surface plane can cause a spontaneous alignment of the magnetic domains visible by Magnetic Force Microscopy (see chapter 4.3.4). High PMA with $Q \gg 1$ leads to a "maze" domain structure and small or no closure domains. Micromagnetic simulations on samples with low PMA (see fig. 2.3(a), for Q=0.35) and with high PMA (see Fig. 2.3(b), for Q=1.5) show the different size of Bloch domain walls and closure domains depending on Q. The domain formation also governs the typical shape of the hysteresis curve. For magnetic recording media with typically high PMA, the magnetization with respect to an external magnetic field is shown in fig. 2.3(c), together with the domain evolution at each step.

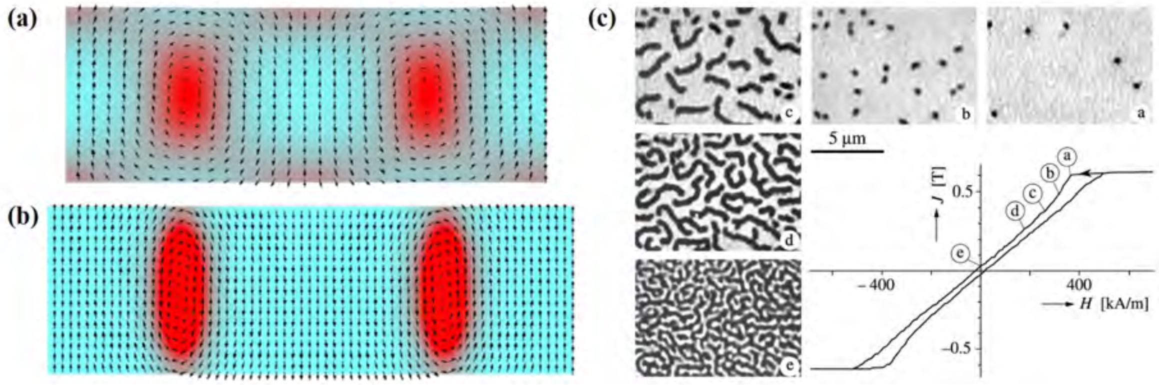

Figure 2.3: (a,b) Micromagnetic simulation for FePd layers with 40 nm thickness and (a) Q=0.35 and (b) Q=1.5, taken from [22]. (c) Bubble and band domain growth in a perpendicular recording medium (Co with 20 at% Cr) of 622 nm thickness, taken from [16].

Coming from saturation, the magnetization drops fast while cylindrical domains ("bubble domains") in opposite direction to the external field nucleate. Upon further reduction of the external field, these cylindrical domains evolve into a maze structure which results in a linear magnetization [16].

2.2 Superconductivity

This section provides an overview on the basic mechanisms occuring in defected, thin film, and low temperature superconductors like Nb. First, the microscopic theory by Bardeen, Cooper and Schrieffer (BCS-theory) on the origin of the superconducting state is presented, followed by the phenomenological Ginzburg-Landau (GL) theory. After an introduction into basic tools, aspects on impurity and size effects following from the GL theory and its further developments are presented. The last sections briefly deal with the magnetization of defected thin film type-II superconductors, with a focus on Nb.

2.2.1 Microscopic theory

The condensation of conduction band electrons into a superconducting state of lower energy can be described microscopically with a theory developed by Bardeen, Cooper and Schrieffer [23, 24]. The main aspect is a formation of sets of two electrons in the normal conducting state near the Fermi energy E_F into a bound pair of energy below E_F via an attractive potential given by an interaction with lattice vibrations [25, 26]. In a simplified model, the two electrons are interacting only with each other over long distances via the Coulomb repulsion and a virtual exchange phonon with wave vector $\vec{q}$, resulting in a retarded interaction process (see Fig. 2.4). The negative charge of one electron is screened by nearby attracted positive ions, leading to vibrations of the positive ions with a plasma frequency $\Omega_p(\vec{q})$ and to the attraction of the second electron. The total interaction potential V is attractive, if the phonon mediated part predominates over the Coulomb interaction of the electrons. This is accomplished if the energy difference of the electrons before and after the phonon exchange is $(E_{\vec{k}} - E_{\vec{k}'}) < \hbar\Omega_p(\vec{q}) \ll E_F$ [14, 23]. Each such a pair of electrons is called a Cooper pair. This model already contains basic superconducting properties found in earlier experiments like the Meissner effect [27] and infinite conductivity [28], but is missing any boundary conditions or spatial inhomogeneities [29].

The single wavefunctions of both electrons can be described by Bloch states with momentum $\vec{k}$ and spin $\vec{\sigma}$. In the BCS approach, a virtual phonon transfers a momentum $\hbar\vec{q}$ from an electron with wavevector $\vec{k}_1$ to a second electron with wavevector $\vec{k}_2$. To determine $\vec{k}_1$ and $\vec{k}_2$ and their respective spin values, two basic principles have to be considered: First, the total momentum has to be conserved. Second, the Pauli principle states that the total wavefunction (consisting of a spatial part $\phi(\vec{r}_1, \vec{r}_2)$ and a spin part $\chi(\vec{\sigma}_1, \vec{\sigma}_2)$) has to be antisymmetric. In case of an isotropic V the spatial part of the total wavefunction has to be symmetric, yielding an antisymmetric spin part. As a result, the ground state of the total wavefunction is built from pairs of electrons with $\vec{k}_1 = -\vec{k}_2$ and $\vec{\sigma}_1 = -\vec{\sigma}_2$. This corresponds to a singlet paired two-electron state with total spin S=0 and a projection on the spin quantization axis (here z-axis) S_z=0. Figure 2.4 displays the attractive interaction via lattice vibrations together with the direction and spin of singlet Cooper pairs. Due to the weak attractive potential as opposed to the strong Coulomb repulsion, the electrons interact over large distances.

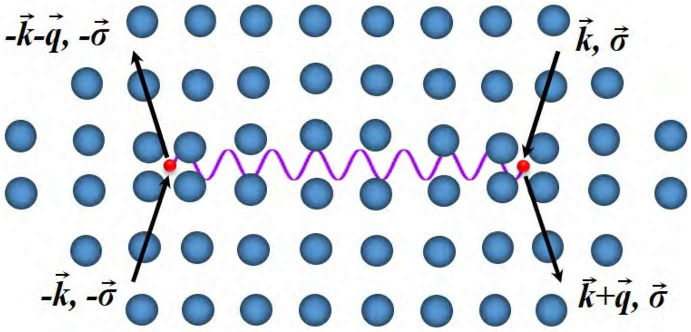
$-\vec{k}-\vec{q}, -\vec{\sigma}$
$\vec{k}, \vec{\sigma}$
$-\vec{k}, -\vec{\sigma}$
$\vec{k}+\vec{q}, \vec{\sigma}$

Figure 2.4: Attractive phonon interaction vs. repulsive Coulomb interaction of a spin-singlet Cooper pair.

In section 2.4.2 it is shown that also wavefunctions of spin-triplet Cooper pairs with S=1 can be stable under certain conditions, which was already suggested by BCS [24]. Possible spin wavefunctions and their respective total spin values and quantum numbers are listed in table 2.1 [14]. A BCS ground state of spin-singlet Cooper pairs consists of symmetric orbital wavefunctions like s-wave or d-wave character, whereas antisymmetric orbital wavefunctions belong to p-wave or f-wave symmetries.

S	S_z	wavefunction in Dirac-notation
0	0	$\frac{1}{\sqrt{2}}(\lvert\uparrow\downarrow\rangle - \lvert\downarrow\uparrow\rangle)$
1	-1	$\lvert\downarrow\downarrow\rangle$
1	0	$\frac{1}{\sqrt{2}}(\lvert\uparrow\downarrow\rangle + \lvert\downarrow\uparrow\rangle)$
1	1	$\lvert\uparrow\uparrow\rangle$

Table 2.1: Spin wavefunctions, total spins and spin projection on the z-axis, S_z, of superconducting two-electron systems.

To get an idea about the ground state energy, some theoretical approaches have to be taken into account. As the new BCS ground state consists of a large number of pairs, it is convenient to use an expression of the wave function in second quantization and in the mean-field approach, so that each pair occupation probability depends only on the average occupation probability of all other states. This results in an expectation value $E_{\vec{k}}$ for each occupied state $\vec{k}$ as given in (2.6) [24, 29]:

$$E_{\vec{k}} = \sqrt{|\Delta_{\vec{k}}|^2 + \xi_{\vec{k}}^2}, \tag{2.6}$$

with kinetic single-electron energies $\xi_{\vec{k}}$ (relative to the Fermi energy), and the energy gap $\Delta_{\vec{k}}$ between the BCS ground state and an excited energy state. $\Delta_{\vec{k}} \neq 0$ yields a stable BCS ground state, whereas for $\Delta_{\vec{k}} = 0$ the normal conducting state with all electrons remaining in the Fermi sea will persist until T=0 [29].

Collectively, the concept of the BCS theory not only introduces Cooper pairs and their excitations above the gap, but also links to previous studies from the London [30] and Pippard [31] theories on the magnetic field penetration depth λ_L and a static coherence length ξ_0. λ_L (first described by F. and H. London) corresponds to the depth where the exponentially decaying magnetic field has decreased to $1/e$, in accordance with the perfect diamagnetic behavior of superconductors, i.e. the Meissner effect [27]. If an external magnetic field smaller than a thermodynamic critical field $\mu_0 H_\mathrm{ext} < B_\mathrm{c}$ is applied to the superconductor, it causes a superconducting current circulating in a depth $\sim \lambda_\mathrm{L}$ below the surface to expel the magnetic flux. Above B_c, the formation of Cooper pairs is energetically not favorable and the normal conducting state is retrieved. ξ_0 corresponds to the smallest size of Cooper pair wave packets. It can be compared with the mean free path in normal conductors, as its value is related to the impurity density and a non-local theory has to be applied if any penetrating field is not homogeneous over ξ_0 [29]. Both values, i.e. λ_L and ξ_0, are essential parameters of superconducting materials and depend on the chosen material, on (magnetic and non-magnetic) impurities, and on the material dimensions. These effects will be discussed in detail in the following sections. In the BCS theory, λ_L at $T = 0$ and ξ_0 are given by (2.7) [24].

$$\lambda_\mathrm{L}(0) = \sqrt{\frac{m}{\mu_0 n e^2}}, \tag{2.7a}$$

$$\xi_0 = 0.18 \frac{\hbar v_\mathrm{F}}{k_\mathrm{B} T_\mathrm{c}}, \tag{2.7b}$$

where m and e are the mass and charge of a free electron, μ_0 the vacuum permeability, n the upper limit of Cooper pair density (i.e., all conduction band electrons), v_F the Fermi velocity, and T_c the critical temperature of superconductivity.

However, the microscopic BCS theory fails to describe spatial variations of the superconducting state, e.g. given by surfaces and interfaces [24], which are an integral part of this thesis. In this regard, the authors Bardeen, Cooper and Schrieffer themselves refer to the phenomenological description by Ginzburg and Landau [32].

2.2.2 Ginzburg-Landau theory

Ginzburg and Landau (GL) established a macroscopic theory based on a spatially varying complex wavefunction $\psi(r)$ (also called "order parameter") as parameter for the pair density $n_\mathrm{S} = |\psi|^2$ in a power series of the free energy F and including the interaction with an external magnetic vector potential $\mathbf{A}$ (see (2.8a)) [32]. It predicts electrodynamic responses of the superconductor and can be derived from the microscopic BCS theory as shown by Gor‘kov [33]. The GL theory was a groundbreaking improvement of the London theory [30], which introduced the electrodynamic treatment of superconductivity and considered the superconducting carrier density as constant parameter in space but varying in temperature from zero at the critical temperature T_c to a maximum value at T=0. Aside from λ_L, the GL theory and its extensions by Abrikosov and Gor‘kov use a temperature dependent coherence length $\xi_\mathrm{GL}(T)$ and parameter $\kappa(T) = \frac{\lambda_\mathrm{L}(T)}{\xi_\mathrm{GL}(T)}$.

$$F = F_\mathrm{N} + \alpha|\psi|^2 + \frac{\beta}{2}|\psi|^4 + \frac{1}{2m}|(-i\hbar\nabla - \frac{2e\mathbf{A}}{c})\psi|^2 + \frac{h^2}{8\pi}, \tag{2.8a}$$

$$\xi_\mathrm{GL}^2 \frac{d^2\psi}{dx^2} + \psi - \psi^3 = 0. \tag{2.8b}$$

Equation (2.8a) describes the free energy of a superconducting condensate with the electron mass m and charge e [34]. This formulation already considers that the GL theory can be derived by BCS and that the superconducting particles are Cooper pairs. α and β are expansion coefficients and can be related to ξ_GL. A minimization of (2.8a) with respect to ψ^* (the complex conjugate of ψ) and setting $H_\mathrm{ext} = 0$ yields equation (2.8b) with $\xi_\mathrm{GL}^2(T) = -\frac{\hbar}{2m|\alpha(T)|}$. Thus, ξ_GL represents the coherence length of ψ and denotes the distance over which the wavefunction ψ is varying in space [29]. With the use of κ, GL have shown a fundamental difference between superconducting materials with $\kappa < \frac{1}{\sqrt{2}}$ and $\kappa > \frac{1}{\sqrt{2}}$. In the former case, the surface energy between a superconducting and a normal conducting state is always positive below B_c, resulting in a homogeneous superconducting state. For the latter, the surface energy is negative even below the critical field, resulting in the formation of normal and superconducting areas, later called the type-II superconductors [35]. In this work we focus mainly on the type-II superconductor Nb.

A type-II superconductor consists of three phases dependent on temperature, field, and pressure, separated by two critical fields B_{c1} and B_{c2}: (i) the Meissner phase for $\mu_0 H_{\mathrm{ext}} < B_{\mathrm{c1}}$ in which the external magnetic field is expelled as in type-I superconductors, with a perfect diamagnetic behavior and a positive surface energy, (ii) the Shubnikov phase in the range $B_{\mathrm{c1}} < \mu_0 H_{\mathrm{ext}} < B_{\mathrm{c2}}$ where the surface energy becomes negative and vortices penetrate throughout the sample in direction of the applied field, and (iii) the normal conducting phase. If $\mu_0 H_{\mathrm{ext}} > B_{\mathrm{c2}}$, the external magnetic field exceeds the condensation energy of Cooper pairs and the superconducting phase breaks down. The critical fields B_{c1} and B_{c2} are closely related to the superconducting parameters λ_{L} and ξ_{GL}:

$$B_{\mathrm{c1}}(T) = \frac{\Phi_0}{4\pi\lambda_{\mathrm{L}}^2(T)}(\ln\kappa(T) + 0.08) \tag{2.9a}$$

$$B_{\mathrm{c2}}(T) = \frac{\Phi_0}{2\pi\xi_{\mathrm{GL}}^2(T)}, \tag{2.9b}$$

with the magnetic flux quantum $\Phi_0 = \frac{2\pi\hbar}{2e}$ [36]. Both λ_{L} and ξ_{GL} (and therefore B_{c1} and B_{c2}) are temperature dependent. The exact functions strongly change with the value of $\kappa(T)$ [34]. Near T_{c} (2.10a) and (2.10b) follow from the GL theory including the BCS parameters ξ_0 and $\lambda_{\mathrm{L}}(0)$:

$$\lambda_{\mathrm{L}}(t) = \frac{\lambda_{\mathrm{L}}(0)}{\sqrt{2(1-t)}} \tag{2.10a}$$

$$\xi_{\mathrm{GL}}(t) = 0.74\frac{\xi_0}{\sqrt{1-t}}, \tag{2.10b}$$

with $t = \frac{T}{T_{\mathrm{c}}}$. Near T_{c}, the bulk critical fields are approximately linear functions of t.

Spatial evolutions of $|\psi|^2$ at interfaces of the superconductor to other non-superconducting materials are considered by solving (2.8a) under special boundary conditions. The simplest case is given by a superconductor-to-vacuum interface or to an insulating material with $|\psi| = 0$ at the interface and $|\psi| = 1$ inside the bulk superconductor. Within this approach and assuming the penetration of a homogeneous external magnetic field

$\mu_0 H_{\mathrm{ext}}$, the magnetic field amplitude will decrease after entering the superconducting material within the depth λ_{L}. ξ_{GL} denotes the range of increase in $|\psi|$ (see Fig. 2.5 for a type-II superconductor) [14, 37].

If the superconductor is placed next to a normal conducting metal (N) or to a ferromagnetic material (F), $|\psi|$ will penetrate into the neighboring layer, depending on the electronic band structure of the metal and the interface conditions. This leads to the so called proximity effects which are discussed in detail by de Gennes et al. [38, 39]. A detailed discussion on the proximity to ferromagnetic materials (S/F interfaces) is given in section 2.4.

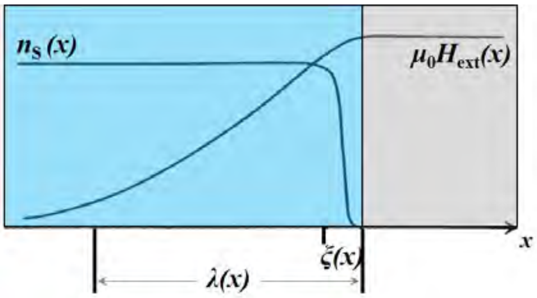

Figure 2.5: Superconductor (blue) to insulator (grey) interface with spatially varying Cooper pair density $n_{\mathrm{S}}(x)$ and the superconducting parameters $\xi_{\mathrm{GL}}(x)$ and $\lambda_{\mathrm{L}}(x)$ in an applied magnetic field $\mu_0 H_{\mathrm{ext}}(x)$.

In analogy to the above discussion, the Shubnikov phase of a type-II superconductor can be described with multiple N/S interfaces by the evolution of normal conducting areas carrying the magnetic flux (vortices). The negative surface energy inside the Shubnikov phase of a type-II superconductor stabilizes the formation of the vortex state [14]. These vortices are surrounded by the superconducting condensate. Inside the vortex cores, $|\psi|$ decreases to 0 in the length scale of ξ_{GL}. Each vortex is surrounded by Cooper pair currents with density J_{S} in a range of λ_{L}, enclosing the magnetic field as shown in Fig. 2.6(a). Typically, one vortex contains exactly one flux quantum Φ_0 [35], but especially in thin film superconductors so called "giant vortices" with $N \cdot \Phi_0$ can be stable [40, 41].

At B_{c1}, the first vortex starts to develop inside the superconductor. With increasing applied field, the density of vortices will increase, yielding a vortex lattice (see Fig. 2.6(b)) with lattice constant $a = \sqrt{\frac{2\Phi_0}{\sqrt{3}\mu_0 H_{\mathrm{ext}}}}$ (under consideration of a triangular lattice and in the absence of pinning effects) [42]. At $\mu_0 H_{\mathrm{ext}} = B_{\mathrm{c2}}$ the vortex lattice has reached a critical density. The vortex cores start to overlap, forming the normal conducting state.

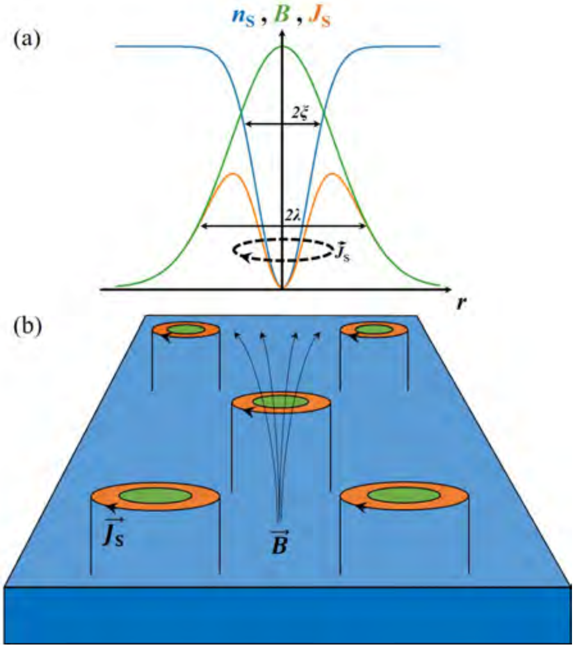

Figure 2.6: Shubnikov phase of a type-II bulk superconductor, inspired from [43]. (a) Radial distribution of the Cooper pair density n_S (blue), the magnetic field B inside the vortices (green), and the supercurrent density J_S enclosing the magnetic field (orange). (b) Top view on a triangular vortex lattice (same color code).

2.2.3 Dirty superconductors

All relations shown in the former section were based on clean superconductors. Typically, a large number of defects reduces the normal state conductance σ of electrons due to a lower value of mean free path l. Analogous to the decrease of σ with l in the normal conducting state, in the superconducting state $\xi_{\mathrm{GL}}(T)$ is reduced with decreasing l, associated with an increase in $\lambda_{\mathrm{L}}(T)$. The case $l \gg \xi_0$ is called "clean limit", $l \ll \xi_0$ is referred to as the "extreme dirty limit" [14, 29]. Equations (2.11) are valid for $T \approx T_{\mathrm{c}}$ in the extreme dirty limit [29].

$$\lambda_{\mathrm{L,dirty}}(t) = \frac{\lambda_{\mathrm{L}}(0)}{\sqrt{2(1-t)}} \cdot \sqrt{\frac{\xi_0}{1.33l}}, \tag{2.11a}$$

$$\xi_{\mathrm{GL,dirty}}(t) = 0.855\sqrt{\frac{\xi_0 l}{1-t}}, \tag{2.11b}$$

$$\kappa_{\mathrm{dirty}}(t) = 0.715\frac{\lambda_{\mathrm{L}}(0)}{l}. \tag{2.11c}$$

Thus, B_{c1} will increase, whereas B_{c2} will decrease upon increasing l. Also the value of κ increases with decreasing l, leading to several investigations on the question if type-I superconductors can become type-II [44][45].

Inducing defects into superconducting materials can also be of practical use, for example to artificially change the intrinsic parameters as mentioned above, or to pin vortices. At the defect position, the free energy of the system is reduced, leading to a favored vortex nucleation [46]. Several groups found a remarkable increased critical current density J_{c} by inserting vortex pinning centers [47, 48]. J_{c} is an essential parameter for superconducting devices like SQUIDS or transistors.

However, when the size of the superconducting material is reduced, surface and confinement effects become an important issue and need to be considered.

2.2.4 Small superconductors

If one or more dimensions of the superconducting system is smaller than λ_{L} and/or ξ_{GL}, it is called a “small” superconductor. Peculiar effects arise for example due to an incomplete Meissner effect when λ_{L} is larger than the layer thickness d, and the magnetic field penetration is nearly homogeneous in the superconductor [49, 50]. Also a change in the density of states and the phonon modes at the sample surface (important for electron-phonon coupled BCS superconductors) can cause variations from bulk effects [43]. In literature, mostly impacts on B_{c}, T_{c} and J_{c} are discussed as they influence device operations, which in turn result from changes in λ_{L} and ξ_{GL}. Two major regimes of small superconductors are first the mesoscopic regime with sizes down to approximately 20 nm, and second the quantum size regime below 20 nm. Further on I will concentrate on the mesoscopic regime, as the used Nb films are of thicknesses similar to λ_{L} and ξ_{GL} but larger than 20 nm. Within this regime, surface effects and size constraints need to be considered.

Within the Ginzburg-Landau theory, surface effects are introduced by superconductor-to-vacuum interfaces. St. James and de Gennes [51] have examined the GL equations of a semi-infinite sample (which was later extended by the consideration of a thin film with thickness $d < \xi_{\mathrm{GL}}$ [52]). They have shown that for a type-II superconductor in a field applied perpendicular to the sample surface the highest critical field is still B_{c2}, whereas in a field applied in the surface plane, superconductivity will be stable until the so called surface critical field $B_{\mathrm{c3}} > B_{\mathrm{c2}}$. Inserting a semi-infinite sample with the sample surface at $x = 0$ and minimizing the free energy, (2.8a) leads to the eigenvalue problem (2.12) [34]:

$$\frac{1}{2m}(-i\hbar\nabla - \frac{2e}{c}\mathbf{A})^2\psi + \alpha\psi = 0. \tag{2.12}$$

In a parallel field with boundary condition $\frac{d\psi}{dx} = 0$, the solution of (2.12) is given by the eigenvalue α:

$$\alpha = -g_0\frac{e\hbar}{mc}\mu_0 H_{\mathrm{ext}}, \tag{2.13}$$

with the applied field $\mu_0 H_{\mathrm{ext}}$ and a factor g_0, which turns out to be the inverse proportionality factor between B_{c3} and B_{c2}:

$$B_{\mathrm{c3}} = \frac{1}{g_0}B_{\mathrm{c2}}. \tag{2.14}$$

The above used boundary conditions for surface superconductivity in a parallel field lead to $g_0 = 0.59$ and $B_{\mathrm{c3}} = 1.69B_{\mathrm{c2}}$. Different to bulk nucleation below B_{c2}, the nucleation for $B_{\mathrm{c2}} < \mu_0 H_{\mathrm{ext}} < B_{\mathrm{c3}}$ appears only near the sample surface as a thin superconducting sheath within a depth of $\sqrt{g_0}\xi_{\mathrm{GL}}$, and ψ varies as shown in Fig. 2.7. As it is purely a surface effect, critical fields measured with magnetization (see chapter 4.3.5) vary from results of resistivity measurements, in which also a thin superconducting surface sheath near B_{c3} changes the resistive behavior [51].

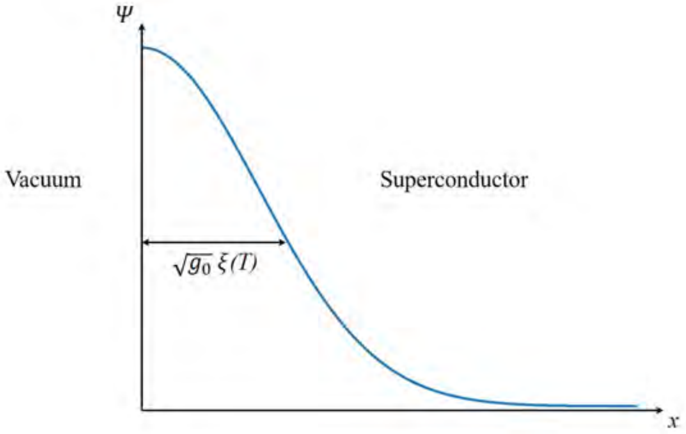

Figure 2.7: Spatial variation of $\psi(x)$ for surface superconductivity in a parallel magnetic field $B_{\mathrm{c2}}<\mu_0 H_{\mathrm{ext}}<B_{\mathrm{c3}}$ at a superconductor to vacuum interface.

In thin films with two boundary conditions at every side of the superconductor, the same considerations with two boundary conditions instead of one have to be done. Apart from the critical fields also the actual values of λ and ξ vary with the film thickness due to surface boundary effects as well as structural anisotropies [53]. For convenience (and as in resistivity measurements it cannot be distinguished between $B_{\mathrm{c}2}$ and $B_{\mathrm{c}3}$), the highest critical field for an in-plane direction of the external magnetic field will be called $B^*_{\mathrm{c},||}$. In out-of-plane direction the highest critical field is not affected by surface effects and it holds that $B^*_{\mathrm{c},\perp} = B_{\mathrm{c}2}$ [29]. Similarly, the effective (dirty) λ_{L} and ξ_{GL} are now defined as $\lambda_{L,||}$ and $\xi_{\mathrm{GL},||}$ for the components parallel to the thin film surface and $\lambda_{L,\perp}$ and $\xi_{\mathrm{GL},\perp}$ for the components perpendicular to the thin film surface. For a first overview, the ratio of $B^*_{\mathrm{c},||}$ to $B_{\mathrm{c}2}$ is given in (2.15) for the limits of very small and very large film thicknesses d .

$$\frac{d^2}{\xi^2_{\mathrm{GL}}(T)} \ll 1 : \frac{B^*_{\mathrm{c},||}}{B_{\mathrm{c}2}} \rightarrow \mathrm{inf}, \tag{2.15a}$$

$$\frac{d^2}{\xi^2_{\mathrm{GL}}(T)} \gg 1 : \frac{B^*_{\mathrm{c},||}}{B_{\mathrm{c}2}} = 1.69. \tag{2.15b}$$

If $d \ll \xi_{\mathrm{GL}}$, the angular dependence between the critical fields in (2.16) was obtained by Tinkham [54]:

$$\left|\frac{B_{\mathrm{c}}(\theta)^* \sin\theta}{B^*_{\mathrm{c},\perp}}\right| + \left|\frac{B_{\mathrm{c}}(\theta)^* \cos\theta}{B^*_{\mathrm{c},||}}\right| = 1 \tag{2.16}$$

A more precise dependence of the superconducting values on d for the dirty limit can only be analytically calculated for the limits (i) $d > 2\xi_{\mathrm{GL}}$ [55, 56] and (ii) $d < \xi_{\mathrm{GL}}$ [52]. Additionally, Lawrence and Doniach [57] have shown that taking into account an anisotropic Ginzburg-Landau theory, the highest critical field (as it is characterized by vortices in the direction of the field with currents enclosing the vortex in a plane perpendicular to the field direction), is given by the anisotropic coherence length values in a direction perpendicular to the applied field [29]. $B^*_{\mathrm{c},\perp}$ will only depend on $\xi_{\mathrm{GL},||}$, whereas $B^*_{\mathrm{c},||}$ depends on $\xi_{\mathrm{GL},||}$ and $\xi_{\mathrm{GL},\perp}$. For the first case with $d > 2\xi_{\mathrm{GL}}$, equations (2.17) (using the dirty coherence length given in (2.11b)) are a good approximation to the critical fields [51, 55].

$$B^*_{\mathrm{c},\perp}(t) = \frac{\Phi_0}{2\pi\xi^2_{\mathrm{GL},||}(0)}(1-t), \tag{2.17a}$$

$$B^*_{\mathrm{c},||}(T) = \frac{1.69\Phi_0}{2\pi\xi_{\mathrm{GL},||}(0)\xi_{\mathrm{GL},\perp}(0)}(1-t). \tag{2.17b}$$

Strictly speaking, for $d<\xi_{\mathrm{GL}}$ a model developed by Pippard [31] based on non-local electrodynamics in the framework of BCS gives the exact solutions for thin, dirty films [52]. However, Harper and Tinkham [52] stated that deviations to the local theory are minor and can be neglected. Thus, (2.18) provide good approximations to the upper critical fields:

$$B^*_{\mathrm{c},\perp}(t) = \frac{\Phi_0}{2\pi\xi^2_{\mathrm{GL},||}(0)}(1-t), \tag{2.18a}$$

$$B^*_{\mathrm{c},||}(t) = \frac{\sqrt{3}\Phi_0}{\pi d\xi_{\mathrm{GL},\perp}(0)}\sqrt{1-t}. \tag{2.18b}$$

It should be noted, that the model of Lawrence and Doniach [57] as developed for layered superconducting structures is mainly used for the high-temperature superconductors, but can also be applied for thin film low-temperature superconductors like Nb [53, 58, 59]. As can be seen by the above formulas, the highest critical field is always connected to the coherence length. The lower critical field B_{c1} is given by (2.9a) and related to the penetration depth. In bulk superconductors, λ_{L} defines the radius on which screening currents flow around the Abrikosov vortices and where they effectively screen the external magnetic field. For thin films with $d \ll \lambda_{\mathrm{L}}$, Pearl [60] has shown that due to the geometry of the thin film, the radius of screening currents in an external magnetic field perpendicular to the film plane extends to the Pearl penetration depth $\Lambda = \frac{\lambda_{\mathrm{L}}^2}{d}$ [60]. The vortex radius broadens with decreasing films thickness. This also has far reaching consequences for the lower critical field, as near T_{c} (2.9a) for thin films is written as (2.19a) [33]:

$$B_{\mathrm{c1},\perp}(T) = \frac{\Phi_0}{4\pi\Lambda^2(T)}(\ln\kappa(T)), \tag{2.19a}$$

$$\Lambda = \lambda_\perp(t) = \frac{\lambda^2_{\mathrm{L,dirty}}(t)}{d}. \tag{2.19b}$$

Nonetheless, the density n_S of Cooper pairs is not altered by Λ but still related to λ_L [29].

All together, the above formulas suggest a decrease of B_{c1} with d, but an increase of B_{c2}, as ξ_{GL} decreases with the mean free path and hence with d. In contrast, the incomplete Meissner effect occuring at $\lambda_L<d$ causes an increase of B_{c1}, and in the quantum size regime, B_{c2} decreases with size reduction [61].

2.2.5 Magnetization of type-II superconductors

Magnetic hysteresis loops in dependence on an external magnetic field $M(H)$ are a basic probe to investigate the superconducting state. In the Shubnikov phase, the formation of vortices and their movement in a magnetic field strongly determines the magnetic behavior, and pinning of vortices by structural or magnetic defects can influence the magnetization drastically. First, $M(H)$ for an ideal bulk type II superconductor will be presented, followed by a short description of pinning and shape effects.
In the Meissner state, the penetrating magnetic flux is fully screened by supercurrents flowing below the surface and it holds $M = -\mu_0 H_{ext}$. After passing B_{c1}, vortices form inside the superconductor with increasing density as the magnetic field rises (see chapter 2.2.2). This leads to susceptibilities $\chi \neq -1$ and the magnetic induction inside the sample becomes nonzero. The value of magnetization will decrease monotonically until B_{c2} is reached and the normal state of the material is recovered. Figure 2.8 shows schematically the reversible $M(H)$ loop of a perfect, non-defected bulk superconductor with the Meissner phase in applied fields below B_{c1} and the Shubnikov phase in applied fields $B_{c1}<\mu_0 H_{ext}<B_{c2}$.

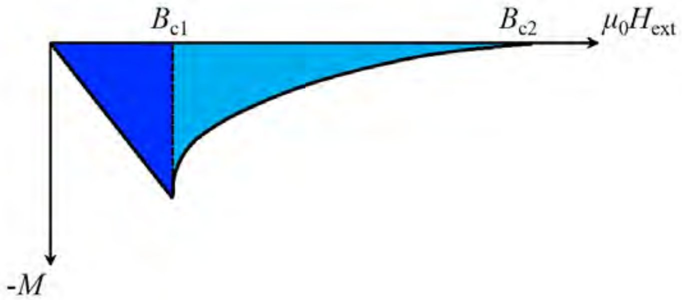

Figure 2.8: Magnetization with respect to external magnetic field for a perfect undefected bulk type-II superconductor with critical fields B_{c1} and B_{c2}.

Structural or magnetic defects, grain boundaries, and their impact on hysteresis loops

were studied by various groups, resulting in two well-known theories - (i) the Bean model where the critical current density are assumed to be field-independent [62] and (ii) the Kim-Anderson model which introduces field-dependent pinning effects and the respective field dependent critical current density [63]. Details of these studies are beyond the scope of this work and can be obtained from the literature.
For thin films where also geometrical effects have to be considered, Maksimova et al. [64] have computed the $M(H)$ loops in the Bean and the Kim-Anderson models. Figure 2.9 shows the $M(H)$ loops of a type II superconducting film in a perpendicular applied magnetic field and B_{c2} being larger than the presented field range. The geometry of the film is defined by its width W (i.e., component perpendicular to the applied field) and its thickness d (i.e., component parallel to the applied field).

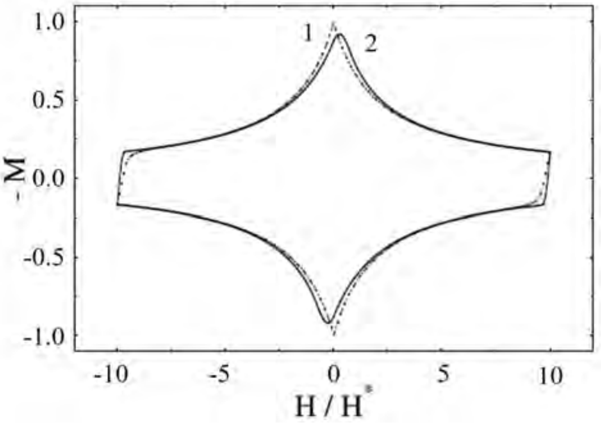

Figure 2.9: Magnetic hysteresis for superconductors including irreversibility mechanisms and bulk pinning (KA-model), taken from [64]. (1) Narrow thin film (i.e., $W < \lambda_{\mathrm{L}}^2/d$ and $d < \lambda_{\mathrm{L}}$) with $H^* = \frac{8\pi j_{\mathrm{p}}\lambda_{\mathrm{L}}^2}{cW}$, and (2) wide thick film with $H^* = \frac{2\pi j_{\mathrm{p}} W}{c}$, with the depinning current density j_{p} and the velocity of light c. The magnetization is given in units of $\frac{j_{\mathrm{p}}W}{8c}$. Note (i) the plot of negative magnetization and (ii) the definition of values in cgs-units.

As was verified experimentally, hysteresis loops of superconductor and normal metal composites result in a superposition of the respective single hysteresis loops [65].

2.2.6 Nb thin films

The work in this thesis focuses on superconducting Nb thin films. Nb as elemental type-II superconductor is an easy-to-grow and thoroughly studied material with relatively high T_{c} (9.26 K in bulk Nb [66]), paving the way for more detailed studies on proximity effects to ferromagnetic materials.

A magnetic hysteresis measurement on bulk Nb is given in Fig. 2.10 and shows the measured B_{c1} and B_{c2} values [67].

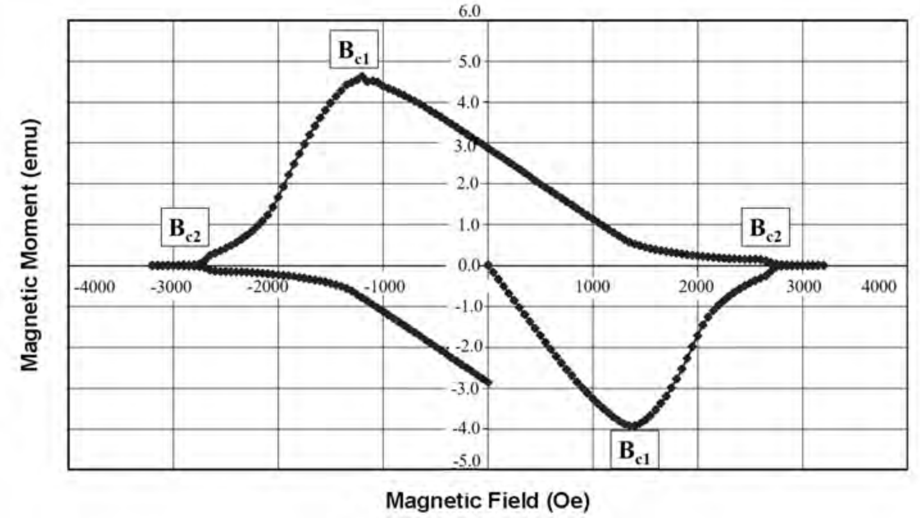

Figure 2.10: Magnetic hysteresis of bulk Nb adapted from [67].

Typical bulk superconducting properties of pure Nb are listed in table 2.2. These values depend markedly on the purity of the investigated Nb and can vary with decreasing mean free path. From (2.11c) it can be derived that κ increases with decreasing purity, the value of 0.7 very near to the transition to type-I superconductivity was obtained for ultra-pure bulk Nb [68]. Particularly, surface oxidation (e.g. due to aging) has a significant impact on the samples properties. Halbritter et al. [69] have studied the oxidation of Nb in air as well as in oxygen atmosphere and have shown that in both cases a Nb_2O_5 layer forms on the Nb surface with a thickness up to 6 nm. Strain and further oxygen dissolution into the bulk Nb lead to a modification of superconducting parameters, like lower T_c and ξ_{GL} as well as higher B_{c2}.

$B_{c1}(0)$	$B_{c2}(0)$	$T_c(0)$	ξ_0	$\lambda_L(0)$	$\kappa(0)$
120 mT [68]	380 mT [68]	9.26 K [66]	40.7 nm [70]	39.0 nm [71]	~0.7 [68]

Table 2.2: Literature values of superconducting parameters for pure bulk Nb.

Schöck et al. [53] have investigated Nb thin films of various thicknesses regarding their upper critical field and coherence length. As explained in section 2.2.4, for thick films in an in-plane applied field typically surface superconductivity exhibits the highest critical field value. However, if $d<\xi_{GL}$ peculiar effects arise. Schöck et al. have shown that depending on the Nb thickness and with decreasing temperature in a field applied parallel to the sample surface, a transition from 2D superconductivity with B_{c2} as highest critical field to surface superconductivity with B_{c3} as highest critical field occurs with decreasing temperature. The 2D superconducting behavior is referred to a square-root dependence of critical field on temperature, as given in (2.18b) for $d<\xi_{\mathrm{GL}}$, whereas surface superconductivity is given by a linear temperature dependence as shown in (2.17b) for $d>2\xi_{\mathrm{GL}}$ (see Fig. 2.11). Arrows mark the reduced temperature t^* at which the crossover from a parabolic 2D temperature dependence to a linear temperature dependence takes place.

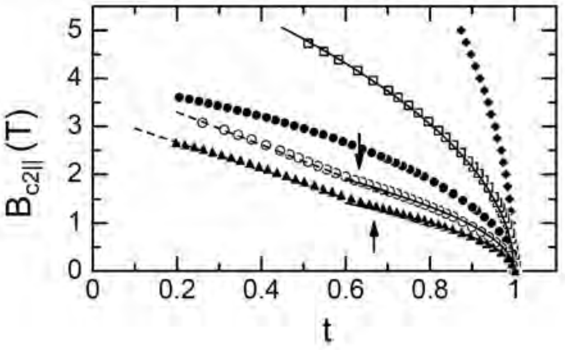

Figure 2.11: Parallel critical field $B_{\mathrm{c2},||}(t)$ measured for Nb thin films, taken from [53]. Arrows indicate the temperature t^* below which surface superconductivity comes into play due to a decrease of ξ_{GL} with decreasing temperature, details can be taken from the main text. Solid and dashed lines show the square-root and linear behavior above and below t^*, respectively.

Their results for Nb films of different thicknesses are listed in table 2.3. For 10 - 27.5 nm, the samples were too thin to show surface superconductivity and no value for $\xi_{\mathrm{GL},\perp}$ was obtained.

d [nm]	$B_{\mathrm{c2},\perp}(0)$ [T]	$B_{\mathrm{c2},\|\|}(0)$ [T]	$B_{\mathrm{c3},\|\|}(0)$ [T]	$\xi_{\mathrm{GL},\perp}(0)$ [nm]	$\xi_{\mathrm{GL},\|\|}(0)$ [nm]
10	4.06	12.67	—	—	9
20	3.97	6.26	—	—	9.1
27.5	3.81	4.46	—	—	9.3
40	3.04	2.74	2.94	18.2	10.4
46	3.10	2.41	2.57	21.0	10.3

Table 2.3: Literature values of thin film Nb [53] at $T = 0$. $B_{\mathrm{c2},\perp}$ and $B_{\mathrm{c2},||}$ were calculated from the coherence lengths.

A thickness dependence of $\lambda_{\mathrm{L}}(0)$ can be measured for example with neutron scattering [72, 73] or high-frequency ac susceptbility techniques [29]. Using microwave resonance and transmission methods, Gubin et al. [74] investigated magnetron sputtered Nb thin films and obtained a dependence of T_c and $\lambda_\mathrm{L}(0)$ on d as shown in Fig. 2.12.

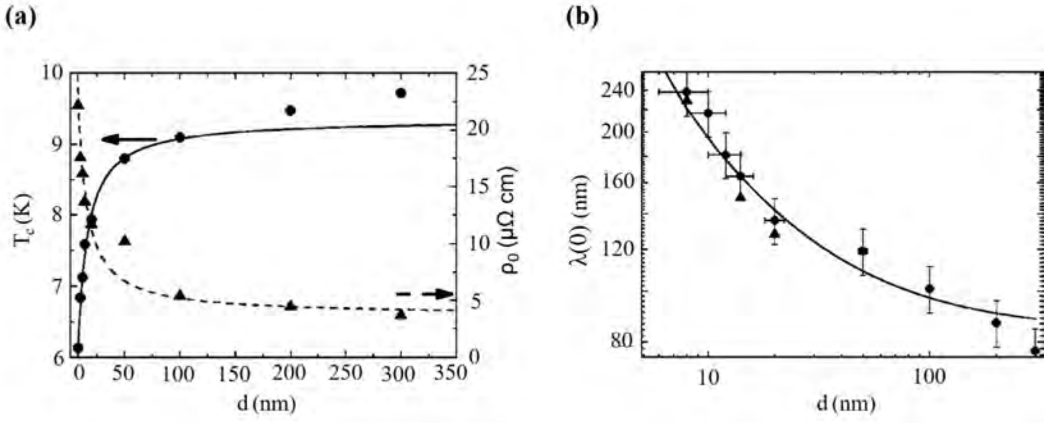

Figure 2.12: Thickness dependence of (a) T_c and the residual resistivity ρ_0 and (b) $\lambda_\mathrm{L}(0)$ at zero temperature for Nb thin films, taken from [74].

2.3 Proximity effects in S/N structures

Proximity effects at any superconductor/normal-metal (S/N) interface cause a spatial variation in the Cooper pair density n as well as in T_c and in the coherence length ξ_GL due to a “leakage” of Cooper pairs from S into N [39]. In other words, the superconducting gap Δ is unequal to zero even inside the metal, decreasing over a length scale ξ_N, which is often referred to a “coherence length” of Cooper pairs inside the metal [39], a “characteristic length of superconducting correlation decay” [6] or a “penetration depth of Cooper pairs” [75]. Due to the reduced density n near the superconductors surface, T_c is reduced from its bulk value [39]. The thinner the superconducting thickness, the stronger T_c will be suppressed and superconductivity will be destroyed if a critical thickness is reached [6, 76].

The density of Cooper pair penetration and its length scale ξ_N are dependent on the interface transparency, temperature, mean free path l, density of states in both materials and other interface conditions like the surface roughness [51]. Here, a perfect interface transparency is given by the condition $\nu_{\mathrm{F}\uparrow}\nu_{\mathrm{F}\downarrow} = \nu_\mathrm{S}^2$, with the two Fermi velocities of the two spin polarizations inside F and the Fermi velocity ν_S inside S [6]. ξ_N can reach long distances inside a metal and is calculated for dirty systems using (2.20) [77]:

$$\xi_\mathrm{N} = \sqrt{\frac{D_\mathrm{N}}{2\pi k_\mathrm{B} T}}, \tag{2.20}$$

with $D_{\mathrm{N}} = \nu_{\mathrm{F}} l/3$ being the diffusion constant of the normal metal and the Boltzmann constant k_{B}. Heterostructures of S/N/S systems where the Cooper pair wavefunctions between both S-layers overlap are used for Josephson-junctions in SQUID devices or for Rapid Single Flux Quantum (RSFQ) logic circuits [77]. Interfaces of a superconductor with vacuum or insulating materials do not show a leakage effect.

A microscopic image of the penetration of Cooper pairs into N is given by Andreev reflections [78] (see Fig. 2.13): Cooper pairs from S are transmitted into N as hole-like and electron-like quasiparticles carrying the superconducting current over the length scale ξ_{N} with a coherent phase relation before they dephase at a distance $z>\xi_{\mathrm{N}}$ from the surface [79]. In the opposite direction, single quasiparticles (electron or hole-like) are not able to pass directly into the superconductor, if the Fermi Energy E_{F} of the normal metal lies in the superconducting gap. Instead, two electrons near the Fermi energy E_{F} with wavevectors $\vec{k}_1 = -\vec{k}_2$ and spins $\vec{\sigma}_1 = -\vec{\sigma}_2$ impinging on the surface are transferred together as Cooper pair into S. More often this is referred to one electron being reflected at the interface as a hole with opposite momentum and spin [80].

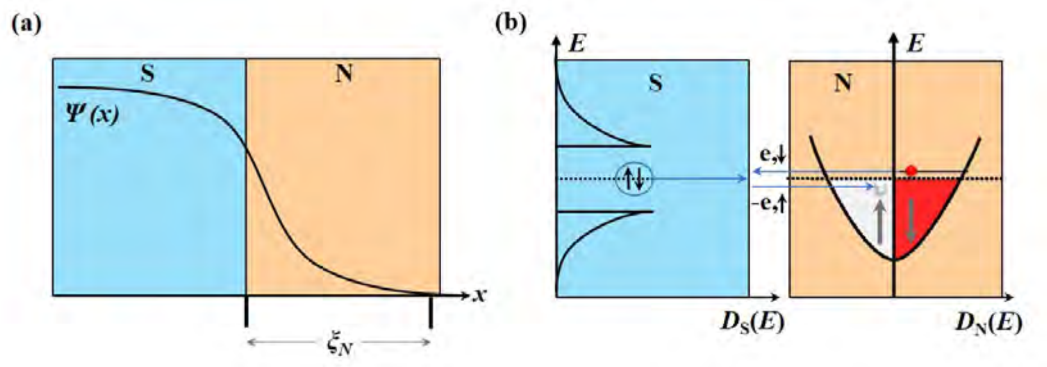

Figure 2.13: S(blue)/N(orange) heterostructure with (a) the order parameter $\psi(x)$ at the interface and the penetration length ξ_{N} of Cooper pairs into N and (b) a schematic sketch of the Andreev reflection. A Cooper pair inside S penetrates in form of quasiparticles with opposite spin and momentum ("electron-like" and "hole-like" quasiparticles) into N and vice versa. Additionally plotted are the density of states $D_{\mathrm{S}}(E)$ inside the superconductor and $D_{\mathrm{N}}(E)$ inside the normal metal, the up and down spin-bands of the normal metal, and the Fermi energy E_{F}.

2.4 Proximity effects in S/F structures

Two fundamental pair breaking effects due to an external magnetic field applied to the superconductor lead to a transition from the superconducting back to the normal conducting state in a superconductor(S)/ferromagnet(F) system. At first, in the so called "orbital effect" a magnetic field acting on the opposite momenta of both electrons in a Cooper pair leads to a circulation of the two electrons around the penetrating magnetic field via the Lorentz force [81, 82]. If a critical field is reached, the electron pairs break and a normal resistant state is recovered. The orbital effect is as well the origin for the vortex state of a type-II superconductor, where the Cooper pairs circulate around each magnetic field vortex. The limiting field is given by the second critical field of a type-II superconductor $B_{c2} = \Phi_0/2\pi\xi^2$.

The second pair breaking effect is originated in the Pauli limitation: the applied magnetic field acts via the Zeeman interaction with both electrons and leads to pair breaking due to an alignment of both electrons if the Pauli limiting field B_p is exceeded [8–11]. Both processes are schematically shown in Fig. 2.14.

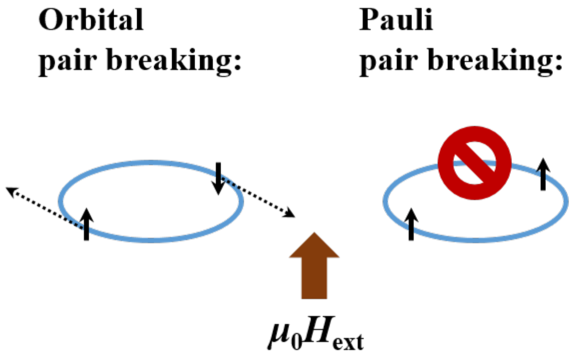

Figure 2.14: Pair breaking effects in spin-singlet Cooper pair components. The orbital pair breaking (left) leads to a circulation of both electrons via the Lorentz force and destroys the Cooper pair above B_{c2}. The Pauli pair breaking (right) leads to an alignment of the spins in a Cooper pair and thus destroys spin-singlet components of Cooper pairs.

Both events limit the total upper critical field, though typically the orbital pair breaking is stronger in bulk systems and the paramagnetic effect can be neglected [83].

The Pauli paramagnetic limit becomes more important in very thin or dirty superconductors [11], or if the S layer is coupled to the exchange field of a ferromagnetic layer [6]. In a S/F system, the exchange field E_ex leads to a lower energy value of spins in a quantization axis parallel ("up") to the exchange field in relation to spins in a quantization axis antiparallel ("down") to the exchange field in the ferromagnetic layer (see Fig. 2.15). Cooper pairs reflecting from the S/F interface in terms of Andreev reflections see different energy values, so that a spin up quasiparticle decreases in energy by E_ex, whereas the spin down quasiparticle increases in energy by E_ex in terms of their kinetic energy values [6].

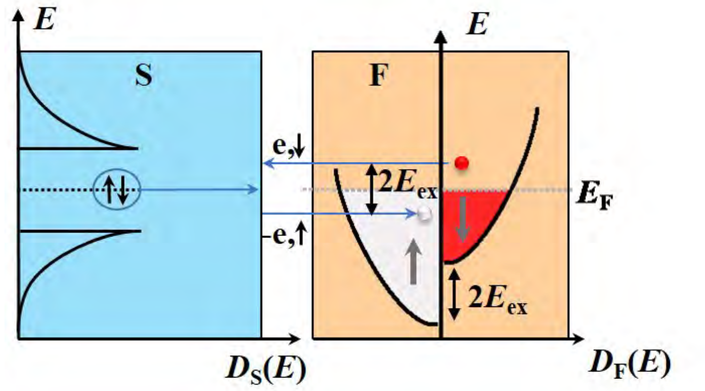

Figure 2.15: S/F interface with Andreev reflection of the two spins of the Cooper pair into different energy bands (red for spin down and white for spin up bands) of the F layer with a resutling difference in energy of $2E_{\mathrm{ex}}$.

The wavevector relation does not comply $\vec{k}_1 = -\vec{k}_2$ (with a zero center of mass momentum) anymore as explained for spin-singlet Cooper pairs in a s-wave superconductor. Their k-values change to $\vec{k}_1 = \vec{k} + \delta\vec{k}$ and $\vec{k}_2 = -\vec{k} + \delta\vec{k}$. The resulting total difference of $2|\delta\vec{k}|$=$2E_{\mathrm{ex}}/\nu_{\mathrm{F}}$ (with the Fermi wavenumber ν_{F}) of the still bound Cooper pair results in a center-of-mass momentum $\pm\delta\vec{k}$. The Cooper pair wavefunction obtains a phase shift of $2\delta\vec{k}\cdot\vec{r}$ and the spin-singlet Cooper pair with spin configuration $(\uparrow\downarrow - \downarrow\uparrow)$ becomes a mixture of spin-singlet components $(\uparrow\downarrow - \downarrow\uparrow)$ and spin-triplet components with zero total spin $(\uparrow\downarrow + \downarrow\uparrow)$ at the S/F interface (2.22)[84]:

$$\begin{aligned}(\uparrow\downarrow - \downarrow\uparrow) \quad &\rightarrow \quad (\uparrow\downarrow e^{i2\delta\vec{k}\cdot\vec{r}} - \downarrow\uparrow e^{-i2\delta\vec{k}\cdot\vec{r}}) \qquad (2.21)\\ &= \quad (\uparrow\downarrow - \downarrow\uparrow)\cos(2\delta\vec{k}\cdot\vec{r}) + i(\uparrow\downarrow + \downarrow\uparrow)\sin(2\delta\vec{k}\cdot\vec{r}). \qquad (2.22)\end{aligned}$$

A leakage of such Cooper pairs into F leads to an oscillation of the order parameter ψ as function of distance from the S surface, see Fig. 2.16(a). Such an oscillation occuring in S/F structures is a contrast to the monotonic behavior of ψ for S/N proximity effects.

Inside S, $|\psi|^2$ of the spin-triplet components decays to zero, leaving only spin-singlet components in the bulk s-wave superconductor as described by the BCS theory.

Inside F, ψ comprises a complex wavevector and a complex coherence length $\xi_{\mathrm{F}}^{-1} = \xi_{\mathrm{F},1}^{-1} + i\xi_{\mathrm{F},2}^{-1}$ [77]. $\xi_{\mathrm{F},1}$ represents the decay length of Cooper pair penetration inside F, and $\xi_{\mathrm{F},2}$ the oscillation length. For dirty materials $\xi_{\mathrm{F},1} = \xi_{\mathrm{F},2} = \sqrt{D_{\mathrm{F}}/E_{\mathrm{ex}}}$, with the diffusion length $D_\mathrm{F} = 1/3\nu_\mathrm{F} l$ of the F layer. The oscillation comprises a spatially dependent phase which also gives rise to the dependence of all parameters on the ferromagnetic thickness d_F. Figure 2.16(b) shows the oscillation of T_c with d_F for S/F systems in contrast to S/N systems [85].

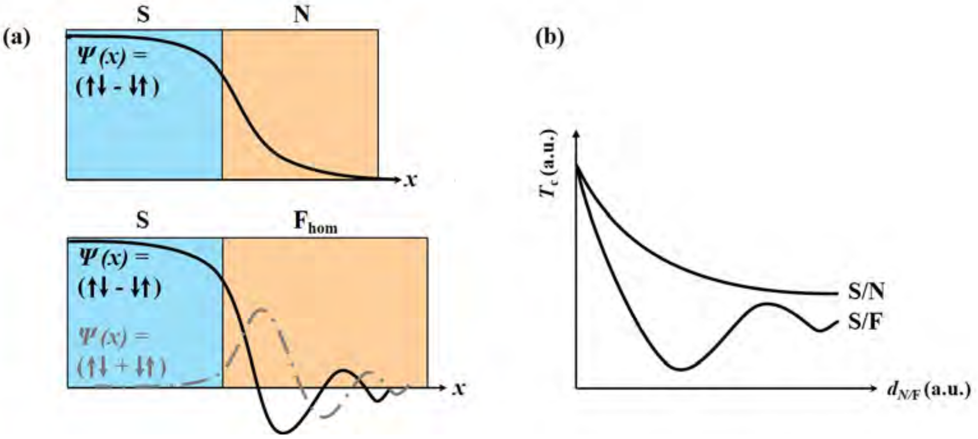

Figure 2.16: Comparison of S/N and S/$\mathrm{F_{hom}}$ proximity effects with a homogeneous magnetization inside $\mathrm{F_{hom}}$. (a) $\psi(x)$ of the spin-singlet components decays monotonically over x inside N. Inside S/$\mathrm{F_{hom}}$, the shift of energy bands for up and down spin orientation leads to an oscillation in $\psi(x)$ and a phase shift for the spin-singlet (black line) and spin-triplet (grey line) components with $S_z = 0$. (b) Dependence of T_c on the thickness of the proximity coupled layer. In S/N, T_c decreases monotonically with increasing d_N, whereas in S/$\mathrm{F_{hom}}$, T_c oscillates with increasing d_F. Figure (b) is inspired from [85].

Usually, $\xi_\mathrm{F} \ll \xi_\mathrm{S}$ (with the coherence length ξ_S of the bulk superconducting state) and the Cooper pair density inside F decays on very short length scales [6]. This oscillatory behavior is also observed for magnetic impurities inside the superconductor, first described by Fulde and Ferrell [86], and Larkin and Ovchinnikov [87] (called FFLO state) and can be described with the same physics.

Another consequence from a direct coupling of F and S is the inverse proximity effect, due to which the magnetization of the F-layer is changed. It can be seen as the opposite case in comparison to a reduction of the superconducting order parameter inside S due to leakage of Cooper pairs into F. The inverse proximity effect leads to three different phenomena described shortly in the following paragraph: (i) an induction of magnetization into S, (ii) the reduction of magnetization of the F layer, and (iii) the so called “cryptoferromagnetic state” [6]. All these phenomena are strong for small thicknesses of F compared to S.

Apart from the exponential decay of any penetrating magnetic field into S and its diamagnetic behavior due to the Meissner effect, the inverse proximity effect leads to an effective orientation of spins inside the S layer. If a metallic ferromagnet with free electrons in the conduction band is in direct contact with a superconducting layer, the proximity effect could lead to the case that one electron of the Cooper pair is located inside F, whereas the other electron is located in S, see Fig. 2.17. The electron within F will contain a spin orientation parallel to the exchange field, leading to an antiparallel spin for the electron in S. Hence, a magnetization in inverse direction to the exchange field inside F will be induced into S. This phenomenon was experimentally observed by Stahn et al. [88] using neutron reflectometry. Additionally, Chakhalian et al. [89] have reported on a rearrangement of the magnetic domain structure and strongly temperature dependent domain and domain wall thicknesses in $YBa_2Cu_3O_7/La_{2/3}Ca_{1/3}MnO_3$ heterostructures after transition into the superconducting state by off-specular neutron reflectivity.

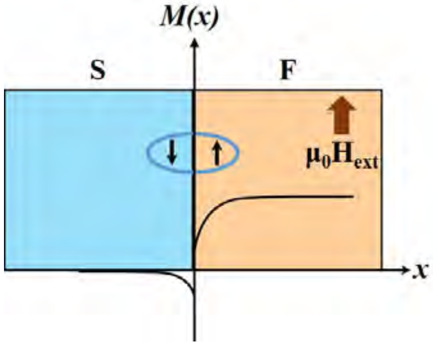

Figure 2.17: Sketch of the inverse proximity effect on the magnetization: the homogeneous magnetization orientation of the F layer can cause spin-singlet Cooper pairs with a spin up electron inside F and a spin down electron inside S. This leads to a reduced magnetization at the interface of the F layer and a reverse magnetization induced at the interface of the S layer.

The second phenomena is simply described by the fact that by the Andreev reflection electrons from F form Cooper pairs inside S and the total density of free electrons inside F is reduced.

Third, the cryptoferromagnetic state is discussed rather ambiguously in the literature and its possible existence could be theoretically predicted only for thin layers of weak ferromagnets with low Curie temperatures and exchange constants [90]. It describes a reformation of magnetization orientation inside the (formerly homogeneous) ferromagnetic layer, if by that the averaged exchange field acting on the superconductor in the region of superconducting coherence length is reduced and leads to an energy minimization of the whole F/S system in the superconducting state. This can, for example, be realized by the formation of a periodic magnetic structure or a domain formation with periodicity much less than the superconducting coherence length [6, 90–92]. Garifullin et al. [93] obtained indications for this state in V/Pd$_{1-x}$Fe$_x$ heterostructures with low x and a Curie-temperature of 100 K below a thickness of the ferromagnetic layer of $\sim 4\,\mathrm{nm}$. However, one of the authors argued that the observed reduced magnetization could also be due to other inverse proximity effects discussed above [92].

2.4.1 Domain-superconductivity

The formerly homogeneous superconducting state in a thin S film can be confined into small areas by taking advantage of the orbital pair breaking effect, if a magnetic field acts only on a small area of the thin film. This is particular to S/F systems with a magnetically domain structured F layer. Superconductivity preferably nucleates where the overlap of the external magnetic field $\mu_0\vec{H}_{\mathrm{ext}}$ with the stray fields $\vec{B}_{\mathrm{d}}$ of the ferromagnet leads to minimum magnetic field strength. If in zero applied field the minimum of $|\vec{B}_{\mathrm{d}}|$ is located above the domain wall (typically for large domain width D_{domain} in comparison to the F thickness d_{F} [94]), superconductivity will first nucleate close to the domain walls while passing T_{c} [7], which is called Domain-Wall-Superconductivity (DWS) (see Fig. 2.18(a)). In an external magnetic field in z-direction, $\vec{B}_{\mathrm{d}}$ is enhanced in direction of $\mu_0\vec{H}_{\mathrm{ext}}$, but compensated in the reverse direction. If due to this field compensation superconductivity is stable only over reverse oriented domains, it is called Reverse-Domain-Superconductivity (RDS) (see Fig. 2.18(b)). To ensure that for the DWS and RDS observation only orbital pair breaking without paramagnetic pair breaking (or direct proximity effects) acts on the Cooper pairs, in most studies an insulating I layer is inserted between S and F.

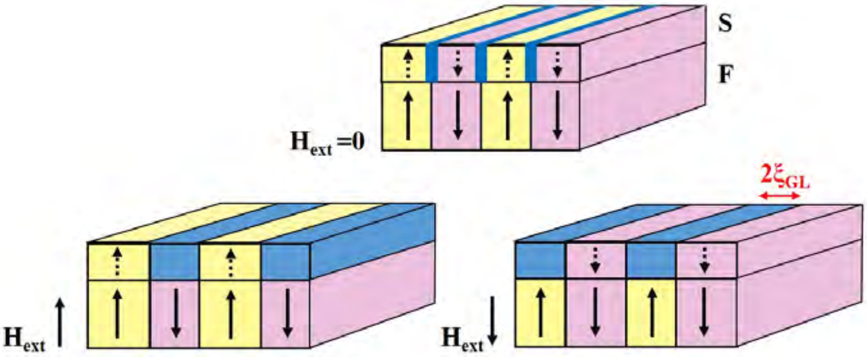

Figure 2.18: Schematic representation of an S/F system with S being a paramagnetic metal above T_c. Domain-Wall-Superconductivity (DWS) nucleates in zero applied field (top) and Reverse-Domain-Superconductivity (RDS) nucleates in an applied field perpendicular to the sample surface (bottom). Blue color denotes superconducting nucleation inside S, whereas yellow and red represent a normal conducting state of F and S in different orientations of magnetization. In the RDS state, in the direction of applied field the superconductor is in the paramagnetic state with stray fields penetrating from the F layer. On top of magnetic domains in reverse direction to the applied field, superconductivity nucleates near T_c. If $2\xi_{\mathrm{GL}} < D_{\mathrm{domain}}$, isolated superconductivity is possible.

Both, DWS and RDS, are limited by the highest critical field B_c^* by the relation $|\mu_0\vec{H}_{\mathrm{ext}} + \vec{B}_{\mathrm{d}}| < B_c^*$ and by the coherence length ξ_{GL} near T_c. If $2\xi_{\mathrm{GL}}(T_c) > D_{\mathrm{domain}}$, superconducting nuclei overlap and no domain superconducting state evolves. In the following and in the analysis section, the highest critical field will be called B_c^*, as it can be limited by various effects like surface superconductivity, size constraints or proximity effects. Near T_c, where B_c^* is in the range of the stray field values, superconductivity is destroyed and recovered by small changes in $\mu_0\vec{H}_{\mathrm{ext}}$. In this way, DWS and RDS can be observed as separate minima in resistance measurements with respect to an applied field. For low T, $|\mu_0\vec{H}_{\mathrm{ext}} + \vec{B}_{\mathrm{d}}| \ll B_c^*$ and superconductivity is stable over both domain orientations in the whole range of $\pm B_c^*$, which is the Complete-Superconducting (CS) state [95].

The formation of stray fields on top of the ferromagnetic layer strongly depends on its domain and layer thicknesses and thus different nucleation processes near zero field are possible. Following the primary theoretical studies of DWS nucleation due to stray fields with a step function of $|\vec{B}_{\mathrm{d}}|$ by Buzdin et al. [96] and Aladyshkin et al. [97], further studies were set up on DWS in different stray field configurations with lateral and transverse inhomogeneity to determine the T_c dependence on an applied field $\mu_0 H_{\mathrm{ext}}$. Aladyshkin and Moshchalkov [98] studied the nucleation of superconducting order parameter in the framework of the GL theory for different ferromagnetic domain thicknesses D_domain and relations of layer thicknesses d_S and d_F of the superconducting and ferromagnetic thin films as function of applied field and assuming stray field configurations of the ferromagnetic layer following equation (2.23) [94]. All these studies assume a pure orbital influence of the stray fields on the superconducting layer without proximity effects, e.g. by introducing a thin insulating spacer layer between S and F.

$$-B_x + iB_z = 4 * M_\mathrm{S} * (\ln(\tan \pi \frac{x + \imath z}{2D_\mathrm{domain}}) - \ln(\tan \pi \frac{x + \imath z - \imath d_\mathrm{F}}{2D_\mathrm{domain}})), \tag{2.23}$$

with the saturation magnetization M_S of the F film and the stray field components B_x and B_z in x and z direction, respectively (note that this equation is given in cgs units).

For an out-of-plane applied field and within an approximation of infinitely thin S layers, they obtained a DWS nucleation at $\mu_0 H_\mathrm{ext} = 0$ for domain periods of $D_\mathrm{domain} \approx 4d_\mathrm{F}$ and a subsequent growth into the nucleation on top of domain centers for increasing field values. For much larger domain periods, no DWS is obtained, whereas for smaller domain periods ($D_\mathrm{domain} \approx d_\mathrm{F}$) the order parameter overlaps over several domains as explained above and a complete superconducting state evolves.

For thick S layers, DWS nucleates also for large $D_\mathrm{domain}/d_\mathrm{F}$ ratios. Figure 2.19 shows the T_c dependence of an out-of-plane applied field H_ext for different S layer thicknesses on top of a domain structured F layer with a large ratio $D_\mathrm{domain}/d_\mathrm{F} = 20$ and a saturation magnetization of $M_\mathrm{S} = 500\,\mathrm{Oe}$. The linear growth of T_c at $H_\mathrm{ext} = 0$ for $d_\mathrm{S} \to 0$ indicates a nucleation on top of the domain centers, whereas a deviation from this linear growth for finite d_S thicknesses indicates DWS nucleation [98]. The dashed line corresponds to the absence of stray fields.

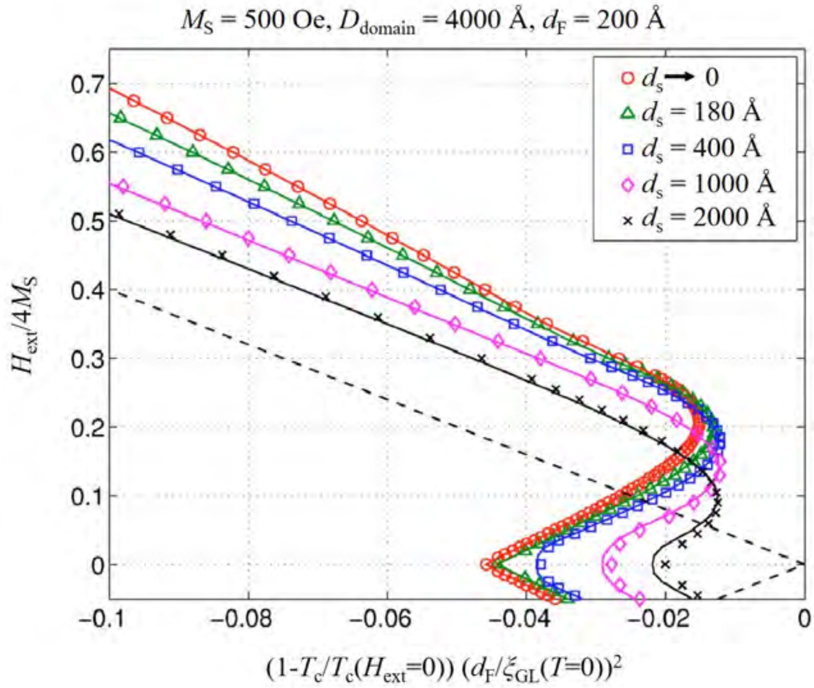

Figure 2.19: The transformation of the phase transition line $T_c(H_{ext})$ with increasing thickness d_S of the superconducting film: $d_S \to 0$ (red), $d_S = 180\,\mathring{A}$ (green), $d_S = 400\,\mathring{A}$ (blue), $d_S = 1000\,\mathring{A}$ (magenta), and $d_S = 2000\,\mathring{A}$ (black). The dashed line is the reference dependence for M_S=0, adapted from [98].

Using again the approximation of a step-like function of B_d and an isolated domain (without periodic structure), Aladyshkin et al. [97] predicted a change of critical temperature ΔT_c^{orb} due to the orbital influence of F on S as given in (2.24a). At low applied fields with a reduced field value in z-direction $b_z = \frac{\mu_0 H_{ext}}{B_{z,max}} \ll 1$ (and $B_{z,max}$ being the amplitude of stray field strength in z-direction), $T_c(b)$ for the evolution of DWS can be calculated by (2.24b), showing a nonlinear dependence of T_c near $H_{ext} = 0$ for DWS.

$$\Delta T_c^{orb} = 2\pi B_{z,max} T_{c(H_{ext}=0)} \xi_{GL}(T=0)^2/\Phi_0, \tag{2.24a}$$

$$T_c(b) = \Delta T_c^{orb}(\frac{1}{2} - E_{min})b^4 + \Delta T_c^{orb}(2E_{min} - \frac{1}{2})b^2 + T_c(0). \tag{2.24b}$$

Here, E_{min} is an eigenvalue of the Ginzburg-Landau equation for the highest possible applied field with superconducting nucleation in special boundary conditions [99], in this case given by the domain-wall-superconductivity. The calculation is based on a model where the domain wall width w_{DW} is much thinner than the Ginzburg-Landau coherence length: $w_{\mathrm{DW}} \ll \xi_{\mathrm{GL}}$ [97]. Experimentally, these observations were first studied by Yang et al. [7, 100], who confirmed a DWS observation following (2.24b).

The influence of domain- and domain-wall superconductivity on the vortex nucleation was experimentally studied by Di Giorgio and Bobba et al. [101, 102] by low-temperature MFM measurements in an applied field perpendicular to the surface of a Nb/Py heterostructure (perpendicular to the lateral domain formation). They observed the confinement of vortices into domains of one orientation for an applied field perpendicular to the sample surface, confirming the above discussed domain superconductivity. Additionally, the vortices still form a hexagonal Abrikosov vortex lattice in the case of straight domains as shown on the left side of Fig. 2.20, whereas no lattice is formed in the presence of magnetic defects (i.e. deviations from a stripe domain formation), as can be seen on the right side of Fig. 2.20. This behavior is similar to the favored vortex nucleation at structural defects due to a reduced free energy at the defect site [46] discussed in section 2.2.3.

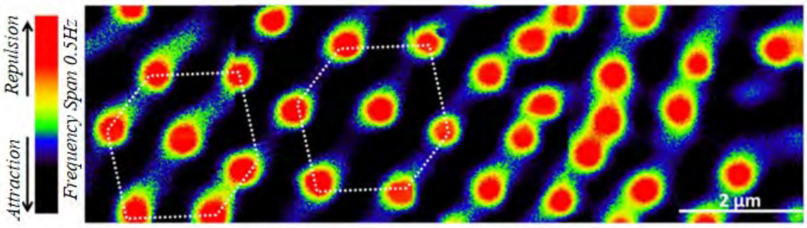

Figure 2.20: Low-temperature MFM measurement of the vortex formation in a Nb/Py heterostructure below T_{c} and acquired in a field of 19 Oe of the MFM-tip, i.e. perpendicular to the sample surface, taken from [101].

2.4.2 Long-range proximity effects

The penetration of Cooper pairs into the ferromagnetic layer of a proximity coupled S/F structure is typically limited to short length scales $\xi_{\mathrm{F}} \ll \xi_{\mathrm{S}}$ [6] due to orbital and paramagnetic pair breaking. Under certain conditions, the penetration depth ξ_{F} into the F-layer is comparable to ξ_{S} and ξ_{N}, in what is referred to as the "Long-Ranged Proximity Effect" (LRPE). Such LRPE can have different origins like aligned spin-triplet Cooper pair components [103], midgap states in d-wave superconductors [104] or the penetration of the spin components of a spin-singlet Cooper pair on each side of a transverse domain wall in a half-metallic ferromagnet [105]. From these, only the formation of spin-triplet Cooper pair components can apply to the S/F structures used in this thesis, as the superconducting material Nb is a s-wave BCS superconductor and the ferromagnetic material FePd is not a half-metallic ferromagnet with full spin polarization in the respective domains.

As discussed in the beginning of this section, in proximity coupled S/F structures spin-singlet Cooper pairs with $(\uparrow\downarrow - \downarrow\uparrow)$ transform into a mixture of spin-singlet and spin-triplet Cooper pair components with zero spin projection on the z-axis, $S_z = 0$ (with the z-axis being aligned with the magnetization axis of the F layer) at the S/F interface, see equation (2.22). These $S_z = 0$ spin-triplet components can turn into $S_z = \pm 1$ spin-triplet components due to a rotating or inhomogeneous magnetic field orientation at the F surface [103], with a magnetic inhomogeneity on the length scale of ξ_{GL}. Due to the spin alignment of both electrons, Cooper pairs with $S_z = \pm 1$ (i.e. $\uparrow\uparrow$ or $\downarrow\downarrow$ along the z-axis of the magnetization inside F) are not shifted in phase by spin dependent energy bands of the F layer. A penetration of spin-triplet components with symmetric spin functions into F does not lead to an oscillation, and the exchange field has no pair breaking effect on the Cooper pairs. Hence, the penetration of such spin-triplet pairs comprises long coherence length $\xi_{\mathrm{F,long}}$ in comparison to $\xi_{\mathrm{F,short}}$ in S/F systems with homogeneous magnetization. $\xi_{\mathrm{F,long}}$ can reach values similar to ξ_{N} in S/N structures and ξ_{S} in bulk superconductors [6]. Spin-singlet components and spin-triplet components with $S_z = 0$ still show an oscillating order parameter inside F with short coherence length. Inside the S layer, the amplitude of all spin-triplet components decays with increasing distance from the S/F surface. A comparison of S/F systems with homogeneous and inhomogeneous magnetization at the interface is schematically shown in Fig. 2.21.

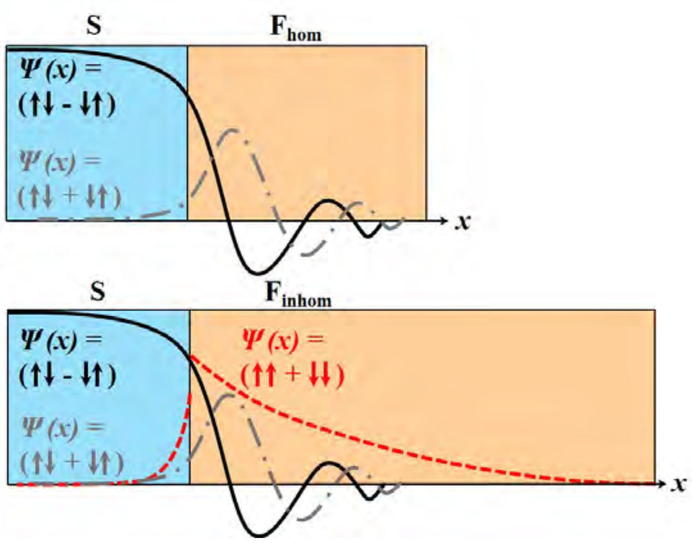

Figure 2.21: Comparison of the penetration of Cooper pair components into a homogeneous ferromagnet (top) and an inhomogeneous ferromagnet (bottom) inside a S/F heterostructure. Black lines denote spin-singlet components, grey spin-triplet components with $S_z = 0$ and red spin-triplet components with $S_z = \pm 1$. At the S/F$_{\text{inhom}}$ interface, the magnetization rotation leads to a formation of spin-triplet components with $S_z = \pm 1$ and large coherence length.

Bergeret et al. [103] have described the formation of Cooper pairs with symmetric spin functions mathematically, using an s-wave superconducting layer in proximity to an F layer with a magnetic domain wall at the S/F interface. They assumed, that the order parameter is symmetric in space in both layers for all spin components. To comply with the Pauli principle, the total wavefunction $\psi = \psi(k) \circledast \psi(\sigma) \circledast \psi(\omega)$ (with ω being the frequency of the wavefunction) has to be antisymmetric. Triplet spin components with even spin functions therefore have to be odd in frequency (in time), i.e. $\psi_1(\vec{r}, t)\psi_2(\vec{r}, t')$ is antisymmetric with respect to a time permutation. This is called a "s-wave odd triplet superconducting state" [106]. A comprehensive overview on different superconducting states with even or odd momentum and frequency can be found in [2].

Apart from magnetic domain walls at the S/F interface, also F1/S/F2 spin valve structures with different magnetization orientation of the two ferromagnetic layers F1 and F2, or S/F structures with spin active interfaces are possible generators of odd frequency spin-triplet components [106]. For convenience, these odd frequency spin-triplet components are called LRTC ("Long-Ranged spin-Triplet Components").

2.4.2.1 Applications

In the past decade, various investigations on F/S/F or S/F1/F2 heterostructures with different magnetization orientations in the F1 and F2 layers show their potential replacement of conventional F/N/F spin valve structures [5, 107–109]. Devices based on LRTC's show colossal magnetoresistance effects and additionally provide spin currents with low power dissipation and high-speed information processing [1].

To take advantage of a generation of LRTC in current device structures, they need to be controllable, for example by application of an external field or by temperature variation. Basic subsystems of F/S/F or S/F1/F2 without LRTC, just on the basis of spin-singlet Cooper pair components, already show a possible on and off switching of suppercurrent passing through the structure. By a change of critical temperature due to a parallel (T_c^P) or antiparallel (T_c^AP) magnetization configuration of the two F layers, superconductivity can be destroyed and recovered [110]. Pair breaking effects due to the exchange field of the ferromagnets acting on the spin-singlet Cooper pairs are stronger if the two ferromagnetic layers are magnetized parallel to each other and lower if they are magnetized antiparallel to each other, resulting in a lower T_c for the parallel state: $T_\mathrm{c}^\mathrm{P} < T_\mathrm{c}^\mathrm{AP}$, see Fig. 2.22. The difference $\Delta T_\mathrm{c} = T_\mathrm{c}^\mathrm{AP} - T_\mathrm{c}^\mathrm{P}$ is an important value as for operation temperatures $T_\mathrm{c}^\mathrm{P} < T_\mathrm{op} < T_\mathrm{c}^\mathrm{AP}$ such a spin valve structure can be switched on or off [6, 110].

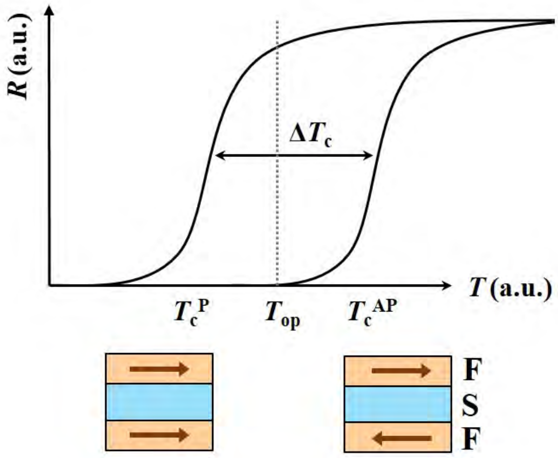

Figure 2.22: F (red)/S (blue)/F (red) structure with homogeneous magnetization inside the F layers and a critical temperature T_c^P for a parallel magnetization configuration and T_c^AP for an antiparallel magnetization configuration. If the device is operated at $T_\mathrm{c}^\mathrm{P} < T_\mathrm{op} < T_\mathrm{c}^\mathrm{AP}$, it can be switched from normal to superconducting resistance state by switching the two ferromagnets in parallel or antiparallel configuration in an external magnetic field.

For S/F multilayer systems based on a generation of only spin-singlet components of Cooper pairs, ΔT_{c} values up to ~400 mK have been reached [5].
With the generation of LRTC (e.g. for a non-collinear magnetization configuration), Fominov et al [107] have shown theoretically, that in a S/F1/F2 spin valve structure the critical temperature T_{c}^{tr} of odd-frequency spin-triplet components is lower than both, $T_{\mathrm{c}}^{\mathrm{P}}$ and $T_{\mathrm{c}}^{\mathrm{AP}}$, of spin-singlet components. Due to the large coherence length of the LRTC, the S layer is coupled with both the F1 and F2 layers (see Fig. 2.23(a)), if the two F layers are magnetized con-collinearly. Without LRTC (i.e. in parallel or antiparallel magnetization orientation), only S and F1 are effectively coupled, see Fig. 2.23(b,c). In the non-collinear configuration, this leads to a higher density of Cooper pair transfer from S to the F layers, and thus to a lower value of T_{c} [107].

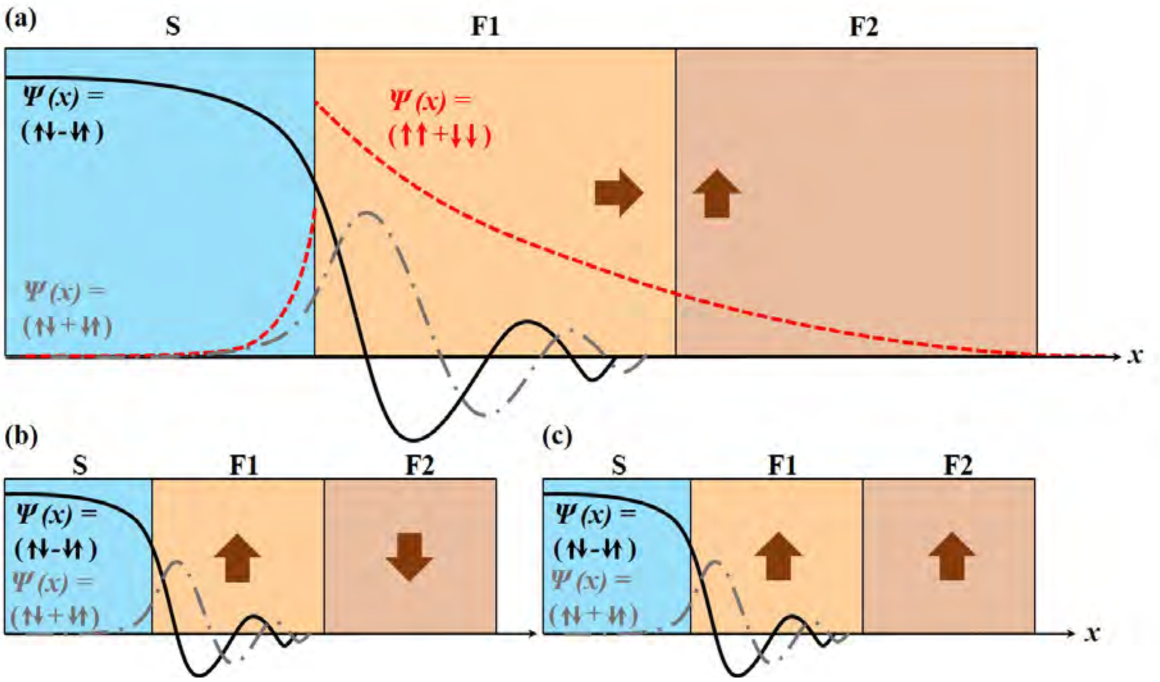

Figure 2.23: S (blue)/F1 (light red)/F2 (dark red) structure. (a) non-collinear magnetization configuration, where additionaly to the short ranged (↑↓ − ↓↑) and (↑↓ + ↓↑) components also the long ranged (↑↑) and (↓↓) components appear. Black lines denote spin-singlet components, grey spin-triplet components with $S_{\mathrm{z}}=0$ and red spin-triplet components with $S_{\mathrm{z}}=\pm1$. (b) antiparallel magnetization configuration, and (c) parallel magnetization configuration, with only short ranged Cooper pair penetration.

Experimental evidence for LRTC as supercurrent carriers can be obtained indirectly via layer thickness dependent conductance measurements [103, 111], via a long-ranged Josephson effect [12, 84, 112–114], by tunneling spectroscopy [115], or by a change of T_c as explained above [116]. Using field dependent resistivity measurements at constant temperature of an S/F1/F2 spin valve, Zdravkov et al. [116] have shown a minimum in T_c for a non-collinear alignment (i.e. at the coercive field H_{coerc}) of the two F layers, which is smaller than T_c^{AP} and T_c^{P}. This minimum in critical temperature comes along with a maximum in resistivity as can be seen in Fig. 2.24, and is referred to the occurence of LRTC.

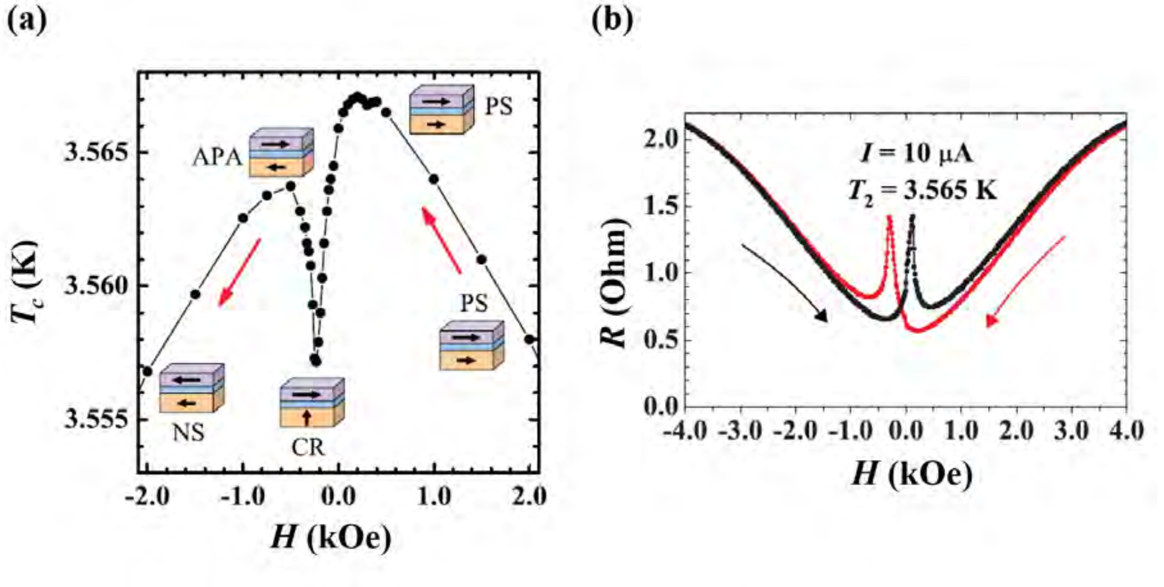

Figure 2.24: (a) Dependence of the critical temperature T_c on the magnetic field for different relative magnetization orientations of the F1 and F2 layers, marked in dark and light red. The thin blue layer between F1 and F2 denotes a normal conducting interlayer to independently switch the magnetization inside the two F layers. (b) Resistance measurements with respect to an external field H at constant temperature for the sample shown in (a). Figure taken from [116].

Instead of F/S/F spin valve structures with homogeneous but misaligned ferromagnets, also intrinsic inhomogeneous ferromagnetic structures can be used to generate LRTC. They have been investigated in ferromagnets with Bloch or Néel domain walls at the interface [84, 117], with conical ferromagnets [118, 119], with Heusler alloys [120] or in strongly spin orbit coupled S/F structures [121, 122]. In case of half-metallic ferromagnets with full spin polarization, additionally a fully spin-polarized supercurrent is assured [2, 123].

In this work, bilayers of the superconductor Nb and a domain structured FePd layer are investigated regarding direct and inverse proximity effects. Two competing phenomena are studied in one heterostructure system: The stray-field generated DWS and RDS as described in section 2.4.1, and LRTC as described in the beginning of section 2.4.2. Both are shown to arise due to the lateral inhomogeneous magnetic state of FePd, and depend on the strength of PMA as well as the orientation of an external applied magnetic field. Depth-resolved measurements of the lateral magnetic profile in these bilayers are presented using neutron scattering techniques, which will be discussed in the following chapter.

Chapter 3

Neutron scattering theory

Neutron scattering is a non-destructive tool to probe the depth-resolved magnetic proximity effects at S/F interfaces in thin film multilayers on a broad length scale from picometer to some hundred µm. In view of a full description of the underlying theory, first a general introduction into scattering processes and the correlation between the measured scattering cross sections and the magnetic moments within the sample is given. Subsequently, reflectometry on such multilayer systems is treated in detail, first for only nuclear scattering and second for magnetic scattering. Finally, this chapter is completed with the model system which is used to simulate the observed neutron measurements.

3.1 Basics on scattering theory

The interaction processes of neutrons with matter (introduced as scattering potential $V(\vec{r})$) have to be described in a quantum mechanical way by solving the Schrödinger's equation

$$(-\frac{\hbar}{2m_n}\Delta + V(\vec{r}))\psi = i\hbar\frac{\partial}{\partial t}\psi, \tag{3.1}$$

with the neutron rest mass m_n and wave function ψ [124]. The neutron beam interacts with both the nuclei and the magnetic field inside the sample. For simplification, first only the nuclear interaction processes will be described and later extended by magnetic scattering. To solve 3.1, an elastic scattering event is assumed so that the time-dependent $\chi(t)$ and spatial solutions $\phi(\vec{r})$ of ψ can be treated independently:

$$\psi(\vec{r},t) = \phi(\vec{r})e^{\frac{-iEt}{\hbar}}. \tag{3.2}$$

Additionally, the Fraunhofer approximation (the sample size is small compared to the distances to the neutron source and detector) and the assumption of a monochromatic incident neutron beam is used. Within this ansatz, the solution of $\phi(\vec{r})$ far away from the scattering event ($r \to \infty$) can be written as overlap of an incident plane wave with wave vector $\vec{k}$ together with a scattered spherical wave [124]:

$$\phi(\vec{r}) \sim e^{i\vec{k}\vec{r}} + f_k(\theta,\varphi)\frac{e^{i\vec{k}\vec{r}}}{r}, \tag{3.3}$$

where $f_k(\theta,\varphi)$ is called the scattering amplitude which depends on the scattering potential $V(\vec{r})$. Using $f_k(\theta,\varphi)$, information on the sample structure are obtained by a measurement of the cross section σ as will be discussed in detail later. The dependence of f_k on $V(\vec{r})$ can only be obtained approximately with the Green's-function method. This method first simplifies the problem of an unknown scattering potential $V(\vec{r})$ by solving a scattering event on a point-like sample described be the δ-function [125]. In a second step, the spatial wave function after scattering at $V(\vec{r})$ is obtained by the Lippmann-Schwinger-equation:

$$\phi(\vec{r}) = \phi_0(\vec{r}) + \frac{2m_n}{\hbar^2}\int G(\vec{r},\vec{r}\,')V(\vec{r}\,')\phi(\vec{r}\,')d^3r\,', \tag{3.4}$$

with the solution $\phi_0(\vec{r})$ without scattering event (plane wave) and the Green's-function $G(\vec{r},\vec{r}\,')$. Thus, a good Ansatz for $G(\vec{r},\vec{r}\,')$ will help solving $\phi(\vec{r})$. It can be shown that $G(\vec{r},\vec{r}\,') = \frac{e^{ik|\vec{r}-\vec{r}\,'|}}{4\pi|\vec{r}-\vec{r}\,'|}$ is a solution for the Green's-function [124]. $\vec{r}$ is the position vector of a scattered wave from a point-like scatterer ($G \equiv \delta$-function) so that the emitted wave in direction $\vec{r}$ is a spherical wave. For a finite-sized volume, $V(\vec{r}\,')$ at positions $\vec{r}\,'$ relative to $\vec{r}$ inside the sample leads to multiple scattering events, each emitting a spherical wave.

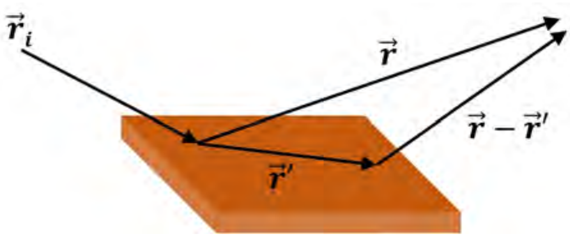

Figure 3.1: Scattering of the incident wave (i) at a point-like scatterer with V being the δ-function and the scattered wave in direction $\vec{r}$ and (ii) after multiple scattering within a finite sample volume with scattering directions $\vec{r}'$ inside the sample.

Still, a solution for $\phi(\vec{r})$ can only be obtained by further approximations with the so called Born series, where scattering events are expressed as operations $\mathbf{G}V$ acting on $\phi_0(\vec{r})$. As example, equation (3.5) shows the second Born series approximation [124, 126]:

$$\phi(\vec{r}) = \phi_0(\vec{r}) + \mathbf{G}V\phi_0(\vec{r}) + \mathbf{G}V\mathbf{G}V\phi_0(\vec{r}). \tag{3.5}$$

The first element of (3.5) describes the incident plane wave, the second element a single scattering event, and the third element a two-time scattering event. For neutron scattering on small samples, typically the first Born approximation (so called kinematic scattering theory) is a good measure for $\phi(\vec{r})$, as V is weak and multiple scattering events can be neglected [126]. Now $\phi(\vec{r})$ can be written as:

$$\phi(\vec{r}) = e^{i\vec{k}\vec{r}} + \frac{2m_n}{\hbar^2}\int \frac{e^{i\vec{k}|\vec{r}-\vec{r}'|}}{4\pi|\vec{r}-\vec{r}'|} V(\vec{r}')\phi(\vec{r}')d^3r\,'. \tag{3.6}$$

For $\vec{r} \to \infty$ with using $\vec{R} = \vec{r} - \vec{r}'$ and $Q = \vec{k}\,' - \vec{k}$ we get:

$$\phi(\vec{R}) = e^{i\vec{k}\vec{R}} + \frac{2m_n}{\hbar^2}\frac{e^{i\vec{k}\vec{R}}}{4\pi R}\int V(\vec{r}')e^{-i\vec{Q}\vec{r}'}d^3r\,', \tag{3.7}$$

and with using equation (3.3):

$$f(\vec{Q}) = \frac{m_n}{2\pi\hbar^2}\int V(\vec{r}')e^{-i\vec{Q}\vec{r}'}d^3r\,'. \tag{3.8}$$

By a measurement of the intensity I with respect to $\vec{Q}$ with $I(\vec{Q}) \sim |f(\vec{Q})|^2$, V can be deduced by integrating (3.8). In scattering experiments, only a fraction of the total cross-section in the solid angle $d\Omega$ is measured at the detector. The differential cross-section $\frac{d\sigma}{d\Omega}$ with $\sigma = \int \frac{d\sigma(\theta,\varphi)}{d\Omega} d\Omega$ is a value for the scattering amplitude in direction θ and φ and is proportional to the impinging particles dn in $d\Omega$ per total flux J [124]:

$$\frac{d\sigma}{d\Omega} = \frac{dn}{J d\Omega} = |f(\vec{Q})|^2. \tag{3.9}$$

Reverting to the relation $\vec{Q} = \vec{k}\,' - \vec{k}$ it has to be noted that this so-called scattering vector is an important value in scattering techniques, as $\hbar\vec{Q}$ represents the momentum transfer from $\vec{k}$ to $\vec{k}\,'$ during the scattering event and which is measured during the experiment. Throughout this chapter, elastic scattering is assumed which means that $|\vec{k}| = |\vec{k}\,'|$ and $\vec{Q}$ has to fulfill the Laue-condition $\vec{Q} = \vec{G}$ with $\vec{G}$ being a reciprocal lattice vector [127]. This is illustrated in two dimensions Fig. 3.5 using the Ewald construction: The Laue condition is only fulfilled for scattering at reciprocal lattice points (so that $\vec{Q} = \vec{G}$) on the circle of the Ewald sphere with radius k. Also the Bragg condition (3.10) using $|\vec{k}| = \frac{2\pi}{\lambda}$ and the lattice spacing d has to be fulfilled.

$$2d \sin\theta = n\lambda \tag{3.10}$$

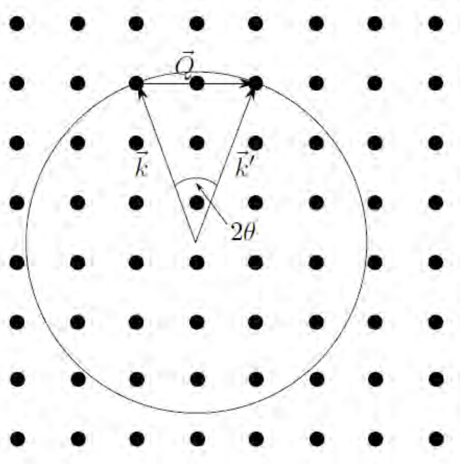

Figure 3.2: Ewald sphere of radius $|\vec{k}| = |\vec{k}\,'|$. Scattering can only occur at reciprocal lattice points which fall on the Ewald sphere. Adapted from [128].

Based on the relations shown in this chapter, theoretical tools for specular and off-specular reflectivity will be given in the following chapters which will provide information on depth-resolved and lateral correlations in a thin film. Using a polarized neutron beam and polarization analysis, also information on the magnetization vector $\vec{M}$ inside the layers of the thin film can be obtained. Within this thesis, Polarized Neutron Reflectometry (PNR) is used to investigate the depth-resolved magnetic structure and Grazing-Incidence Small-Angle Neutron Scattering (GISANS) is used to study lateral correlations such as magnetic domains in the S/F thin films.

3.2 Reflectometry on thin film heterostructures

Various neutron reflectometry techniques were developed to probe correlations on different length scales - either with a focus on the depth resolution or on spatial patterns such as magnetic domain arrangements, self-assembled nano-particles, and block copolymers. Due to small values of Q in reflectometry, it is especially suited to study thin films with thicknesses in the nanometer to micrometer range.

PNR is a specular reflectometry method (i.e. the incident angle equals the reflected angle $\theta_i = \theta_f$) with which information on the out-of-plane oriented Q_z and hence on layer thicknesses or depth-correlated roughnesses in a multilayer system can be investigated. Taking advantage of a polarized neutron beam, the vector magnetization $\vec{M}$ of each layer is probed. Typical macroscopic measurements of the magnetization (see chapter 4.3.5) average over the whole sample volume, whereas PNR gives depth-resolved information on $\vec{M}$. All information in the in-plane direction are averaged and other methods like off-specular scattering have to be used.

Off-specular scattering describes reflectometry methods in which scattering is probed over the whole range of $\vec{Q} = (\vec{Q_x}, \vec{Q_y}, \vec{Q_z})$ and with a focus on lateral correlations. Here, a position sensitive detector is needed. Whereas in typical off-specular geometries Q_x is examined for structures in the plane of incidence, in the GISANS geometry Q_y and therefore lateral structures in a plane perpendicular to the incident plane can be investigated [129]. GISANS is performed at very low θ_i close to the angle of total reflection θ_c, enabling the investigation of correlations below 100 nm. A variation of θ_i facilitates to probe at different depths with higher resolution. The smaller θ_i, the more surface sensitive is the performed measurement.

Figure 3.3 shows (i) the specular reflection with $\theta = \theta_i = \theta_f$ and (ii) off-specular scattered signals in the $Q_y - Q_z$-map in GISANS configuration.

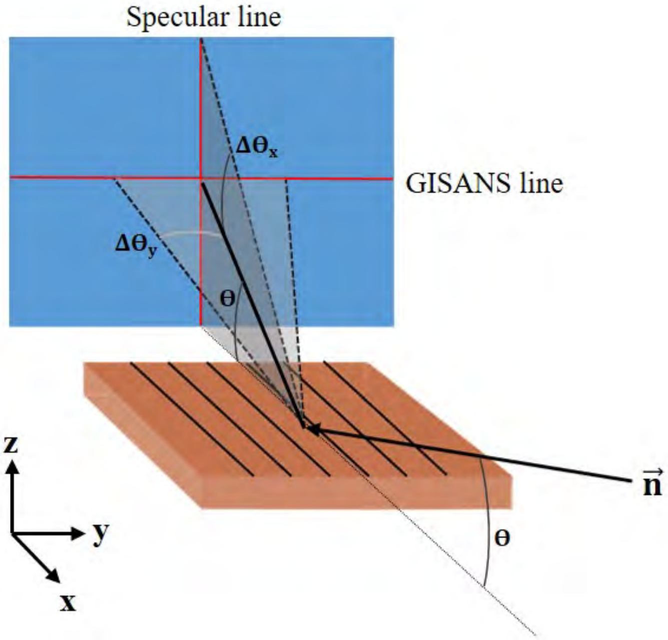

Figure 3.3: Overview on the measurement configurations for specular and GISANS reflecometry methods: For specular reflectometry, specularly scattered signals at $\theta = \theta_i = \theta_f$ are measured as function of θ, whereas in GISANS configuration at fixed θ_i the $Q_y - Q_z$-map is measured on a 2D detector.

Important for all reflectometry techniques is the correlation length. In specular reflectometry, the correlation length in z-direction L_z is typically larger than the total thickness of a multilayer system to get coherent scattering from all layers. The lateral correlation lengths, important for off-specular scattering, determine whether spatial patterns like domains can be probed. This is illustrated in Fig. 3.4. If the correlation lengths L_x and L_y are smaller than the respective domain sizes, one sees an incoherent superposition of scattering from single domains. Only if L_x and L_y are larger than the domain sizes, lateral correlations are detected as peaks in the reciprocal space map. For nuclear scattering this is important for domains of different scattering length density ρ and for magnetic scattering for different magnetization orientations in the domains.

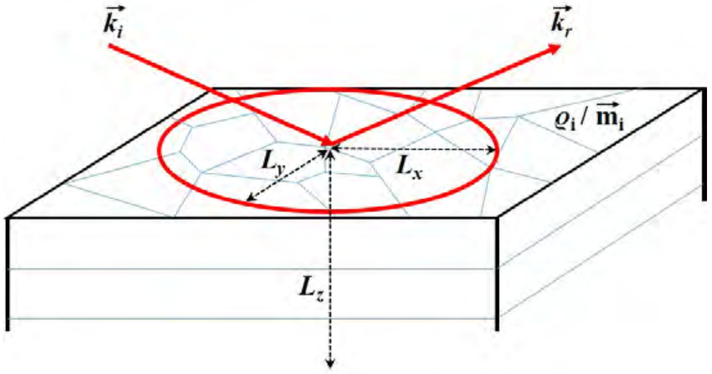

Figure 3.4: Thin film sample with lateral domains of different density ρ_i and/or magnetic moments $\vec{m}_i$, and a layered structure denoted with light blue lines. The coherence volume of the incoming beam spreads over L=(L_x, L_y, L_z).

In combination, PNR and GISANS provide a powerful tool to investigate depth-resolved lateral magnetic patterns. First, an introduction into specular reflectometry in general will be given based on only nuclear scattering. Scattering on a multilayer system is presented in terms of the Parratt formalism. Second, mathematical tools of off-specular neutron scattering are presented including the Distorted-Wave Born Approximation (DWBA). Subsequently, the scattering potential will be extended by a magnetic term in the last chapter.

3.2.1 Specular reflectometry

As already introduced, in reflectometry only small Q_z are probed. For layers with a homogeneous nuclear density distribution ρ_n, this yields a scattering potential [130]:

$$V = \frac{2\pi\hbar^2}{m_\mathrm{n}}\rho_\mathrm{n} = \frac{2\pi\hbar^2}{m_\mathrm{n}}\sum_j N_j b_j, \tag{3.11}$$

where N_j and b_j are the number of nuclei per unit volume and the coherent scattering length of a nucleus j, respectively. Inserting (3.11) into (3.1) and assuming that V is independent of the in-plane directions x and y, yields plane wave solutions for $\psi(z)$. Hence, the same formalisms as in classical optics can be used to obtain the reflectivity R as function of Q_z, as measured in PNR. For convencience, here and in the analysis chapter, Q_z is defined as $|\vec{Q}_z| = |(\vec{k}_f - \vec{k}_i)_z|$, with $\vec{k}_i$ as wave vector of the incident beam in an angle θ_i and $\vec{k}_f$ the wave vector of the reflected beam in the angle θ_f. As opposed to classical optics, the angles are defined as between the sample surface and the plane of incidence. Additionally, $\vec{k}_0$ shall be the wave vector in air and $\vec{k}_r$ the refracted wave vector inside the sample (see Fig. 3.5).

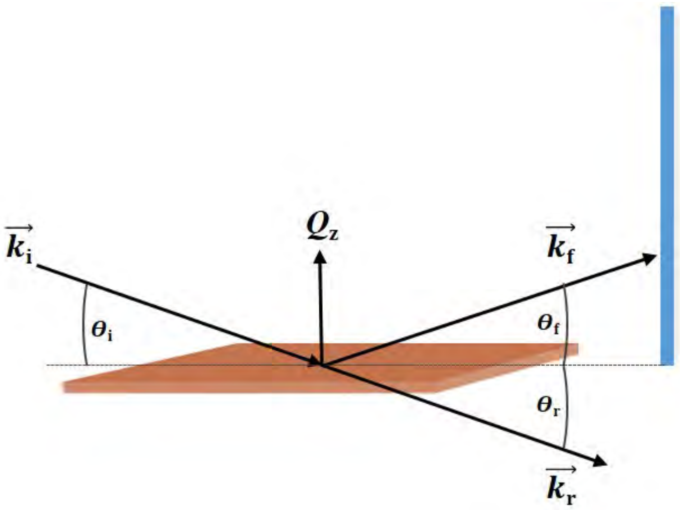

Figure 3.5: Measurement setup for specular reflection: the outgoing beam is scattered in an angle $\theta_f = \theta_i$ resulting in an out-of-plane oriented $Q = Q_z$, and refracted in direction θ_r. Red color denotes the sample and blue color the detector.

With the index of refraction $n = \frac{k_r}{k_0} = \sqrt{1 - \frac{4\pi\rho}{k_0^2}}$, the Fresnel reflectivity can be deduced to:

$$R = |r|^2 = |\frac{\theta_i - n\theta_r}{\theta_i + n\theta_r}|^2, \tag{3.12}$$

$$\tag{3.13}$$

With the angle of incidence θ_i, and the into the sample refracted angle θ_r. Together with Snell's law, the critical angle of reflection θ_c with its respective wave number k_c and scattering vector magnitude Q_c is written as [131]:

$$\theta_c \sim \lambda\sqrt{\frac{\rho}{\pi}}, \tag{3.14}$$

$$k_c = \frac{2\pi}{\lambda}\sin\theta_c \sim \sqrt{4\pi\rho}, \tag{3.15}$$

$$Q_c = \frac{4\pi}{\lambda}\sin\theta_c \sim \sqrt{16\pi\rho}. \tag{3.16}$$

In the case of a homogeneous layer with a sharp interface between two semi-infinite media like a bulk sample and air, this leads to a reflectivity depending on Q_z shown in (3.17):

$$R(Q_z) = \left| \frac{Q_z - \sqrt{Q_z^2 - Q_c^2}}{Q + \sqrt{Q_z^2 - Qc^2}} \right|^2 . \tag{3.17}$$

If the surface is not sharp but exhibits a certain roughness, the in-plane averaged refractive index (given in this case as overlap of air and sample) changes statistically with depth at the surface, and an exponential damping term has to be multiplied with (3.17). An even more complicated situation comes into play when considering reflectometry on a multilayer system instead of one homogeneous layer. In this case, the scattering length density ρ_l and the refraction and transmission coefficients r_l and t_l change in each layer l. The wavefunction ψ_l inside layer l is of the form 3.18 [132]:

$$\psi_l(z, \vec{s}) = e^{i\vec{\kappa}\cdot\vec{s}}(e^{+ik_{z,l}z}t_l + e^{-ik_{z,l}z}r_l), \tag{3.18}$$

with the in-plane components $\vec{\kappa}$ of $\vec{k}$ and $\vec{s}$ of $\vec{r}$. Additionally, at the interfaces the wavefunctions have to fulfill the continuity relations $\psi_l = \psi_{l+1}$ and $\frac{\partial \psi_l}{\partial z} = \frac{\partial \psi_{l+1}}{\partial z}$. The calculation of all coefficients and the interface conditions yield 2(N+1) number of equations, where N is the total number of layers in the multilayer system [131]. A solution for this set of formulas can be obtained by a refinement of r_l and t_l for each layer until the simulation fits to the reflectometry measurement, a method developed by Parratt [133].

In this work, the program GenX [134] is used for the analysis of X-ray specular scattering. GenX is based on the Parratt recursion and simulates a reflectivity dataset regarding a chosen multilayer model. The measure of quality for this simulation is the Figure Of Merit (FOM) which describes the deviation from a simulation to the measurement regarding a chosen approach. One example is the “chi-squared FOM” which weights the absolute difference between a simulated dataset and the measurement with the errorbars, or the “sintth4 FOM” which scales the difference of the simulated and measured datasets with $\sin(2\theta)^4$ [134]. Specular neutron scattering in this thesis is used with a polarized neutron beam as described in section 3.2.3 to probe the magnetic depth-profile. Simulations of specular reflectivities for polarized neutron reflectometry are as well based on the Parrat formalism.

3.2.2 Off-specular scattering

Specular reflectometry averages signals from the whole in-plane projection of the beam coherence volume and thus is mostly useful if the layers are homogeneously magnetized. If information coming from periodic, lateral inhomogeneities is to be investigated, off-specular scattering has to be considered. The first off-specular geometry shown in Fig. 3.6(a), probes in-plane patterns in the µm region leading to a non-zero Q_x. Lateral domains in the nm scale need to be studied at smaller incident angles with the GISANS technique shown in Fig. 3.6(b). The neutron beam impinges on the surface with an angle close to θ_c and the correlation lengths probed here range from a few nanometers to roughly 100 nm [129]. Any domain pattern with periodicity in the y-direction gives rise to scattering intensities in Q_y. The Q_y-line at specularly scattered Q_z where $\theta = \theta_i = \theta_f$ is called the "GISANS"-line. Scattering intensities at higher Q_z are caused by off-specular scattering with a certain Q_x and the "Specular"-line in Fig. 3.6(b) is also called the "Off-specular"-line. The focus in this thesis is on measurements in GISANS geometry due to the small periodicity of magnetic domains in the S/F heterostructures consisting of Nb and FePd.

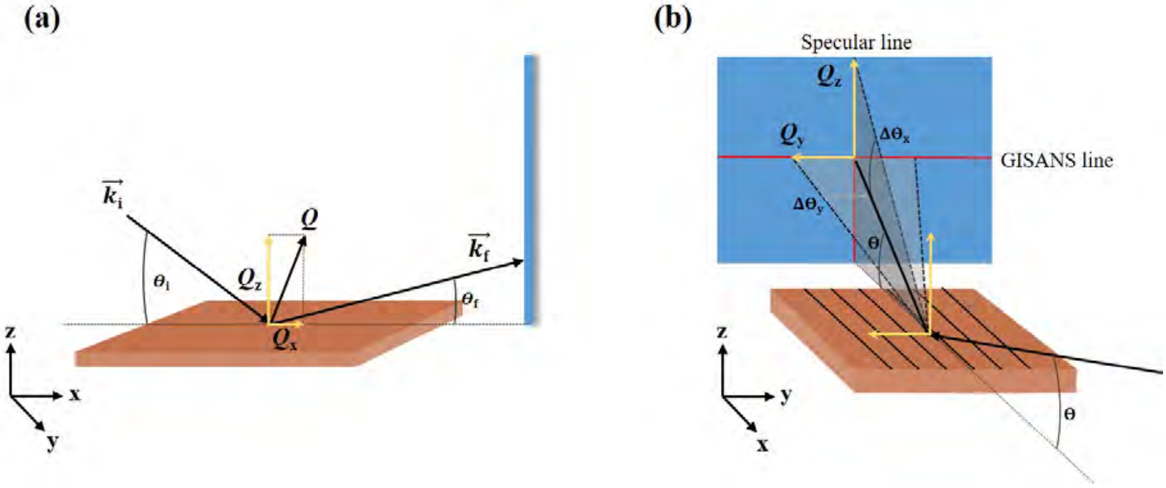

Figure 3.6: (a) Measurement setup for off-specular reflection where Q_x and Q_z are probed. (b) Measurement setup for GISANS where Q_y and Q_z are probed. On the detector, the GISANS line and specular line are drawn in red.

Another reason why GISANS is suitable for the study of the out-of-plane magnetic domains as described in chapter 2.1.3 are the closure domains at the surfaces of the

FePd layer. As GISANS is performed with an angle close to θ_c, surface near structures can be probed with increasing intensity as the angle is reduced. As can be seen in Fig. 3.7, the penetration depth Λ of neutrons into the sample increases sharply at θ_c. At lower angles, only an evanescent wave forms at the sample surface and the neutron wave is localized at the surface, only penetrating the first ~10 nm. The highest scattering cross-sections are obtained at the critical angle of reflection.

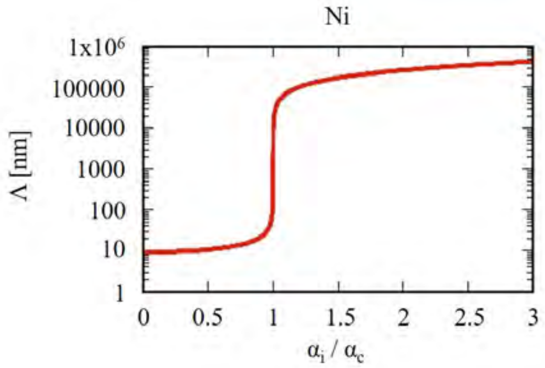

Figure 3.7: Penetration depth of the neutron beam Λ into Nickel as function of the incident angle α_i at a neutron wavelength of 6 Å.

The scattering vector $\vec{Q}$ in both off-specular geometries is calculated by the incident and reflected angles θ_i and θ_f and the off-specularly scattered angles $\Delta\theta_y$ and $\Delta\theta_x$, defined as $\Delta\theta_x = \theta_f - \theta_i$ (see Fig. 3.6) and in small-angle approximation given by [135]:

$$\begin{pmatrix} Q_x \\ Q_y \\ Q_z \end{pmatrix} = \frac{2\pi}{\lambda} \begin{pmatrix} \theta_i \Delta\theta_x + \frac{(\Delta\theta_x)^2}{2} + \frac{(\Delta\theta_y)^2}{2} \\ \Delta\theta_y \\ 2\theta_i + \Delta\theta_x \end{pmatrix} \tag{3.19}$$

As $\theta_i \approx \theta_c$, the scattering is affected by dynamical effects which are not part of the Born approximation used for higher incident angles. Here, another theory based on the DWBA has to be employed [132]. The DWBA makes use of the quantum mechanical perturbation theory and describes the scattering potential from a lateral inhomogeneous pattern in layer l which is divided into (i) a non-perturbed part $V_{0,l}$ due to a lateral homogeneous density distribution and (ii) a pertubation potential $V_l(\vec{s})$ with $\vec{s}$ as 2D vector lying in the sample surface, see Fig. 3.8.

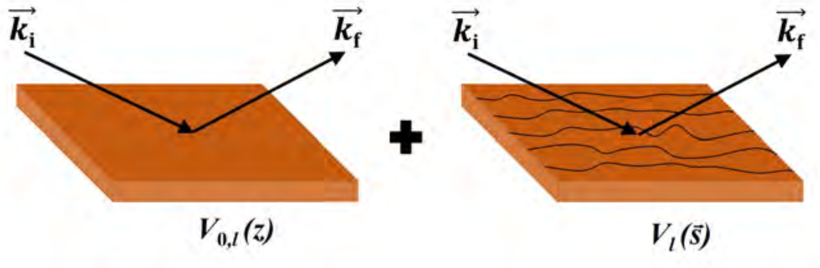

Figure 3.8: (a) Non-perturbed scattering potential $V_{0,l}$ of a homogeneous sample and (b) pertubation potential $V_l(\vec{s})$ of a sample with lateral inhomogeneous structural or magnetic density.

$V_{0,l}$ leads to specular reflection, whereas $V_l(\vec{s})$ leads to off-specular scattering and is composed of density fluctuations with $V_l(\vec{s}) = \frac{2\pi\hbar^2}{m_n}\rho_{N,l}(\vec{s})$ or magnetic fluctuations, treated in chapter 3.2.3.

In the following quantum mechanical description, the lateral average of the operator $\hat{V}_l(\vec{s})$ is zero. The perturbation potential acts only on the non-pertubed wave functions, so that $\hat{V}_l(\vec{s})$ acts on the incident plane wave ψ^i, which afterwards interferes with the scattered wavefunction ψ^f from the specular scattered wave. This leads to a scattering cross section as in (3.20) [132, 136]:

$$\frac{d\sigma}{d\Omega} = \langle f\rangle^2 = (\frac{m_n}{2\pi\hbar^2})^2 \left\langle \left| \langle\psi_l^f|\, \hat{V}_l(\vec{s})\, |\psi_l^i\rangle \right|^2 \right\rangle , \tag{3.20}$$

with the scattering amplitude f, ψ_l^f being the scattered wavefunction inside layer l and ψ_l^i the wavefunction inside l just before the scattering event. They are solutions of the non-pertubed potential $V_{0,l}$ and incoming wave vectors $\vec{k}_i$ and $-\vec{k}_f$, respectively, and can be calculated each by the Parratt formalism analoguous to section 3.2.1: $\psi_l^{i(f)}$ is given by the refraction and transmission coefficients r_l and t_l which act on the incident and scattered wave function in air (see eq. 3.21) [132]:

$$|\psi_l^{i(f)}(\vec{r})\rangle = e^{i\vec{\kappa}^{i(f)}\cdot\vec{s}}(e^{\overset{+}{(-)}i\hat{k}_{z,l}^{i(f)}z}\hat{t}_l^{i(f)} + e^{\underset{-}{(+)}i\hat{k}_{z,l}^{i(f)}z}\hat{r}_l^{i(f)})\,|\psi_0^{i(f)}\rangle\,. \tag{3.21}$$

In Fourier space, $\hat{V}_l(\vec{s})$ is rewritten to the potential $\mathcal{F}(\hat{V}_l(\vec{s}))$:

$$\begin{aligned}\mathcal{F}(\hat{V}_l(\vec{s})) &= \frac{m_n}{2\pi\hbar^2}\int e^{-i\vec{Q}_{||}\vec{s}}\hat{V}_l(\vec{s})d^2\vec{s}, && (3.22)\\ &= \int e^{-i\vec{Q}_{||}\vec{s}}\tilde{\rho}_{N,l}(\vec{s})\cdot\hat{1}\,d^2\vec{s}. && (3.23)\end{aligned}$$

$\tilde{\rho}_{N,l}$ represents the scattering length density fluctuation of the perturbed scattering potential (in contrast to the averaged $\rho_{N,l}$ of the non-perturbed potential). The terms 3.23 and 3.21 can be inserted in the Fourier transformed 3.20, and the solution of $\frac{d\sigma}{d\Omega}(\vec{Q})$ is fully given by the reflection and transmission coefficients, the interface conditions, and the scattering length density of each layer.

3.2.3 Magnetic reflectometry and off-specular scattering

In ferromagnetic layers, magnetic scattering is caused by the interaction of dipolar magnetic moments of the incident neutrons with the internal magnetic field generated by the dipolar moments of unpaired electrons. Also an interaction with nuclear spins gives small contributions to the magnetic scattering, but is neglected here due to the much higher contribution from free electrons and only small applied magnetic fields during the measurements. To investigate quantitatively the internal magnetic induction $\vec{B}$, a polarized neutron beam with the polarization vector $\vec{P}$ has to be used. If the magnetization $\vec{M}$ inside the sample is parallel to the polarization direction $\vec{P}$ of the neutrons, their spin direction is conserved, whereas for $\vec{M}$ not parallel to $\vec{P}$, the neutron spin direction is flipped.

PNR

The wavefunction $\Psi(z)$ of the neutrons is no longer one-dimensional as described above, but a two-dimensional spinor $\begin{pmatrix}\Psi^+(z)\\ \Psi^-(z)\end{pmatrix}$. The Hamiltonian has be a 2x2 matrix where the interaction potential V can either flip or not flip the polarization of the incident beam [130]:

$$\left[-\frac{\hbar^2}{2m_n}\frac{\partial^2}{\partial z^2}\begin{pmatrix}1 & 0\\ 0 & 1\end{pmatrix}+\begin{pmatrix}V^{++}(z) & V^{+-}(z)\\ V^{-+}(z) & V^{--}(z)\end{pmatrix}\right]\begin{pmatrix}\Psi^+(z)\\ \Psi^-(z)\end{pmatrix} = E\begin{pmatrix}1 & 0\\ 0 & 1\end{pmatrix}\begin{pmatrix}\Psi^+(z)\\ \Psi^-(z)\end{pmatrix}, \quad (3.24)$$

with a matrix V given as overlap of nuclear and magnetic parts $V = V_N + V_M$. The magnetic potential can be written as $V_M = -\mu_{\mathrm{n}}\vec{\sigma}\cdot\vec{B} = \frac{2\pi\hbar^2}{m_n}\rho_M\vec{\sigma}\cdot\vec{b}$, with the neutron magnetic moment μ_{n}, the spin-Pauli matrices $\vec{\sigma}$ [137], and the unit vector $\vec{b}$ of the induction $\vec{B}$ projected onto the surface plane [138]. The coupled equations are written in terms of the components of $\vec{b}$ parallel and antiparallel to $\vec{P}$ in (3.25). It becomes obvious that the two spinor components are coupled for any field direction not parallel to $\vec{P}$.

$$\frac{\partial^2}{\partial z^2}\psi^+(z) + [k_z^2 - 4\pi(\rho_N + \rho_M b_{||})]\psi^+(z) + [4i\pi\rho_M b_\perp]\psi^-(z) = 0, \tag{3.25a}$$

$$\frac{\partial^2}{\partial z^2}\psi^-(z) + [k_z^2 - 4\pi(\rho_N - \rho_M b_{||})]\psi^-(z) - [4i\pi\rho_M b_\perp]\psi^+(z) = 0, \tag{3.25b}$$

with the component of $\vec{b}$ parallel to an external field, $b_{||}$, contributing to the Non-Spin-Flip (NSF) channels of the measurement and the component perpendicular to an external field, $b_\perp$, contributing to the Spin-Flip (SF) channels. Solving 3.25 leads to a spin-dependent reflectivity. Four channels are distinguished if the incident neutron polarization $\vec{P}_{\mathrm{i}}$ as well as the reflected neutron polarization $\vec{P}_{\mathrm{f}}$ are measured: R^{++}, R^{--} (NSF-channels), as well as R^{+-}, and R^{-+} (SF-channels), where the first index corresponds to $\vec{P}_{\mathrm{i}}$ and the second index to $\vec{P}_{\mathrm{f}}$. A more detailed derivation of R in case of spin-dependent scattering can be found in [130].

GISANS

A simulation of polarized GISANS measurements is based on the DWBA as described in 3.2.2. The perturbation potential now is given as sum of nuclear and magnetic parts (3.26a) with its Fourier transformed counterpart (3.26b):

$$\hat{V}_l(\vec{s}) = \frac{2\pi\hbar^2}{m_n}(\tilde{\rho}_{N,l}(\vec{s}) \cdot \hat{1} + \tilde{\rho}_{M,l}(\vec{s})\vec{\sigma} \cdot \vec{b}_l), \tag{3.26a}$$

$$\mathcal{F}(\hat{V}_l(\vec{s})) = \int e^{-i\vec{Q}_{||}\vec{s}}(\tilde{\rho}_{N,l}(\vec{s}) \cdot \hat{1} + \tilde{\rho}_{M,l}(\vec{s}))\vec{\sigma} \cdot \vec{b}_l)d^2\vec{s}, \tag{3.26b}$$

with the magnetic unity vector $\vec{b}_l$ of magnetic moments in layer l and the lateral nuclear and magnetic scattering length density fluctuations $\tilde{\rho}_{N,l}$ and $\tilde{\rho}_{M,l}$, respectively. In case of the ferromagnetic thin film FePd layers in this thesis, $V_l(\vec{s})$ denotes the periodic domain pattern, including out-of-plane as well as in-plane domains. One main task in section 5.4.4 is to determine a model consisting of out-of-plane and in-plane domains describing $V_l(\vec{s})$ such that its scattering cross-section coincides with the performed GISANS measurements. It has to be noted again, that any magnetic moment parallel to $\vec{P}$ gives rise to NSF, whereas moments perpendicular to $\vec{P}$ give rise to SF scattering.

Since polarized GISANS measurements enable to scrutinize depth-resolved lateral magnetic fluctuations in a quantitative way and to distinguish between in-plane magnetized domain walls and out-of-plane magnetized bulk domains, it is the tool of choice to investigate proximity effects in the S/F system Nb/FePd. Other methods like X-ray Magnetic Circular Dichroism (XMCD), or muon-spectroscopy as well probe the magnetic fluctuations in the sample. However, with soft XMCD lower layers of the heterostructure cannot be probed, and in muon-spectroscopy the depth and lateral resolutions are lower than in GISANS.

	Pol. GISANS [139]	Soft XMCD [20, 140]
(+)	vector-magnetometry	vector-magnetometry
	high magnetic sensitivty	high magnetic sensitivty
	non-destructive	non-destructive
	quantitative analysis	high brilliance of sources
	high penetration depth	
(-)	low brilliance of sources	for a quantitative analysis, ϵ_r at the adsorption edges needs to be known
		penetration depth only ~10 nm

Table 3.1: Comparison af advantages and disadvantages of GISANS and soft XMCD.

Often it is useful to support GISANS investigations by GISAXS (Grazing-Incidence Small-Angle X-ray Scattering), which allows one to identify the chemical depth-profile in thin film multilayers [141]. A comparison of results from both techniques helps to reduce the set of unknown parameters in GISANS. Table 3.1 compares some advantages (+) and disadvantages (-) of GISANS, GISAXS, and soft XMCD.

3.2.4 Simulation of GISANS measurements on thin film FePd

Materials exhibiting strong PMA often obtain a maze-domain structure with randomly oriented, short-range ordered magnetic domains. A calculation of the scattering cross-section of such structures requires complex theoretical descriptions. In this thesis, simulations of GISANS measurements from FePd thin films with PMA are based on calculations derived by Toperverg [142]. The model is extended by (i) the paracrystal theory and (ii) an integration over all possible in-plane domain orientations of the considered maze structure.

In the paracrystal theory [143], scattering objects in an ordered lattice can randomly deviate from their regular position, leading to an incomplete long-range order [144]. Korolkov et al. [145] have formulated the GISANS pattern (within the DWBA as explained in sec. 3.2.2) of randomly oriented lamellae on a flat substrate by using the paracrystal theory as well as by considering a maze lamella structure. To describe the maze pattern, small units of an ordered subsystem are rotated within the surface plane. The total scattering cross-section results from an integration over all possible rotation angles.

In the following, an example model system including the paracrystal theory for a maze domain pattern is given for magnetic domains in FePd thin films with PMA. Following Kittel [146] (and the theory on magnetic domains in sections 2.1.2-2.1.3), thin films with PMA exhibit Bloch domain walls as well as Néel caps on the layer surfaces (closure domains). This was experimentally proven by Dürr et al. [21] using circular dichroism x-ray resonant magnetic scattering. A universal system to describe any strength of PMA includes out-of-plane oriented domains, closure domains, and domain walls of adjustable sizes and depths. Here, one unit shall consist of two half up and one full down-oriented magnetic domains of width D_{domain} shown as side-view in Fig. 3.9(a), and two Bloch domain walls with a chiral magnetic structure seperating the out-of-plane domains and with triangular shaped closure domains at the FePd surfaces.

The top-view in Fig. 3.9(b) shows possible rotations of such a unit by an angle ξ with respect to the measured, fixed Q_y-direction. L_x denotes the correlation length of the units in x-direction, i.e. the length of an ordered subsystem with parallel domains. The paracrystal theory in this picture describes a random deviation of the domain position to the left or the right in figure 3.9(a). This random deviation is given by a Gaussian distribution function with a standard deviation parameter ω [144].

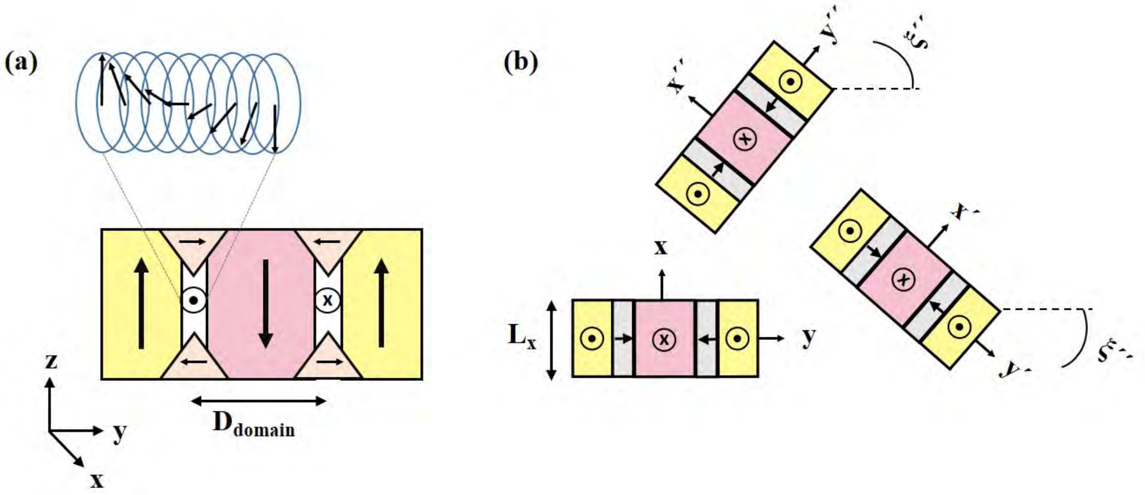

Figure 3.9: (a) Side-view of one unit with one up- and one down-oriented domain of FePd with high PMA and a domain width of D_{domain}. (b) Top-view of three not correlated units with various in-plane rotation angles ξ and a mean correlation length L_x. Inspired by [145].

Fig. 3.10 displays the surface domain structure of two FePd thin films used in this thesis with (a) high PMA and a maze pattern and (b) low PMA and parallely aligned magnetic domains. Yellow rectangular boxes enclose two structural units (two up- and two down-domains) each. In (a) the correlation length L_x is of the order of D_{domain} or smaller, and the cross-section is given by a sum over several ξ. Aligned domains in (b) are calculated with $L_x \gg D_{\text{domain}}$ and a fixed ξ.

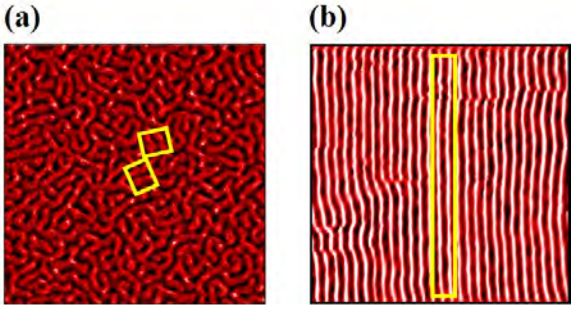

Figure 3.10: 3x3 μm measurements of the surface domain pattern of (a) FePd with high PMA and (b) FePd with low PMA. Yellow rectangular boxes mark two units of aligned domains in both images.

In the analysis of GISANS measurements at room temperature in section 5.4.4, a FePd layer with a stripe domain structure and large closure domains will be investigated, whereas at low temperatures in section 7, FePd with high PMA and a maze domain structure will lead to a consideration of small closure domains but an observable chirality within the Bloch domain walls.

Chapter 4

Experimental methods

For an investigation of S/F proximity effects in thin film heterostructures of Nb/FePd by macroscopic as well as microscopic characterization techniques, these films have to show good surface and interface qualities, which will be obtained by the growth under ultra-high vacuum using Molecular Beam Epitaxy (MBE).
The first section introduces the main concepts of the MBE growth technique and is followed by the various in-situ and ex-situ characterization techniques employed, with a special focus on the investigation of magnetic and electrical properties of the Nb/FePd bilayers.

4.1 Molecular Beam Epitaxy

To study proximity effects in a multilayer system, the quality of each grown film as well as the interface conditions are essential parameters and are defined by the growth technique. Essential criteria are the sample environment, the substrate conditions and the growth rates of each material [92]. At first, the sample environment should have a low impurity level with high mean free path to avoid contamination during the growth process. Secondly, the substrate temperature mainly governs kinetic factors like adsorption and diffusion rates. Roughness and material of the chosen substrate further determine strain and defects occuring during the layer growth. The third important parameter, i.e. the growth rate of the deposited material, plays an important role for the roughness of the deposited layer [147]. Considering a layer composed of different materials, the correct stochiometry is as well defined by the ratio of the individual material growth rates.
For thin film multilayer systems the MBE is a widely used method, as it meets various

requirements: It typically has a base pressure in UHV-range resulting in a high mean free path, much larger than the chamber size. Due to the UHV-conditions, growth far from thermodynamical equilibrium and at defined substrate temperatures can be conducted to control the growth mode. MBE offers the possibility to grow with monolayer precision due to low beam rates, so that atomically smooth surfaces can be achieved [147]. Each material is stored in a separate cell, which enables a desired stochiometry in the heterostructures. Furthermore, the operation in Ultra-High-Vacuum (UHV) allows the use of in-situ characterization methods like Reflection High-Energy Electron Diffraction (RHEED), Low-Energy Electron Diffraction (LEED) and Auger Electron Spectroscopy (AES), which will be explained in the following sections.

These advantages make MBE the method of choice for many semiconducting devices, quantum materials and nanostructures used in modern technology [147, 148].

4.1.1 Basic growth mechanisms

The term "epitaxy" describes an oriented growth of a deposit onto a substrate or film. A growth process with the same kind of material of the desired film and the substrate is called "homoepitaxy", and on a substrate of different kind "heteroepitaxy" [149]. In this section, the basic thermodynamic processes for the growth of heteroepitaxial mulitlayer systems with regard to the above mentioned parameters will be discussed.

Assuming a thermodynamic equilibrium state, the surface energies of the substrate and the deposit (γ_S and γ_A, respectively) as well as the interface energy γ_I between them determines the quality of the grown layer. If the substrate energy γ_S exceeds $\gamma_A + \gamma_I$, a smooth layer-by-layer growth is achieved due to a strong binding of the adatoms to the substrate. For $\gamma_S < \gamma_A + \gamma_I$, islands will form in the deposited film [92] as the binding between the adatoms is stronger than to the substrate. The first case is also called "Frank-van der Merve" growth, the preferred growth mode for thin film multilayers, the latter "Volmer-Weber" growth (see Fig. 4.1(a) and (b)). Fig. 4.1(c) shows the "Stranski-Krastanov" growth, a combination of a layer-by-layer and island growth. Also here initially $\gamma_S > \gamma_A + \gamma_I$ is required but accompanied by strain effects in the deposited film. Strain in epitaxially grown thin films can occur due to lattice mismatch, not compatible crystallographic orientations or surface reconstructions [147, 149]. After reaching a critical thickness, the strain will release into defects and causes a higher value of $\gamma_A + \gamma_I$ compared to γ_S, resulting in island growth.

The above mentioned growth criteria only hold in thermal equilibrium, opening the need for non-equilibrium models to describe kinetic processes like adsoprtion, desorption and diffusion of deposited atoms . These can be introduced for example in DFT and

Monte Carlo based simulations [92]. High surface kinetics is needed to assure a perfect crystal growth [147]. Thus, depending on the deposit and the substrate, it might be necessary to grow at elevated substrate temperatures.

For example, FePd grows in an ordered $L1_0$-phase with monoatomic layers of Fe and Pd at 600 K substrate temperature, whereas at 300 K substrate temperature a disordered fcc phase is developed [150].

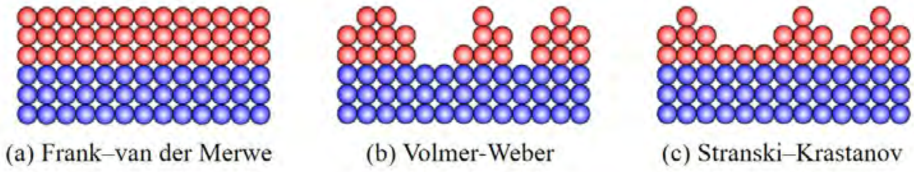
(a) Frank–van der Merwe (b) Volmer-Weber (c) Stranski–Krastanov

Figure 4.1: Three growth modes in heteroepitaxial deposition: (a) Layer-by-layer growth, (b) island-growth due to low binding of adatoms to the substrate surface, and (c) mixed layer-by-layer and island-growth. Taken from [128].

4.1.2 MBE-Setup

All samples used in this work are grown with a state-of-the-art MBE M600 system from DCA Instruments Finland. Fig. 4.2(a) shows the top view of the MBE which consists of three parts: The load lock to insert the substrates (operated in high vacuum), the buffer line to connect the load lock with the main deposition chamber, and the main chamber (base pressure of $\approx 10^{-10}$ mbar). All three parts can be pumped and vented separately by closing the shutters (in Fig. 4.2(a) marked by vertical black lines). LEED and AES instrumentations are installed inside the buffer line for sample characterization. Samples are moved from the buffer line to the main chamber with a transfer rod. Inside the main chamber, the samples are positioned upside-down in a manipulator in the center of the deposition chamber which is displayed in Fig. 4.2(b). The manipulator contains a heater element for substrate annealing above the sample position and can be heated up to 1000°C. Directly below the sample position, a Quartz Microbalance (QMB) can be inserted to calibrate the deposition rates. By deposition of any material on the quartz crystal, its mass and therefore its resonant frequency are changed, which can be detected and calibrated to the growth rate [151]. A shutter between the QMB and the sample prevents deposition during the calibration process. After calibration, the QMB is removed from the center position to open the way to the sample position. For the growth of thin film heterostructures, chemical purity is a major issue. Contamination in the chamber can cause surface oxidation and structural defects, leading even to amorphous growth. During the growth process, the contamination in the chamber is monitored with a residual gas analyzer (RGA). For material deposition, six Knudsen effusion cells and two Electron Beam Evaporators (EBV's, each with 4 crucible positions) are located around the main chamber. In the effusion cells the solid material is stored in crucibles, which is heated by surrounding filaments connected to a high voltage power supply. The desorption process of material inside the crucibles is controlled by temperature via the applied voltage, which itself is regulated with Eurotherm Proportional-Integral-Derivative controllers (PID). The crucibles inside the EBV's can be exposed to an electron beam. The rate from material inside the EBV's is separately controlled by two seperate QMB´s.

In this work, the materials Fe and Pd are evaporated from effusion cells, whereas Cr, MgO and Nb are stored each in an EBV crucible. A RHEED instrumentation inside the main chamber enables an in-situ growth monitoring and surface quality investigation (explained in detail in 4.2.1). The RHEED screen is located opposite to its electron beam source. The LEED and RHEED setups and working principles will be explained in section 4.2.

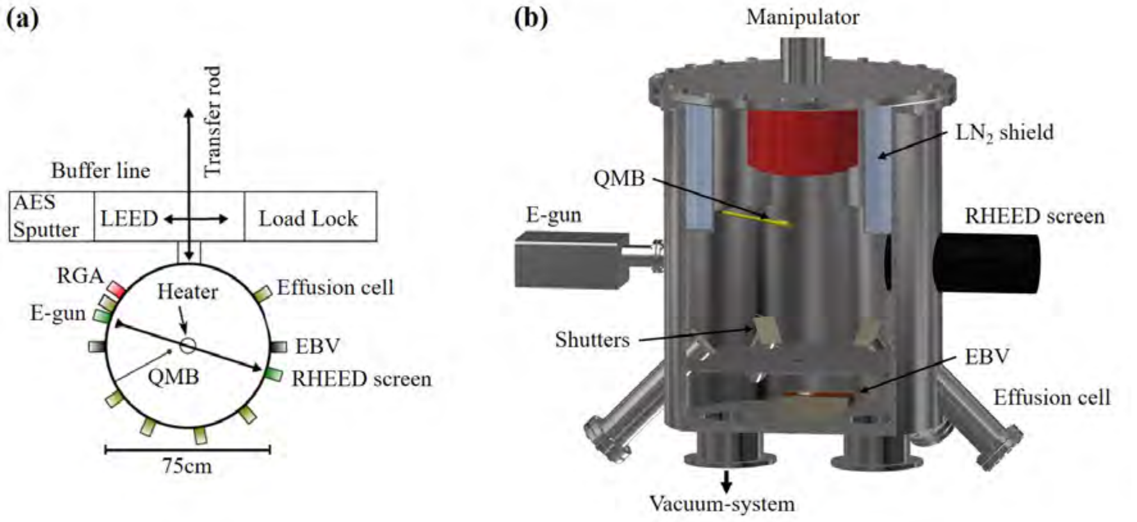

Figure 4.2: Setup of the OMBE system: (a) overview on the Load Lock, the Buffer line (including LEED and AES measurement setups), the transfer rod to move samples to the deposition chamber, and the main chamber. (b) Side view on the main chamber with the vacuum system and the effusion cells and electron beam evaporators at the bottom, and the upper part of the OMBE system as described in the text. Based on [128].

In Fig. 4.2(b) a more detailed side view of the main chamber displays the positions of all instrumentations with respect to the manipulater and substrate position. It can be seen, that the RHEED screen and its respective electron gun are mounted in grazing incidence to the substrate. The effusion cells are located in the lower segment of the chamber. Any evaporated material can be screened from the main chamber by separated shutters for each evaporation cell. Also both EBV's can be closed by distinct shutters. At the bottom, two vacuum pumps are connected to the main chamber: One cryopump and one turbo molecular pump, which is itself connected to a backing scroll pump. Further reduction of ambient pressure is reached by the liquid nitrogen shielding. By inserting LN_2 into the shield, the chamber walls are cooled down, leading to condensation of residual gas atoms. The buffer line is pumped by one turbomolecular pump and one ion getter pump, the load-lock is connected to an own small turbo molecular pump with a backing scroll pump.

4.2 In-situ characterization methods

One of the main advantages of sample growth using MBE is the possibility of tracking the growth process with in-situ characterization methods like RHEED. In this way, crystallinity, surface roughness and reconstructions can be observed as function of the layer thickness during the growth process. Due to its versatility, RHEED is one of the most important techniques for in-situ growth control in an MBE process [147]. Other techniques like LEED and AES can help to analyze the crystal structure and stoichiometry without breaking UHV.

4.2.1 Reflection High-Energy Electron Diffraction

In Reflection High-Energy Electron Diffraction (RHEED), an electron beam with an energy of 15 keV penetrates the surface of the substrate or growing layer in grazing incidence (1°-3°) and is reflected to a fluorescence screen. Referring back to chapter 3.1, we can use the Ewald sphere to analyze the reflected intensity. Due to the low incident angle, a 2D-reflection from the topmost layers can be assumed, leading to 1D rods of the surface reciprocal lattice. Additionally, the Ewald sphere diameter (due to the high beam energy) is much larger than the reciprocal atomic lattice spacings. Both these properties of RHEED promote sharp diffraction spots on the RHEED screen if the electron beam is assumed to be scattered from a smooth, crystalline surface (see Fig. 4.3). However, several deviations from these assumptions can arise [147]: (i) Broad and smeared-out scattering intensities result from the fact that also the 1D reciprocal lattice rods of surface atoms and as well the Ewald sphere itself have finite thicknesses. (ii) On a rough surface islands lead to additional scattering spots. (iii) The electron beam penetrates deeper into the surface and multiple scattering effects can occur. (iv)

Surface reconstructions cause intermediate reflection spots in between the reflection signals from the bulk crystal structure. Despite all these considerations, a quantitative analysis of the surface unit cell is possible, but challenging [147].

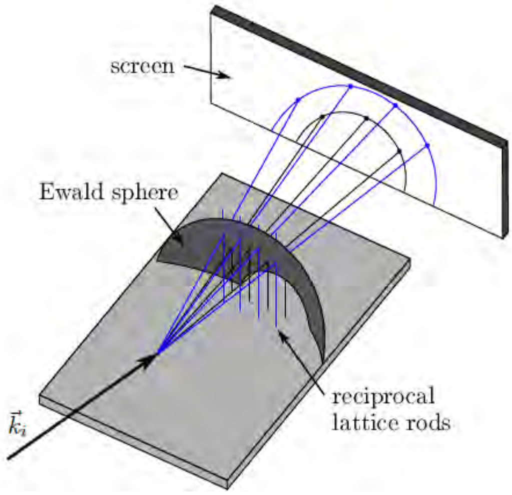

Figure 4.3: RHEED measurement setup and scattering intensities for reflection on a perfect surface and bulk crystal structure, forming sharp spots on the RHEED screen due to scattering at 1D reciprocal lattice rods. Taken from [128].

Figure 4.4(a) shows an example of a RHEED image after reflection from an annealed MgO substrate, whereas in Fig. 4.4(b) and (c) smeared reflections from a smooth surface but with structural domains or terraces (like in the deposited FePd) and reflection from a surface covered with islands (like in the deposited Nb) are visible, respectively. For details of growth conditions and sample qualities see chapter 5.

Additionally to the main RHEED reflections, sharp diagonal scattering lines range from the zeroth order peak to the end of the RHEED screen, which are called Kikuchi lines and result from incoherent scattering [152]. They appear for smooth surfaces and ordered crystal structures and smear out due to structural defects, domain patterns or high surface roughness [147]. As the appearance of Kikuchi lines due to high crystalline perfection is independent of the elastic scattering forming the main RHEED intensities, they can give additional information on the sample quality.

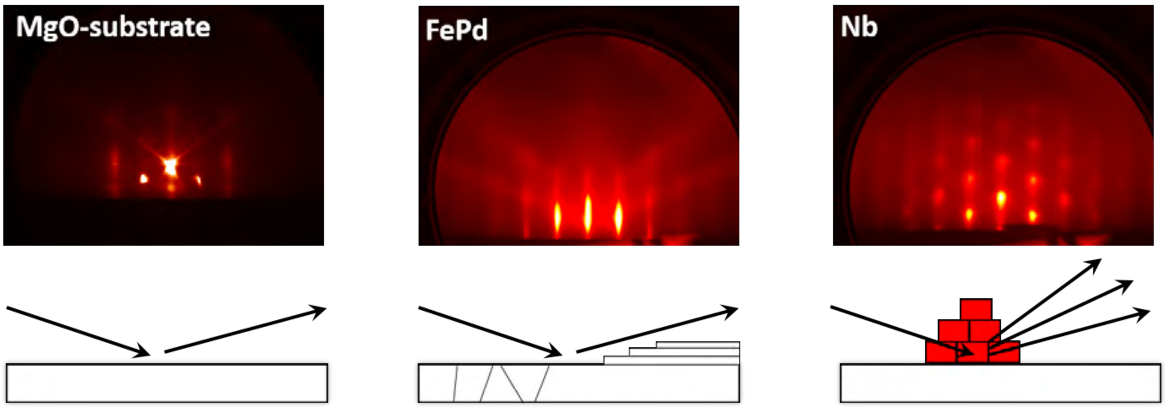

Figure 4.4: RHEED patterns of (a) a smooth MgO substrate after annealing, sharp Kikuchi lines denote a flat surface and high crystalline order, (b) an FePd layer with elongated RHEED intensities and smeared-out Kikuchi lines which accounts for some crystalline imperfections or terraces on the surface and (c) an Nb layer with a rough surface and island growth, visible in the multiple, smeared-out and point-like scattering features without any visible Kikuchi lines.

Another functional use of monitoring RHEED intensities is their oscillation during the time of a layer growth process (I(t)). Despite the uncertainty which step in the current growth process is related to which exact I(t), the change in RHEED intensity is strongly correlated with the closing of each monolayer. Haeni et al. [153] have shown in an example of shuttered $SrTiO_3$ growth, that by monitoring RHEED intensities a stoichiometry control and a precise monolayer coverage of Sr or Ti is possible.
In this work, RHEED will be mainly used for a qualitative analysis of the surface roughness and reconstruction as well as for monitoring RHEED intensities with time during the shuttered FePd growth process (for details see chapter 5.3.2). The electron beam has an energy of 15 keV and impinges on the surface in an angle of 2°.

4.2.2 Low-Energy Electron Diffraction

In contrast to RHEED, the electron beam in Low-Energy Electron Diffraction (LEED) is impinging perpendicular to the surface with a smaller energy of typically 10-1000 eV [154] see Fig. 4.5. Due to their small energy and short penetration depth, the primary electrons are backscattered from the surface-near region and hit a fluorescence screen. To ensure visible fluorescence intensities, the energy of the impinging electrons is first increased by an accelerating grid. If the Bragg condition is fullfilled and a constant lattice spacing is assumed, sharp scattering spots are observed. Still, the perpendicular setup yields only information about the in-plane lattice constant and the in-plane crystal structure near the layer surface. The LEED instrument of the described OMBE system works at energies between 50-300 eV.

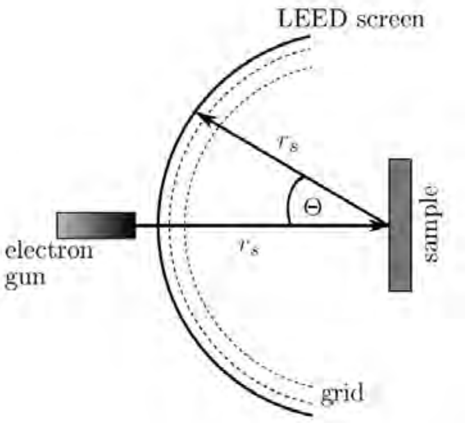

Figure 4.5: LEED measurement setup: The electron beam impinges on the sample surface in an angle of 90° and is reflected and accelerated towards the LEED screen by an accelerator grid. Taken from [128].

For comparison, Fig. 4.6(a) shows the LEED image of a tetragonal $L1_0$-ordered FePd smooth surface, whereas in Fig. 4.6(b) the absence of any diffraction spots of a Nb layer suggest an in-plane disordered growth.

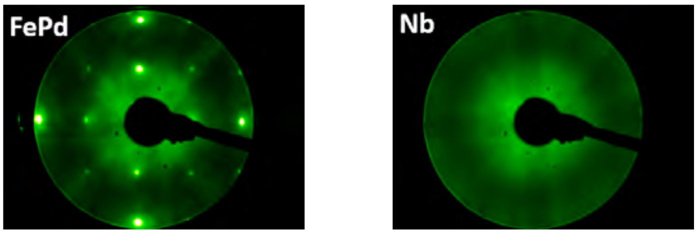

Figure 4.6: LEED images of (a) an $L1_0$-ordered FePd lattice with an in-plane rectangular lattice and (b) an in-plane disordered lattice of a Nb layer.

4.3 Ex-situ characterization methods

Various in-house experimental setups are used to determine structural, magnetic or electronic sample characteristics of the heterostructures. Additionally, the operation of instruments at large-scale neutron facilities, like KWS-3 and vSANS, aid in scrutinizing depth-resolved lateral magnetic structures from room-temperature down to the superconducting state of Nb. All relevant techniques are described in the following sections.

4.3.1 X-Ray Reflectometry and Diffractometry

X-ray Reflectometry (XRR) on thin film structures can give information on the layer thickness, surface roughness and density of each layer. Corresponding simulations are performed using GenX [134] and are described in detail in chapter 3.2.1. X-ray Diffractometry (XRD) is used to determine structural characteristics such as lattice plane orientations and the long-range order parameter of the two-component material FePd. Both techniques are performed in a Bruker AXS D8 Advanced system as schematically shown in Fig. 4.7

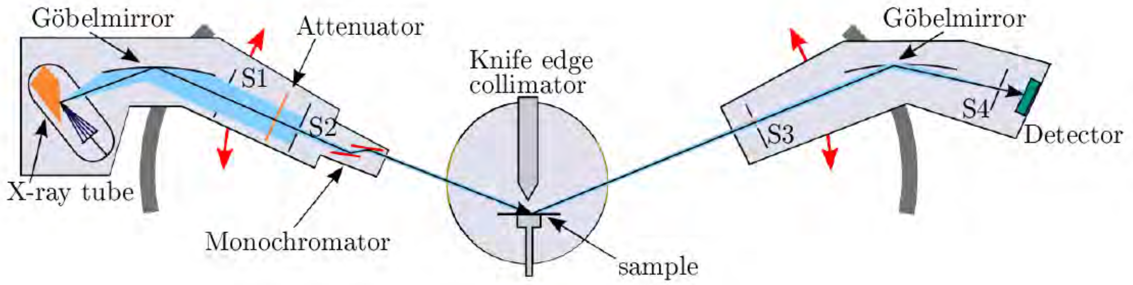

Figure 4.7: Instrument Setup of the D8 Reflectometer and Diffractometer with the X-ray tube (left), the sample stage (middle) and the detector (right), taken from [128].

Using a cupper electrode, the Cu-K$_{\alpha1}$ X-ray radiation with $\lambda = 0.154\,\mathrm{nm}$ is selected by two monochromators: a Goebel-mirror directly opposite to the Cu electrode producing a parallel X-ray beam and a Channel-Cut Ge(002) crystal placed behind the beam collimating slit system. An automatic rotary absorber attenuates high beam intensities which can occur under low incident angles on the detector. The sample environment consists of a fixed stage (i.e. only out-of-plane information on the crystalline structure is measured) and a Knife Edge collimator to reduce the background at the sample position. The detector system on the right in Fig. 4.7 is composed of another slit system and a Göbel mirror to achieve a well collimated beam on the one-dimensional scintillation detector. Reflectometry as well as diffractometry measurements are performed in a $\omega{-}2\theta$-scan by rotating the X-ray tube and detector along the grey marked circle in Fig. 4.7. The available angular range is $0° - 110°$.

4.3.2 Scanning Transmission Electron Microscopy

The heterostructure morphology and the interface quality are imaged by Scanning Transmission Electron Microscopy (STEM). Generally, two operation modes are distinguished: the Bright-Field mode to detect the direct (unscattered) beam, and the

Dark-Field mode for scattered electrons. To detect both, the bright-field and the dark-field images, typically a detector setup as sketched in Fig. 4.8 is used, with annular dark field detector rings. Additionally, High-Angle Annular Dark-Field (HAADF) measurements are obtained at higher scattering angles. Signals in the HAADF images are caused by incoherently and elastically scattered electrons, which at high scattering angles dominate over the coherently scattered electrons due to the influence of the Debye-Waller factor on the coherent beam [155]. The intensity of HAADF images scales with the atomic number Z of compositions in the sample, leading to a high sensitivity for high-Z components [152]. Using the Energy-dispersive X-ray Spectroscopy (EDX) setup, a chemical analysis is conducted to obtain element-specific information on the heterostructures. The high-energy electron beam causes excitation processes of inner-shell electrons, and characteristic X-ray radiation is emitted from electrons of higher energy migrating to the empty lower energy state and leads to an element specific X-ray spectrum.

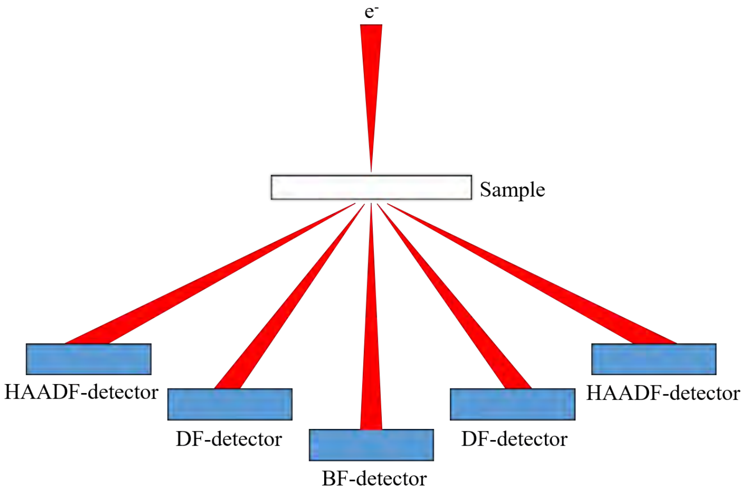

Figure 4.8: Detector arrangement for Bright-Field, Dark-Field, and High-Angle Annular Dark-Field measurements in STEM [152]. The path of scattered and detected electrons after transition through the sample is depicted in red.

To analyze the heterostructure morphology, cross-sectional images of the layer stack are desired. For high-resolution STEM images, the sample has to be thinned down to a thickness of $\sim 100\,\mathrm{nm}$ by Focused Ion Beam Milling (FIB). Before the FIB thinning, Au and C protection layers are deposited on the surface region which are then used as TEM lamella for cross-sectional images. Subsequently, this sample portion is cut out by the FIB milling and placed on a TEM grid for a further fine-milling step. Two different instruments have been used at an accelerating voltage of 200 kV - (i) the FEI Titan G2 80-200 CREWLEY [156] and (ii) the FEI Titan G3 50-300 PICO [157] systems, in which strong spherical aberration correctors as well as probe-forming lens systems to achieve a spatial resolution $< 1\,\mathrm{nm}$ are implemented. All measurements are performed together with Juri Barthel from the Ernst Ruska-Centre for Microscopy and Spectroscopy with Electrons (ER-C).

4.3.3 Rutherford Backscattering Spectrometry

The layer stoichiometry and thickness are probed by Rutherford Backscattering Spectrometry (RBS). A high-energy He^+ ion beam is accelerated to 1.4 MeV and inserted perpendicular to the sample surface. Due to Coulomb repulsion, the charged He ions are backscattered and obtain an element specific energy loss and deflection angle [158]. Thus, a spectroscopic measurement of the scattering cross-section $\sigma(E)$ allows a determination of depth-resolved sample composition. Equation (4.1) yields σ with respect to the scattered energy E and the scattering angle ϕ [159]:

$$\sigma = \Omega \left(\frac{Z_1 Z_2 e^2}{2E} \right)^2 \frac{(\cos\phi + \cos\Delta)^2}{\sin^4\phi \cos\Delta}, \tag{4.1}$$

with the solid acceptance angle Ω of the detector, the atomic numbers Z_1 and Z_2 of the He^+ ions and the target ions, respectively, and the abbreviation $\cos\Delta = \sqrt{1 - x^2 \sin^2\phi}$ (and x being the relative mass of the incident ions to the sample).

In this work, the RBS measurements are performed by Jürgen Schubert from the Peter Grünberg Institut (PGI-9) and analyzed using the RUMP software [159] to obtain each layer stoichiometry. Due to the high error in layer thickness calculation (∼10%), for the thickness calibration the above explained XRR simulations are employed.

4.3.4 Atomic and Magnetic Force Microscopy

In scanning probe microscopy, a sharp tip (with a tip curvature of ∼10 nm), mounted at the front of a cantilever holder, scans the sample surface as shown in Fig. 4.9(a). Due to interactions between the sample surface and the tip, information on the surface topography, magnetic structures, elasticity, adhesion, etc. can be retrieved by using different sub-techniques [160]. Here, Atomic Force Microscopy (AFM) and Magnetic

Force Microscopy (MFM) are used to measure the sample topography and lateral magnetic domain structure.

Upon approaching the sample surface, the tip is bent due to the sample-tip interactions. The resulting potential is the well-known Lennard-Jones potential between two interacting particles [161] displayed in Fig. 4.9(b). If the tip is additionally coated with a magnetic material, the tip-sample interactions by magnetic stray fields will shift the tips resonance frequency Δf and phase (see Fig. 4.9(c)).
In this work, the system is driven in the ac intermittent contact mode (or "tapping" mode), in which the tip is forced to oscillate close to its resonance frequency. At large distances (i.e. "Free Oscillation" (FO) regime), no interaction between tip and sample takes place. Reducing the distance between the tip and the sample, the "non-contact" (NC) regime is reached, and the tip experiences a weak attractive potential. A further approach to the sample surface results in a strong repulsive interaction (i.e. "contact" regime) due to Van-der-Waals interactions. The tip deflection is detected by a laser beam which is reflected from the tip's backside onto a position-sensitive photodetector, which records the amplitude, phase, and frequency shift of the oscillating tip. Each line of the scan is passed twice, once close to the sample surface to detect the topographic image, and once at a preset distance above the sample surface where the topography cannot be detected, but magnetic stray fields still act on the tip and change its resonance frequency and phase.

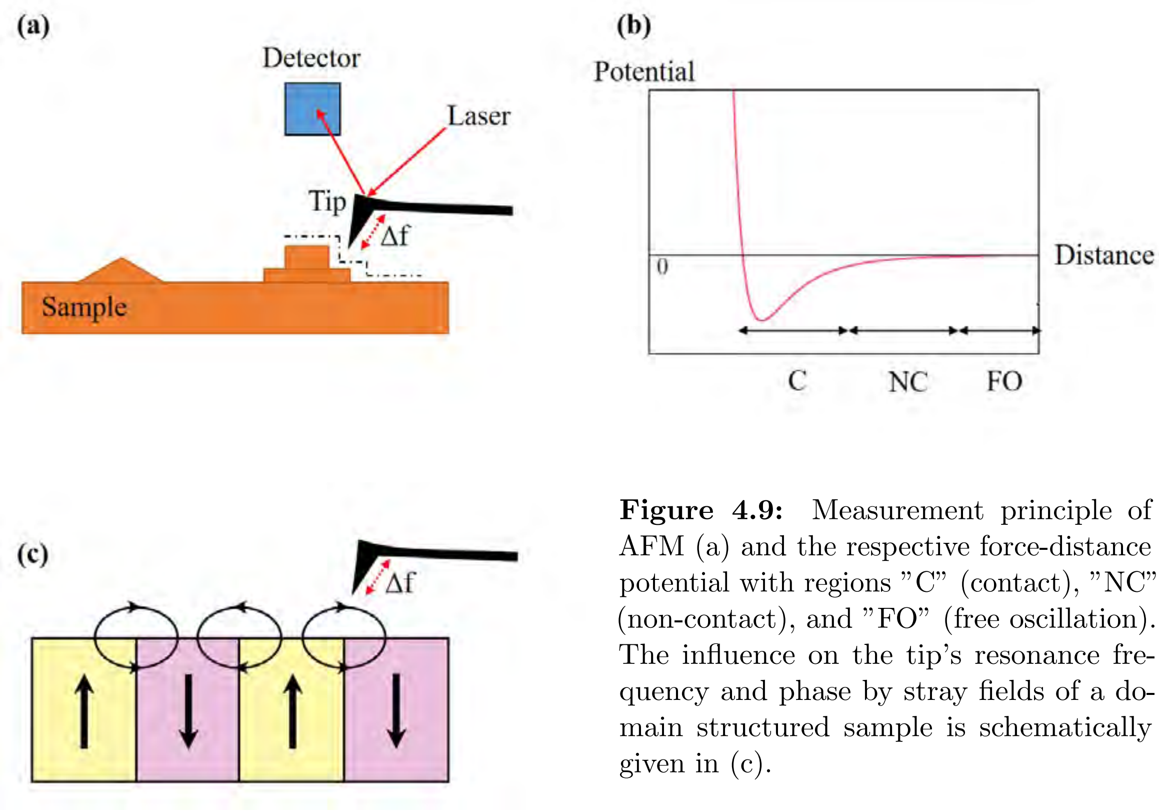

Figure 4.9: Measurement principle of AFM (a) and the respective force-distance potential with regions "C" (contact), "NC" (non-contact), and "FO" (free oscillation). The influence on the tip's resonance frequency and phase by stray fields of a domain structured sample is schematically given in (c).

All AFM and MFM measurements are performed in an Agilent 5400 microscope in the ac intermittent contact mode.

4.3.5 Magnetic Properties Measurement System

Magnetic hysteresis loops are conducted with high sensitivity in a SQUID (Superconducting QUantum Interference Device)-Magnetometer. A SQUID consists of a high-temperature superconducting ring in which thin insulating layers (Josephson junctions) serve as detector for small changes in an external magnetic field penetrating through the SQUID coil. A supercurrent is applied through the Josephson-junctions and recombined with a resulting phase relation depending on the change in magnetic field and a periodicity of the magnetic flux quantum Φ_0. A dc-SQUID is based on two Josephson-junctions, whereas a rf-SQUID uses one Josephson-junction.
Here, the employed instrument is a Quantum Design Magnetic Properties Measurement System (MPMS) based on a rf-SQUID with a sensitivity of $10^{-11}\,\mathrm{Am}^2$ and a maximum magnetic field strength of 7 T, which can be operated in DC- or RSO- (reciprocating sample option)-mode [162]. A sketch of the instrument setup is given in Fig. 4.10. The sample is mounted in the desired measurement direction inside a straw and inserted into

a second-order gradiometer pick-up coil to reduce any noise from the applied magnetic field. By a sample movement through the pick-up coil a voltage is induced into the coil, with a response function of a magnetic dipole in an external magnetic field, and further transferred to the rf-SQUID device which measures the induced voltage with high sensitivity [162].

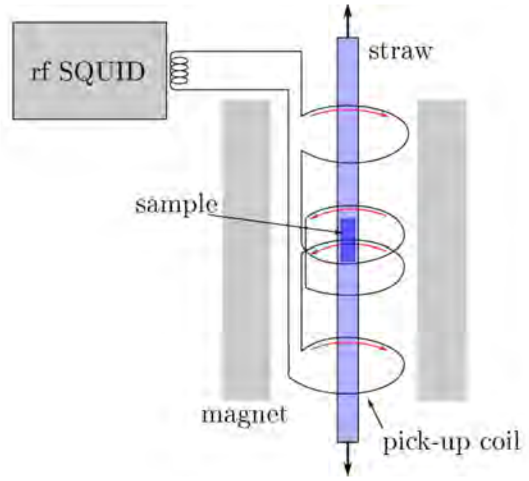

Figure 4.10: Schematic instrument setup of the rf-SQUID and the sample environment: the sample is mounted in a straw and placed between pick-up coils to transfer the induced voltage to the rf-SQUID. Taken from [128].

4.3.6 Physical Properties Measurement System

Measurements of the sheet resistivity with respect to temperature and field are obtained in a Quantum Design Dynacool-PPMS (Physical Properties Measurement System) in Electric Transport Option (ETO) with an ac current of 10 μA and a frequency of 18 Hz. It can be operated with fields up to 9 T and temperatures down to 1.9 K. The sample is contacted in a linear four-point-probe setup with equal spacing using a wire bonder. In such a setup, the sheet resistivity ρ is calculated by (4.2) with the thickness d of the measured layer and a point-spacing s dependent value f_2 [163].

$$\rho = \frac{\pi}{\ln 2} d \left(\frac{V}{I}\right) f_2, \quad s \ll d \tag{4.2}$$

4.3.7 Large scale facility instruments

Depth-resolved lateral structural and magnetic correlations are probed by GISAXS and GISANS, respectively. To achieve preliminary information on the chemical depth-profile, GISAXS experiments are carried out in-house at GALAXI in the JCNS-2 institute of Forschungszentrum Jülich. Based on the results from GISAXS, an investigation on the magnetic correlations on mesoscopic length scale is conducted by GISANS measurements at the large-scale neutron facilities Heinz Maier-Leibnitz Zentrum (MLZ) in Garching, Germany (at the insrument line KWS-3) and the NIST Center for Neutron Research (NIST-NCNR) in Gaithersburg, USA (at the instrument line vSANS).

4.3.7.1 GALAXI

At the Gallium Anode Low-Angle X-ray Instrument (GALAXI), SAXS and GISAXS measurements can be performed by either a transmission sample geometry or grazing-incidence geometry, respectively. A high-brilliance metaljet X-ray source by Bruker AXS provides Ga $\mathrm{K}_{\mathrm{alpha}}$ radiation with $\lambda = 0.13414\,\mathrm{nm}$, which is monochromatized by parabolic Montel-type optics. The beam collimation is performed by two slits S1 and S2 (see Fig. 4.11), S3 serves as background slit. A 2D-position sensitive Pilatus 1M detector is placed behind an adjustable flight path length of 835 - 3535 mm to measure Q-ranges from $4 \cdot 10^{-2}$ - $8\,\mathrm{nm}^{-1}$. All tubes can be evacuated independently to a pressure of $<1\,\mathrm{mbar}$.

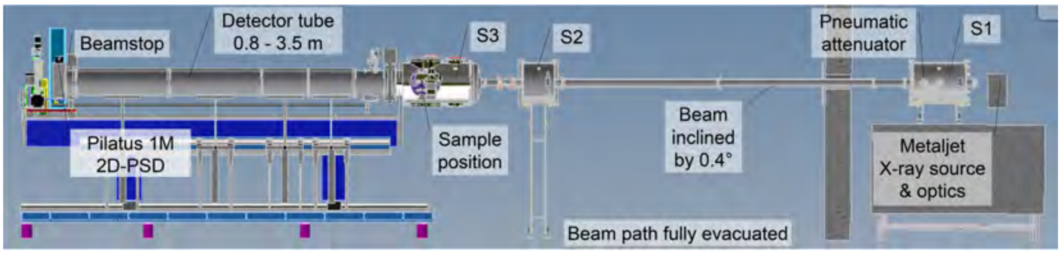

Figure 4.11: Instrument setup of GALAXI, taken from [141].

4.3.7.2 KWS-3

The schematic setup of the Klein-Winkel-Streuung-3 (KWS-3) instrument line is depicted in Fig. 4.12. It can be operated in a wavelength range of $\lambda = 10\text{-}30\,\text{Å}$ with a wavelength spread of $\frac{\Delta\lambda}{\lambda} = 0.2$, selected by a MgLi velocity selector. After the entrance aperture, the unpolarized neutron beam is directed to a double-focussing toroidal mirror, providing a wavelength resolution of $\delta Q = 10^{-4}\,\text{Å}^{-1}$ [164] and advantages in intensity over pinhole focusing as typical for SANS instruments. The collimation is given only by the entrance pinhole and the toroidal mirror itself. Both the entrance aperture and the 2D positional sensitive detector are placed at the focus points of the mirror, leading to a one-to-one image of the entrance aperture onto the detector [165]. The sample can be mounted on various sample position stages depending on the desired Q-range.

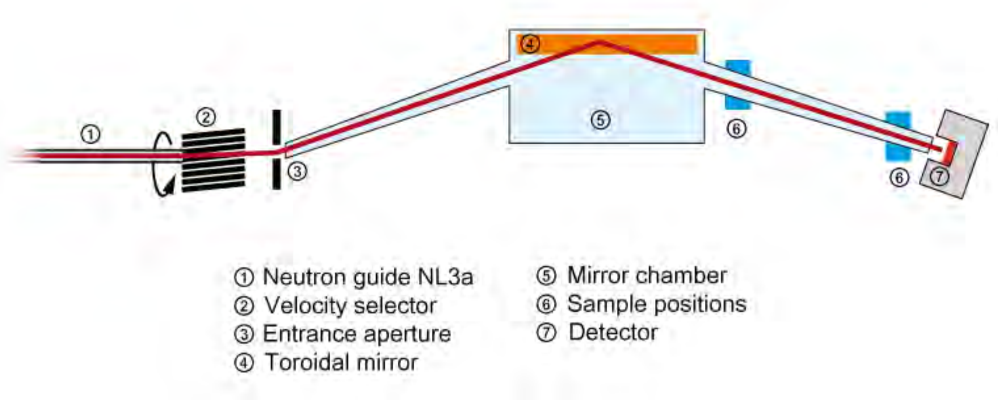
①
②
③
④
⑤
⑥
⑥
⑦
① Neutron guide NL3a
② Velocity selector
③ Entrance aperture
④ Toroidal mirror
⑤ Mirror chamber
⑥ Sample positions
⑦ Detector

Figure 4.12: Instrument setup of KWS-3, taken from [164].

4.3.7.3 vSANS

Polarized GISANS measurements with full polarization analysis are performed at the very Small Angle Neutron Scattering (vSANS) instrument at the NG3 beamline at NIST-NCNR. Due to its very long setup with a maximum flight path of 45 m and detector positions at various distances, a broad Q-range is probed [166]. In contrast to KWS-3, a pinhole SANS technique is used, with rectangular collimation slits for the here presented measurements. For pinhole SANS, the collimation is given by the entrance pinhole and the sample pinhole [165].

Fig. 4.13 sketches the instrument setup of vSANS: an unpolarized neutron beam is polarized by a super mirror cavity consisting of FeSi multilayers and can be flipped to achieve the desired polarization orientation at the sample position. The polarization of the scattered beam is analyzed using a ^{3}He spin filter.

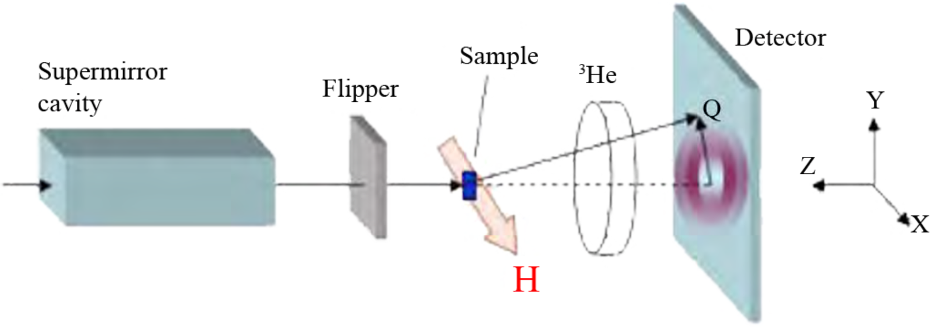
Supermirror cavity
Flipper
Sample
³He
Detector
Q
H
Y
Z
X

Figure 4.13: Instrument setup of vSANS, taken from [167].

For the GISANS measurements at vSANS, a sample holder was designed on which two samples can be placed and brought into the beam position during cooling by an attached cryofinger. The holder is made of bulk aluminium, the sample stages are surrounded by thin sheets of cadmium to prevent background scattering. During the measurement, the temperature is controlled by two sensors A and B, with temperatures T_A and T_B, respectively. Figure 4.14 shows the Al sample holder and the position of sensor B in between two sample stages. Sensor A is positioned at the top of the cryofinger.

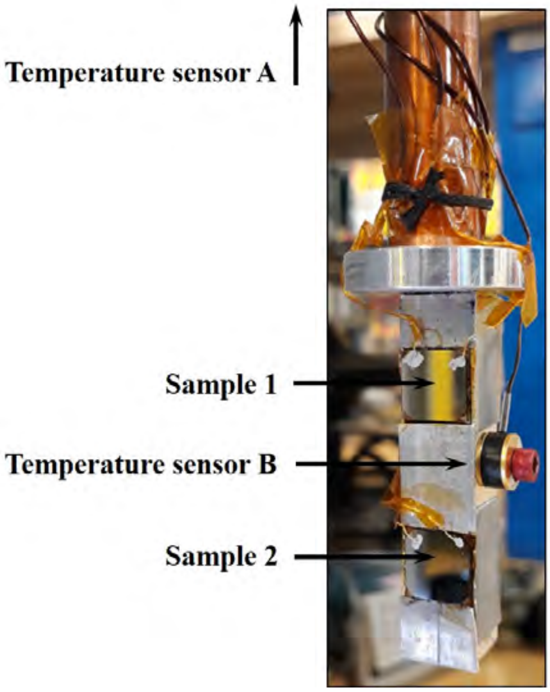

Figure 4.14: vSANS sample holder with two sample stages and the temperature sensor B mounted in between the sample positions for a precise temperature monitoring.

Chapter 5

Growth and room temperature characterization

The main objective in this work are direct and inverse proximity effects in Nb/FePd heterostructures grown by MBE. Whereas information on the domain structure in FePd in general were given in chapter 2, the present chapter starts with an introduction on the growth of FePd with controllable strength of PMA and magnetic domain configuration. Subsequently, in-situ and ex-situ characterizations at room-temperature are presented in sections 5.3.3 and 5.4, respectively. This chapter concludes with the measurement and simulation of Grazing-Incidence Small-Angle Neutron Scattering (GISANS) at room-temperature in section 5.4.4. These investigations will be used as basis for the analysis of S/F proximity effects at low-temperatures.

5.1 FePd in the L1_0-phase

The L1_0-ordered phase is a tetragonal derivative of the fcc-phase with a reduced point group symmetry of P4/mmm [19] and lattice parameters $a = b \neq c$. Its prototype CuAu and related materials like FePd order in alternating atomic planes as illustrated in Fig. 5.1.

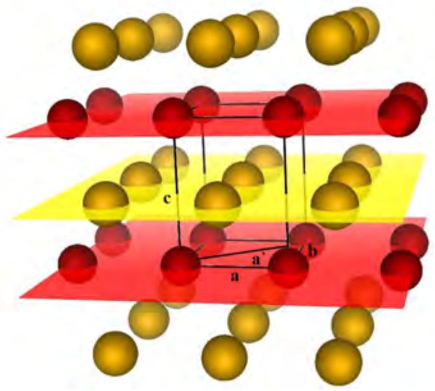

Figure 5.1: Layered structure of $L1_0$-phase materials with different atoms depicted by different colors. The black lines connect the tP2 unit cell with lattice parameters $a = b \neq c$, whereas the tP4 unit cell is shifted to the tP2 cell by an in-plane rotation of 45° (drawn with VESTA [168]).

The 2-atom unit cell has a Pearson symbol of tP2. The parent fcc structure with disordered atom sites is based on a larger unit cell with Pearson symbol tP4 (4 atoms per cell) resulting from a 45° shift of the tP2 cell and with lattice parameters $a' = a \cdot \sqrt{2} = b' \neq c'$. The lattice parameters for both unit cells as well as for the fcc disordered phase are listed in table 5.1.

lattice parameter	tP2	tP4	fcc
a	2.722	3.849	3.807
b	2.722	3.849	3.807
c	3.714	3.714	3.807

Table 5.1: Lattice parameters in (Å) of the tP2 and tP4 unit cells of $L1_0$-ordered FePd and the respective atomically disordered fcc phase [169].

The magnetocrystalline anisotropy in chemically ordered FePd thin films results from symmetry breaking during the fcc to tetragonal phase transition. The tetragonal crystal symmetry causes a different magnetization process along the [001] and <100> directions due to crystal-field interactions as well as the spin-orbit coupling within the alloy [15]. Thin film FePd in the $L1_0$-phase breaks into magnetic domains aligned along ±[001] with a Curie temperature of $T_C = 723\,\text{K}$, a saturation magnetization of $M_S \sim 1 \cdot 10^6\ \text{A/m}$ [19] and an exchange constant of $A \sim 10^{-11}\ \text{J/m}$ [173]. A reduction of structural order and/or the Fe content in the compound leads to a lower exchange constant and hence a lower T_C value. The structural long-range order depends the exact growth conditions which are treated in the following section.

5.2 FePd with varying PMA

Using MBE it is possible to tune the growth of FePd with different long-range order parameters as well as different degrees of PMA via changing the substrate temperature or growth mode. In codeposition, where Fe and Pd are simultaneously evaporated onto the substrate at elevated substrate temperatures ($\mathrm{T_s}\sim 600\,\mathrm{K}$), the $\mathrm{L1_0}$-phase with a high degree of chemical ordering and strong PMA is achieved [17]. Lowering $\mathrm{T_s}$ to $300\,\mathrm{K}$ results in an disordered fcc structure with weak PMA, and an in-plane easy axis (and $Q < 1$) [150] as described in chapter 2.1. Using shuttered growth with an alternating evaporation of Fe and Pd by closing the respective shutters of the evaporation cells with a constant evaporation time for each cell can lead, even at T_s=300 K, to an intermediate chemical ordering due to the artificially grown monolayer-by-monolayer structure of the $\mathrm{L1_0}$-phase. The strength of PMA and easy axis orientation in such samples are strongly thickness dependent. Gehanno et al. [171] used this growth method to investigate the thickness dependence of K_u, the easy axis orientation, and the stripe domain width D_domain. They found that a critical thickness of $\sim 30\,\mathrm{nm}$ exists, below which no magnetic domains are observed and the magnetic moments are aligned in the surface plane. Above the critical thickness, K_u, D_domain, and the Bloch domain wall width δ_{DW}, increase with thickness, with an increasing amount of out-of-plane oriented magnetic domains until a saturation value is obtained. Such transitions from weak to strong PMA with layer thickness in uniaxial thin films were calculated by Virot et al. [172] and shown in Fig. 5.2. The domain wall width of a FePd thin film with $K_u = 1 \cdot 10^6\ \mathrm{J/m^3}$ is calculated to be 10 nm in [173].

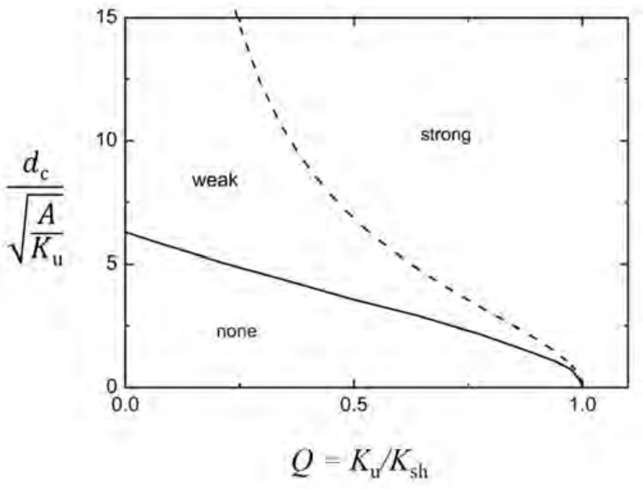

Figure 5.2: Critical thickness d_c with respect to $Q = \frac{K_u}{K_{sh}}$ for uniaxial thin films, Figure adapted from Virot et al. [172]. The area above the dashed line denotes thicknesses and Q values leading to strong PMA, whereas between the dashed and solid lines a weak PMA is evolved. Below the solid line, no PMA occurs in the thin film.

5.3 Sample growth

The primary objective of this thesis is to obtain fundamental relationships between the superconducting (S) and ferromagnetic (F) order parameters in Nb(S)/FePd(F) heterostructures, depending on the strength of PMA in the F-layer and the lateral domain orientation. Detailed insight into the origin of a superconducting response to stray fields from the ferromagnet or to an external magnetic field can only be gained after investigating the bare F and S layers.

In this section, first an overview on all important samples and their main objectives will be given, followed by an explanation of the basic growth mechanisms of the S/F heterostructures. Finally, a section on in-situ characterizations during/after the growth process and ex-situ room-temperature measurements to examine structural and magnetic properties of all samples is presented.

The samples are named regarding the following criteria:

- degree of magnetocrystalline anisotropy: ′high′ for high PMA, ′low′ for low PMA and ′mid′ for medium PMA,
- layer stack: ′F′ for heterostructures with FePd as toplayer and without Nb, ′S′ for bare superconducting thin films without FePd, and ′S/F′ for respective bilayer structures,

- growth order of samples with similar characteristics (for example '$\mathrm{F}_{\mathrm{high}}$'(1)-(4)).

Samples $\mathrm{F}_{\mathrm{high}}$-$\mathrm{F}_{\mathrm{low}}$ are used to investigate the appropriate growth mode and structural/magnetic characteristics of: (i) a maze domain structure with high PMA, (ii) a stripe domain structure with parallely aligned magnetic domains, and (iii) a sample that combines both medium to high PMA and stripe domains ('$\mathrm{F}'_{\mathrm{mid}}$). Bare Nb layers can be grown with high structural quality onto MgO at $T_{\mathrm{s}} = 820\,\mathrm{K}$ [174]. However, if Nb is grown at this temperature on FePd, Fe starts to diffuse into the Pd lattice as can be seen from HAADF-STEM measurements on $\mathrm{SF}_{\mathrm{low}}$ in the supplementary information Fig. 9.2. Therefore, bare S layers grown at a lower $T_{\mathrm{s}} = 320\,\mathrm{K}$ (samples S(1) and S(2)) are compared with S(3) and S(4) grown at $T_{\mathrm{s}} = 820\,\mathrm{K}$. Together with the Nb thickness, the crystallinity and structural order of Nb defines superconducting properties such as the critical temperature T_{c} and the upper critical field $\mathrm{B}_{\mathrm{c}}^{*}$.
Influence of the MgO substrate on the bare Nb films is investigated by a comparison sample S(5) with Nb grown on Silica.

The main focus lies on the S/F bilayers with S and F in direct proximity which are used to scrutinize phenomena like DWS and RDS, as well as the occurrence of long-ranged spin-triplet Cooper pairs (chapters 2.4.1 and 2.4.2, respectively). To distinguish stray field from proximity effects, reference samples with an additional insulating MgO layer are grown between Nb and FePd in the S/I/F samples. This procedure is illustrated in Fig. 5.3.

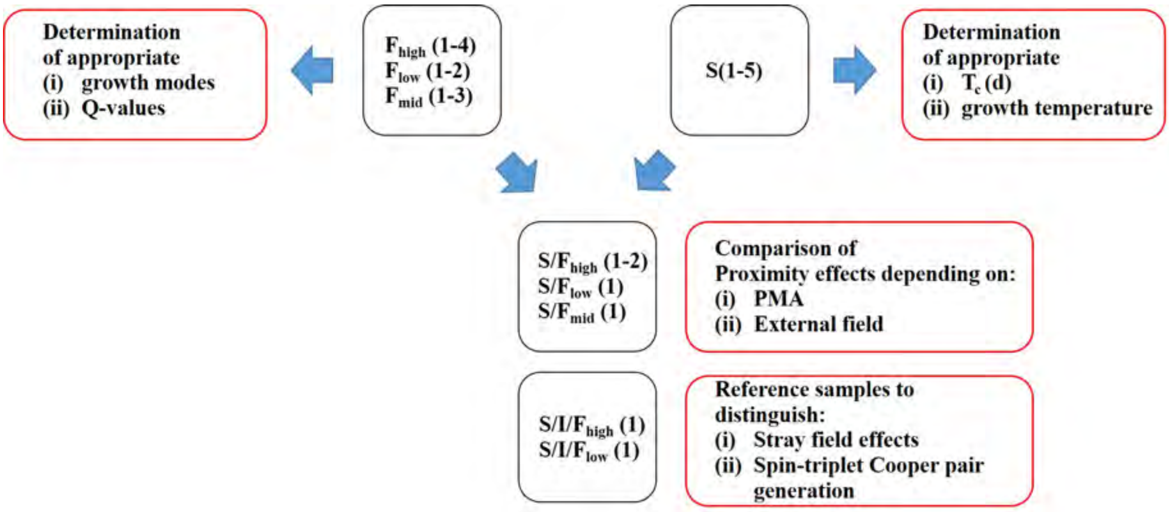
Determination
of appropriate
(i) growth modes
(ii) Q-values
$\mathrm{F}_{\mathrm{high}}$ (1-4)
$\mathrm{F}_{\mathrm{low}}$ (1-2)
$\mathrm{F}_{\mathrm{mid}}$ (1-3)
S(1-5)
Determination
of appropriate
(i) T_{c} (d)
(ii) growth temperature
S/$\mathrm{F}_{\mathrm{high}}$ (1-2)
S/$\mathrm{F}_{\mathrm{low}}$ (1)
S/$\mathrm{F}_{\mathrm{mid}}$ (1)
Comparison of
Proximity effects depending on:
(i) PMA
(ii) External field
S/I/$\mathrm{F}_{\mathrm{high}}$ (1)
S/I/$\mathrm{F}_{\mathrm{low}}$ (1)
Reference samples to
distinguish:
(i) Stray field effects
(ii) Spin-triplet Cooper pair generation

Figure 5.3: Sample growth procedure: first, bare F and S layers are grown to determine suitable growth processes for high, low and medium PMA in the F layer, and layer thicknesses as well as substrate temperatures of the S-layer which determines $T_{\mathrm{c}}(d)$. In a second step, S/F samples are investigated and compared with S/I/F samples.

Throughout this thesis, for every characterization technique usually one representative measurement from each sample stack with low, medium, and high PMA is described. Comparative measurements from other samples of the same stack are listed in the supplementary information in chapter 9. Additional sample information that is not provided within the text (like the surface roughness, all layer thicknesses, and sample growth information for each sample) is listed in the supplementary in tables 9.1-9.6.

5.3.1 Growth procedure

Epitaxial single crystalline FePd thin films are grown by a Pd/FePd/Pd/Cr/MgO heterostructure stack as shown in Fig. 5.4(a). A thin seed layer of Cr (∼2 nm) with a growth direction of (001)[110] onto the MgO(001)[100] substrate facilitates the growth of an epitaxial Pd (001)[100] buffer layer (∼60 nm) of good crystalline quality [150]. Due to the smaller lattice mismatch of a_{Pd} to the 45° in-plane rotated tP4 unit cell of FePd with $a_{\mathrm{FePd}} = 3.85\,\text{Å}$, such an orientation is favored compared to the tP2 cell with 2.722 Å [17, 169]. A confirmation of such a cell orientation in the here grown heterostructures is given by STEM measurements on $\mathrm{SF_{mid}}(1)$ in the supplementary information in Fig. 9.1. Superconducting Nb layers of thicknesses ∼40 nm are grown on top of FePd using electron gun evaporation, whereas the Pd and FePd layers are evaporated from effusion cells. For the S/F samples, Nb is grown in direct contact to FePd, whereas in the S/I/F samples an additional MgO layer is deposited in between FePd and Nb preventing proximity effects. A thin capping layer (2-5 nm) of either Pd or Cr protects against direct oxidation. However, in the next sections of this chapter, RBS and STEM-EDX measurements will demonstrate an oxidation of Nb after a sample aging of a few months. Furthermore, HAADF-STEM and STEM-EDX measurements on samples $\mathrm{SIF_{high}}(1)$, $\mathrm{SF_{low}}(1)$ and $\mathrm{SF_{mid}}(1)$ reveal an epitaxial growth of all layers except Nb (see figures 9.3, 9.4 and 9.5 in the supplementary information, which also show some planar and point defects in both the Pd and FePd layers).

An initial annealing of the MgO lattice to 720 K for 1 h and a subsequent heating to 820 K for 10 min provides a flat MgO surface which is confirmed by RHEED. After the growth of Pd at 300 K, the sample is annealed to temperatures between 620 K - 720 K for 30 min. Substrate temperatures during the FePd growth depend on the desired strength of PMA and are explained below. Nb is deposited by electron beam evaporation at either $T_{\mathrm{s}} = 320\,\mathrm{K}$ or $T_{\mathrm{s}} = 820\,\mathrm{K}$ as described above. Figure 5.4 illustrates that Nb exhibits a large lattice mismatch to FePd. Nb films deposited onto the FePd layer at 320 K show an out-of-plane epitaxial order but an in-plane disordered structure as confirmed by HAADF-STEM meausurements (displayed in the upper images of figures 9.3 and 9.4). In $\mathrm{SF_{low}}$, Nb was deposited at 820 K to test an epitaxial growth on FePd. Unfortunaly it was not possible to repeat the growth of $\mathrm{SF_{low}}(1)$ with Nb at $T_s = 320\,\mathrm{K}$. However, FePd in $\mathrm{SF_{low}}(1)$ still exhibits a $\mathrm{L1_0}$-ordered phase at the interface to Nb as confirmed by the HAADF-STEM image in Fig. 9.4. In section 5.4.3 it will be shown, that a stripe domain structure exists in $\mathrm{SF_{low}}(1)$ as expected. A detailed annealing procedure of all samples is given in tables 9.1-9.6.

The lattice constants of each layer in an orientation with respect to the given MgO lattice and the sample stack are displayed in Fig. 5.4(a) for the S/F samples and in Fig. 5.4(b) for the S/I/F samples. In Fig. 5.4(a), the HAADF-STEM EDX elemental map measured at Titan (s. chapter 4.3.2) on $\mathrm{SF_{mid}}(1)$ confirmes the displayed layer stack on the left and the growth of a thin seed layer of Cr between MgO and Pd to prevent a diffusion of Pd into the MgO substrate. The coloring of the EDX elemental map for the displayed atoms is given in the legend. The HAADF STEM image of $\mathrm{SIF_{high}}(1)$ in Fig. 5.4(b) measured at PICO reveals a spatial separation of FePd and Nb by a thin MgO interlayer. It has to be noted, that some structural defects in the FePd layer of $\mathrm{SIF_{high}}(1)$ lead to holes in the surface region of FePd which are filled by the subsequently grown MgO and Nb. These hole-like defects are analyzed in detail in section 5.4.2 with a comparison of HAADF-STEM EDX and AFM measurements.

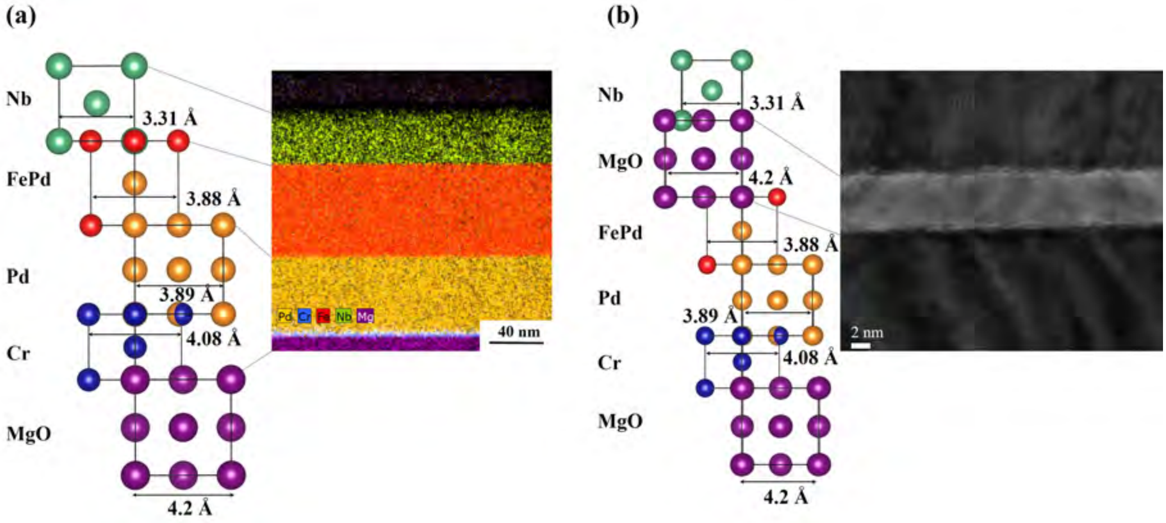

Figure 5.4: Heterostructure of (a) S/F samples with an EDX-STEM measurement of $\mathrm{SF_{mid}}$ and (b) S/I/F samples with a bright-field STEM measurement of $\mathrm{SIF_{high}}$. In the schematically drawn layer stacks, violet color denotes Mg of the MgO layer, yellow color Pd, red color Fe, and green color Nb.

5.3.2 Growth of FePd with high, low, and medium PMA

As mentioned in the previous section 5.2, FePd with varying degree of PMA are grown by adapting the growth conditions. In all $\mathrm{F_{high}}$ samples, the FePd layer is grown in codeposition at elevated substrate temperatures $T_\mathrm{s} = 500\,\mathrm{K}$ or $670\,\mathrm{K}$, with intended thicknesses of $\sim$50 nm. For $\mathrm{F_{low}}$, a shuttered growth of Fe and Pd at $\mathrm{T_s} = 300\,\mathrm{K}$ with intended thicknesses of 35 nm is used to achieve Q values near 1 but with high in-plane magnetic components to allow a parallel formation of magnetic domains. For samples with both, high PMA and stripe domains, first a shuttered FePd layer is grown using the growth process of $\mathrm{F_{low}}$ samples, followed by a second layer with the growth mode of $\mathrm{F_{high}}$. Both FePd layers in $\mathrm{F_{mid}}$ are intended to acquire thicknesses of 35 nm. The assumed domain formations in the FePd layer of $\mathrm{F_{high}}$-$\mathrm{F_{low}}$ are sketched in Fig. 5.5 together with the respective growth modes. The magnetic domains and their orientations are depicted with different colors and arrows, respectively.

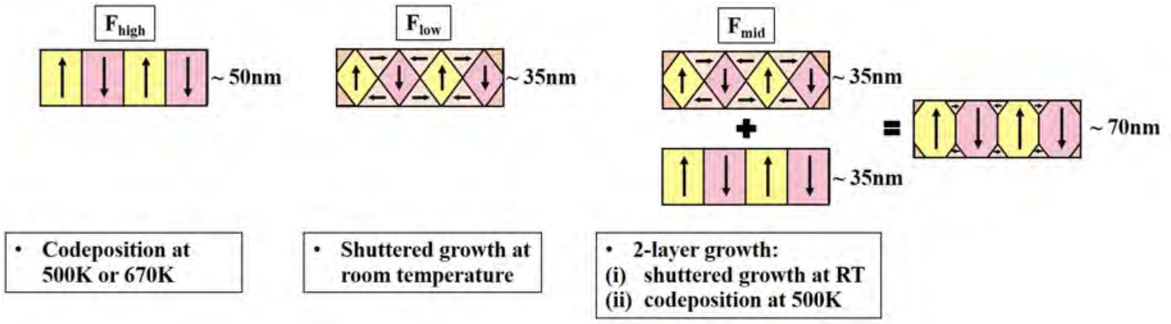
$\mathrm{F_{high}}$
~ 50nm
$\mathrm{F_{low}}$
~ 35nm
$\mathrm{F_{mid}}$
~ 35nm
+
=
~ 70nm
~ 35nm
• Codeposition at 500K or 670K
• Shuttered growth at room temperature
• 2-layer growth:
(i) shuttered growth at RT
(ii) codeposition at 500K

Figure 5.5: Growth mode (bottom) and expected domain formation (top) of FePd layers with high, low, and medium PMA, as well as their layer thicknesses. $\mathrm{F_{mid}}$ consists of two FePd layers with first low and second high PMA, which together yield a magnetic formation with intermediate PMA. Different colors and arrows denote the magnetic domains and their orientation, respectively.

5.3.3 In-situ characterization

After the growth of each layer, RHEED images were taken to qualitatively examine the surface roughness and surface reconstructions. In contrast to the FePd layer, the reflection of the Nb layer exhibits additional scattering intensities without the existence of Kikuchi lines denoting a rough surface and structural defects (see Fig. 5.6). Reflection images of the FePd layer still show elongated but sharp scattering streaks, indicating a flat surface without islands. According to the HAADF-STEM measurement presented in the next chapter in Fig. 5.11(c), lattice defects in the FePd layer can cause slightly smeared intensities of the Kikuchi lines.

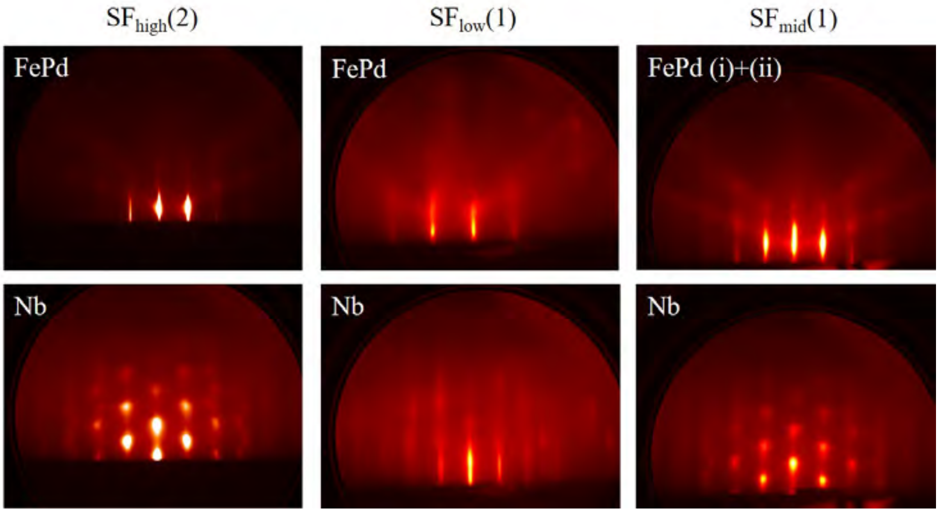

Figure 5.6: RHEED measurements taken at room temperature after the growth of the FePd layers (top) and the Nb layers (bottom) of samples $\mathrm{SF_{high}}(2)$, $\mathrm{SF_{low}}(1)$, and $\mathrm{SF_{mid}}(1)$.

By tracking the RHEED-oscillation intensity $\mathrm{I_{RHEED}(t)}$ of the first order peak in zeroth Laue order (i.e. left and right to the specular spot) with time, the monolayer-by-monolayer growth is monitored. The growth of one full monolayer corresponds to one oscillation period in $\mathrm{I_{RHEED}(t)}$. While in codeposition one full period is determined by the growth of the FePd superlattice with two full monolayers (Fe and Pd), in the shuttered mode one oscillation corresponds to one monolayer of either Fe or Pd. In this way, an incomplete monolayer coverage leads to a specific beat frequency in shuttered mode [153]. The higher the beat frequency, the less the deviation from a full monolayer coverage. These RHEED-oscillations were tracked for all FePd layers grown in shuttered mode and show that approximately the first half of the shuttered FePd layer obtains beat frequencies ranging from 5-20 oscillations, whereas the second half grows with an infinite beat frequency, showing a perfect FePd superlattice growth of the $\mathrm{L1_0}$-phase. An example of $\mathrm{F_{mid}}(1)$ can be found in the supplementary information in Fig. 9.6.

Using LEED, the in-plane epitaxial order of FePd and Nb is analyzed in Fig. 5.7. Sharp reflection spots in the FePd layers show the in-plane ordered lattice of the tetragonal $\mathrm{L1_0}$-phase. Nb layers do not exhibit any in-plane structural order, neither at $T_\mathrm{s} = 320\,\mathrm{K}$ as used for $\mathrm{SF_{high}}$ and $\mathrm{SF_{mid}}$ nor at $T_\mathrm{s} = 820\,\mathrm{K}$ as used for $\mathrm{SF_{low}}$.

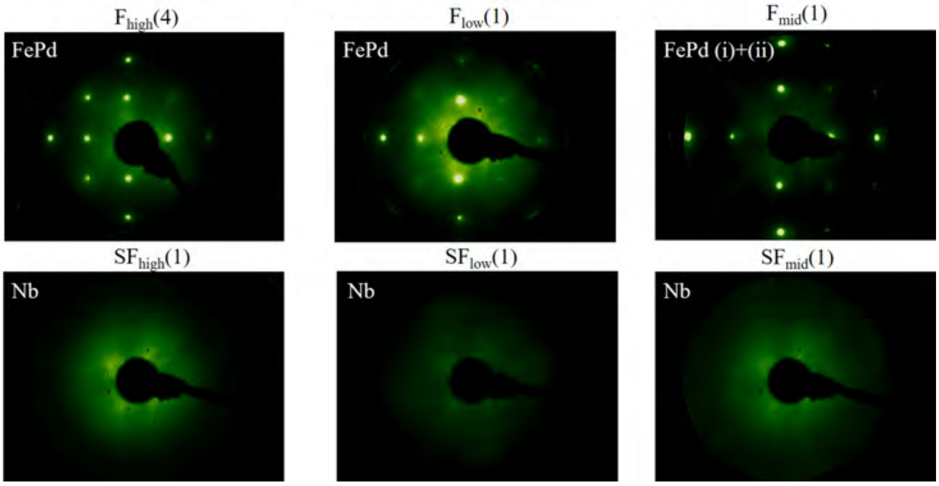

$F_{high}(4)$
FePd
$F_{low}(1)$
FePd
$F_{mid}(1)$
FePd (i)+(ii)
$SF_{high}(1)$
Nb
$SF_{low}(1)$
Nb
$SF_{mid}(1)$
Nb

Figure 5.7: LEED measurements taken after the growth of FePd (top) of the F samples and after Nb (bottom) of the S/F samples with high, low, and medium PMA.

A comparison of S(2) and S(3) with Nb grown at different substrate temperatures in Fig. 5.8 reveals that at elevated substrate temperatures of $T_s = 820\,\mathrm{K}$ in S(3), Nb can be grown with a smooth surface including surface reconstructions as indicated by reflection rods of lower intensity in between the main reflections of the out-of-plane ordered Nb bulk lattice rods. Still, in LEED no in-plane structural order is observed.

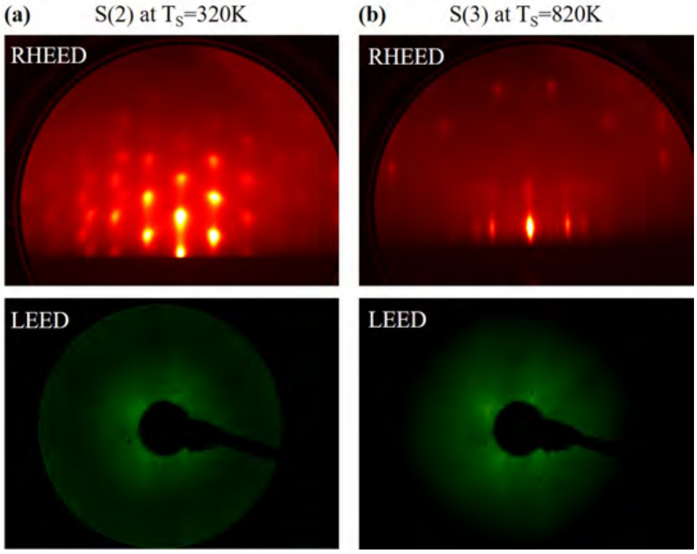

(a)
S(2) at T_S=320K
(b)
S(3) at T_S=820K
RHEED
RHEED
LEED
LEED

Figure 5.8: RHEED (top) and LEED (bottom) of S(2) and S(3) grown at different substrate temperatures T_s. The RHEED images show an island growth at T_s=320 K and an ordered out-of-plane growth with surface reconstructions at T_s=820 K. In LEED, no in-plane structural order is observed in both cases.

In summary, three different growth procedures are utilized to grow S/F bilayers with FePd consisting of low, medium, and high PMA. All FePd layers exhibit flat surfaces as well as good out-of-plane and in-plane structural order as measured by RHEED and LEED, whereas Nb layers grown at T_s=320 K exhibit strong island growth without in-plane structural order. However, the surface oxidation presented in section 5.4.1 determines the superconducting state more than a high surface roughness.

Samples with bare F layers are treated in the following sections to investigate structural and magnetic configurations and will be compared with respective S/F bilayers. Bare S layers are used to determine the thickness and growth temperature dependent T_c values which will be compared with the T_c values of S/F and S/I/F heterostructures in chapter 6.

5.4 Ex-situ characterization

5.4.1 X-ray reflectometry and diffractometry

All layer thicknesses and interface roughnesses are obtained by fitting the reflectometry curves using GenX. The results are compared with RBS measurements to reveal the composition of materials inside the heterostructures, particularly in the FePd layer. RBS measurements of $F_{\text{high}}(3)$ and $F_{\text{low}}(2)$ reveal that layers grown at elevated temperatures in codeposition exhibit an Fe_1Pd_1 composition, whereas layers grown in shuttered mode at room temperature can only be simulated by a $Fe_1Pd_{0.85}$ composition (see Fig. 9.8 in the supplementary). These compositions are also obtained from the reflectometry fits with different Scattering Length Density (SLD) of FePd with low and high PMA. Within GenX, the SLD's for X-ray scattering of a specific composition are based on the Henke tables [175].

XRR results of $F_{\text{mid}}(1)$ are fit by GenX with two FePd layers - (i) with a 1:0.85 composition and (ii) with a 1:1 composition which yields better figure of merits than only one FePd layer with intermixed compositions. These compositions are then assumed for all shuttered and codeposited FePd layers also in the reflectometry fits by adapting the SLD. In RBS, these two FePd layers cannot be resolved. The best fitting RBS simulation of sample $F_{\text{mid}}(1)$ shown in 9.8 is composed of one FePd layer with 1:1 composition and lower thickness than obtained by XRR which can result from to a low resolution within the RBS measurement, or an intermixing of the Pd and the two FePd layers covered in the XRR results by high interface roughnesses.

The SLD of all toplayers is altered by a small composition of oxygen additionally to the toplayer material. The ratio of oxygen to the deposited material is fit to the measurements in a range [0,1], whereas all other scattering length densities are taken as given in GenX for the respective material. The layer thicknesses used for the GenX simulations are listed for all samples in tables 9.1-9.6. XRR measurements and respective SLD plots of $F_{\text{high}}(4)$, $F_{\text{low}}(1)$ and $F_{\text{mid}}(2)$ are shown in figures 5.9. In the SLD plots, the zero position on the x-axis defines the substrate surface. It has to be noted, that the densities of the shuttered FePd layers in $F_{\text{low}}(1)$ and $F_{\text{mid}}(2)$ are slightly different, leading to different SLD values for the respective $Fe_1Pd_{0.85}$ layers. The density of the toplayer of FePd inside all three samples defines the critical angle of total reflection inside the XRR simulations and can therefore be determined with high precision.

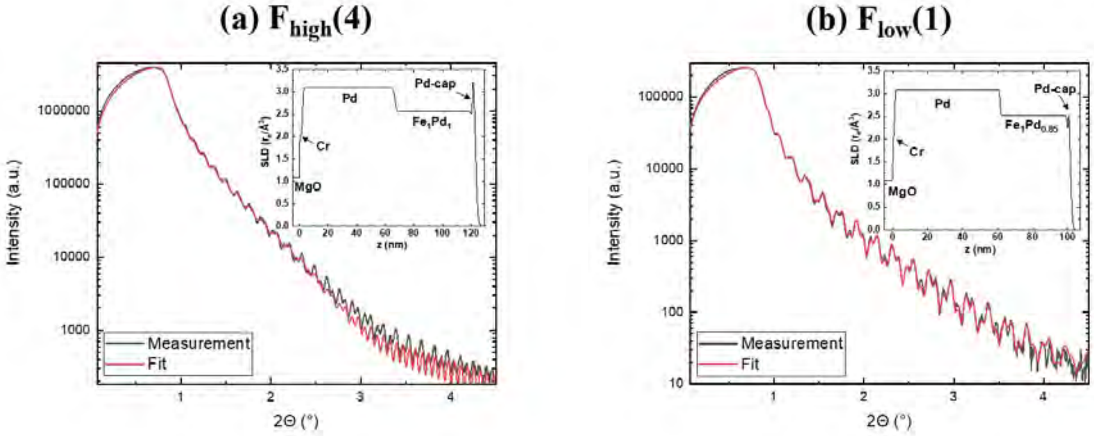

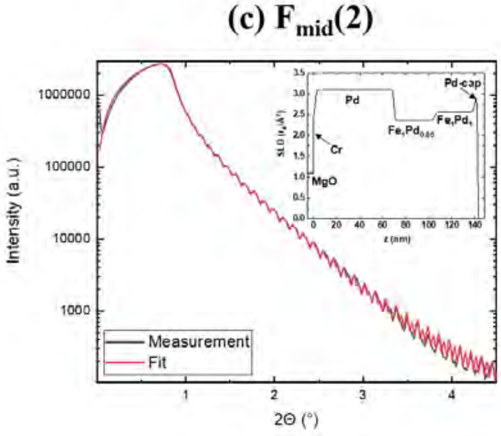

Figure 5.9: X-ray reflectometry measurements of F$_{\mathrm{high}}$(4), F$_{\mathrm{low}}$(1) and F$_{\mathrm{mid}}$(2) with respective fits regarding the layer thicknesses and values given in tables 9.1-9.6. The insets show the SLD as function of depth inside the sample. FePd with 1:1 and 1:0.85 composition exhibits different SLD values.

Regarding the S/F samples, high interface roughnesses and oxidation of Nb as explained in chapter 2.2.6 lead to high errorbars in the XRR fit results which are noted in table 9.4. Sample SF$_{\mathrm{low}}$(1) where Nb is deposited at $T_{\mathrm{s}} = 820\,\mathrm{K}$ shows an interdiffusion between the FePd and Pd layers leading to a formation of $\mathrm{Fe_1Pd_1/Fe_1Pd_3/Fe}_x\mathrm{Pd}_{1-x}\mathrm{/Pd}$ stack instead of $\mathrm{Fe_1Pd_1/Pd}$. In SF$_{\mathrm{mid}}$(1), the two FePd layers cannot be distinguished in the XRR fit due to a high interface roughness. Therefore the thicknesses of $\mathrm{Fe_1Pd_1}$ and $\mathrm{Fe_1Pd_{0.85}}$ of SF$_{\mathrm{mid}}$(1) are listed in total as $\mathrm{d_{FePd}} = (35{+}35){\pm}5 = 70 \pm 5\,\mathrm{nm}$ in table 9.4. In the supplementary information, the cases of SF$_{\mathrm{high}}$(2), SF$_{\mathrm{low}}$(1) and SF$_{\mathrm{mid}}$(1) are treated in detail and compared with results from STEM-EDX measurements (see Fig. 9.7).

From the RBS measurement of SIF$_{\mathrm{high}}$, the composition of oxygen in Nb is estimated at ~20%. Figure 5.10(a) shows the XRR measurement and the resulting fit to SIF$_{\mathrm{high}}$(1) with thicknesses given in table 9.5, and Fig. 5.10(b) displays the respective RBS measurement using the same thicknesses and a 1:1 composition of Fe to Pd as well as an oxygen content of ∼20% inside the Nb layer. Such an oxygen content inside the superconducting Nb is observed as well in the STEM-EDX measurements in Fig. 9.7 in the supplementary information. RBS measurements on F_{high}-F_{low} can be found in the supplementary in Fig. 9.8. The sensitivity of both measurement types to light elements such as oxygen is very low (e.g., for RBS the error is >10%). For better a precision, the oxygen content needs to be checked with other measurement techniques such as X-ray Photoelectron Spectroscopy (XPS) or Hard X-ray Photoelectron Spectroscopy (HAXPES).

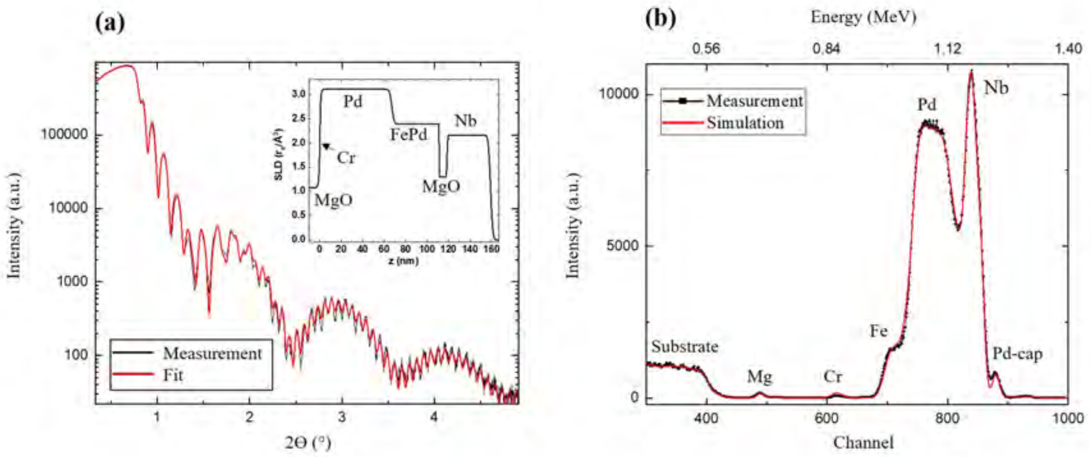

Figure 5.10: (a) XRR measurement and fit regarding the same thicknesses and compositions of $\mathrm{SIF}_{\mathrm{high}}$(1) as taken for the RBS simulation shown in (b), all values are listed in table 9.5. From the RBS measurement, a oxygen content of ∼20% was revealed in the Nb layer, leading to a reduced SLD of Nb within the XRR fit.

However, all S/F and S/I/F samples show a magnetic domain structure from the $L1_0$-ordered FePd phase (see section 5.4.3). The long-range order of this ordered phase is evaluated by XRD measurements. The ratio of the integrated intensities of the FePd (001) superlattice reflection and the FePd (002) fundamental reflection results from a mixed disordered fcc and the ordered tetragonally distorted crystal structure. The calculation of the order parameter S is given in equation (5.1) [17, 176]. Results vary between S=0 for a nonstoichiometric phase to S=1 for the completely ordered, stoichiometric FePd phase.

$$\frac{A_{001}}{A_{002}} = \frac{LP(\theta_{001})FF^{*}_{001}\sin(\theta_{002})}{LP(\theta_{002})FF^{*}_{002}\sin(\theta_{001})}, \tag{5.1a}$$

$$LP(\theta) = \frac{1 + \cos^2(2\theta)cos^2(2\alpha)}{(1 + cos^2(2\alpha)sin(2\theta))}, \tag{5.1b}$$

$$FF^*_{001} = 4S\left[(f_{Fe}e^{-M_{001}} - f_{Pd}e^{-M_{001}})^2 + (\Delta_{Fe}e^{-M_{001}} - \Delta_{Pd}e^{-M_{001}})^2\right), \tag{5.1c}$$

$$FF^*_{002} = 4\left[(f_{Fe}e^{-M_{002}} + f_{Pd}e^{-M_{002}})^2 + (\Delta_{Fe}e^{-M_{002}} + \Delta_{Pd}e^{-M_{002}})^2\right). \tag{5.1d}$$

Values of A are the integrated XRD intensities, LP(θ) the Lorentz-polarization factor with the angle α of the monochromator, FF* square of the structure factors, f_{Fe}, f_{Pd}, Δ_{Fe} and Δ_{Pd} the real and imaginary parts of atomic scattering amplitudes, and M the Debye-Waller factor with $M = B(\frac{\sin(\theta)}{\lambda})^2$ and $\mathrm{B_{Fe}}$=$\mathrm{B_{Pd}}$=B, for the (001) and (002) reflections, respectively. In the D8-system, a Channel-Cut Ge(220) crystal is inserted with a Bragg angle of α=22.67°. The integrated intensities are taken from the XRD measurements at positions $2\theta_{001}$=~24.5° and $2\theta_{002}$=~50°. For the constant factors f_{Fe}, f_{Pd}, Δ_{Fe} and Δ_{Pd}, as well as for M and B values are taken from [17] which are calculated for epitaxial FePd thin films with low and high PMA (see table 9.7 in the supplementary). In Fig. 5.11, the XRD measurements and resulting values of S are displayed for $\mathrm{F_{high}}$(4), $\mathrm{F_{low}}$(2) and $\mathrm{F_{mid}}$(3). The value of S is calculated from the integrated intensities of the raw data, whereas for clarity Fig. 5.11(a) shows the smoothed data sets. Even in the samples of high anisotropy, which are codeposited at T_{s}=500 K, the long-range order is not complete, which is referenced by structural defects in the FePd layer denoted by red arrows in the HAADF-STEM image 5.11(c).

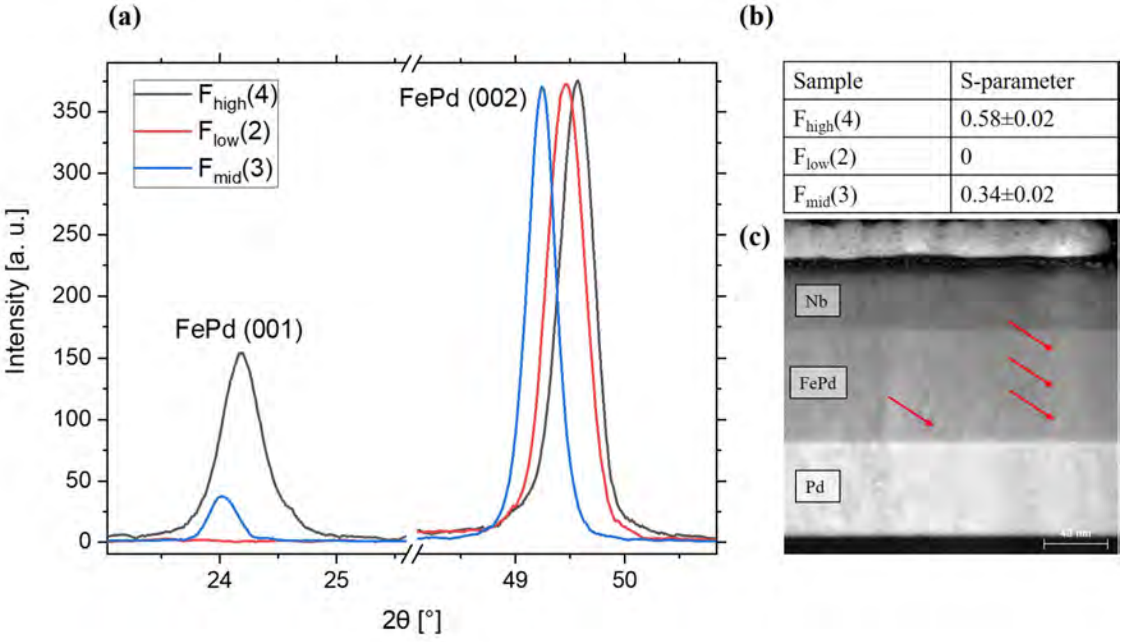

Sample	S-parameter
$F_{high}(4)$	0.58±0.02
$F_{low}(2)$	0
$F_{mid}(3)$	0.34±0.02

Figure 5.11: (a) FePd(001) and FePd(002) peaks of XRD measurements regarding samples $F_{\mathrm{high}}(4)$, $F_{\mathrm{low}}(2)$ and $F_{\mathrm{mid}}(3)$. The relation of integrated intensities from the (001) to the (002) reflection is proportional to the long-range order parameter S shown in table (b). All values of S are less than 1, for example resulting from plane defects inside the FePd layer of $SF_{\mathrm{mid}}(1)$ as marked by red arrows in (c).

5.4.2 Surface analysis

The root-mean-square surface roughness σ_{rms} of single F layers measured by AFM directly after growth has values $\sigma_{\mathrm{rms}} < 4\,\text{Å}$. AFM images of all three sample stacks with low, high and medium PMA are given in Fig. 5.12. Only FePd grown with high PMA shows surface terraces with steps along the <110> crystalline direction. These correspond to the existence of planar defects along the FePd(111) direction sketched in Fig. 5.12(d) as observed by Gehanno [17] by use of dark-field electron microscopy on high-PMA FePd thin films grown on Pd/Cr/MgO. Halley et al. [177] have ascribed these terraces along the <110> FePd crystalline direction to bi-atomic steps resulting from a misfit between the FePd and Pd layer surfaces. They are only observable for highly chemical ordered FePd thin films, for further details see [177, 178].

In samples $F_{\mathrm{low}}(2)$ and $F_{\mathrm{mid}}(2)$, these terraces are not observed with AFM, as expected following the results from Halley et al. However, the HAADF-STEM image in Fig. 5.11(c) clearly reveals the existence of planar defects also in FePd layers of lower anisotropy.

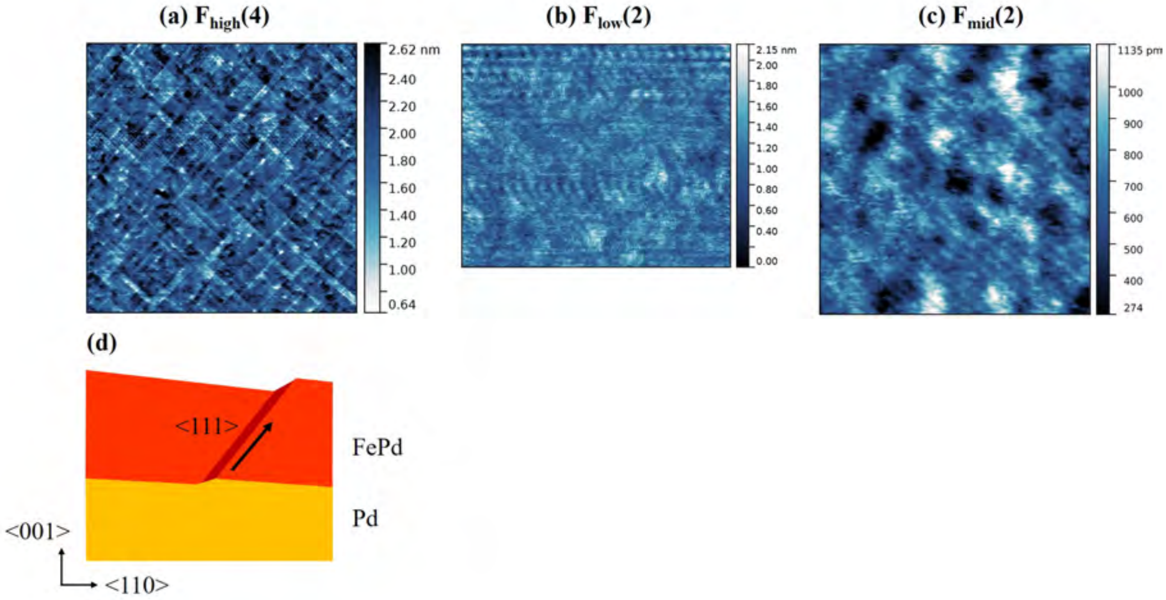
(a) $F_{high}(4)$
2.62 nm
2.40
2.20
2.00
1.80
1.60
1.40
1.20
1.00
0.64
(b) $F_{low}(2)$
2.15 nm
2.00
1.80
1.60
1.40
1.20
1.00
0.80
0.60
0.40
0.00
(c) $F_{mid}(2)$
1135 pm
1000
900
800
700
600
500
400
274
(d)
<111>
FePd
Pd
<001>
<110>

Figure 5.12: (a) 3x3µm AFM measurement of sample $F_{high}(4)$, (b) $F_{low}(2)$ (with 2.5x3µm) and $F_{mid}(2)$ (3x3µm). (d) Plane defects along (111) in a thin film FePd layer of strong PMA can cause surface terraces visible in sample F_{high} in (a), Figure inspired from [17].

In Fig. 5.13 the AFM measurements of sample $F_{high}(4)$ are an example of the increased surface roughness and the evolution of islands of height > 20 nm after 3 weeks of sample aging. Due to this island formation, new samples with the same growth methods needed to be fabricated for neutron measurements causing the high number of samples with similar characteristics.

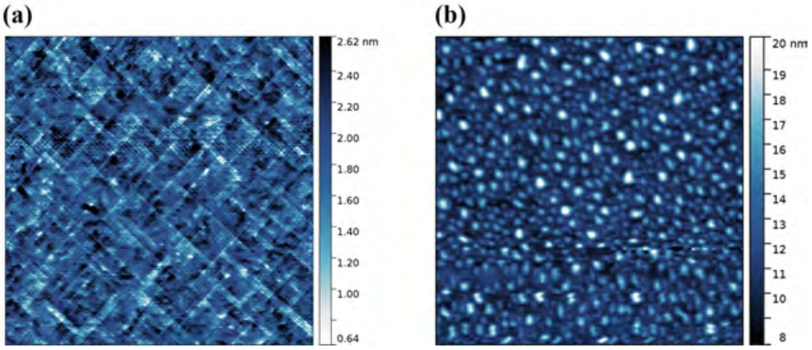

Figure 5.13: 3x3µm AFM measurements of sample $F_{high}(4)$ in the as-grown state with a flat surface (a) and after three weeks of sample aging with islands of ~20 nm height (b).

In contrast to the single F layers, the S/F systems exhibit island formations on the Nb surface directly after growth as pointed out in the previous chapter by RHEED measurements. Examples of AFM measurements on $SF_{high}(2)$, $SF_{low}(1)$, and $SF_{mid}(1)$ are shown in Fig. 9.9 in the supplementary information. Samples $SF_{high}(2)$ and $SIF_{high}(1)$ with high PMA additionally exhibit holes in the Nb surface. A comparison with STEM measurements on $SIF_{high}(1)$ (see Fig. 5.14) reveals the existence of ∼20-30 nm deep voids inside the FePd layer which are filled with the subsequently grown MgO and Nb. Fig. 5.14(b) shows that FePd and Nb are still well separated by MgO. The void-to-surface ratio is ∼1% which was evaluated by adding a mask at points where the surface height is >60 % above the minimum height level on a 8x8µm sized AFM measurement (see Fig. 9.10 in the supplementary).

In conclusion it is assumed that due to the low void-to-surface ratio of ∼1% and the still existing MgO barrier between the FePd and Nb layers, the macroscopic superconducting effects are not affected by these defects and proximity effects are prevented in $SIF_{high}(1)$.

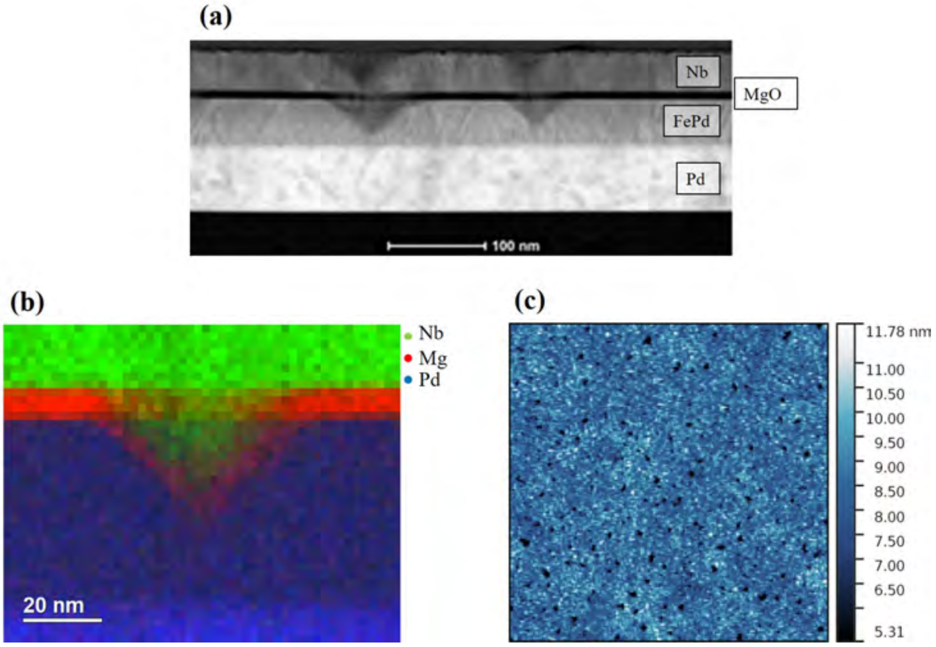

Figure 5.14: Void formation in $SIF_{high}(1)$: (a) HAADF-STEM measurement with side view on the Nb/MgO/FePd/Pd/Cr/MgO heterostructure, (b) HAADF-STEM EDX measurement where the FePd void is filled with MgO and Nb and (c) top-view on the void-formation given by a 3x3µm sized AFM measurement.

5.4.3 Magnetic domain structure and macroscopic magnetization

Zero-field measurements of the surface domain pattern are performed at room temperature by Magnetic Force Microscopy (MFM) to evaluate the lateral domain pattern

and period, whereas magnetic hysteresis loops are obtained by measurements in an out-of-plane and in-plane applied field using the Magnetic Properties Measurement System (MPMS). The strength of PMA (expressed by the quality factor Q as mentioned in chapter 2.1) is calculated from the hysteresis loops as follows:
The effective uniaxial anisotropy K_{eff} (given by the sum of the magnetocrystalline and shape anisotropy $K_{\mathrm{eff}} = K_{\mathrm{u}} + K_{\mathrm{sh}}$) is obtained by the integral over the difference from the out-of-plane and the in-plane hysteresis loops [179], see equation 5.2(a). The quality factor Q is then calculated by the ratio of K_{u} and the shape anisotropy $K_{\mathrm{sh}}=\frac{1}{2}\mu_0 M_{\mathrm{s}}^2$ [150], see equation 5.2(b)

$$K_{\mathrm{eff}} = K_{\mathrm{u}} - \frac{1}{2}\mu_0 M_{\mathrm{s}}^2 = \int_0^{M_{\mathrm{s}}} (H_{\perp} - H_{||}) dM, \tag{5.2a}$$

$$Q = \frac{K_{\mathrm{u}}}{\frac{1}{2}\mu_0 M_{\mathrm{s}}^2}, \tag{5.2b}$$

The growth conditions of $\mathrm{F_{high}}$-$\mathrm{F_{low}}$ and the degree of PMA significantly alter the domain configuration and stripe thickness as mentioned in section 5.2. Table 5.2 lists the range of measured domain thicknesses for bare F layers of different PMA in comparison with their Q and S-values. The domain thicknesses are taken directly after the sample growth without previous field history. The respective MFM and hysteresis loop measurements are given in the supplementary in Fig. 9.11. The trend of the domain thicknesses and Q values for samples with different PMA fits well to the observed long-range order parameter in chapter 5.4.1: High PMA comprises a high long-range order due to the evolution of the $\mathrm{L1_0}$-phase, whereas low PMA obeys nearly zero long-range order. Samples with medium PMA in total comprise medium long-range order as the signals of both FePd layers with low and high PMA overlap.

Sample type	w (nm)	Domain orientation	PMA	Q	S
$\mathrm{F_{high}}$	(80-120)±5	maze	high	(1.8-2.23)±0.5	~0.5-0.6
$\mathrm{F_{low}}$	49±1 - 63±4	stripes	low	0.47±0.05 - 0.7±0.01	~0-0.2
$\mathrm{F_{mid}}$	(58-60)±1	stripes	medium	(1.40-1.46)±0.04	~0.3

Table 5.2: Comparison of magnetic and structural properties of all F samples with high, medium, and low anisotropy. Domain thicknesses w and the magnetic patterning are taken from MFM measurements in the as grown state of the samples.

The domain thickness increases with increasing strength of magnetocrystalline anisotropy marked by high Q values. Additionally, samples comprising low PMA grown in shuttered

mode exhibit a parallely aligned domain formation (called ′stripes′), whereas samples with high PMA show a maze domain structure. Samples consisting of two FePd layers show both - high Q values and a stripe domain structure - probably due to a magnetic coupling between the subsequently grown FePd layers at room temperature and at T_s=500 K. S/F bilayers exhibit the same characteristics, indicating no influence of the Nb layer growth on top of FePd on the magnetic structure.
The origin of the stripe configuration during the growth process is discussed diversely in the literature. In [17], three possible reasons are listed for FePd thin films with low PMA: (i) in fully structural disordered systems of bulk cubic FePd the easy magnetization axis is along [111], leaving an easy magnetization axis along <110> in disordered thin films. (ii) Durand et al. [180] have found a preferential magnetization direction in Fe and Fe/Pd thin films according to the chamber geometry and the incident Fe flux direction during growth. (iii) Weber et al. [181] have shown that a substrate misorientation of 0.1° can cause as well a preferential magnetization direction. Apart from a parallel domain nucleation during the growth process due to structural reasons, also a minimazation of exchange energy is a possible reason for a parallel alignment of in-plane oriented closure domains and domain walls in FePd with weak PMA [22].
Similar to [17], a systematic study of the direction of preferential domain alignment is not carried out within this thesis.

Figure 5.15(a) displays for all three S/F samples a sketch of the magnetic domain configuration as it is assumed from the MFM and hysteresis loops measurements at room temperature which are presented in Fig. 5.15(b) and (c), respectively. The top (blue) layer denotes Nb and the bottom the FePd layer comprising a magnetic domain structure with an orientation of magnetic moments depicted with different colors and arrows.

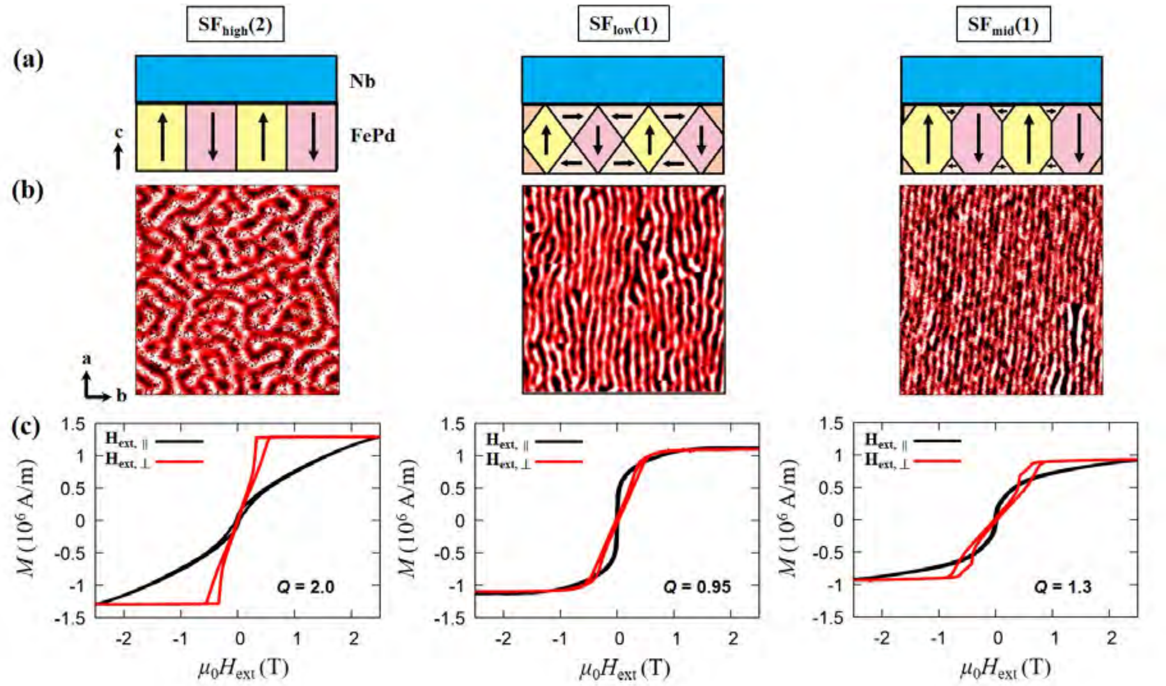

Figure 5.15: From left to right: SF$_{\text{high}}$(2), SF$_{\text{low}}$(1), and SF$_{\text{mid}}$(1), respectively. (a) Schematic view of the magnetic domain formation inside the FePd layer and the toplayer of Nb in direction of the c-axis of L1$_0$-ordered FePd. (b) (3×3 µm) zero-field MFM measurements in the as-grown state of SF$_{\text{high}}$(2) and SF$_{\text{mid}}$(1) and after demagnetization of SF$_{\text{low}}$(1). (c) Hysteresis loops measured at 300 K with $H_{\text{ext},||}$ in the surface plane and $H_{\text{ext},\perp}$ perpendicular to the surface plane, adapted from [182]. All measurements are obtained at 300 K.

Due to the high Curie temperature of FePd with T_{Curie}=723 K [19], all samples are ferromagnetic at room temperature. SF$_{\text{high}}$(2) and SF$_{\text{mid}}$(1) with $Q>1$ exhibit the typical behavior of a domain structured F thin film with the easy axis aligned along the c-direction. Starting from saturation in an out-of-plane applied field, the magnetization drops fast while cylindrical domains evolve into band-domains with a linear magnetization dependency [16, 150] (see chapter 2.1.3). In contrast, SF$_{\text{low}}$(1) with $Q<1$ displays an easy magnetization axis in the in-plane direction.

It has to be noted, that the MFM image of sample SF$_{\text{low}}$(1) in Fig. 5.15(b) is taken after an in-plane oscillating demagnetization. Directly after growth, it consisted of a maze domain structure, probably due to the annealing of the FePd layer during the subsequently grown Nb at T_{s}=820 K.

A more detailed investigation of the domain pattern with field history of the samples is given for F$_{\text{mid}}$(3) in Fig. 5.16. In the as-grown state, this sample comprises a perfect stripe pattern within the measured range of 3x3µm, see Fig. 5.16(a). The distortion on top of the image results from a sample movement during the initial measurement time. A subsequent application of an external magnetic field H_{ext}=700 mT in out-of-plane direction leads to a maze domain structure with a slight preferred orientation in the original stripe direction, see Fig. 5.16(b). Fig. 5.16(c) proves that the parallel domain formation can be retrieved by application of an in-plane oscillating magnetic field in direction of the initial stripe formation (demagnetization-process) as was shown in [183].

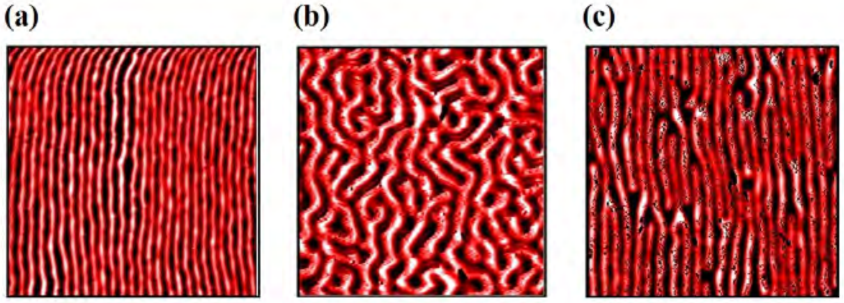

Figure 5.16: 3x3µm MFM measurements of $\mathrm{F_{low}}(3)$ after application of (a) 0 mT, (b) 700mT in an out-of-plane applied external field and (c) after in-plane oscillating demagnetization, adapted from [183].

5.4.4 GISANS at room temperature

Using GISANS at room-temperature, quantitative measurements of the depth-resolved lateral domain profiles of FePd thin films are performed. Within this section, the bare FePd layer of sample $\mathrm{F_{high}}(2)$ is investigated and the results are used as basis for low-temperature analyses of GISANS at Nb/FePd bilayers in chapter 7.

In contrast to $\mathrm{F_{high}}(1)$, (3) and (4), the FePd layer of $\mathrm{F_{high}}(2)$ is grown by electron-gun evaporation and with a low thickness of $d_{\mathrm{FePd}} = 38 \pm 2\,\mathrm{nm}$ near the critical thickness of PMA evolution (similar to $\mathrm{F_{mid}}$). In the as-grown state, a stripe domain structure is observed as shown in the supplementary in Fig. 9.12(a). Unfortunately, a high drift of the sample causes a smeared MFM image. Thus, no clear information on the quality of the alignment of magnetic domains or the domain thickness is obtained. The hysteresis loops shown in 9.12(b) reveal $Q = 1.8 \pm 0.05$ and are carried out after the zero-field GISANS measurements treated in the following. Such a Q-value lies between the values of medium and high PMA samples (see table 9.8) and explains together with the small layer thickness the observed stripe domain structure.

GISANS measurements with an unpolarized neutron beam of wave vector $\vec{k} = (k_x, 0, k_z)$ were performed by Sonja Schröder and Grigol Abuladze at a sample-to-detector distance of $d_{sd} = 1.23\,\mathrm{m}$, and a neutron wavelength of $\lambda = 12.8\,\mathrm{Å}$ with a wavelength spread of $\Delta\lambda/\lambda = 17\,\%$. The magnetic stripes are aligned along x to probe the domain pattern along the y-direction (see Fig. 5.17(a)). An additional measurement with the stripes aligned along y as in Fig. 5.17(b) was used to prove an alignement of magnetic domains in stripes rather then in a maze structure. Figures 5.17(c,d) show the measured Q_y-Q_z-maps, respectively. The blue horizontal line in Fig. 5.17(c) denotes the GISANS signal at the total reflection edge with $\alpha_\mathrm{i} = \alpha_\mathrm{f}$ at an incident angle of $\alpha_\mathrm{i} = 0.96°$ and $Q_z = 0.165\,\mathrm{nm}^{-1}$, which at the angle of total reflection corresponds to the Yoneda line. The direct beam position is at $Q_y = Q_z = 0\,\mathrm{nm}^{-1}$, with reduced intensity due to an inserted beam stop.

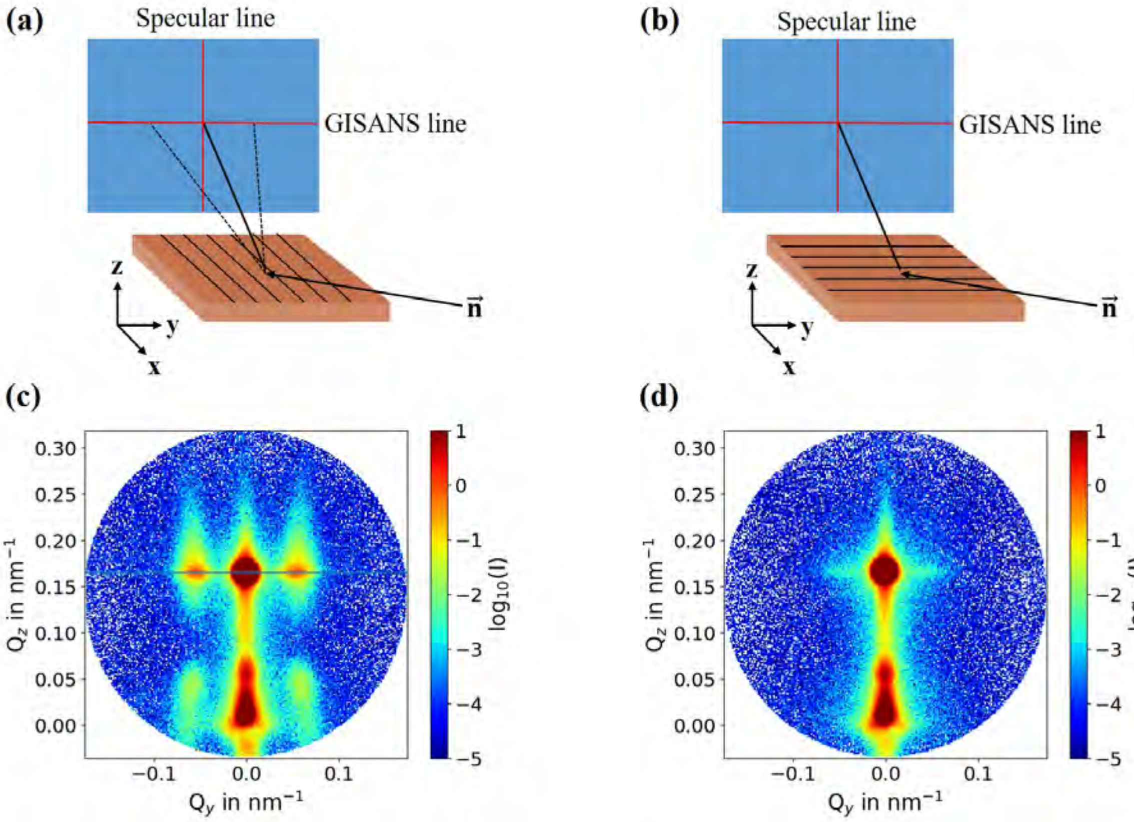

Figure 5.17: (a) Schematic sample alignment with the magnetic stripes aligned along x to probe the domain structure with finite periodicity in y-direction and (b) aligned along y with infinite periodicity in y-direction. (c,b) Respective Q_y-Q_z-maps of the GISANS measurements shown in (a) and (b), at an incident angle of $\alpha_\mathrm{i} = 0.96°$ and a direct beam located at $Q_y = Q_z = 0\,\mathrm{nm}^{-1}$. The blue horizontal line denotes the GISANS line at $Q_z = 0.165\,\mathrm{nm}^{-1}$, which at the critical angle of total reflection corresponds to the Yoneda line.

To model the lateral magnetic depth-profile of the FePd layer in $\mathrm{F_{high}}(2)$, the Q_y-Q_z-map in Fig. 5.17(c) is simulated using the DWBA. Included in the model are the paracrystal theory as described in section 3.2.4, diffuse scattering from rough surfaces, and the possibility of a not fully aligned stripe orientation along $\vec{x}$ by allowing a small angular range for ξ, the rotation angle of the domain units around $\vec{z}$ as shown in Fig. 3.9. Following boundaries are considered for the simulation parameters:

- The sample stack and all layer thicknesses are kept as reported in table 9.1 and an averaged interface roughness of 9Å is taken from the XRR simulations using GenX.
- Following the results from micromagnetic simulations on FePd with different degree of PMA in [22], the size of closure domains increases with decreasing strength of PMA. Due to the stripe configuration and the lower PMA compared to other $\mathrm{F}_{\mathrm{high}}$ samples, the existence of large closure domains is assumed. The maximum possible width of closure domains at the FePd surfaces is given by half the domain period, the maximum depth by half the FePd layer thickness.
- Using a polarized neutron beam and polarization analysis, a chirality inside the domain walls is observable if the propagation vector of the helical Bloch wall is parallel to a nonzero component of the polarization vector [184, 185]. Here, an unpolarized neutron beam is used and no domain walls can be detected. Therefore, they are not considered in this section.
- The correlation length along the x-direction, L_x, shall be much larger then the domain period D_{domain} due to the parallel alignment of magnetic domains.

Figures 5.18(a,b) display the measured and simulated Q_y-Q_z-maps for the best fitting parameters (listed in the supplementary in table 9.9), respectively. Q_z-values for $\alpha_f < 0$ are not simulated. For this, the transmission through the substrate needs to be considered which is not part of the used simulation program. A cut through the GISANS line at $Q_z = 0.165\,\mathrm{nm}^{-1}$ in both images with a small integration range in Q_z of $\Delta Q_z = \pm 0.005\,\mathrm{nm}^{-1}$ yields the intensity with respect to Q_y as given in 5.18(c). Figure 5.18(d) shows the sizes of out-of-plane magnetic domains and in-plane oriented closure domains together with the FePd layer thickness for the presented model.

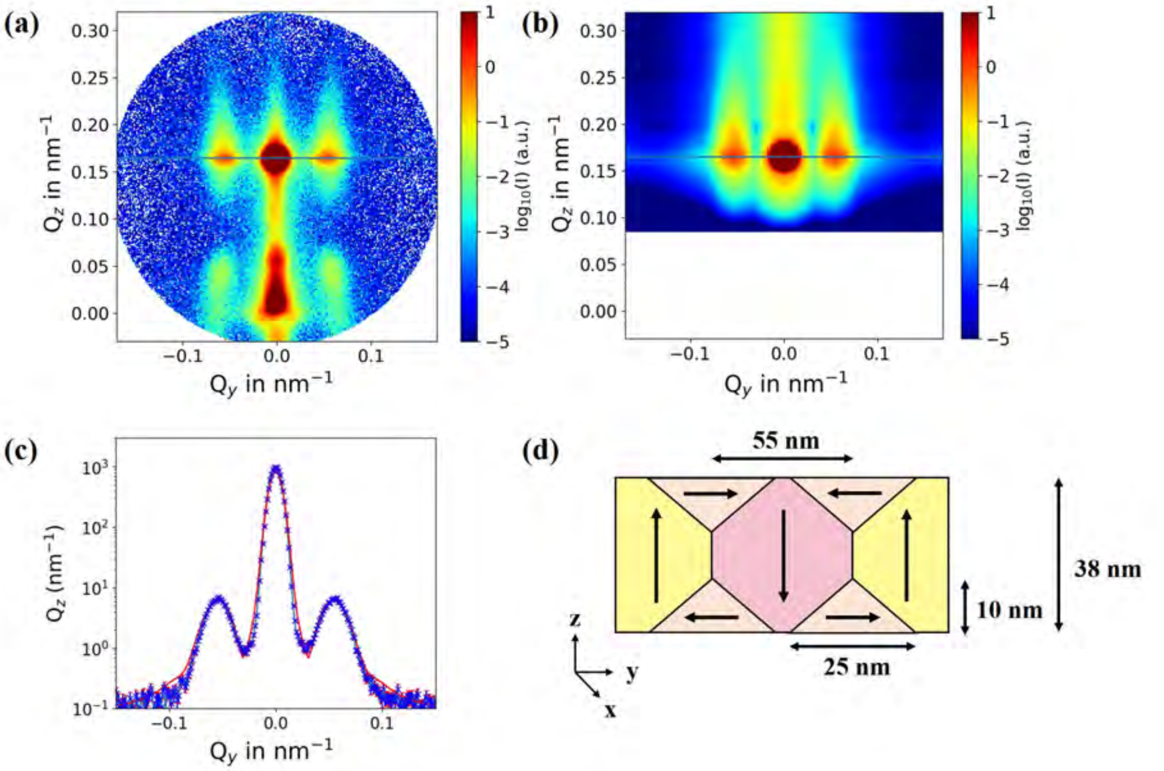

Figure 5.18: (a) Q_y-Q_z-map of the room-temperature GISANS measurement on FePd. (b) Corresponding simulated Q_y-Q_z-map. (c) $I(Q_y)$ at the GISANS line with a small integration range of Q_z for the measurement (blue data points) and the simulation (red line). (d) Schematics of the shape and sizes of the simulated domain structure inside the FePd layer of the simulated layer stack given in table 9.9, including closure domains with in-plane magnetic moments and out-of-plane oriented magnetic domains.

Figures 5.18(a,b) both show elongated GISANS peaks in Q_y, which is implemented in the simulation by (i) a finite angular range of $\Delta\xi = \pm 10°$ in the lateral domain orientation and (ii) an increased disorder parameter ω. On the one hand, higher angles ξ with respect to Q_y lead to higher effective domain width seen by the neutron beam and an extension of the GISANS peaks to lower Q_y. On the other hand, following Lazzari et al. [144] an increase in the disorder parameter ω causes flattened Bragg peaks with increasing FWHM.

The observed triangular shaped decrease in intensity and the form of the GISANS peaks at higher Q_z depends strongly on the width and depth of the closure domains. Additionally, no third order Bragg peaks are visible at higher Q_y as was reported in [183], and is realized in this simulation by diffuse scattering due to rough layer surfaces, as well as the domain disorder ω. Still, the simulation fails to describe the fast decrease in intensity on the specular line visible in the measurement. One reason can be that in the employed model, the total intensity is averaged over scattering intensities from all domain units, without taking into account the asymmetric nature of the neutron beam coherence volume with $L_x \gg L_y$ (see Fig. 3.4). A first average over the scattering amplitudes of all domain units within one coherence volume of the neutron beam and a second average over the scattering intensities of all coherence volumes will be tested in future to reproduce the intensity in the specular line.

However, the presented results prove the applicability of the DWBA under consideration of the paracrystal theory to describe the lateral magnetic depth-profile measured by GISANS. Especially the form and size of closure domains as obtained here can be proven by further measurements at various incident angles. Lower α_i will lead to a higher surface sensitivity due to lower neutron penetration depth.

5.5 Conclusions

FePd thin films with varying strength of PMA and adjustable lateral domain configurations have been grown by MBE and characterized at room temperature. A combination of codeposition and shuttered growth leads to a stripe domain pattern together with high PMA and $Q > 1$. Results from XRD, hysteresis measurements, and MFM together confirm the expectations on the structural and magnetic order with dependence on the different growth processes: codeposition at elevated temperatures causes high order parameters S, large domain width D_{domain} with a maze domain pattern, and high Q values, which are characteristic for FePd with high PMA. Low PMA is attributed to lower S, smaller D_{domain} and large closure domains leading to a stripe domain pattern. The structural quality has been checked in-situ and ex-situ by electron-, X-ray, and neutron scattering techniques as well as by RBS. Plane defects along the (111) crystalline direction cause terraces on the FePd layer surfaces, and oxidation processes lead to an increased surface roughness. However, the strength of PMA and its domain configuration are not altered by sample aging.

GISANS experiments have been succesfully performed to investigate the lateral magnetic depth-profile at room temperature, in particular the size of closure domains at the FePd surfaces. The experiments are simulated using a model based on the DWBA including the paracrystal theory with a domain bending described by a random distribution function and a serpentine domain structure represented by a finite angular range of possible in-plane domain orientations. Thus, GISANS proves to be a powerful tool to scrutinize the depth-resolved magnetic domain pattern and can be employed to detect proximity effects at S/F interfaces as will be investigated in the following chapter.

Moreover, using a polarized neutron beam and polarization analysis, scattering from in-plane and out-of-plane magnetic moments can be distinguished, and also opens the possibility to detect a magnetic chirality within the domain walls.

Chapter 6

Low-temperature characterization

While the previous chapter concentrated on a structural and magnetic characterization of the S/F systems at room temperature, in this chapter a comprehensive investigation at low temperatures is presented to study the Domain-Wall-Superconductivity (DWS), Reverse-Domain-Superconductivity (RDS), and long-ranged spin-triplet components (LRTC) of Cooper pairs as described in section 2.4.

First, the coexistence of superconductivity and ferromagnetism at $T<T_\mathrm{c}$ is probed by magnetic hysteresis measurements in section 6.1. Results of S/F and S/I/F samples are compared with hysteresis loops from bare S films. Subsequently, magnetotransport measurements in (i) out-of-plane applied magnetic field and (ii) in-plane applied magnetic field are conducted to probe the existence of DWS, RDS and LRTC in the heterostructures in sections 6.2 and 6.3, respectively.

6.1 Coexistance of superconductivity and ferromagnetism

A verification of the coexistance of superconductivity and ferromagnetism is undertaken by magnetization measurements in an external magnetic field $M(H_{\mathrm{ext}})$ at temperatures varying from $T{>}T_{\mathrm{c}}$ to $T \ll T_{\mathrm{c}}$ [65]. The calculation of T_{c} reported for each sample in table 9.10 in the supplementary is based on resistivity measurements with respect to temperature $\rho(T)$ and described in the following section 6.2.
Above T_{c} in the paramagnetic state of Nb, the SF bilayers exhibit hysteresis loops typical for domain structured ferromagnetic thin films with an easy magnetization axis in the c-direction (see chapter 2.1.3 in general and chapter 5.4.3 for FePd at room temperature). The magnetic response of bare S films below T_{c} is a "star-shaped" hysteresis curve as discussed in chapter 2.2.5. The field position at maximum magnetization corresponds to the first critical field B_{c1}, whereas a closing of the up- and down-loops denotes the upper critical field B_{c}^{*}. Following the equations for small sized superconductors outlined in chapter 2.2.4, B_{c1} decreases with the Nb thickness d_{S} whereas B_{c}^{*} increases with d_{S}.

Figure 6.1(a) shows M with respect to an out-of-plane applied field $H_{\mathrm{ext},\perp}$ (i) at $T{>}T_{\mathrm{c}}$ (300 K and 10 K) and (ii) at $T{<}T_{\mathrm{c}}$ (6.0 K and 5.6 K) for $\mathrm{SF}_{\mathrm{high}}(2)$. Between 300 K and 10 K the hysteresis loops do not change significantly, showing the same coercive field H_{coerc} and saturation magnetization M_{s}. Near to the critical temperature of $\mathrm{SF}_{\mathrm{high}}(2)$ ($T_{\mathrm{c}} = 6.958 \pm 0.001\,\mathrm{K}$) superconductivity starts to nucleate, resulting in overlapping signals of ferromagnetism and superconductivity still with similar H_{coerc} and M_{s} values. A further reduction of T leads to increasing superconducting responses.

A comparison of magnetization measurements at $T{<}T_{\mathrm{c}}$ of samples $\mathrm{SF}_{\mathrm{high}}(2)$ and S(5) with the same d_{S} as in $\mathrm{SF}_{\mathrm{high}}(2)$ (see Fig. 6.1(b)) proves that the hysteresis loops in Fig. 6.1(a) result from the sum of ferromagnetic and superconducting responses. The signal of S(5) corresponds to the "star-shaped" hysteretic response of thin S films. Here, the first critical field B_{c1} is observed to be almost zero whereas the upper critical field B_{c}^{*} increases with decreasing temperature. All bare S layers in S(1)-S(4) exhibit equivalent hysteresis loops as in sample S(5).

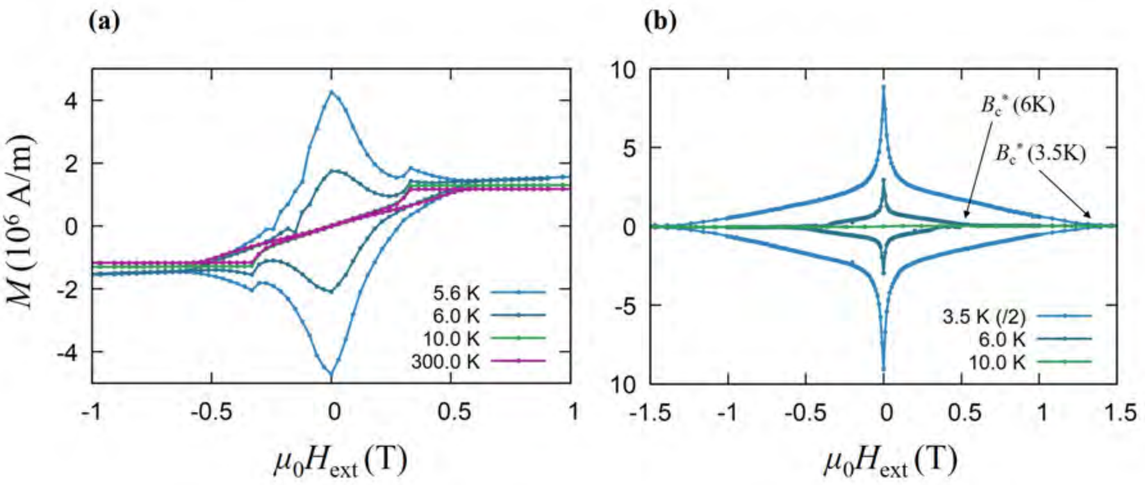

Figure 6.1: (a) $M(H_{\mathrm{ext},\perp})$ of $\mathrm{SF}_{\mathrm{high}}(2)$ measured at various temperatures indicated by the legend. (b) Hysteresis loops of S(5) with corresponding Nb thickness to $\mathrm{SF}_{\mathrm{high}}(2)$ (d_{Nb}=39 nm, see tables 9.1-9.6).

Samples of lower anisotropy exhibit as well overlapping ferromagnetic and superconducting hysteresis loops as shown in Fig. 6.2. In $\mathrm{SF}_{\mathrm{low}}(1)$ and $\mathrm{SF}_{\mathrm{mid}}(1)$, the superconducting responses exhibit smaller $M(B_{\mathrm{c1}})$ in comparison to the ferromagnetic response than in $\mathrm{SF}_{\mathrm{high}}(2)$. This can result from a variety of causes: (i) different d_{S} (see table 9.4), (ii) less strength of PMA and (iii) different structural defects within each Nb layer.

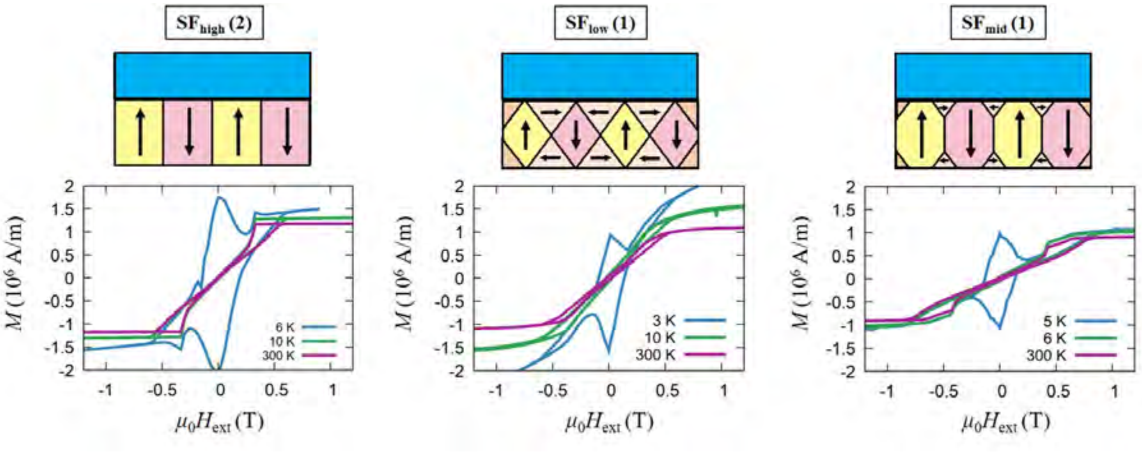

Figure 6.2: $M(H_{\mathrm{ext},\perp})$ of $\mathrm{SF}_{\mathrm{high}}(2)$, $\mathrm{SF}_{\mathrm{low}}(1)$ and $\mathrm{SF}_{\mathrm{mid}}(1)$ measured below and above T_{c} in an out-of-plane applied magnetic field, adapted from the supplementary information in [182].

The effect of high exchange coupling on $M(H_{\mathrm{ext},\perp})$ is studied by a comparison of $\mathrm{SF}_{\mathrm{high}}(2)$ and $\mathrm{SIF}_{\mathrm{high}}(1)$ with comparable d_{S}, H_{coerc} and M_{S} (see tables 9.4 and 9.8). At room temperature in Fig. 6.3(a) both signals coincide. After decreasing the temperature to $T = 5.6\,\mathrm{K}$ in Fig. 6.3(b) (below T_c of both samples) the superconducting response in SIF$_\mathrm{high}$(1) exceeds the ferromagnetic response significantly, whereas in SF$_\mathrm{high}$(2) the ferromagnetic hysteresis loop is still visible (note that the signal of SIF$_\mathrm{high}$(1) is reduced by a factor of 8). This can for example result from a difference in the Pauli paramagnetic pair breaking (see chapter 2.4) which is stronger for a direct coupling of Nb to the exchange field of FePd. Due to the thin MgO interlayer of 7.5 nm it is assumed that the orbital pair breaking is equal in both samples.

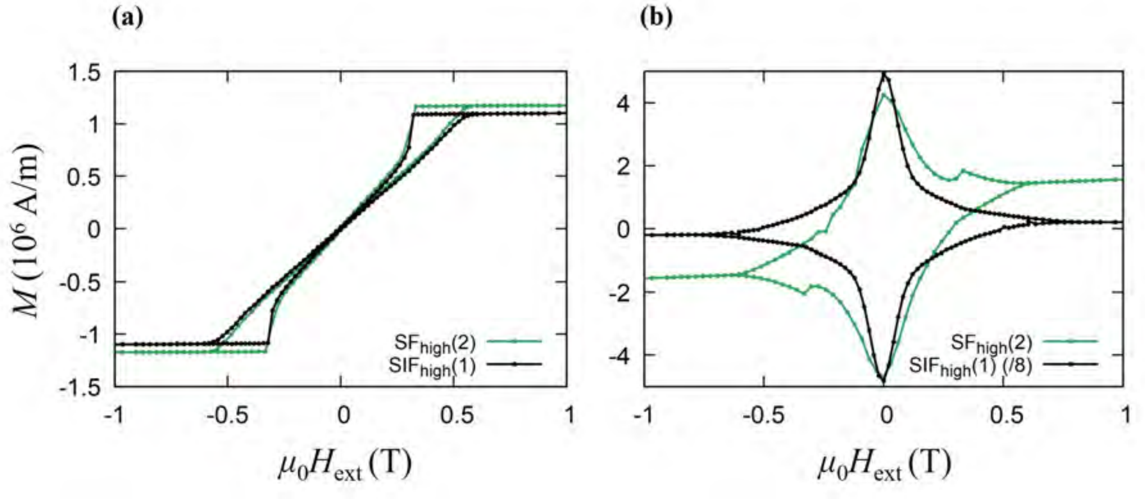

Figure 6.3: (a) $M(H_{\mathrm{ext},\perp})$ of SF$_\mathrm{high}$(2) and its comparison sample SIF$_\mathrm{high}$(1) at $T = 300\,\mathrm{K} > T_\mathrm{c}$ and (b) at $T = 5.6\,\mathrm{K} < T_\mathrm{c}$.

It is concluded that superconductivity and ferromagnetism coexist below T_c in all SF systems and that the domain formation and its magnetic field dependence remain unchanged while passing T_c.

6.2 Magnetotransport with out-of-plane magnetic field

Stray-field and proximity effects of the domain structured FePd on Nb are probed using resistivity measurements in an out-of-plane applied magnetic field $\rho(H_{\mathrm{ext},\perp})$. In preparation, the thin film samples were contacted in the 4-point probe setup using a wire bonder and measured either in the PPMS or the PPMS-Dynacool systems as described in chapter 4.3.6. All sheet resistivities ρ have been calculated employing equation (4.2), with Nb layer thicknesses as reported in tables 9.1-9.6 and point-spacing

dependent values f_2 ranging from 0.89-0.925.
First, results on a sample showing high PMA are discussed in detail and interpreted regarding stray-field generated DWS and RDS. To further confirm such an interpretation, a model from Aladyshkin et al. [97] as introduced in chapter 2.4.1 is fit to the measurements. In a second step, samples with different strength of PMA are compared.

6.2.1 High PMA

Figures 6.4(a) and (b) show $\rho(T)$ at given $H_{\mathrm{ext},\perp}$ of $\mathrm{SF_{high}}(1)$ and S(1), respectively. For $\mathrm{SF_{high}}(1)$ the resistivity decreases to zero in several steps depending on $H_{\mathrm{ext},\perp}$: in zero field, two main steps at $T_{\mathrm{c1}} \sim 8\,\mathrm{K}$ and at $T_{\mathrm{c2}} \sim 7.25\,\mathrm{K}$ exist of which the first exhibits a plateau at $0.6 \cdot 10^{-6}\,\mu\Omega$-cm, vanishing in measurements at $H_{\mathrm{ext},\perp} > 100\,\mathrm{mT}$. T_{c2} stays almost constant until 100 mT and decreases above this value.
In Fig.6.4(c), the magnetoresistance $\rho(H_{\mathrm{ext},\perp})$ is plotted for temperatures near T_{c1} and T_{c2}, showing one resistivity minimum at zero field around T_{c1} (see measurements at 7.70 K and at 7.40 K) and two resistivity minima at $H_{\mathrm{ext},\perp} = \pm\, 100\,\mathrm{mT}$ around T_{c2} (see measurements at 7.30 K - 7.20 K).
In contrast, $\rho(T)$ of S(1) in Fig. 6.4(d) exhibits only one resistivity step for all T corresponding to one minimum in $\rho(H_{\mathrm{ext},\perp})$ which broadens with decreasing temperatures. The measurement loops of $\rho(H_{\mathrm{ext},\perp})$ start at the negative saturation field $-\mathrm{H_{sat}}$ of the samples. Subsequently, $H_{\mathrm{ext},\perp}$ is ramped to $+\mathrm{H_{sat}}$ (red lines) and then back to $-\mathrm{H_{sat}}$ (black lines).

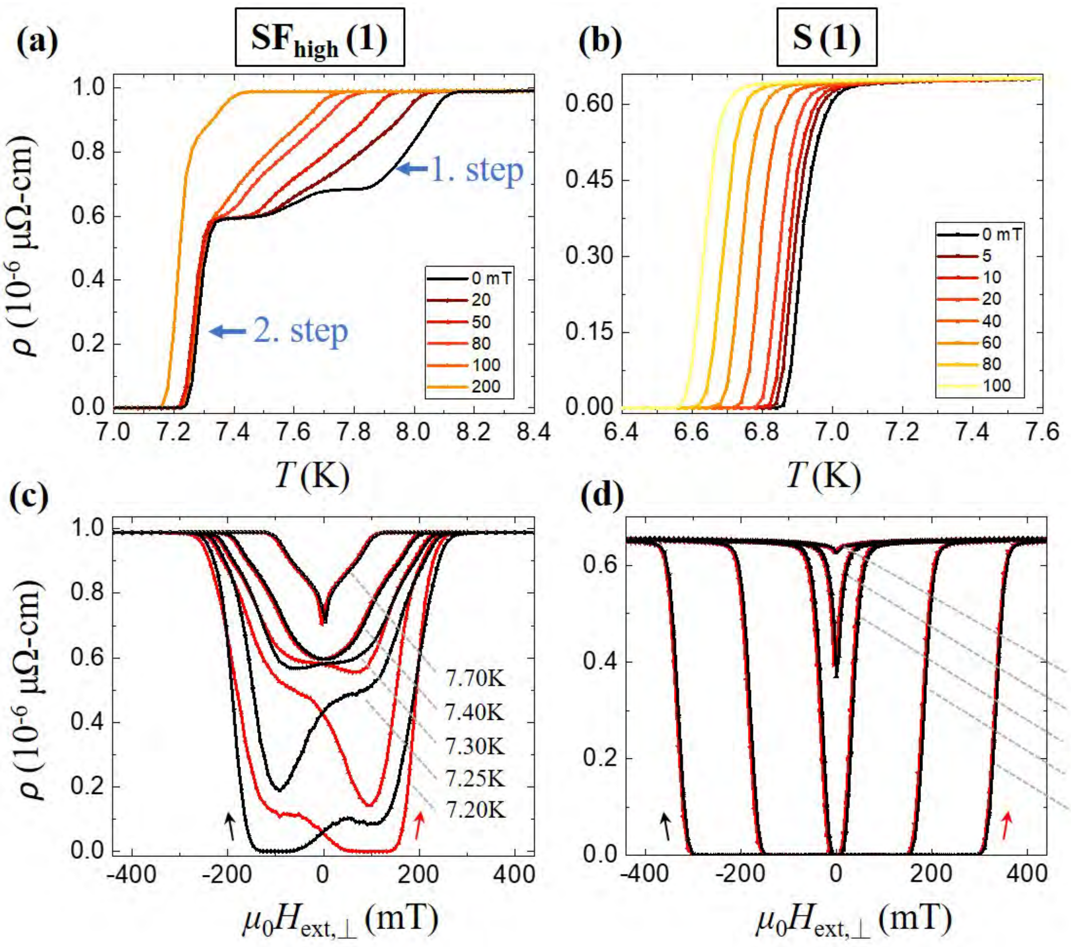

Figure 6.4: $\rho(T)$ measurements in a constant out-of-plane applied field, for $\mathrm{SF_{high}}(1)$ (a) and S(1) (b). (c) $\rho(H_{\mathrm{ext},\perp})$ at constant temperature for $\mathrm{SF_{high}}(1)$ (c) and for S(1) (d).

Sample S(1) follows the expected behavior for thin film Nb layers without proximity effects and zero resistivity in $\rho(H_{\mathrm{ext},\perp})$ between the upper critical fields $\pm B_{\mathrm{c}}^{*}$. For an interpretation of measurements on $\mathrm{SF_{high}}(1)$ where stray fields cause orbital pair breaking in the S layer, a short reminder on DWS and RDS is given in the following. As mentioned earlier, superconductivity preferably nucleates where the overlap of $\mu_0\vec{H}_{\mathrm{ext},\perp}$ with the stray fields $\vec{B}_{\mathrm{d}}$ of the ferromagnet leads to minimum magnetic field strength. DWS occurs in zero applied field while RDS results from a compensation of $\vec{B}_{\mathrm{d}}$ on reverse oriented domains in an applied field. Such a preferred nucleation leads to an increase in T_{c} upon an increasing $\mu_0\vec{H}_{\mathrm{ext},\perp}$ until $\mu_0\vec{H}_{\mathrm{ext},\perp} = B_{\mathrm{d}}$ is reached and T_{c} decreases due to orbital pair breaking. The features in Fig. 6.4(a) and (c) can be explained with an existence of DWS and RDS as schematically displayed in Fig. 6.5: The minimum at $H_{\mathrm{ext},\perp} = 0$ around T_{c1} in $\rho(H_{\mathrm{ext},\perp})$ corresponds to the nucleation of DWS on top of the FePd domain walls, where in-plane magnetic moments of the closure domains and domain walls reduce the stray field strength. The sample is hence superconducting only on top of domain walls causing a decrease in the total resistivity measured between the 4 point contacts but with finite percolation through superconducting and non-superconducting regions and leading to a plateau at $\rho = 0.6 \cdot 10^{-6}\,\mu\Omega$-cm. An increase in $H_{\mathrm{ext},\perp}$ lowers the effect of DWS while RDS evolves above domains in reverse direction to the applied field with a maximum stray field strength of $B_{\mathrm{d}} \approx \pm 100\,\mathrm{mT}$. Upon a nucleation of RDS, the superconducting regions broaden which results in a rapidly decreasing resistivity at T_{c2}. Zero resistivity denotes a Complete-Superconducting state (CS). The results suggest a higher T_{c} for DWS than for RDS, corresponding to T_{c1} and T_{c2}.

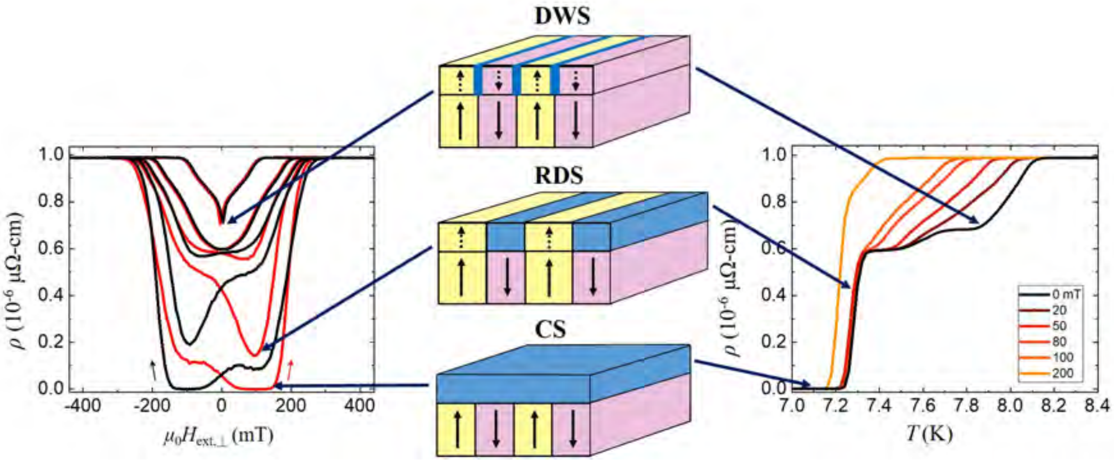

Figure 6.5: Schematic view on a DWS, RDS, and CS formation at different $\rho(H_{\mathrm{ext},\perp})$ (left) and $\rho(T)$ (right).

Due to the subsequent transition to bulk superconductivity with lowering T, T_{c2} is defined as the superconducting critical temperature T_{c} for all S/F samples exhibiting two steps in $\rho(T)$. It is calculated by the maximum value of the derivative of $\rho(T)$ fit by a Gaussian function and listed in the supplementary table 9.10.

The above interpretation can be supported by scrutinizing three conditions for stray field generated DWS and RDS as explained in chapter 2.4.1: (i) a check for isolated DWS and RDS with $2\xi_{\mathrm{GL}} < D_{\mathrm{domain}}$, (ii) an observation of qualitatively similar effects in reference S/I/F samples, and (iii) a fit to the model given by Aladyshkin et al. [97] for the field dependence of T_{c} as described in chapter 2.4.1.

(i) $\xi_{\mathrm{GL}}(T_{\mathrm{c}})$ of the S/F samples is calculated by equation (6.1), with the GL coherence length at $T = 0\,\mathrm{K}$, $\xi_{\mathrm{GL,ref}}(0)$, and critical temperature in zero field, $T_{\mathrm{c,ref}}$, of the respective reference samples S(1-5).

$$\xi_{\mathrm{GL}}(T_{\mathrm{c}}) = \xi_{\mathrm{GL,ref}}(0) / \sqrt{1 - \frac{T_{\mathrm{c}}}{T_{\mathrm{c,ref}}}}. \tag{6.1}$$

The coherence length complies $2\xi_{\mathrm{GL}}(T_{\mathrm{c}}) < D_{\mathrm{domain}}$ for all S/F samples (see table 6.3 in the following section), indicating isolated DWS and RDS.

(ii) A comparison of $\mathrm{SF_{high}}(2)$ and $\mathrm{SIF_{high}}(1)$ is given in Fig. 6.6. Both the $\rho(T)$ and $\rho(H_{\mathrm{ext},\perp})$ curves show qualitatively similar dependencies: two steps in $\rho(T)$ in Figs. (a) and (b) corresponding to DWS and RDS as explained for $\mathrm{SF_{high}}(1)$ above, as well as minima at $H_{\mathrm{ext},\perp} = 0\,\mathrm{mT}$ (due to DWS) and at $H_{\mathrm{ext},\perp} \approx \pm 100\,\mathrm{mT}$ (due to RDS) in Figs. (c) and (d). A third step in $\rho(T)$ at even higher temperatures might be related to surface superconductivity or surface terraces with different T_{c}. T_{c} of the S/I/F reference sample is much higher than for the S/F system without the insulating interlayer, denoting a strong proximity coupling for the latter.
A comparison of Figs. 6.6(c) and 6.4(c) yields that in $\mathrm{SF_{high}}(1)$ the resistivity exhibits only one minimum in each field direction of $\rho(H_{\mathrm{ext},\perp})$, whereas in $\mathrm{SF_{high}}(2)$ two minima are visible at $H_{\mathrm{ext}} \approx \pm\, 100\,\mathrm{mT}$ in each field direction (which is also the case for $\mathrm{SIF_{high}}(1)$). These differences are attributed to the different hysteretic response of $\mathrm{SF_{high}}(1)$ and (2), which also accounts for different resistivity values at the same field position in up and down oriented field ramping. The magnetization near zero field obtains a small but finite H_{coerc} and is different in field increasing and decreasing state. In the RDS state, superconductivity nucleates over domains in reverse direction to H_{ext} and the area of reversed domains is not equal to the area of domains parallel to H_{ext} (see Fig. 2.3(c)). H_{coerc} and $M(H_{\mathrm{coerc}})$ values of $\mathrm{SF_{high}}(1)$ are larger than $\mathrm{H_{coerc}}$ and $M(H_{\mathrm{coerc}})$ of $\mathrm{SF_{high}}(2)$ (see table 9.8 and Fig. 9.13 in the supplementary), leading to a stronger suppressed superconducting state on domains parallel to H_{ext}.
Although the $\mathrm{SF_{high}}(2)$ exhibits proximity coupling between Nb and FePd, the magnetoresistance effects can be explained purely by stray-field generated DWS and RDS.

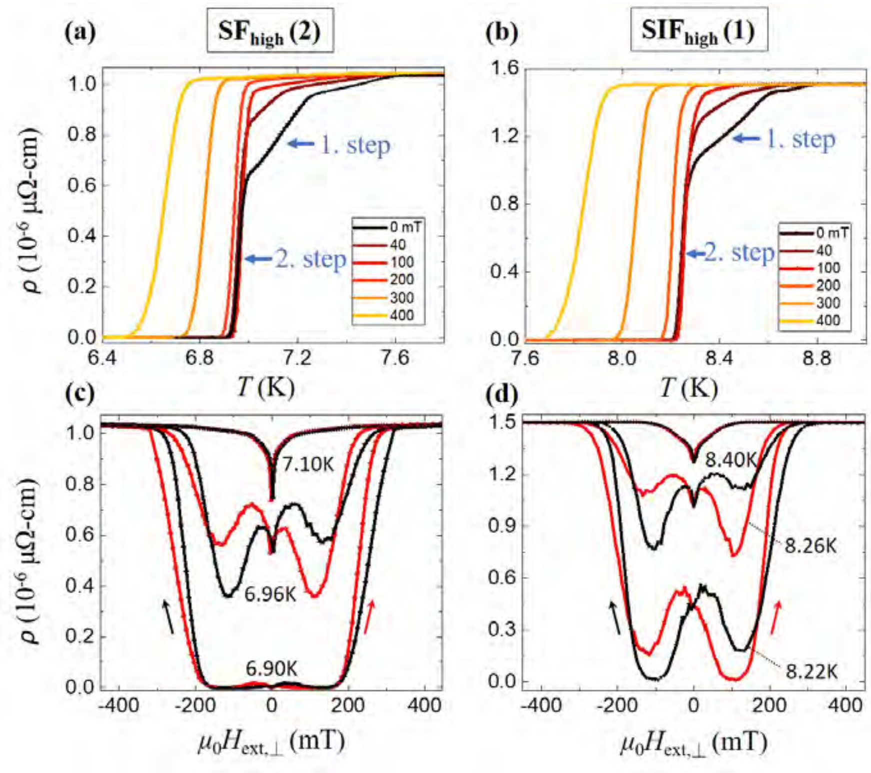

Figure 6.6: (a,b) $\rho(T)$ in a constant out-of-plane applied field, for $\mathrm{SF_{high}}(2)$ and $\mathrm{SIF_{high}}(1)$, respectively. (c) $\rho(H_{\mathrm{ext},\perp})$ at constant temperature for $\mathrm{SF_{high}}(2)$ and for the reference sample $\mathrm{SIF_{high}}(1)$ (d).

(iii) Another evidence for stray-field generated DWS/RDS is given by the field dependence of T_c. Equation (6.2) [97] predicts for DWS a nonlinear dependence of T_c on $H_{\mathrm{ext},\perp}$ at low fields, with the change $\Delta T_\mathrm{c}^{\mathrm{orb}}$ due to orbital effects, the eigenvalue of the GL equations, E_{min}, and the reduced field z-direction, $b_z = \frac{\mu_0 H_{\mathrm{ext},\perp}}{B_{z,\mathrm{max}}}$, as described in chapter 2.4.1.

$$T_\mathrm{c}(b) = \Delta T_\mathrm{c}^{\mathrm{orb}}(\frac{1}{2} - E_{\mathrm{min}})b^4 + \Delta T_\mathrm{c}^{\mathrm{orb}}(2E_{\mathrm{min}} - \frac{1}{2})b^2 + T_\mathrm{c}(0). \tag{6.2}$$

Figure 6.7(a) shows $\mu_0 H_{\mathrm{ext},\perp}(T_\mathrm{c})$ which is extracted from $\rho(T)$ in constant $H_{\mathrm{ext},\perp}$ as plotted in (b). The red line denotes a fit to (6.2), and all fit parameters are given in table 6.1. The datapoint at $H_{\mathrm{ext},\perp} = 0$ is excluded from the fit as here DWS nucleates on top of domain walls or closure domains of finite thickness, which are not assumed in equation (6.2).

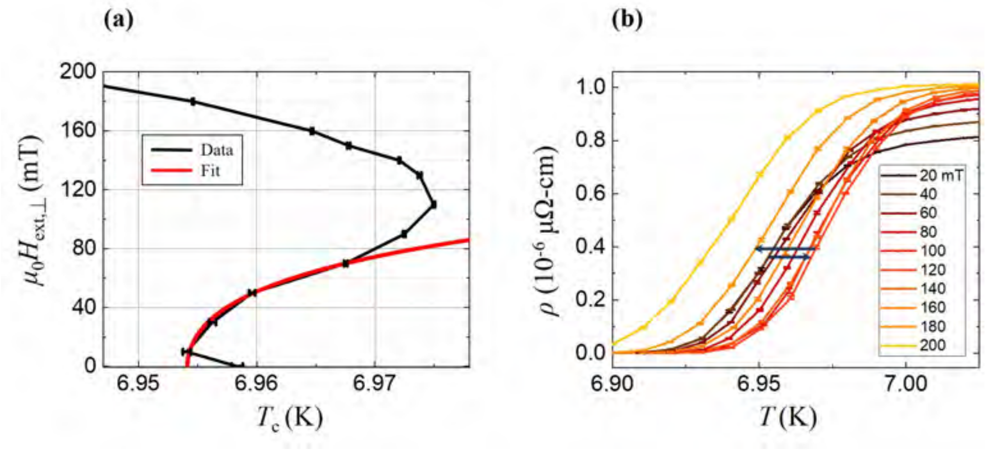

Figure 6.7: (a) $H_{\mathrm{ext},\perp}(T_c)$ as obtained from $\rho(T)$ measurements shown in (b). Blue arrows mark the direction of change in T_c for increasing applied fields.

Parameter	Value
$T_c(0)$	6.954±0.001 K
$\Delta T_c^{\mathrm{orb}}$	0.15±0.04 K
E_{min}	0.32±0.04

Table 6.1: Fit parameters for a model of stray field-generated DWS by [97] on $T_c(\mathrm{H_{ext}})$ of sample $\mathrm{SF_{high}}(2)$.

The maximum stray field value $B_d = 108\,\mathrm{mT}$ corresponds to the RDS minimum at $\rho(100\,\mathrm{mT})$ of the field increasing branch and is given as fixed parameter in the fit. On the one hand the results show that a model containing stray field generated DWS fits well to the measured data, on the other hand they can be compared with surface superconductivity with $E_{\mathrm{min}} = 0.59$ [99]. The fit value $E_{\mathrm{min}} = 0.32 \pm 0.04$ is slightly lower than for surface superconductivity but in the same order of magnitude. Yang et al. [7] observed a similar $E_{\mathrm{min}} = 0.37$ for DWS in a Nb thin film on a ferromagnetic $\mathrm{BaFe_{12}O_{19}}$ substrate for magnetic domains with high domain wall width of $D_{\mathrm{DW}} = 200\,\mathrm{nm}$.
E_{min} is related to B_c^* by $E_{\mathrm{min}} = -mc\alpha/(e\hbar B_c^*)$, with α being the first expansion coefficient from the Ginzburg Landau theory [99]. Using the relation $B_{c3} = B_{c2}/E_{\mathrm{min}} = B_{c2}/0.59$ for surface superconductivity, B_c^* of $\mathrm{SF_{high}}(2)$ needs to be higher for DWS than for conventional surface superconductivity which can explain the high B_c^*-values reported in table 9.10 in the supplementary.

Furthermore, the stray field strength B_d above the FePd layer surface in z-direction is estimated and compared with the measured data by a model from Sonin for domain structured ferromagnetic thin films with easy axis in out-of-plane direction [94] in which $B_\mathrm{d}(x,z)$ depends on M_S, D_domain and d_FM - the saturation magnetization, domain thickness and layer thickness of the ferromagnetic film, respectively (see eq. (6.3)). x denotes the position along one of the in-plane crystallographic axes of the L1_0-phase and z the distance from the FePd layer surface as shown in Fig. 6.8.

$$B_\mathrm{d}(x,z) = \mathrm{Im}(4 * M_\mathrm{S} * (\ln(\tan\pi\frac{x+iz}{2D_\mathrm{domain}}) - \ln(\tan\pi\frac{x+iz-id_\mathrm{FePd}}{2D_\mathrm{domain}}))). \tag{6.3}$$

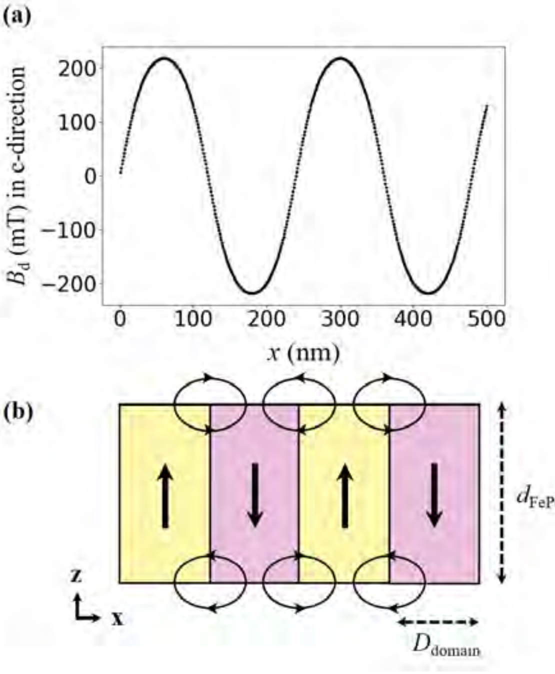

Figure 6.8: (a) Stray fields B_d in c-direction of the FePd crystallographic axes in a distance z=40 nm of the FePd layer in SF$_\mathrm{high}$(2) with infinitely thin domain walls as shown in (b). D_domain denotes the thickness of FePd lateral domains and d_FePd the thickness of the FePd layer.

For $z = 40$ nm, $M_\mathrm{s} = 1200000$ A/m, $D_\mathrm{domain} = 110$ nm, and $d_\mathrm{FePd} = 44$ nm, (6.3) yields $B_\mathrm{d} = 210$ mT, which is higher than the measured value of $B_\mathrm{d} = 108$ mT (note that the values are applied to (6.3) in cgs-units). This can result from (i) an incomplete long-range order of the FePd L1_0-phase in SF$_\mathrm{high}$(2) which comprises S=0.68±0.02, (ii) a reduction of field penetration due to the superconducting screening, and (iii) a finite domain wall thickness in SF$_\mathrm{high}$(2), whereas the model used for the stray field computation assumes infinitely-thin domain walls.

In total it is concluded that the observed effects in $\rho(T)$ and $\rho(H_{\mathrm{ext},\perp})$ result from stray-field generated, isolated DWS and RDS. DWS exhibits the highest T_{c}-value which transitions into RDS with decreasing T and subsequently into a complete superconducting state. The energy eigenvalue of the Ginzburg-Landau equation for the highest possible applied field (here DWS) is lower than for conventional surface superconductivity, resulting in higher B_{c}^{*}. The higher T_{c} of the S/I/F system compared to the S/F layers clearly denotes proximity coupling, but without significant impact on the DWS and RDS states.

6.2.2 Comparison of PMA

In this section the resistivity measurements with respect to temperature and field will be compared for different degrees of magnetocrystalline anisotropy of the S/F samples based on the DWS and RDS conclusions in the previous section.
A magnetic characterization of samples $\mathrm{SF}_{\mathrm{high}}(1{,}2)$, $\mathrm{SF}_{\mathrm{low}}(1)$, and $\mathrm{SF}_{\mathrm{mid}}(1)$ performed in section 5.4.3 yields $Q > 1$ for high and medium anisotropy, and $Q < 1$ in case of low anisotropy but with an out-of-plane oriented stray field configuration still well observable by MFM (see Fig. 5.15), suggesting a magnetic formation as schematically drawn in Fig. 6.9(a). Temperature and field dependence of resistivity in an out-of-plane applied field are shown in Figs. 6.9(b) and (c), respectively. For a calculation of the sheet resistivity ρ, equation (4.2) has been employed with the layer thicknesses given in tables 9.1-9.6, and respective point-spacing dependent values f_2 ranging from 0.89-0.925.

All three samples exhibit more than one resistivity step before a complete superconducting state is reached. In comparison with $\mathrm{SF}_{\mathrm{high}}(1{,}2)$, the same sharp transitions before reaching the complete superconducting state with $\rho(T) = 0\,\mu\Omega$-cm are visible and therefore called T_{c2}. The transition width of the first resistivity step in $\mathrm{SF}_{\mathrm{low}}(1)$ (as displayed in Fig. 6.9(b)) at $H_{\mathrm{ext},\perp} = 0\,\mathrm{mT}$ is much broader than in $\mathrm{SF}_{\mathrm{high}}(1)$ and without any clear plateau in $\rho(T)$. In contrast, $\mathrm{SF}_{\mathrm{mid}}(1)$ displays two sharp resistivity steps at low applied fields ($H_{\mathrm{ext},\perp} < 300\,\mathrm{mT}$) with a plateau at $\rho \approx 0.58\,\mu\Omega$-cm. In samples with high and medium anisotropy, T_{c2} is almost constant below 200 mT and is decreasing fast with temperature at higher fields, whereas T_{c2} of $\mathrm{SF}_{\mathrm{low}}(1)$ decreases monotonously with temperature starting at $H_{\mathrm{ext},\perp} = 0\,\mathrm{mT}$. The dependence of T_{c2} on $H_{\mathrm{ext},\perp}$ is plotted in detail in Fig. 6.10(a).
The $\rho(H_{\mathrm{ext},\perp})$ dependence of $\mathrm{SF}_{\mathrm{mid}}(1)$ is similar to $\mathrm{SF}_{\mathrm{high}}(1)$: one sharp minimum near $H_{\mathrm{ext},\perp} = 0\,\mathrm{mT}$ is observed at temperatures on the plateau of $\rho(T)$ between T_{c1} and T_{c2}, which vanishes at T_{c2} and two minima at ±100 mT evolve. The minimum near 0 mT at

the highest shown temperature in Fig. 6.9(c) in $\mathrm{SF}_{\mathrm{low}}(1)$ is less sharp. Additionally, no well resolved minima are observed at ±100 mT for $T_{\mathrm{c}2}$. The differences in the residual resistance values above T_{c} for the compared samples probably arise from variations in their defect densities and surface oxidation states.

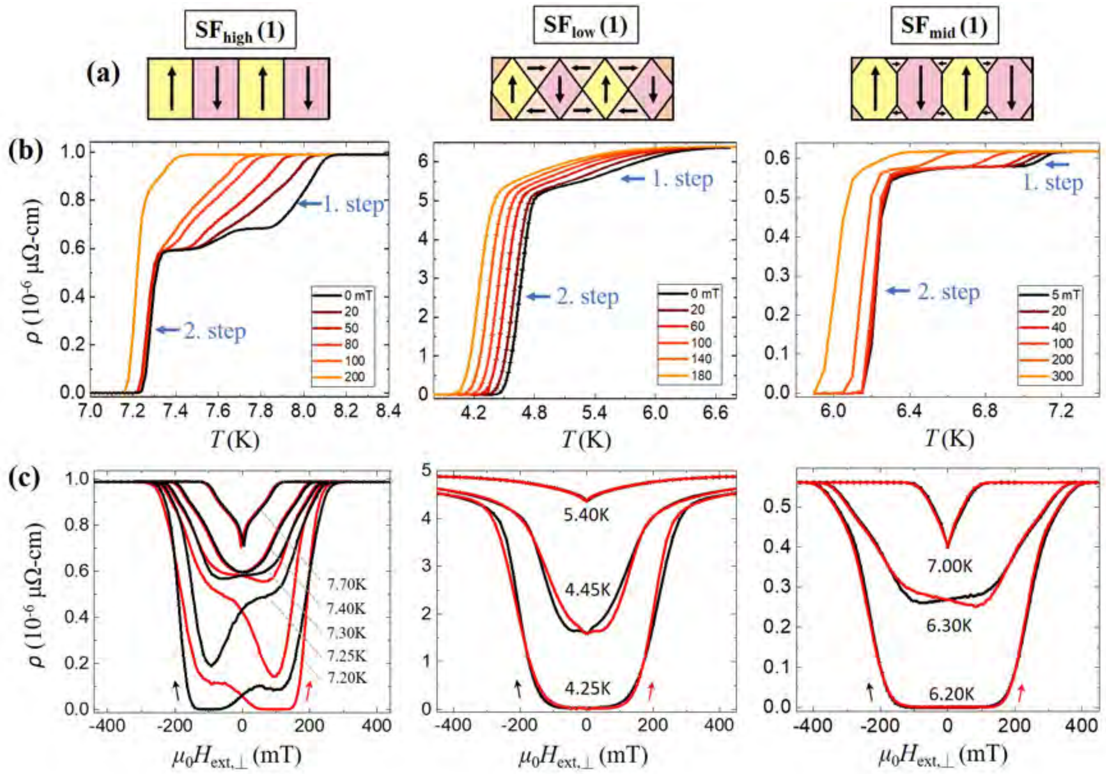

Figure 6.9: From left to right: S/F Samples with high, low, and medium PMA, respectively. (a) Schematic view of the domain formation inside the FePd layer in direction of the c-axis of L10-ordered FePd. (b) $\rho(T)$ in constant out-of-plane applied field. (c) $\rho(H_{\mathrm{ext},\perp})$ at constant temperature.

Following the interpretation of stray-field generated DWS and RDS in the previous section for $\mathrm{SF}_{\mathrm{high}}(1)$ and (2), it is concluded that $\mathrm{SF}_{\mathrm{mid}}(1)$ also exhibits DWS/RDS states at 0 mT and ±100 mT, respectively. Both samples with high and medium anisotropy comprise $Q > 1$ with strong out-of-plane stray fields penetrating the Nb layer and confining the superconducting state. On the contrary, in $\mathrm{SF}_{\mathrm{low}}(1)$ no well-resolved DWS/RDS states are observed.

Such a confinement can lead to 2D superconducting effects. If the superconducting regions are in one or more dimensions smaller than λ_{L} or ξ_{GL} it can for example cause variations of magnetic or electrical properties in the former case, or a change of T_{c} or the superconducting energy gap in the latter case [43]. This was scrutinized by Schöck et al. by resistivity measurements on thin film Nb of different layer thicknesses in an in-plane applied field (and is presented in detail in chapter 2.2.6): the authors reported a transition from 2D-like superconductivity with a square-root dependence of $B^{*}_{\mathrm{c},||}$ on the reduced temperature $t = T/T_{\mathrm{c}}$ to a 3D-like behavior with a linear dependence of $B^{*}_{\mathrm{c},||}$ on t.

$$B_{\mathrm{c2}} \sim \sqrt{1-t} \quad (2\mathrm{D}), \tag{6.4a}$$

$$B_{\mathrm{c2}} \sim (1-t) \quad (3\mathrm{D}). \tag{6.4b}$$

The dependence of T_{c} upon an out-of-plane applied field $H_{\mathrm{ext},\perp}$ of $\mathrm{SF}_{\mathrm{high}}(2)$ in this work is plotted in Fig. 6.10(a). The data is extracted from $\rho(T)$ in a constant external field $H_{\mathrm{ext},\perp}$ as explained in the previous section. A transition from a non-linear to a linear $\mu_0 H_{\mathrm{ext},\perp}(T_{\mathrm{c}})$ regime for $\mathrm{SF}_{\mathrm{high}}(2)$ and $\mathrm{SIF}_{\mathrm{high}}(1)$ at $H^{*}_{\mathrm{ext},\perp}$ is clearly visible. Also in $\mathrm{SF}_{\mathrm{low}}(1)$ there is a kink at $H^{*}_{\mathrm{ext},\perp}$ but a smooth transition into bulk superconductivity is observed. However, the reference bare S layer S(2) exhibits a linear temperature dependence in the whole range of $H_{\mathrm{ext},\perp}$, showing a bulk superconducting behavior for the same Nb thickness as of $\mathrm{SF}_{\mathrm{high}}(2)$ and $\mathrm{SIF}_{\mathrm{high}}(1)$. Unfortunately, resistivity data of $\mathrm{SF}_{\mathrm{mid}}(1)$ was only measured very near T_{c}. Still, the same non-linear trend as for samples with high PMA is obtained. Due to a change of T_{c} after surface oxidation, no further measurements could be performed.

To confirm a 2D-like parabolic temperature dependence below $H^{*}_{\mathrm{ext},\perp}$, in Fig. 6.10(b) a zoom into the region around $T_{\mathrm{c}}(0\,\mathrm{mT})$ and with T_{c} as function of $H^{2}_{\mathrm{ext},\perp}$ is given. After an initial increase in T_{c} due to DWS (as pointed out in the previous section), $H^{2}_{\mathrm{ext},\perp}$ of $\mathrm{SF}_{\mathrm{high}}(2)$ and the reference sample $\mathrm{SIF}_{\mathrm{high}}(1)$ follows a linear temperature dependence as pointed out by the linear fit to the data starting from $40{\cdot}10^{3}\,\mathrm{mT}^{2}$. In contrast, $\mathrm{SF}_{\mathrm{low}}(1)$ shows a linear temperature dependence of $H^{2}_{\mathrm{ext},\perp}$ without any sign for a DWS-related increase in T_{c}.

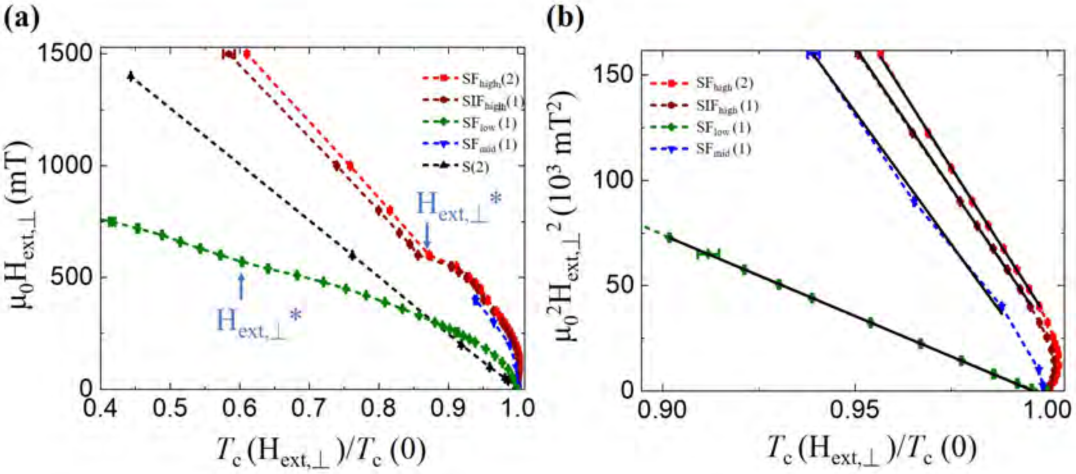

Figure 6.10: (a) External magnetic field $H_{\text{ext},\perp}$ applied out-of-plane to the sample surface with respect to the reduced temperature $T_\text{c}(H_{\text{ext},\perp})/T_\text{c}(0)$, obtained from $\rho(T)$ measurements. (b) Square of $H_{\text{ext},\perp}$ with respect to $T_\text{c}(H_{\text{ext},\perp})/T_\text{c}(0)$ as shown in (a). Black lines denote linear fits to the data points.

The transition from non-linear to linear T_c-dependences at $H^*_{\text{ext},\perp}$ corresponds to the magnetic field value at which the hysteresis loop for out-of-plane applied fields is closing for each sample (i.e. the saturation field for samples with high PMA, see Figs. 5.15(c) and 6.3(a)). Both values are compared in table 6.2. At this point, the domain-superconductivity turns into bulk superconductivity, which promotes the hypothesis that a 2D-superconducting behavior is responsible for the non-linear part of $H_{\text{ext},\perp}(T_\text{c})$.

Sample	$H^*_{\text{ext},\perp}$ (mT)	$H_{\text{ext},\perp}$ at closing hysteresis (mT)
$\text{SF}_\text{high}(2)$	610±20	600±50
$\text{SF}_\text{low}(1)$	560±20	570±30
$\text{SIF}_\text{high}(1)$	610±20	600±50

Table 6.2: Comparison of $H^*_{\text{ext},\perp}$ obtained from Fig. 6.10 and of $H_{\text{ext},\perp}$ at which the hysteresis loops shown in Fig. 5.15(c) close.

In the following, first a comparison of $\xi_{\text{GL},||}(T_\text{c})$ with D_domain will be performed to prove that the resistivity minima in Fig. 6.9 does indeed follow from isolated DWS/RDS. In a second step, $\xi_{\text{GL},||}(T_\text{c})$ and the estimated Pearl penetration depth Λ will be compared with d_Nb, the Bloch domain wall width w_DW and the domain width D_domain to scrutinize a 2D-superconducting effect in the S/F samples. $B^*_{\text{c},\perp}(0\,\text{K})$ is extrapolated from the linear part above $H^*_{\text{ext},\perp}$, and is converted to $\xi_{\text{GL},||}(0\,\text{K})$ using eq. 2.18a from chapter

2.2.4. The values of $T_\mathrm{c}(0\,\mathrm{mT})$, $B^*_{\mathrm{c},\perp}(0\,\mathrm{K})$, and $\xi_{\mathrm{GL},||}(0\,\mathrm{K})$ for all S/F samples are listed in table 9.10 in the supplementary.

(i) $\xi_{\mathrm{GL},||}(T_\mathrm{c})$ obtained by (6.1) is listed in table 6.3. The reference samples for $\xi_{\mathrm{GL,ref}}(0)$ are chosen corresponding to the respective Nb layer thicknesses. The condition $2\xi_{\mathrm{GL},||}(T_\mathrm{c}) < D_\mathrm{domain}$ is fulfilled for each sample, and isolated DWS/RDS is possible.
(ii) A 2D-superconducting behavior in an out-of-plane applied field cannot result from the Nb layer thickness, as all reference samples of similar d_Nb show a linear $H_{\mathrm{ext},\perp}(T_\mathrm{c})$-dependence. Instead of the layer thickness, DWS or RDS effects can generate 2D-superconductivity in the S/F systems. Laterally confined superconducting areas such as DWS on top of domain walls need to be compared with $\xi_{\mathrm{GL},||}(T_\mathrm{c})$ and Λ.
The Bloch wall width is roughly estimated by $w_\mathrm{DW} = \pi\sqrt{A/K_\mathrm{u}}$ [13] with $A = 10^{-11}$ J/m for FePd thin films [173], comprising much larger $\xi_{\mathrm{GL},||}(T_\mathrm{c})$ then w_DW. This result supports the possibility of DWS as origin of the 2D-superconductivity observed in Fig. 6.10. Additionally, from a measurement of the residual resistivity at 10 K, the electron mean free path l_mfp of Nb at low temperatures is calculated by $\rho(10\,\mathrm{K})\cdot l_\mathrm{mfp} = 3.75\cdot 10^{-6}$ µΩ-cm [186] for the bare Nb layers (assuming the same values in S/F systems with similar d_Nb) and listed in table 6.3. From l_mfp and the Nb bulk values for $\lambda_\mathrm{L,BCS}(0)$ and $\xi_\mathrm{0,BCS}$ in table 2.2, Λ at 0 K are estimated using eq. (6.5):

$$\Lambda(0) = \lambda_\perp(0) = \frac{\lambda^2_\mathrm{L,dirty}(0)}{d} = \lambda_\mathrm{L,BCS}(0)\sqrt{\frac{\xi_\mathrm{0,BCS}}{l_\mathrm{mfp}}}. \tag{6.5}$$

Since Λ is increasing with T, the values in table 6.3 denote a lower limit for the penetration depth in Nb in out-of-plane direction, which shows that also the condition $\Lambda > d_\mathrm{Nb}$ can account for the observed 2D effects, for example in $\mathrm{SF_{low}}(1)$.

Sample	w_DW (nm)	D_domain (nm)	d_Nb (nm)	Ref. sample	$l_\mathrm{mfp}(10\,\mathrm{K})$ (nm)	$\xi_{\mathrm{GL},||}(T_\mathrm{c})$ (nm)	$\Lambda(0\,\mathrm{K})$ (nm)
$\mathrm{SF_{high}}(2)$	8.1±0.5	110±3	39±2	S(2)	3.9±0.2	25.9±0.2	56
$\mathrm{SF_{low}}(1)$	12±3	76±3	32±2	S(3)	10.4±0.1	27±4	31
$\mathrm{SF_{mid}}(1)$	11.8±0.8	107±3	37±2	S(2)	3.9±0.2	21.6±0.2	56
$\mathrm{SIF_{high}}(1)$	7.9±0.6	120±3	40±1	S(2)	3.9±0.2	53.0±0.4	56

Table 6.3: Bloch domain wall width w_DW, domain width D_domain and Nb layer thickness d_Nb of samples comprising different PMA in comparison with their respective reference bare S films. By these parameters, the mean free path l_mfp, the GL-coherence length $\xi_{\mathrm{GL},||}(T_\mathrm{c})$ and the Pearl penetration depth $\Lambda(0\,\mathrm{K})$ are calculated.

In conclusion, the comparison of S/F samples comprising different degree of PMA yields that all samples with $Q > 1$ exhibit stray-field generated, isolated DWS and RDS, as well as 2D superconducting effects visible as a parabolic temperature dependence of $H_{\mathrm{ext},\perp}(T_{\mathrm{c}})$. In contrast, in the S/F system comprising low PMA and $Q < 1$ no DWS or RDS is obtained, but still a 2D superconductivity at low applied fields indicates a confined superconducting state due to ξ_{GL} or Λ being smaller than the superconducting regions in $\mathrm{SF}_{\mathrm{low}}(1)$.

6.3 Magnetotransport with in-plane magnetic field

As discussed in the previous section, $\mathrm{SF}_{\mathrm{low}}(1)$ does not show DWS or RDS in an out-of-plane applied field. However, peculiar effects arise in a magnetic field applied in-plane to the sample surface. Following the results from section 5.4.3, only $\mathrm{SF}_{\mathrm{low}}(1)$ exhibits an in-plane easy magnetization axis, still showing a lateral magnetic domain structure, which indicates the formation of large closure domains and non-collinear magnetic moments. Such non-collinear magnetic moments can give rise to a generation of long-ranged spin-triplet components (LRTC) of Cooper pairs with aligned spins (see chapter 2.4.2) and arise purely from proximity effects. Thus, they are suppressed by insertion of an insulating layer between S and F.

First, resistivity measurements in an in-plane applied field, $H_{\mathrm{ext},||}$, are discussed for the S/F and S/I/F samples comprising low PMA. Second, the results are compared for different strength of PMA.

6.3.1 Low PMA

The resistivity of $\mathrm{SF}_{\mathrm{low}}(1)$ dependent upon $H_{\mathrm{ext},||}$ applied along the <100> crystal axis is measured at constant temperatures and displayed in Fig. 6.11(a). Two resistivity minima and one local resistivity maximum at the coercive field in an in-plane field $H_{\mathrm{coerc},||} = 13 \pm 1\,\mathrm{mT}$ (obtained by MPMS) are observed at each given temperature. On the contrary, the reference sample $\mathrm{SIF}_{\mathrm{low}}$ with an insulating layer between Nb and FePd in Fig. 6.11(b) exhibits only one broad resistivity minimum between the upper critical fields $\pm B_{\mathrm{c}}^{*}$ for each temperature.

Additionally, after saturation $\mathrm{SF}_{\mathrm{low}}$ exhibits a maze domain structure without in-plane magnetic anisotropy which is confirmed by the measurement of hysteresis loops in different directions of $H_{\mathrm{ext},||}$ in the sample surface area (see supplementary Fig. 9.14).

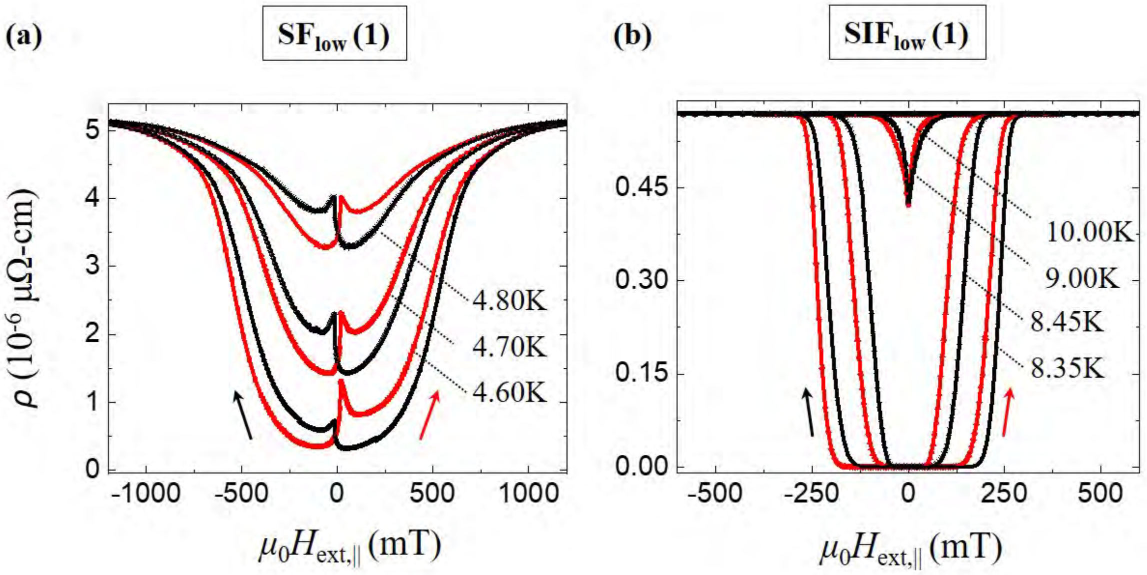

Figure 6.11: $\rho(H_{\mathrm{ext},||})$ at constant temperature for (a) SF$_{\mathrm{low}}$(1) and (b) for the reference sample SIF$_{\mathrm{low}}$(1).

The resistivity features of SIF$_{\mathrm{low}}$ correspond to the typical behavior of a conventional type-II superconducting thin film in an applied field, indicating no visible proximity or stray field effects. Both samples comprise $Q < 1$ with comparable saturation magnetizations M_{S} and coercive field values H_{coerc} (see table 9.8). Therefore, the maxima and minima in the magnetoresistance of SF$_{\mathrm{low}}$ cannot originate from stray field effects as the DWS and RDS phenomena in section 6.2.

For an interpretation of the observed effects, again a short reminder of chapter 2.4.2 is drawn in the following: at S/F interfaces with magnetic inhomogeneity on a length scale of ξ_{GL}, spin-singlet as well as spin-triplet Cooper pair components are created, with total spins $S_{\mathrm{z}} = 0$ and $S_{\mathrm{z}} = \pm 1$ along the z-axis of the magnetization orientation inside F, respectively. Spin-singlet Cooper pairs are short-ranged inside F due to the pair dephasing in an exchange field E_{ex}, where spin-up electrons are decreased in energy by E_{ex} and spin-down electrons are increased by E_{ex}, leading to a finite center-of-mass momentum. In contrast, spin-aligned Cooper pairs are insensitive to the pair dephasing of the F layer and exhibit long coherence length (see Fig. 6.12(a)). These LRTC have been theoretically predicted for S/F structures with magnetic domain walls, conical ferromagnets, or spin-valve structures with a non-collinear magnetization of the two F layers. Their existence can be predicted e.g. by field and temperature dependent resistivity measurements due to following reason: In case of spin-singlet Cooper pairs, the exchange field in S/F1/F2 spin valve structures obtains a maximum if F1 and F2 exhibit parallel (P) magnetization orientations, and has a minimum for an antiparallel (AP) orientation, leading to a positive $\Delta T_{\mathrm{c}} = T_{\mathrm{c}}^{\mathrm{AP}} - T_{\mathrm{c}}^{\mathrm{P}}$. Upon a generation of LRTC, ΔT_{c} is a non-monotonic function of the misalignment angle θ between different magnetization orientations [12, 117], with a minimum in T_{c} at $\theta = 90°$ where the amplitude of LRTC is maximum.

Zdravkov et al. [116] have predicted the existence of LRTC in their S/F1/F2 heterostructures due to a minimum in T_{c} at H_{coerc} where F1 and F2 are magnetized non-collinearly, and corresponding local maxima in T_{c} at AP and P configurations (see Fig. 6.12(b)). A local minimum in T_{c} is directly related to a local maximum in $\rho(H_{\mathrm{ext}})$ at constant temperature (see Fig. 6.12(c)).

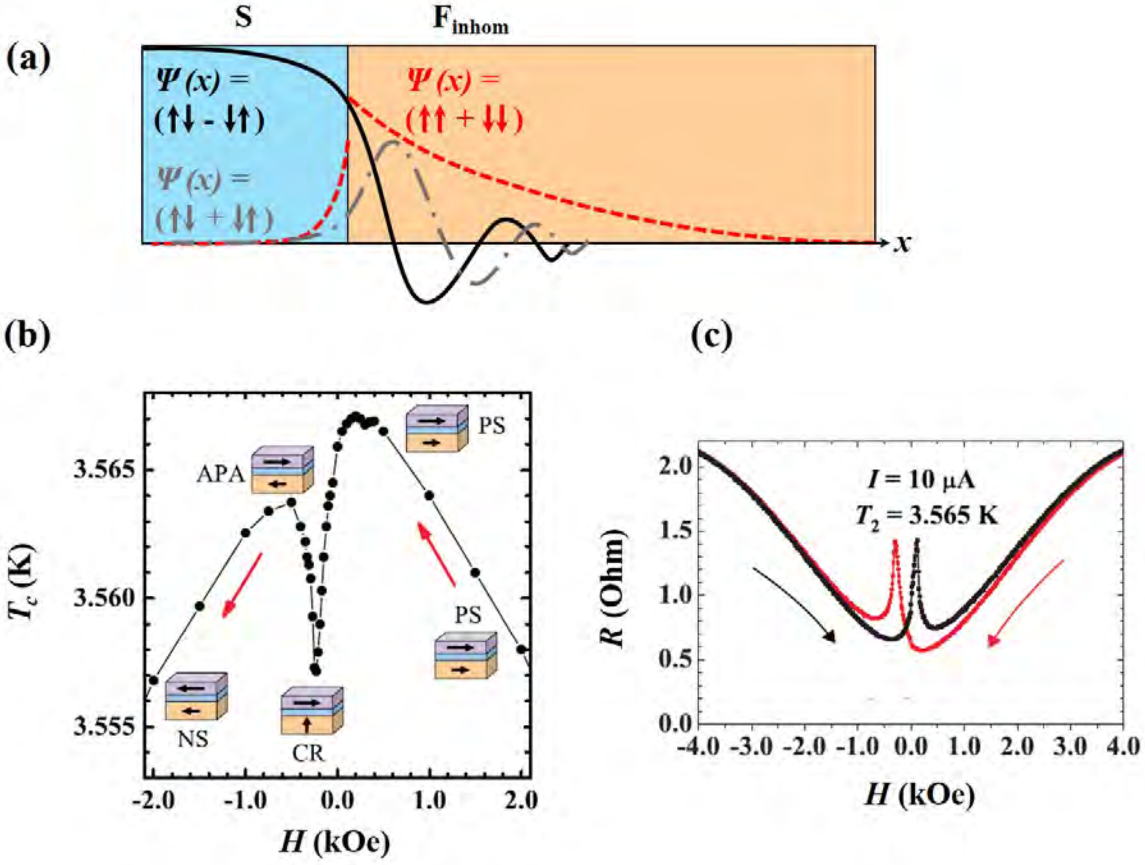

Figure 6.12: (a) Schematic sketch of the penetration of Cooper pair components from S into an inhomogeneous F layer. Black lines denote spin-singlet components, grey spin-triplet components with $S_{\mathrm{z}} = 0$ and red spin-triplet components with $S_{\mathrm{z}} = \pm 1$. (b) Critical temperature T_{c} and (c) resistance R with respect to an external magnetic field H, taken from Zdravkov et al. [116].

The $\rho(H_{\mathrm{ext},||})$ measurements in Fig. 6.11(a) also exhibit local maxima at $H_{\mathrm{coerc},||}$ in both field directions. Additionally, a local minimum in T_{c} at $H_{\mathrm{coerc},||}$ is observed independent of the measurements in Fig. 6.11(a) by $\rho(T)$ measurements, of which T_{c} for each applied field is extracted as explained in the previous chapter. Fig. 6.13 shows T_{c} and the magnetization of $\mathrm{SF_{low}}(1)$ as a function of $H_{\mathrm{ext},||}$. The resistivity measurements are performed after saturation of the sample in a negative field of $\mu_0 H_{\mathrm{ext},||} = -1.5\,\mathrm{T}$, corresponding to the black line in the hysteresis loop. The respective $\rho(T)$ measurements can be found in Fig. 9.15 in the supplementary.

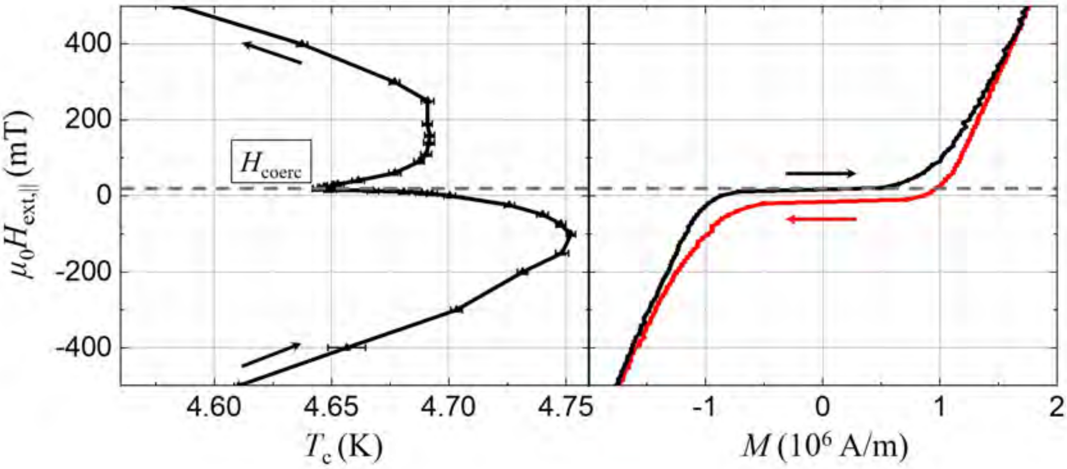

Figure 6.13: $H_{\mathrm{ext},||}(T_{\mathrm{c}})$ of $\mathrm{SF_{low}}$ (left), all data points are measured after saturation of the sample in a negative magnetic field. The corresponding hysteresis loop (right) is measured in both field sweep direcitons at $T = 3.5\,\mathrm{K}$, adapted from [182].

The minimum in T_{c} and corresponding maximum in $\rho(H_{\mathrm{ext},||})$ at $H_{\mathrm{coerc},||}$ of $\mathrm{SF_{low}}$ suggest the formation of LRTC. This assumption is supported by the following three observations: (i) at $H_{\mathrm{coerc},||}$ the misalignment angle between the magnetization orientations between the domain walls, closure domains, and out-of-plane domains is maximum, allowing a high density of LRTC. (ii) $\mathrm{SF_{low}}$ consists of a non-collinear magnetic configuration as shown in the schematic image in Fig. 6.9(a), with an equilibrium domain thickness of $D_{\mathrm{domain}} = 76 \pm 3\,\mathrm{nm}$. The coherence length at T_{c} of $\mathrm{SF_{low}}$ is $\xi_{\mathrm{GL},||}(T_{\mathrm{c}}) = 27 \pm 4\,\mathrm{nm}$ (see table 6.3), which is lower than the period of the lateral magnetic inhomogeneity. (iii) All observed magnetoresistance features originate from proximity effects other than stray field effects (like vortex movements or the above discussed DWS/RDS), as no such maxima in $\rho(H_{\mathrm{ext},||})$ are observed in the reference $\mathrm{SIF_{low}}(1)$ sample.

Measurements of $\rho(H_{\mathrm{ext},||})$ at various angles ϕ with respect to the sample surface in Fig. 6.14 indicate a smooth transition from a LRTC generation with a minimum in ρ at $H_{\mathrm{coerc},||}$ for $\phi = 0°$ to a clearly pronounced kink at $\phi = 45°$ and finally to the features observed in $\rho(H_{\mathrm{coerc},\perp})$ (and at $\phi = 90°$) related to out-of-plane oriented magnetic domains. It has to be noted that for $\phi = 0°$ and 45° the magnetoresistance is lower in negative applied fields for an "up-sweep" (i.e. starting from negative saturation) than for a "down-sweep". In contrast, for $\phi = 90°$ a lower resistance is observed for the "down-sweep", which is as well the case for all S/F structures in an out-of-plane applied field in Fig. 6.9.

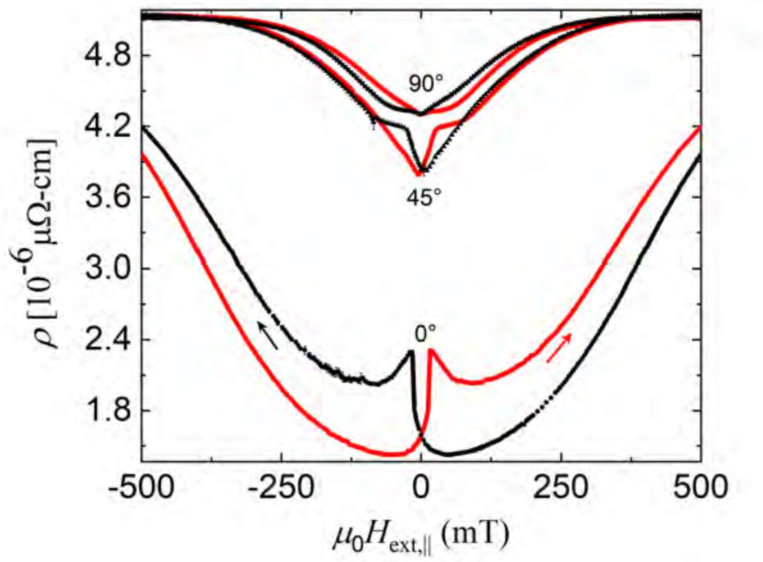

Figure 6.14: $\rho(H_{\mathrm{ext},||})$ at various external magnetic field angles with respect to the sample surface: 0° denotes a magnetic field applied parallel to the <100> axis and 90° a magnetic field applied along the <001> axis (i.e. perpendicular to the sample surface). All measurements are obtained at $T = 4.5\,\mathrm{K}$.

It is concluded that a generation of LRTC with $S_z = \pm 1$ at the S/F interface of $\mathrm{SF_{low}}(1)$ is a possible reason for the observed magnetoresistance features, with highest density of the LRTC amplitude in relation to the amplitude of spin-singlet Cooper pairs at $H_{\mathrm{coerc},||}$. Here, the maximum ΔT_c between $T_c(H_{\mathrm{coerc},||})$ and $T_c^{\max}$ is $\sim$100 mK (see Fig. 6.13).

6.3.2 Comparison of PMA

Figure 6.15(a) shows the schematic domain configuration of samples with different degrees of PMA, together with the measured $\rho(H_{\mathrm{ext},||})$ curves displayed in 6.15(b). Only $\mathrm{SF}_{\mathrm{low}}$ with highest density of in-plane magnetic moments at low applied fields exhibits local maxima in resistivity at $H_{\mathrm{coerc},||}$. However, also $\mathrm{SF}_{\mathrm{high}}(1)$ and $\mathrm{SF}_{\mathrm{mid}}(1)$ show a kink in $\rho(H_{\mathrm{ext},||})$ near $H_{\mathrm{coerc},||}$, which is more pronounced in $\mathrm{SF}_{\mathrm{mid}}(1)$.

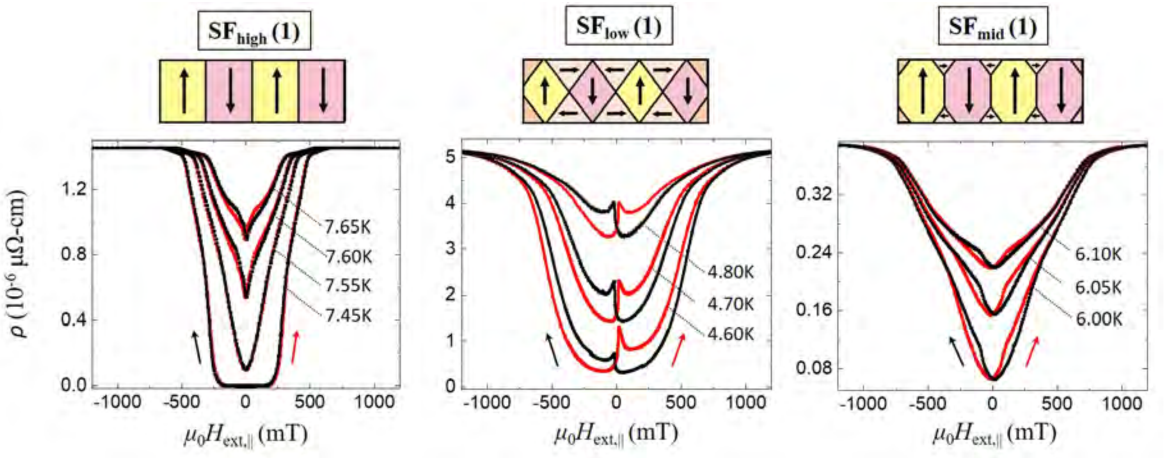

Figure 6.15: From left to right: S/F Samples with high, low, and medium PMA, respectively. (Top) Schematic view of the domain formation inside the FePd layer in direction of the c-axis of L10-ordered FePd. (Bottom) $\rho(H_{\mathrm{ext},||})$ at constant temperature.

The kinks in $\rho(H_{\mathrm{ext},||})$ of $\mathrm{SF}_{\mathrm{high}}(1)$ and $\mathrm{SF}_{\mathrm{mid}}(1)$ are reminiscent of the measurement of $\mathrm{SF}_{\mathrm{low}}(1)$ for $\phi = 45°$ and show lower resistivity values in negative fields for the "up-sweep", in contrast to the measurements performed in an out-of-plane applied field. This suggests a generation of LRTC also in $\mathrm{SF}_{\mathrm{high}}(1)$ and $\mathrm{SF}_{\mathrm{mid}}(1)$. The less pronounced kink in $\mathrm{SF}_{\mathrm{high}}(1)$ could be interpreted in such a way that an overlap of a LRTC generation with features resulting from the out-of-plane oriented magnetic domains is observed, with a density of LRTC lowest for high PMA and highest for low PMA, resulting from a magnetic inhomogeneity near the domain walls and closure domains of FePd.

6.4 Conclusions

In summary, the hysteresis loops in an out-of-plane applied field and the magnetoresistance measurements for both, in-plane and out-of-plane magnetic fields, have been analyzed. The magnetization measurements indicate a coexistence of ferromagnetic and superconducting states in the S/F heterostructures below T_c for all degree of PMA and that the domain formation is not altered by the superconducting state. In an out-of-plane applied field, signatures of stray-field generated, isolated DWS and RDS are observed for samples with $Q > 1$, a statement which is supported by a comparison with theoretical models. All samples exhibit a 2D superconducting effect below the saturation field H_{sat}. For in-plane applied fields, a generation of LRTC in samples comprising low PMA is conjecturable, with highest density at H_{coerc}. The observed maximum ΔT_{c} of ~100 mK is a remarkably high change in superconducting transition temperature due to exchange effects in a S/F bilayer and provides a promising view on the performance of respective F/S/F′ trilayer structures with higher ΔT_{c}.

A generation of LRTC is also suspected for S/F structures with a higher degree of PMA, which has to be elaborated in further experiments.

Chapter 7

Neutron scattering results of high-PMA Nb/FePd

In this chapter, the depth-resolved lateral magnetization profile of a Nb/FePd bilayer with high PMA shall be investigated by low-temperature GISANS experiments. In direct contact, both the ferromagnetic and superconducting states are influenced by proximity and inverse proximity effects as described in section 2.4. First, unpolarized GISANS measurements on $\mathrm{SF_{high}}(1)$ at various temperatures ranging from $T \gg T_\mathrm{c}$ to $T \ll T_\mathrm{c}$ (performed at KWS-3) are scrutinized and compared with resistivity and magnetization measurements in section 7.1. Second, polarized GISANS measurements with polarization analysis on $\mathrm{SF_{high}}(2)$ (carried out at vSANS) are shown in section 7.2 and simulated using the DWBA and the domain-model presented in section 3.2.4.

7.1 Temperature dependence

Zero-field-cooled GISANS with an unpolarized neutron beam is measured for 20 min for each temperature step, starting from 8.3 K ($T > T_\mathrm{c} = 7.250 \pm 0.005$) to 3 K in steps of 0.05 K and at a sample-to-detector distance of 1.8 m, a wavelength of $\lambda = 12.8\,\mathrm{\AA}$ and a wavelength spread of $\Delta\lambda/\lambda = 17\,\%$. Before each measurement, the temperature is stabilized. Following the results obtained in section 6.2.1, $\mathrm{SF_{high}}(1)$ exhibits high PMA with $Q = 1.56 \pm 0.07$ and a maze domain structure with stray-field generated Domain-Wall-Superconductivity (DWS) at temperatures near T_c in zero field, subsequently changing into Reverse-Domain-Superconductivity (RDS) and Complete-Superconductivity (CS) below 7.2 K.

From the Q_y-Q_z-map at each temperature, the intensities of the specular spot and both GISANS peaks are calculated by an integration of intensities in a range $\Delta Q_z = \pm 0.03\,\mathrm{nm}^{-1}$ and $\Delta Q_{y,\mathrm{spec}} = \pm 0.026\,\mathrm{nm}^{-1}$, $\Delta Q_{y,\mathrm{GIS}} = \pm(0.026 - 0.1)\mathrm{nm}^{-1}$ around the peak centers of the specular and GISANS peaks, respectively. Figure 7.1(a) shows one example Q_y-Q_z-map at $T = 8.3\,\mathrm{K}$. In Fig. 7.1(b), the integrated intensities of the specular spot I_{spec} and the sum of integrated intensities of both GISANS peaks I_{GIS} are plotted with their temperature dependence.

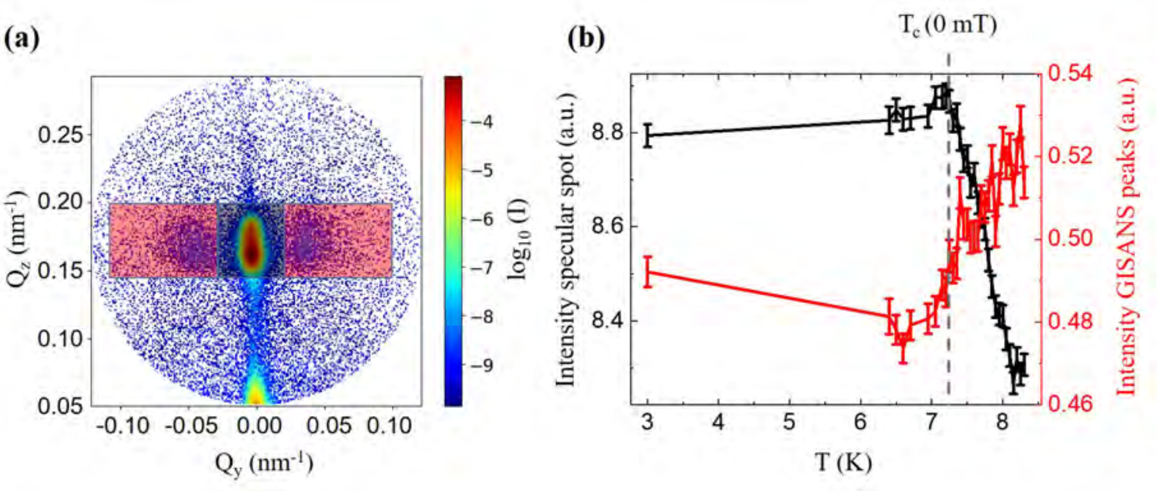

Figure 7.1: (a) Q_y-Q_z-map of $\mathrm{SF_{high}}(1)$ at $T = 8.3\,\mathrm{K}$, above the superconducting critical temperature. (b) Integrated intensities I_{spec} and I_{GIS} over the areas displayed by black and red boxes in (a), respectively, and with dependence on temperature. The grey vertical line denotes $T_{\mathrm{c}} = (7.247 \pm 0.001)\,\mathrm{K}$ of $\mathrm{SF_{high}}(1)$ at $0\,\mathrm{mT}$.

From the GISANS peaks in Fig. 7.1(a), a domain period of $D_{\mathrm{domain}} = 77 \pm 5$ is calculated which fits well to the domain thickness of $86 \pm 10\,\mathrm{nm}$ obtained by MFM. The GISANS and specular peaks are well separated and Fig. 7.1(b) shows a reverse temperature dependence of both peaks: while I_{spec} increases in a small range of 8.15-7.2 K, the I_{GIS} decreases by the same ratio. Below 7.2 K, the peak intensities stay almost constant with temperature. As the position of the specular and GISANS peaks is not altered by temperature, this trend is interpreted as a shift of intensity from the GISANS peaks to the specular spot with decreasing temperature, which indicates a continuous decrease of magnetic fluctuations induced by a change in the domain structure.

In order to investigate the origin of this temperature dependence, $I_{\mathrm{spec}}(T)$ is compared with the temperature dependences of the zero-field cooled measured resistivity $\rho(T)$ and magnetization $M(T)$ of $\mathrm{SF_{high}}(1)$ in Fig. 7.2.

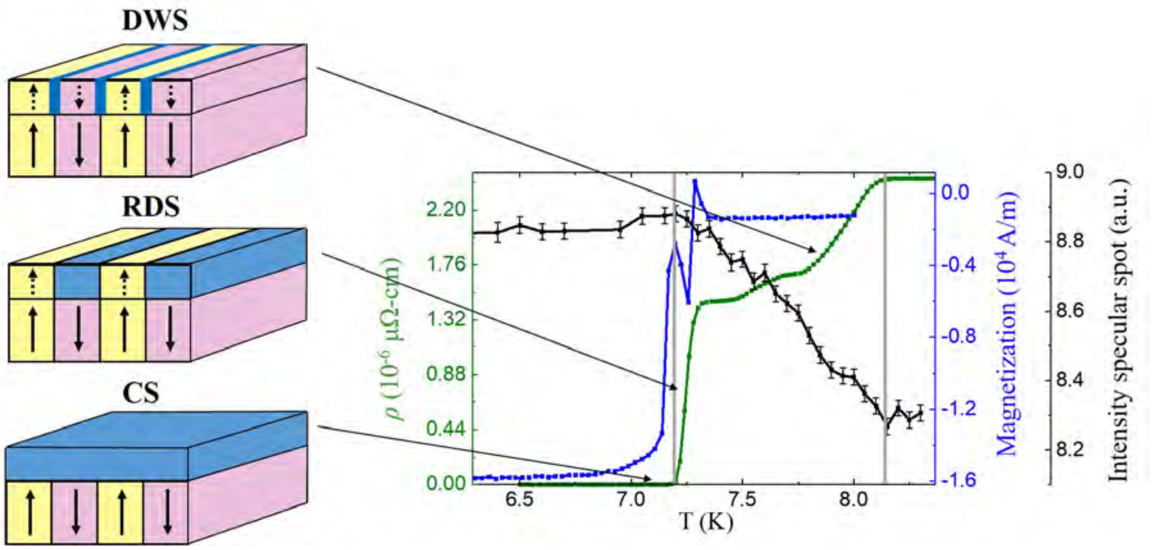

Figure 7.2: Sketch of DWS, RDS and CS formation in $\mathrm{SF}_{\mathrm{high}}(1)$ and the corresponding temperature dependences of ρ, M and I_{spec}.

The connection of the temperature steps in $\rho(T)$ with a change of the non-superconducting state to DWS and RDS, and the following complete superconducting state is indicated by arrows. The increase in I_{spec} with temperature (marked by grey vertical lines) corresponds well to the onset of DWS and the subsequent change into CS. The magnetization in zero field drops at the point of complete superconductivity due to a fully reached Meissner state. The average magnetization change due to the Meissner effect is in the range of $1{\cdot}10^4$ A/m and is much smaller than the inner field of the FePd magnetic domains with $M_{\mathrm{S}} = 1.9 \pm 0.2 \cdot 10^6$ A/m (s. table 9.8). This supports the assumption that the temperature dependence of I_{GIS} is caused by a decrease in the magnetic fluctuations of the FePd magnetic domains.

It is concluded that the shift of intensity from I_{spec} to I_{GIS} is caused by the onset of superconductivity, but is not simply related to the repulsion of magnetic stray fields due to the Meissner effect. It probably results from an inverse proximity effect between Nb and FePd which impacts on the orientation of magnetic moments inside FePd. To investigate the vector magnetization with dependence on temperature and how the magnetic domains are altered by the onset of DWS in detail, polarized GISANS measurements with polarization analysis are presented within the next section.

7.2 Vector magnetization

At the vSANS instrument, polarized GISANS measurements with polarization analysis are performed on $\mathrm{SF_{high}}(2)$ at temperatures of sensor B (see Fig. 4.14) of (i) $T_\mathrm{B} = (10.10 \pm 0.02)\,\mathrm{K} \gg T_\mathrm{c}$ and (ii) $T_\mathrm{B} = (5.60 \pm 0.02)\,\mathrm{K} \ll T_\mathrm{c}$. Similar to $\mathrm{SF_{high}}(1)$, $\mathrm{SF_{high}}(2)$ exhibits high PMA with a maze domain structure, $Q = 2.0 \pm 0.1$ and $T_\mathrm{c} = 6.958 \pm 0.001\,\mathrm{K}$ with stray-field generated DWS near T_c in zero applied field, which changes into CS at $\sim 6.9\,\mathrm{K}$ (see Fig. 6.6 in section 6.2.1).
The sample-to-detector distance in the relevant Q-range is 15.0 m, the neutron wavelength $\lambda = 8\,\mathrm{\AA}$ and the wavelength spread $\Delta\lambda/\lambda = 12\,\%$. After saturating the sample out-of-plane in $-1.5\,\mathrm{T}$, the field is ramped to $+2.6\,\mathrm{mT}$ which is used as guide field for the neutron polarization direction. By application of a guide field perpendicular to the sample surface, the out-of-plane oriented magnetic domains give rise to signals in the Non-Spin-Flip (NSF) channels, whereas closure domains and domain walls are probed in the Spin-Flip (SF) channels.

Figure 7.3 shows the Q_y-Q_z-maps at $T_\mathrm{B} = (10.10 \pm 0.02)\,\mathrm{K}$, the 2D detector measurements at $(5.60 \pm 0.02)\,\mathrm{K}$ are attached in the supplementary information in Fig. 9.17. In the two NSF intensity channels I^{++} and I^{--}, the peak around the specular spot and the GISANS peaks overlap and cannot be clearly distinguished. In contrast, the GISANS peaks in the I^{+-} and I^{-+} channels are well separated from the specular peak area and show an asymmetric intensity distribution: whereas in the I^{-+} channel the intensity of the right GISANS peak is more intense than the left one, this behaviour switches in the I^{-+} channel. The same effect is observed at $(5.60 \pm 0.02)\,\mathrm{K}$, but with an increased asymmetry in the GISANS peak intensities. The sample stage was slightly tilted during the GISANS measurements, visible as offset of the specular peak from the specular line and depicted in the supplementary in Fig. 9.16. Figures 7.3 and 9.17 show the corrected Q_y-Q_z-maps including a rotation angle of 4.7°.

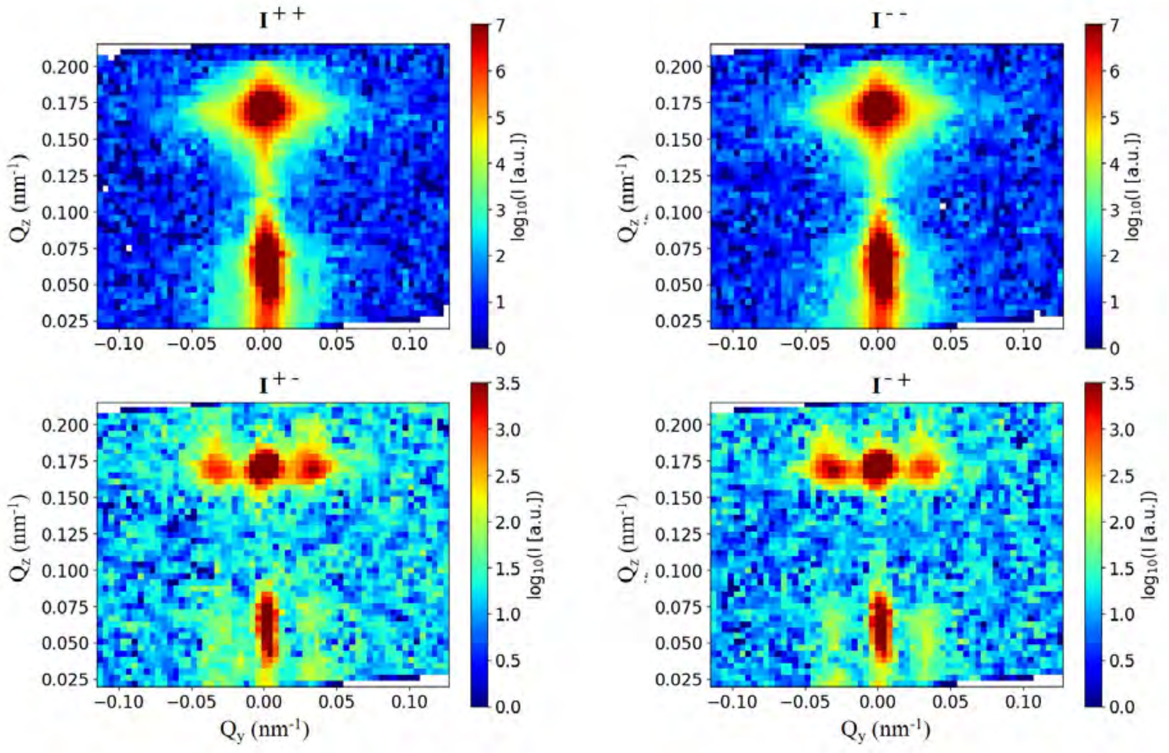

Figure 7.3: Q_y-Q_z-maps of the four different GISANS channels measured at $T_\mathrm{B} = (10.10 \pm 0.02)\,\mathrm{K}$ on $\mathrm{SF_{high}}(2)$ including a rotation angle of 4.7°.

A comparison of $I(Q_y)$ near the GISANS line at $Q_z = 0.17\mathrm{nm}^{-1}$ (integrated over a range of $Q_z = 0.137\,\mathrm{nm}^{-1} - 0.2\,\mathrm{nm}^{-1}$) of all four channels for the two measured temperatures is given in Fig. 7.4. As already observed for $\mathrm{SF_{high}}(1)$ in KWS-3, the GISANS peak position is independent of temperature. In the NSF channels, no temperature dependence of the peak intensities is obtained, whereas in the SF channels, the asymmetry between the left and right GISANS peaks, $\Delta I_{\mathrm{GIS,l\leftrightarrow r}}$, increases with decreasing temperature. The peak around the specular spot in the SF channels indicates a neutron polarization effiency $< 100\%$.

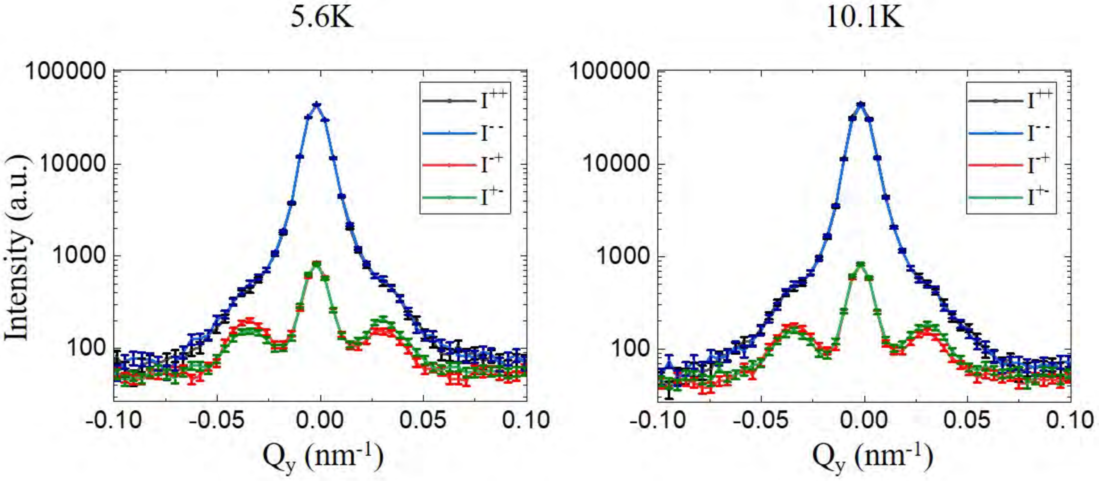

Figure 7.4: $I(Q_y)$ near the GISANS line at $Q_z = 0.17\text{nm}^{-1}$ a temperature of 5.6 K (left) and 10.10 K (right).

To analyse the Q_y-Q_z-maps with dependence on temperature and especially the asymmetry $\Delta I_{\text{GIS,l}\leftrightarrow\text{r}}$, first GISAXS experiments on SF$_{\text{high}}$(2) are scrutinized to determine the diffuse scattering from the layer interfaces which will give information on the peak widths around the specular spots. Second, the model constructed in section 3.2.4 for GISANS on maze domain structures including surface and interface roughnesses and a random distribution function for the domain positions is fit to the experiments.

GISAXS at room temperature on SF$_{\text{high}}$(2) is performed at the angle of total reflection and shown in Fig. 9.18(a) in the supplementary information. Provided that the peak around the specular spot can be approximated by a Voigt function, the FWHM γ of the Lorentzian part of this Voigt function will give the lateral correlation length defined by surface and interface roughnesses. The intensity on the GISAXS line, $I(Q_y)$, is plotted in Fig. 9.18(b). A fit of a Voigt function to $I(Q_y)$ yields $\gamma = 0.0066\,\text{nm}^{-1}$. The lateral correlation length $\xi_{\text{corr}} = \frac{2}{\gamma} = 300\,\text{nm}$ is taken as starting value for ξ_{corr} in the GISANS model. The observed high offspecular scattering together with the short correlation length of 300 nm compared to the sample size of $\sim\ 7 \times 10\,\text{cm}$ explains the high width of the peak around $Q_y = 0\,\text{nm}^{-1}$ in the NSF GISANS channels, which is given by a superposition of the specular peak and strong diffuse scattering from surface roughnesses. This leads to the overlap of the specular and GISANS peaks in Fig. 7.3 and may as well account for the missing T-dependence of I_{spec} and I_{GIS} in the NSF channels of SF$_{\text{high}}$(2) compared to SF$_{\text{high}}$(1) in section 7.1.

Before simulating the GISANS measurements within the DWBA, first the origin of $\Delta I_{\mathrm{GIS,l\leftrightarrow r}}$ has to be resolved and inserted into the model system. Grigoriev et al. [184] have investigated the helical magnetic structure of Dy/Y multilayers by means of the polarization dependent, asymmetric cross-section induced by a helical structure with a non-zero average chirality $\langle C \rangle$. Following [185], scattering cross-sections from helical structures compose into polarization-independent and polarization-dependent parts. The polarization dependent part is determined by a projection of the helix on the sample magnetization and gives rise to an asymmetric scattering part of $\frac{d\sigma}{d\Omega}$ if a non-zero component of $\vec{c}$ (propagation vector of the helix) exists parallel to the polarization $\vec{P}$ [184].

Here, a magnetic chirality is assumed to exist in the Bloch domain walls as sketched in Fig. 7.5 for FePd with high PMA but finite domain wall thickness w_{DW}. The helix propagates with constant handedness within one structural unit along the y-direction. The two Bloch domain walls consist of alternating magnetization in $\pm x$-direction, which resembles a zero net magnetization in the sample plane as no preferential direction due to any in-plane applied field was given during the measurement.

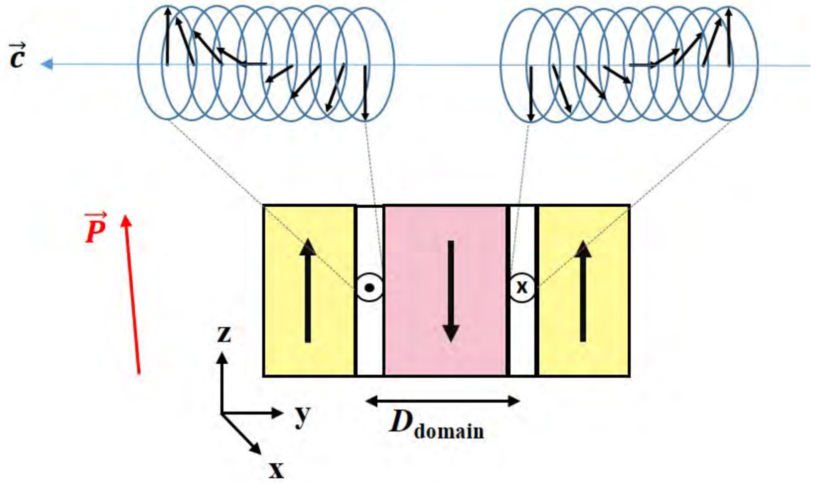

Figure 7.5: Sketch of the domain structure and Bloch domain wall chirality in the model used for the DWBA simulations of GISANS on $\mathrm{SF_{high}}(2)$. Displayed is one structural unit including two half up and one full down oriented magnetic domain as well as two Bloch domain walls. The red arrow denotes the direction of the beam polarization which is tilted by 4.7° with respect to $\vec{z}$ (rotation around the x-axis).

Based on the results of GISANS on a bare FePd layer in section 5.4.4, the DWBA including the paracrystal theory with a finite number of structural units N and a domain disorder parameter ω is inserted into the model. Additionally, following boundaries are considered to simulate the GISANS measurements of $\mathrm{SF}_{\mathrm{high}}(2)$:

- First, the measurements at $T > T_\mathrm{c}$ are fit to obtain information on the magnetic structure of FePd without proximity to a superconducting state. Second, based on these results the measurements at $T < T_\mathrm{c}$ are fit to investigate the influence of superconductivity on the magnetic state of FePd.

- All layer thicknesses are inserted as obtained from XRR in table 9.4, and an average interface roughness of 16 Å is taken from the XRR simulations using GenX.

- Following van der Laan et al. [22], the size of closure domains is inversely related to the strength of PMA. In section 5.4.4, a finite size and depth of closure domains was assumed to explain the stripe configuration of magnetic domains. Here, the maze domain structure and the higher Q value compared to the sample investigated in section 5.4.4 indicate small or no closure domains which are therefore neglected in the model for $\mathrm{SF}_{\mathrm{high}}(2)$.

- The domain wall width of a sample comprising uniaxial magnetocrystalline anisotropy is approximately given by $w_{\mathrm{DW}} = \pi\sqrt{\frac{A}{K_u}}$ [13]. For the FePd layer of $\mathrm{SF}_{\mathrm{high}}(2)$ with $A \sim 10^{-11}$ J/m [173] and $K_u = 1500\,\frac{\mathrm{kJ}}{\mathrm{m}^3}$ this yields $\sim 8\,\mathrm{nm}$.

- The MFM image of $\mathrm{SF}_{\mathrm{high}}(2)$ in Fig. 5.15(b) reveals a maze domain structure and indicates a correlation length of the magnetic domains smaller than the domain width: $L_x < D_{\mathrm{domain}}$. If the orientations of the small domain units are fully random, the average chirality $\langle C \rangle$ would become zero. However, the asymmetry $\Delta I_{\mathrm{GIS,l}\leftrightarrow\mathrm{r}}$ in the present model results from a non-zero $\langle C \rangle$, which indicates a finite angular range of domain orientations. This is further supported by a 2D-FFT analysis of the MFM image in Fig. 5.15(b) (see supplementary Fig. 9.19), which implies a superposition of randomly oriented domains together with a preferential direction of the domain units. The MFM measurement in Fig. 5.15(b) was performed with a scan-direction along one of the edges of the 1x1 cm^2 quadratic sample, which is as well the measurement direction of Q_y. The preferential direction of domain units obtained from the 2D-FFT analysis is either along an angle of 20° or 70° with respect to Q_y [1].

---

[1] Note 1: Unfortunately, it was not determined if the same sample edge for the MFM and GISANS measurements was taken. Note 2: It is assumed, that this preferential direction does not change by lowering the temperature below T_c

- From the MFM image also a disorder parameter in the order of the domain period itself is expected, different to the results of $\mathrm{F}_{\mathrm{high}}(2)$ is section 5.4.4.
- As explained above, the helical propagation vector $\vec{c}$ must obtain a component parallel to the neutron polarization $\vec{P}$. The helical Bloch domain walls propagate within the sample surface plane, whereas in the experiment, $\vec{P}$ was applied perpendicular to the sample surface. Two reasons may lead to a small component of $\vec{c}$ parallel to $\vec{P}$: (i) the tilt of 4.7° of the sample stage during the measurements and (ii) an incomplete rotation of the neutron polarization from the guide to the sample position and further to the detector, which is in detail explained below.

In vSANS, the neutron polarization in the guide from the source to the sample position is along the y-direction (same coordinate system as for the domain model in Fig. 7.5). Subsequently, $\vec{P}$ is turned from y to z by the electromagnet at the sample position and further to the x-direction in the detector guide. This is schematically shown in Fig. 7.6.

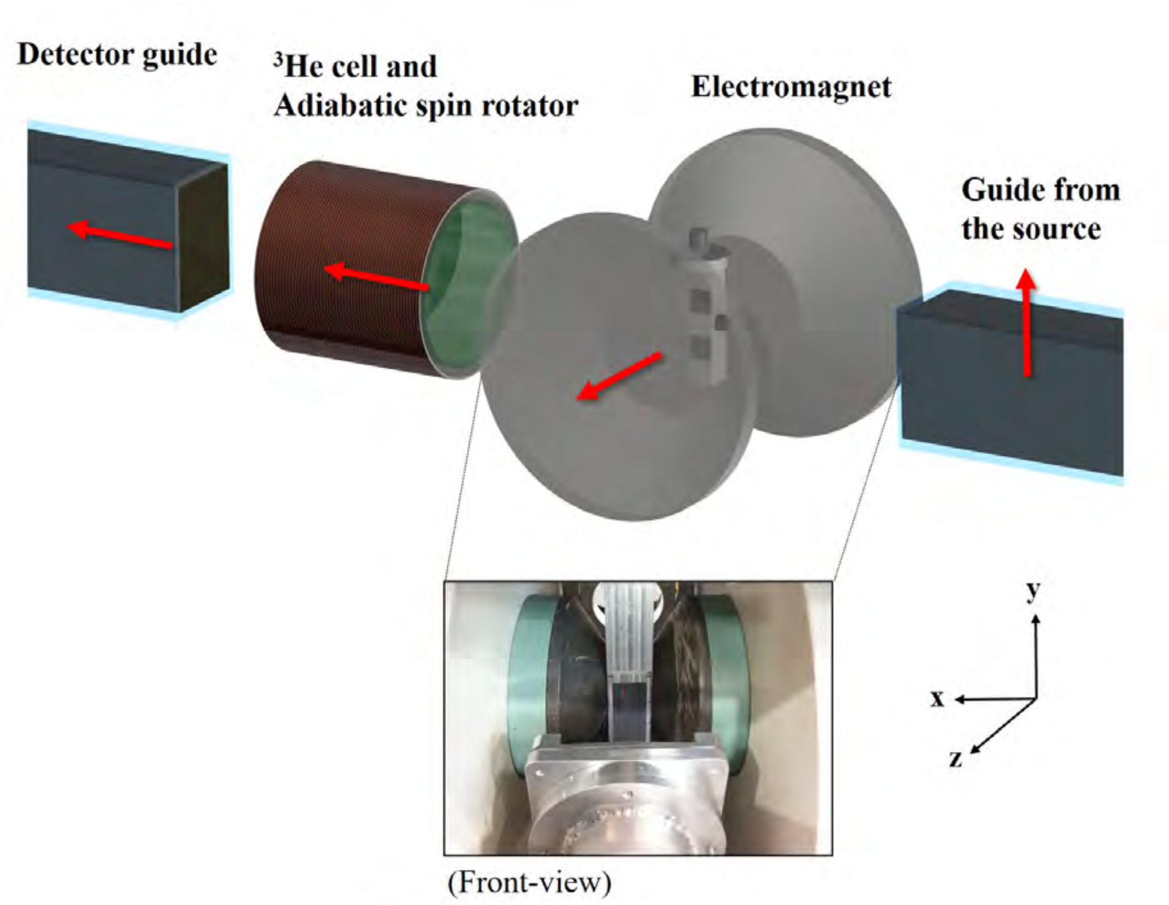

Figure 7.6: vSANS instrument setup and polarization direction in each compound as side-view, and a front-view on the inner part of the electromagnet including the pole-shoes, the cryoshield with the sample holder inside, and the exit of the neutron beam guide.

The guide field was set to 2.6 mT in z-direction and decreases rapidly with respect to the distance to the sample position due to the trapezoidal form of the pole shoes of the electromagnet. The remaining magnetic field strength in y-direction from the entrance neutron guide at the sample position is measured to 1.9 G. An additional small component of ~1.2 G in x-direction results from the ^{3}He analyzer solenoid behind the electromagnet. Although the inner coil should ensure an adiabatic rotation from z to x, the small guide field in z-direction and a large distance to the pole shoes of the electromagnet might lead to an incomplete polarization change on both sides, before and after the sample position[1].
A detailed analysis on the dependence of $\vec{P}$ on the guide field rotation is not part of this thesis, but can in future be simulated with the ray-tracing program VITESS.

---

[1] Personal communication with the NIST-NCNR scientists K. Krycka, J. A. Borchers, W. Chen, and S. M. Watson

Here, it is assumed that a small tilt of the sample surface with respect to the neutron incidence plane leads to a non-zero average component of $\vec{c}$ parallel to $\vec{P}$, which allows an investigation of the Bloch domain wall chirality. This premise is supported by the observation of $\Delta I_{\mathrm{GIS,l\leftrightarrow r}}$ in the SF, other than in the NSF channels, as only the SF channels probe the in-plane magnetic moments in the used measurement configuration.

7.2.1 Results at $T > T_\mathrm{c}$

Considering the above mentioned boundaries for the DWBA simulation, the best fitting results for all four channels of the polarized GISANS measurements at $T_\mathrm{B} = (10.10 \pm 0.02)\,\mathrm{K}$ are given by the parameters listed in table 9.11 in the supplementary information. Figure 7.7 shows the measured and simulated Q_y-Q_z-maps, as well as $I(Q_y)$ integrated over $Q_z = 0.137\,\mathrm{nm}^{-1} - 0.2\,\mathrm{nm}^{-1}$.

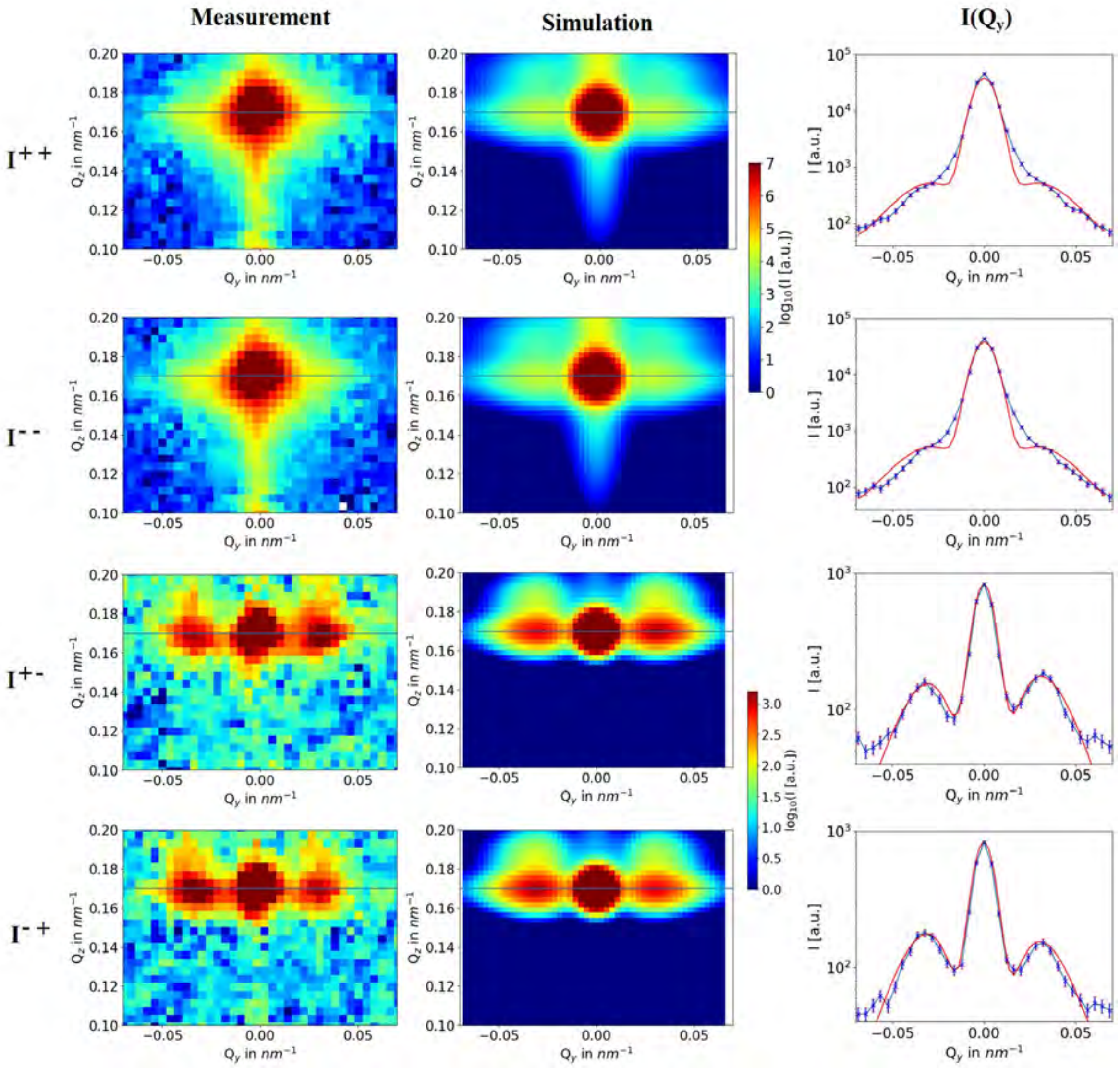

Figure 7.7: (Left) Measured Q_y-Q_z-maps, (middle) simulated Q_y-Q_z-maps, and (right) $I(Q_y)$ near the GISANS line of both Q_y-Q_z-maps for all four GISANS channels at $T_\mathrm{B} = (10.10 \pm 0.02)\,\mathrm{K}$.

An analysis of the simulated parameters and a comparison of the simulated and measured Q_y-Q_z-maps yields:

- The simulated domain period of $D_{\mathrm{Domain}} = (96 \pm 2)\,\mathrm{nm}$ is slightly smaller than $D_{\mathrm{domain}} = (110 \pm 10)\,\mathrm{nm}$ obtained by MFM, which can result from various magnetization cycles in between both measurements. Also, with MFM only the surface pattern in a small area of 3x3 µm is imaged, whereas with GISANS the whole FePd layer is probed.
- The domain wall width $w_{\mathrm{DW}} = (10 \pm 5)\,\mathrm{nm}$ is on the order of the calculated width of $\sim\ 7\,\mathrm{nm}$.
- The high FWHM of GISANS peaks in all four channels is reproduced by large values of the domain disorder parameter $\omega = (100 \pm 20)\,\mathrm{nm}$, which describes a random deviation of the domain position from its mean value (see section 3.2.4). This coincides with $D_{\mathrm{domain}} = (96 \pm 2)\,\mathrm{nm}$, and the above mentioned expectation is confirmed.
- The correlation length of the domain units in x-direction, $L_x = (60 \pm 10)\,\mathrm{nm}$, is smaller than the domain period and displays the maze structure with a high angular range $\Delta\xi$ of domain orientations.
- The peak shape around the specular spot in the simulated NSF channels does not reflect the measured peak shape. For the calculation, it is assumed that the offspecular scattering is given by a Hurst-parameter of 0.5 which yields a Lorentzian function [187]. This could in the future be improved by taking into account another Hurst-Parameter for the NSF peak around $Q_y = 0\,\mathrm{nm}^{-1}$.
- $\alpha = 30°$ appears to be quite large for the neutron polarization tilt with respect to the out-of-plane guide field and has to be checked in the future by VITESS simulations considering the instrument setup and 3D guide field information.
- The simulated range of $\Delta\xi$ as well as the average tilt angle ξ_{av} together strongly determine the GISANS peak position (via the effective domain width depending on the angle between ξ and the neutron incidence plane) and the strength of $\Delta I_{\mathrm{GIS,l}\leftrightarrow\mathrm{r}}$. Domain walls of units with $\xi = 90° - 270°$ possess an opposite direction of propagation $\vec{c}$ to units with $\xi = 270° - 90°$. If $\Delta\xi$ spans over both orientations of chirality, the average value $\langle C \rangle$ is reduced and less asymmetry is present in the GISANS simulations. As mentioned above, the preferential direction ξ_{av} is

assumed to be either 20° or 70° rotated with respect to Q_y. The closer ξ_{av} to 90° (and $\Delta\xi$ spanning over both orientations of chirality), the less is the GISANS peak asymmetry. Assuming $\xi_{\text{av}} = 20°$ leads to a higher asymmetry than obtained in the measurement in Fig. 7.4, and hence only values of ξ_{av} close to 70° are probed. A fine-tuning of the asymmetry in the simulated Q_y-Q_z-maps is then performed by varying $\Delta\xi$. The observed $\Delta I_{\text{GIS,l}\leftrightarrow\text{r}}$ is well reproduced by an intermediate ξ_{av} =70° and a broad angular range of $\Delta\xi = 240°$ spanning over both chirality orientations.

- It has to be noted, that the domain wall width w_{DW}, the domain period D_{domain}, the average rotation angle of simulated domain units ξ_{av}, and its range $\Delta\xi$ together define a special set of parameters for the GISANS peak position, asymmetry and intensity. In a first step, w_{DW} was chosen to be close to the theoretically determined value of 7 nm, and ξ_{av} close to 70°. All other parameters were optimized regarding these two values. In a second step, both w_{DW} and ξ_{av} were varied (and accordingly were the other parameters), until an optimum set of simulations for all four channels was obtained. Some examples of simulations with other parameter sets are given in Fig. 9.20.

Together, the results prove that the chosen domain model under consideration of the paracrystal theory and a maze domain structure can be used to investigate the domain wall character in ferromagnetic samples with PMA. The thicknesses of domain walls and out-of-plane domains can be investigated together due to (i) the chiral character of the Bloch domain walls and (ii) the measurement of both, in-plane and out-of-plane magnetic orientations by polarized GISANS with polarization analysis. An application of an in-plane guide field is proposed to investigate the domain wall chirality with better precision. Also, the easiest accessible domain configuration (FePd comprising high PMA) allows closure domains to be neglected. In further experiments, intermediate and low PMA samples would be an interesting research subject.

7.2.2 Results at $T < T_{\text{c}}$

In comparison to the simulations at $T > T_{\text{c}}$, here all values except the domain wall width are kept constant in order to examine if the increase in $\Delta I_{\text{GIS,l}\leftrightarrow\text{r}}$ with decreasing temperature results from an inverse proximity effect of the superconducting state on the domain wall structure of FePd. Figure 7.8 shows the measured and simulated Q_y-Q_z-maps and $I(Q_y)$ for $w_{\text{DW}} = 20\,\text{nm}$ instead of 10 nm as used for $T > T_{\text{c}}$.

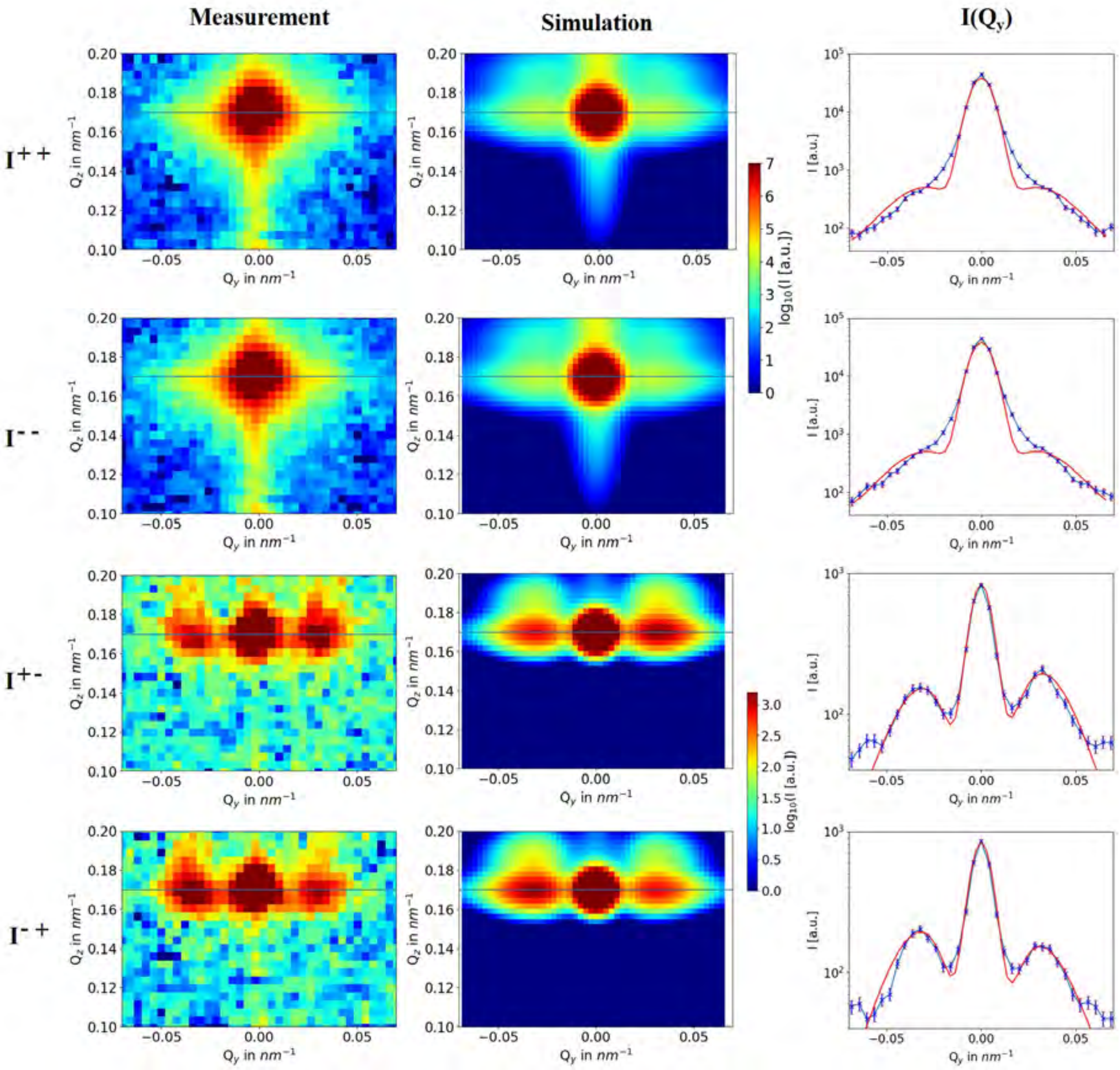

Figure 7.8: (Left) Measured Q_y-Q_z-maps, (middle) simulated Q_y-Q_z-maps, and (right) $I(Q_y)$ near the GISANS line of both Q_y-Q_z-maps for all four GISANS channels at $T_\mathrm{B} = (5.60 \pm 0.02)\,\mathrm{K}$.

No change is visible in the NSF channels, whereas in the SF channels the simulated $\Delta I_{\mathrm{GIS,l}\leftrightarrow\mathrm{r}}$ follows the trend of the measurements. Hence, the observed increase in the peak asymmetry is well described by an increase in w_DW from 10 nm to 20 nm as sketched in Fig. 7.9. By further testing possible w_DW, a maximum range of (20±5) nm is obtained for still fitting $I(Q_y)$.

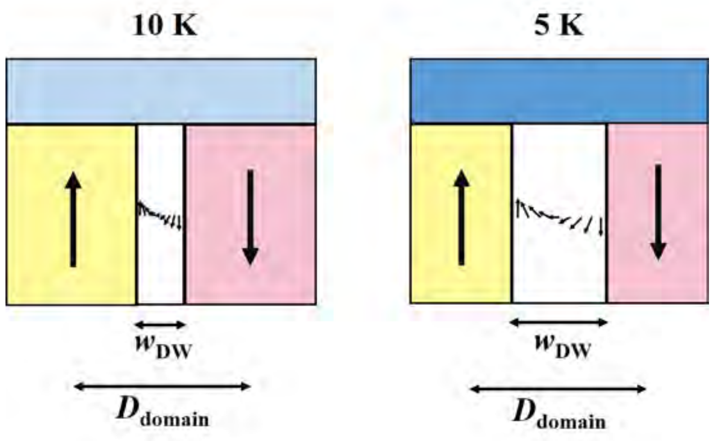

Figure 7.9: Sketch of the increase in domain wall width w_{DW} and constant domain period D_{domain} with decreasing temperature. Light blue color denotes the paramagnetic state of Nb, whereas dark blue denotes the superconducting state.

Typically the effect of ferromagnetism on superconductivity is strong due to the high Curie temperatures of most ferromagnets in comparison to T_{c} of low-T-superconductors like Nb, and the inverse effect is much less pronounced. Still, a modification of the ferromagnetic state due to the onset of superconductivity is possible [6]. Near the domain walls, the superconducting state obtains a higher T_{c} due to less magnetic stray field strength (as already discussed in section 6.2.1), which is the reason for the evolution of DWS in the here investigated high and medium PMA Nb/FePd heterostructures. The pair breaking effect is smaller in vicinity of the domain wall and it may be energetical more favorable to increase the domain wall size in comparison to the out-of-plane domains in order to stabilize the superconducting state. Following Buzdin [6], this effect is strongest if w_{DW} is similar to the superconducting coherence length, $w_{\mathrm{DW}} \sim \xi_{\mathrm{S}}$. In $\mathrm{SF}_{\mathrm{high}}(2)$, $w_{\mathrm{DW}} = 10\text{-}20\,\mathrm{nm}$ and $\xi_{\mathrm{GL},||}(0\,\mathrm{K}) = 9.6 \pm 0.1\,\mathrm{nm}$ (see table 9.10), which gives rise to the assumption that the described inverse proximity effect is feasible. Such a reorientation of magnetic moments by a broadening of the Bloch domain wall is reminiscent of the cryptoferromagnetic inverse proximity effect. As described in section 2.4, a reorientation of magnetic moments is favored if by such the average exchange field is reduced and leads to an energy minimization of the whole F/S system.

Another effect that may impact the magnetic domain structure is the nucleation of superconducting vortices in the Shubnikov phase of Nb. Di Giorgio et al. [101] have encountered a confinement of the vortex nucleation on top of only one domain orientation in Nb/Py bilayers depending on the applied field, as described in section 2.4.1. Due to the unknown value of B_{c1} for the transition of the Shubnikov into the Meissner phase in the here investigated Nb/FePd bilayers, a similar confinement effect can not be excluded, as B_{c1} decreases with the layer thickness d as described in section 2.2.4. Such an effect needs to be validated by low-temperature MFM measurements which allows a detection of magnetic vortices in the superconducting state. Without proximity effects, the vortices obtain a diameter of $2\xi_{\mathrm{GL},||}(T)$, which is smaller than the domain width in the FePd layer of $\mathrm{SF}_{\mathrm{high}}(2)$. An exchange between the in-plane oriented screening currents around such vortices with the magnetic moments inside FePd may lead as well to a broadening of the in-plane magnetic moments in the domain walls.

7.3 Conclusions

Although the Curie temperature of FePd ($T_{\mathrm{C}} = 723\,\mathrm{K}$) is much larger than T_{c} of Nb, two independent measurements on two different high-PMA Nb/FePd samples indicate a modification of the ferromagnetic state while lowering T below the superconducting critical temperature of Nb: (i) in $\mathrm{SF}_{\mathrm{high}}(1)$ the temperature dependence of unpolarized GISANS measurements clearly shows a decrease in magnetic fluctuations with decreasing temperature, and (ii) in $\mathrm{SF}_{\mathrm{high}}(2)$ simulations of polarized GISANS measurements with polarization analysis suggest an increase in the domain wall width by the onset of superconductivity. Such an increase in w_{DW} results in a lower volume of out-of-plane domains which in turn explains the observations of (i).

In summary, GISANS is proven to be sensitive to the inverse proximity effect in S/F bilayers. The temperature dependence of this inverse proximity effect correlates with the transition of Nb from the normal conducting state via the Domain-Wall-Superconductivity to the complete superconducting state.

Chapter 8

Conclusion and outlook

8.1 Summary of room- and low-temperature results

S/F proximity effects in thin film heterostructures of Nb/FePd with varying strength of PMA were investigated, addressing three main objectives: first, to accomplish a reproducible growth process for FePd with varying strength of PMA and a controllable lateral domain pattern; second, to acquire fundamental similarities and differences of the stray-field generated and direct proximity effects for systems exhibiting different strength of PMA by macroscopic resistivity and magnetization methods; third, to reveal the impact of superconductivity on the lateral magnetic depth profile of high-PMA FePd on the mesoscopic length scale by neutron scattering techniques. The implementation of a magnetic domain model including closure domains as well as domain walls by means of the DWBA was tested and proven to recover the measured GISANS images. Concluding results on these three ambitions follow.

(i) Before exploiting the S/F structures in the superconducting state at low temperatures, room-temperature characteristics were examined and a controllable growth of either high-PMA FePd with a maze domain structure, or medium- and low-PMA with a parallelly aligned domain formation was achieved. By a combination of codeposition and shuttered growth techniques, a parallel stripe domain pattern together with $Q > 1$ was realized. This stripe domain pattern transforms into a maze structure after saturation and can be retrieved by an in-plane demagnetizing oscillation. The strength of PMA, as well as the layer qualities were checked by several characterization techniques, which all comply with the given growth temperature and deposition technique. In a FePd layer comprising a stripe domain pattern, the lateral magnetic depth profile was successfully determined by fitting a model with triangular shaped closure domains at the layer surfaces of otherwise out-of-plane magnetic domains to unpolarized GISANS measurements at room-temperature. Together, the application of the paracrystal theory and a simulation of the domain bending allowed recovery of the measured data, including surface roughness effects and the shape of the GISANS peaks at higher Q_y.

(ii) Macroscopic magnetoresistance measurements revealed isolated domain-superconductivity as well as spin-triplet Cooper pair generation with $S_\mathrm{z} = \pm 1$ within one heterostructure system depending on the strength of anisotropy and the orientation of an external magnetic field. An extensive study including first a comparison of features observed in the S/F bilayers with respective S/I/F structures as well as bare S layers, and secondly, an examination of the relevant S and F length scales has been performed to identify stray-field and proximity effects.
Magnetotransport in the out-of-plane direction shows the existence of stray-field generated, isolated Domain-Wall- and Reverse-Domain-Superconductivity in all samples with $Q > 1$. This has been validated by theoretical models and indicates higher critical field values compared to conventional surface superconductivity due to a lower energy eigenvalue in the Ginzburg-Landau theory. Both high-PMA and low-PMA samples exhibit a 2D-superconducting behavior below saturation. This is related to a confinement of superconducting order parameters like ξ_GL and Λ.
Magnetotransport in the in-plane direction indicates a generation of spin-aligned triplet Cooper pairs with $S_\mathrm{z} = \pm 1$ predominantly for low PMA and $Q < 1$ with a maximum density at the coercive field as a result of the non-collinear magnetic configuration. The resulting high change in critical temperature $\Delta T_\mathrm{c} = \sim 100\,\mathrm{mK}$ in such a bilayer motivates further studies on respective F/S/F′ trilayer systems. The existence of LRTC in samples of higher anisotropy is inferred but needs to be further elaborated.

(iii) Two independent GISANS measurements on two Nb/FePd bilayers with high PMA reveal a change in magnetic fluctuations inside the domains while lowering T below T_c. Unpolarized temperature-dependent GISANS shows a reduction of magnetic fluctuations with decreasing temperature. This is related to a decrease in the out-of-plane domain volume alongside an increase in the domain wall width, which is validated by polarized GISANS measurements with polarization analysis above and below T_c. Such an inverse proximity effect changing the FePd domain state cannot be revealed by macroscopic magnetization due to the zero net magnetization. Polarized GISANS therefore proves to be a powerful tool to scrutinize inverse proximity effects of superconducting layers on domain structured ferromagnetic thin films. Additionally, it is demonstrated that the change of magnetic domain configuration correlates with the temperature range of DWS and RDS, before the complete superconducting state is reached.

8.2 Scope of future work

The field of proximity effects and a controllable superconducting state by a ferromagnetic template in S/F heterostructures is still the focus of current research. This work imparts an insight into the interplay between stray-field, direct, and inverse proximity effects. Following is a short outlook regarding three different promising future projects.

GISANS on Nb/FePd with varying PMA

It is proposed to perform subsequent experiments with polarized GISANS and polarization analysis on domain structured Nb/FePd with an in-plane neutron polarization to confirm the predicted strong inverse proximity effects. Using an in-plane polarization state, GISANS is fully sensitive to the in-plane oriented Bloch domain wall chirality. Measurements on intermediate- and low-PMA samples by GISANS will further complete this study and help to gain a better understanding of the inverse proximity effects in samples comprising DWS as well as long-ranged spin-triplet Cooper pairs. Taking advantage of the parallel alignment of magnetic domains in intermediate- and low-PMA Nb/FePd, such experiments allow a more straightforward simulation with fewer parameters. Finally, also a comparison study on S/I/F heterostructures with high and low PMA using polarized GISANS is recommended. A neutron experiment proposal regarding an in-plane polarization state is already confirmed but needed to be rescheduled due to the current epidemic situation.

It should be noted that magnetic hysteresis experiments at low temperatures show a strong dependence of a lower critical field on the proximity coupling. A comparison of hysteresis measurements of samples $\mathrm{SF_{high}}(1)$, $\mathrm{SIF_{high}}(1)$, and the bare S layer S(2) of similar Nb thicknesses ranging between 39 nm-41 nm and the same Nb growth procedures is given in Fig. 8.1. Whereas both the bare S layer and the proximity coupled $\mathrm{SF_{high}}(1)$ display a nearly zero lower critical field and a direct transformation to the Shubnikov phase, the comparison $\mathrm{SIF_{high}}(1)$ sample with an additional MgO insulating interlayer shows a clear change in the lower critical field value. The same effect is observed for the low-PMA samples $\mathrm{SF_{low}}(1)$ and $\mathrm{SIF_{low}}(1)$. This interesting behavior could be related to a superposition of effects from an incomplete Meissner effect due to $\Lambda(0\,\mathrm{K}) > \mathrm{d}$ and magnetic stray fields from the FePd domain structure and thus needs to be further investigated. The strong difference in the lower critical field can significantly alter results from polarized GISANS measurements in guiding field on S/F and S/I/F samples and should be considered during such experiments.

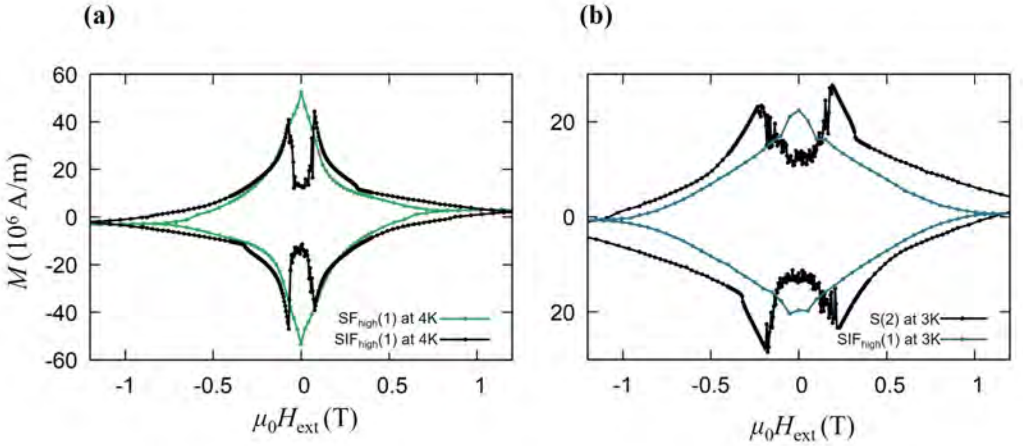

Figure 8.1: $M(H_{\mathrm{ext},\perp})$ of (a) $\mathrm{SF}_{\mathrm{high}}(1)$ and its comparison sample $\mathrm{SIF}_{\mathrm{high}}(1)$ at $T = 4\,\mathrm{K}$ and (b) S(2) and $\mathrm{SIF}_{\mathrm{high}}(1)$ at $T = 3\,\mathrm{K}$. The Nb layers of all displayed samples exhibit similar layer thicknesses.

Evidence for the origin of the observed effects in an increased H_{c1} value of $\mathrm{SIF}_{\mathrm{high}}(1)$ could be provided by performing low-temperature MFM measurements which reveal the superconducting state being either in the Meissner or the Shubnikov phase.

Magnetotransport in F/S/F′ trilayers of FePd/Nb/FePd

Macroscopic magnetotransport measurements indicate an intriguing relationship between stray-field generated domain-superconductivity and the occurrence of spin-triplet Cooper pairs. Scrutinizing the angular dependence of the magnetotransport in samples of varying PMA is promising for novel studies of the interplay between two major effects arising in S/F-structures: stray-field and direct proximity effects. The existence of spin-triplet Cooper pairs can be verified, for example, by low-temperature scanning tunnelling spectroscopy. Due to the additive pair breaking effect by two interfaces between Nb and the laterally inhomogeneous domain structured FePd, an even higher ΔT_{c} may be gained by engineering a respective F/S/F′ device.

Due to the amorphic growth of Nb on FePd, a seed for the epitaxial growth of the upper F layer of such a F/S/F′ heterostructure is needed. It is proposed to test a growth process as schematically drawn in Fig. 8.2: after growing the first, epitaxial FePd layer, it can be etched partially so that the subsequently grown Nb and the second FePd layer still grow locally on the Pd buffer which shall reinforce an epitaxial growth of the upper FePd layer.

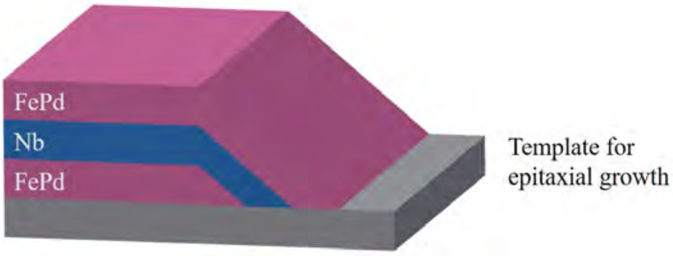

Figure 8.2: Trilayer structure enforcing an epitaxial growth of both the lower and upper FePd layers by the bottom template (here Pd).

DWS and spin-triplet Cooper pair generation in HTS/FePd

Modern developments show the great potential of superconducting spintronic devices based on the more robust high-temperature superconductors (HTS) like $YBa_2Cu_3O_7$ (YBCO) to ferromagnetic or ferromagnetic-insulating materials [1, 188, 189]. The results presented in this thesis on the low-temperature superconductor Nb in proximity to FePd can be applied to equivalent structures using YBCO instead of Nb. Two central aspects have to be considered for a successful study on the depth-dependent magnetic correlations near the interface of YBCO and FePd: (i) the epitaxial growth of YBCO/FePd bilayers with smooth surface and interface roughnesses allowing GISANS measurements, and (ii) the much shorter superconducting coherence lengths of YBCO with $\xi_{\mathrm{ab}}(0\mathrm{K}) \sim 1.6\,\mathrm{nm}$ and $\xi_{\mathrm{c}}(0\mathrm{K}) \sim 0.2 - 0.3\,\mathrm{nm}$ [190].

(i) Following [191], superconducting perovskite $YBa_2Cu_3O_7$ films require substrate temperatures of $\sim 800°\mathrm{C}$ and obtain lattice constants of $a = 3.823\,\text{Å}$, $b = 3.88\,\text{Å}$, and $c = 11.68\,\text{Å}$. The in-plane lattice constants of perovskite YBCO fit well to the tP4 unit cell lattice constants of FePd with $a = b = 3.849\,\text{Å}$ [169]. However, Fe is very volatile under application of elevated temperatures. For a successful growth of YBCO and FePd bilayers a heterostructure system of FePd/$YBa_2Cu_3O_7$/STO/MgO is suggested, with STO as buffer layer on a MgO(001) substrate[1]. The superconducting state of YBCO is highly sensitive to its oxidation state [192], which therefore needs to be checked after the subsequent growth of FePd.

---

[1] Personal communication with M. Hussein and M. Faley from Forschungszentrum Jülich GmbH

(ii) Essential for the occurence of proximity effects in S/F heterostructures are the characteristic S and F length scales, here the coherence length of YBCO and the domain and domain wall sizes of FePd. Due to the very short coherence lengths in YBCO, one would expect mostly a stray-field modulated superconductivity rather than a proximity effect [188]. Nonetheless, several research groups detected a long-ranged proximity effect in YBCO coupled to a ferromagnet or a ferromagnetic insulator [115, 189, 193, 194]. Possible reasons suggested by Peña et al. [193] are: (i) the d-wave superconducting nature of YBCO with midgap states along the <110> surface planes [104] where quasiparticles can tunnel over long distances; (ii) domain walls in a half-metallic ferromagnet in which the two electrons of a spin-singlet Cooper pair penetrate into F along opposite sites of the domain wall if $w_{\mathrm{DW}} < \xi$; and (iii) due to the generation of spin-triplet Cooper pairs which was predicted to cause long-range proximity effects in $La_{2/3}Ca_{1/3}MnO_3$/(100)$YBa_2Cu_3O_{7-\delta}$ [115]. HTS/F heterostructures are a highly topical issue and an application of knowledge gained in this thesis to YBCO/FePd bilayers seems a promising future project to contribute to the current fundamental research on S/F proximity effects.

Chapter 9

Supplementary information

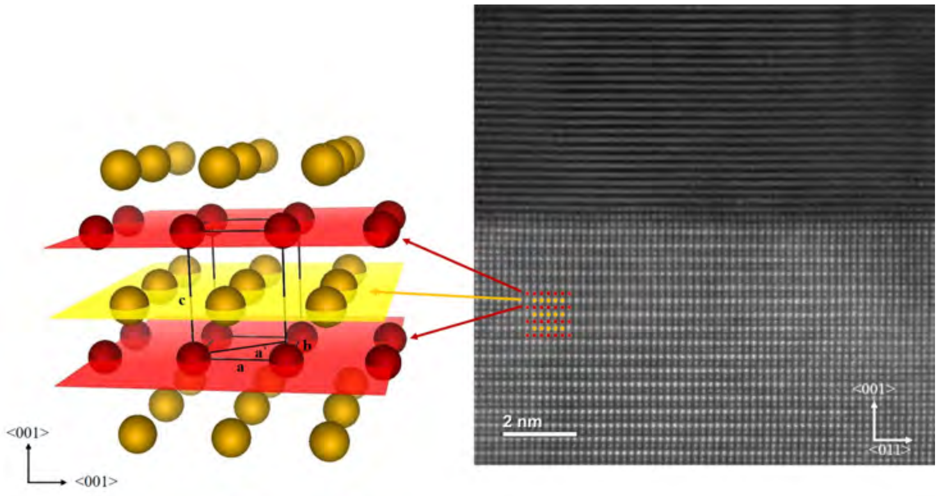

Figure 9.1: (Left) $L1_0$-ordered phase with an atomic monolayer growth of the two materials in the compound. (Right) HAADF-STEM measurement of the Nb/FePd interface in $SF_{mid}(1)$ with an overlay of the tP4 unit cell of $L1_0$-ordered FePd with Fe and Pd marked as red and yellow dots. In the HAADF-STEM image, the in-plane <011> crystalline direction of the FePd tP2 unit cell as shown on the right is displayed, which corresponds to the <100> direction of the tP4 unit cell.

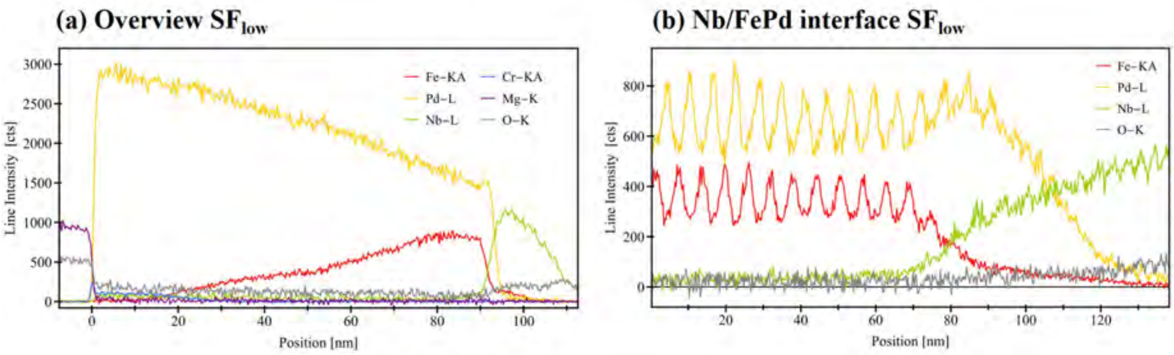

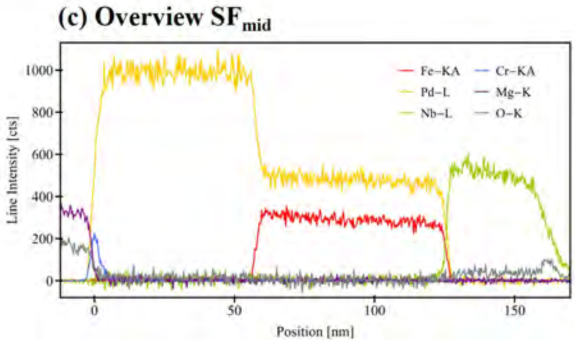

Figure 9.2: (a) EDX line-profile through the depth of the heterostructure of SF$_{\text{low}}$(1), showing a diffusion of Fe deep into the Pd layer. Only the first 20 nm of the Pd layer are free of Fe which can be seen in the HAADF-STEM images in 9.4. Also a high oxygen content of ∼25% in comparison to the Nb content is revealed in the Nb layer. (b) EDX line-profile in out-of-plane direction at the Nb/FePd interface shows a monolayer-by-monolayer growth of L1$_0$-ordered FePd. (c) The EDX line-profile through the depth of the heterostructure of SF$_{\text{mid}}$(1). In contrast to SF$_{\text{low}}$(1), the Pd and FePd layers obtain sharp interfaces and only little interdiffusion between each layer of the heterostructure. The oxygen content inside Nb amounts to ∼10% in comparison to Nb.
Colors are indicated in the legend.

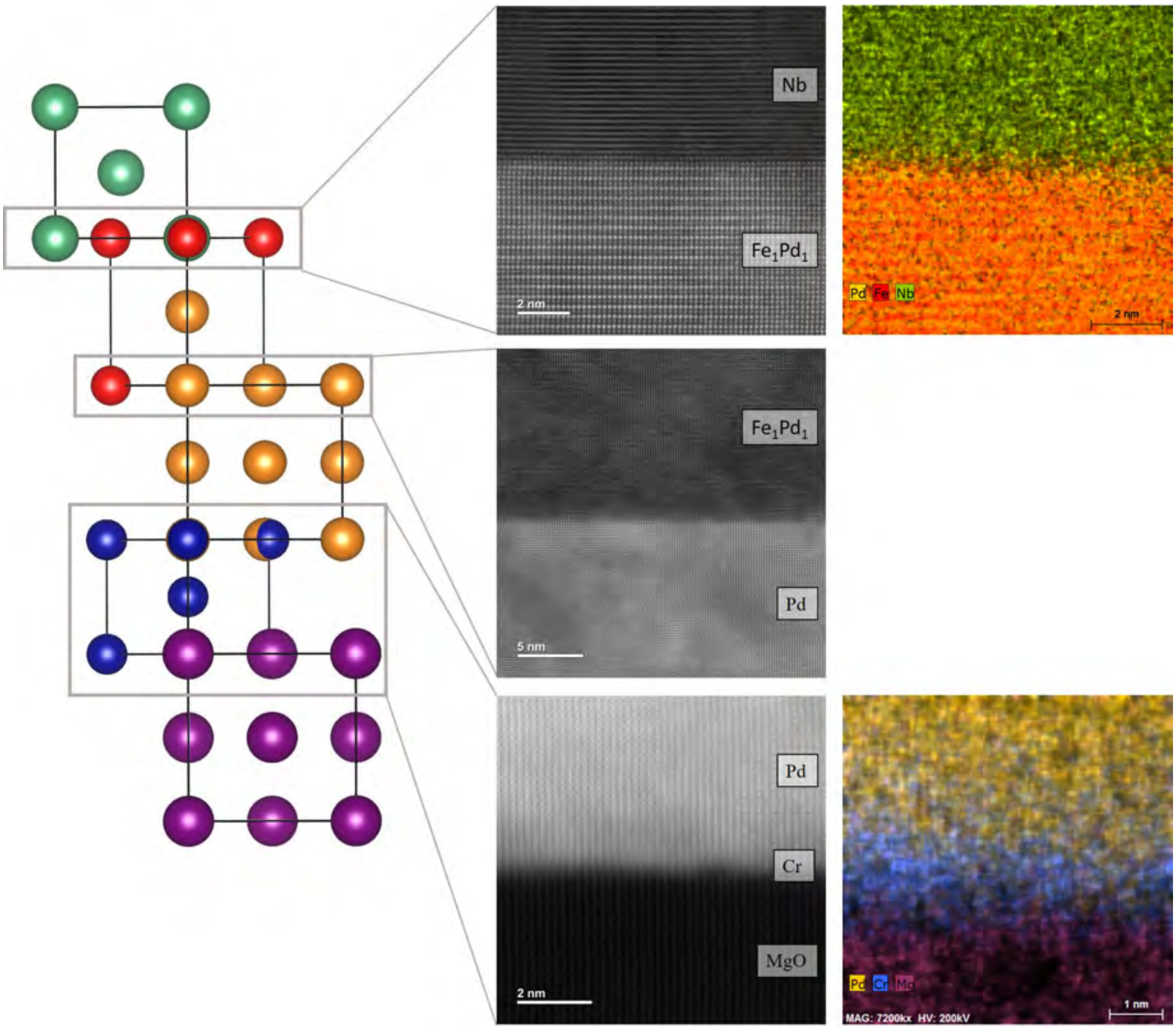
Nb
Fe1Pd1
2 nm
Pd Fe Nb
2 nm
Fe1Pd1
Pd
5 nm
Pd
Cr
MgO
2 nm
Pd Cr Mg
MAG: 7200kx HV: 200kV
1 nm

Figure 9.3: Sample stack of S/F samples (left) and HAADF-STEM measurements of $SF_{mid}(1)$ (middle). The measurements reveal an epitaxial growth of Pd and FePd. The Nb layer acquires an out-of-plane order but in the in-plane direction, the structural order is missing which leads to lines in the STEM measurement. STEM EDX-elemental maps are shown on the right and prove the existence of (i) a thin Cr layer between MgO and Pd, (ii) the monolayer structure of the $L1_0$-ordered FePd phase, and (iii) that the atomic diffusion at the Nb/FePd interface is limited to a few monolayers.
Colors are indicated in the legend.

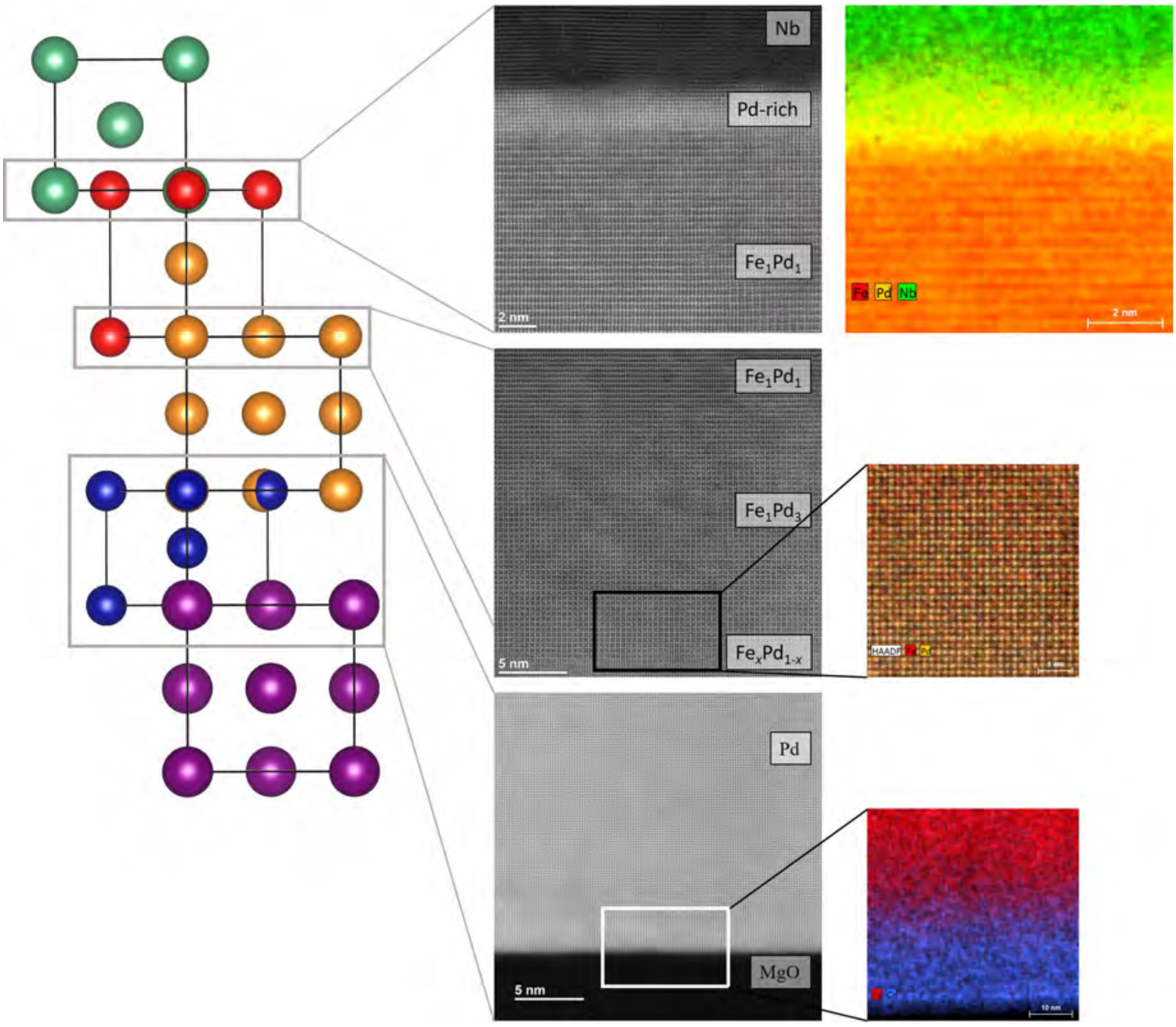
Nb
Pd-rich
Fe1Pd1
2 nm
Fe Pd Nb
2 nm
Fe1Pd1
Fe1Pd3
FexPd1-x
5 nm
HAADF Fe Pd
Pd
MgO
5 nm
10 nm

Figure 9.4: Sample stack of S/F samples (left) and HAADF-STEM measurements of $\mathrm{SF_{low}}(1)$ (middle). The high substrate temperature of $\mathrm{SF_{high}}$ with $T_\mathrm{s} = 820\,\mathrm{K}$ has lead to an interdiffusion of the FePd and Pd layers. Nearly defect-free Pd is grown in the vicinity of MgO which subsequently mixes with Pd; forming first a $\mathrm{Fe}_x\mathrm{Pd}_{1-x}$ layer with a small amount of Fe; and in a second step a $\mathrm{Fe_1Pd_3}$ layer, which can be revealed by the STEM-EDX elemental map on the right. Near the FePd/Nb interface, the $\mathrm{L1_0}$-ordered phase of $\mathrm{Fe_1Pd_1}$ is established. Colors are indicated in the legend.

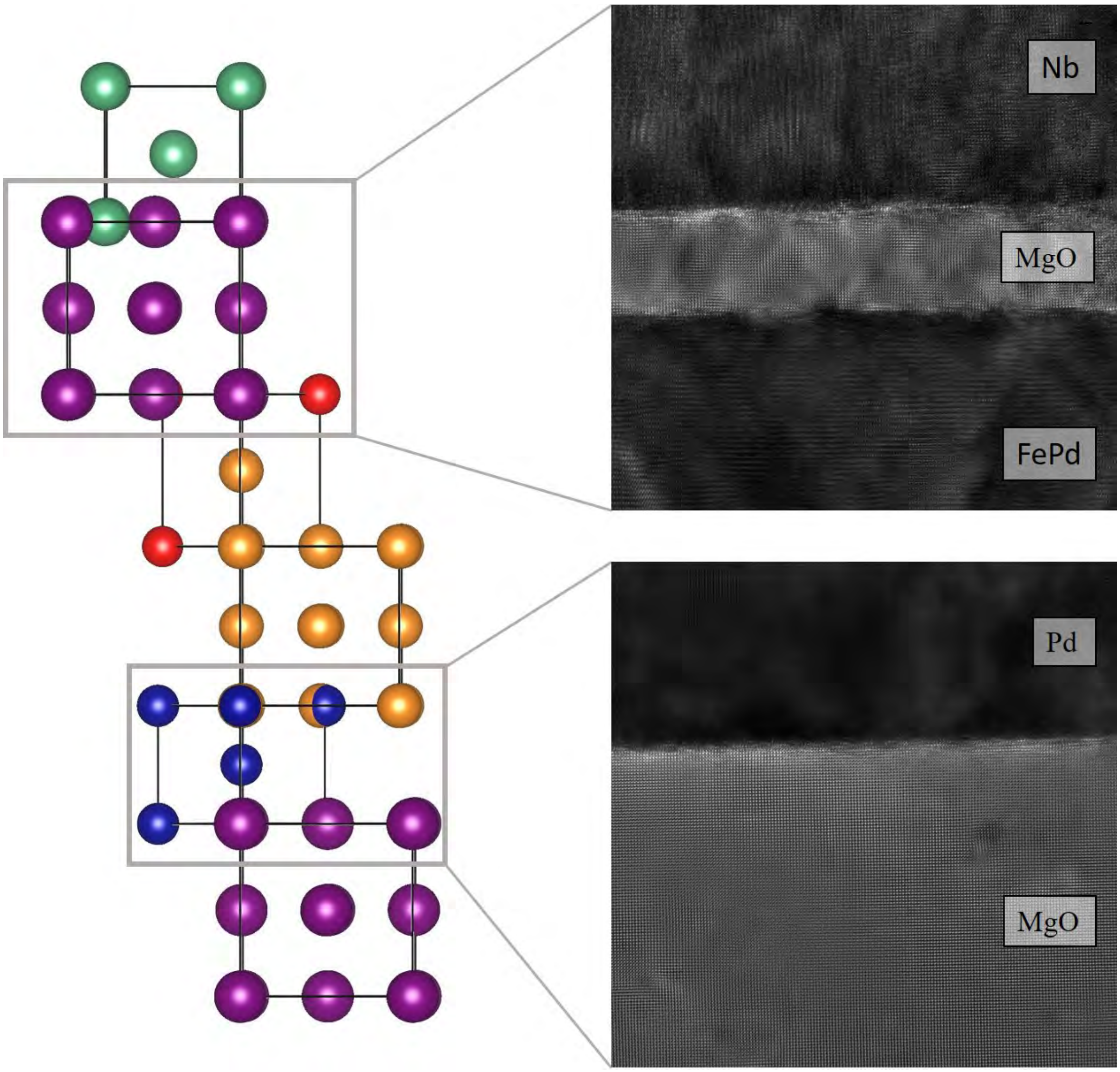

Figure 9.5: Sample stack of S/I/F samples (left) and STEM measurements of $\mathrm{SIF_{high}}(1)$ (right). Different to the HAADF-STEM measurements, here the sample was not thinned by FIB preparation as much as samples $\mathrm{SF_{mid}}(1)$ and $\mathrm{SF_{low}}(1)$. The epitaxy cannot be proven here due to the high sample thickness. Still it can be seen that the FePd and Nb layers are well separated by a thin MgO interlayer. Some structural defects are present also in the annealed MgO substrate.

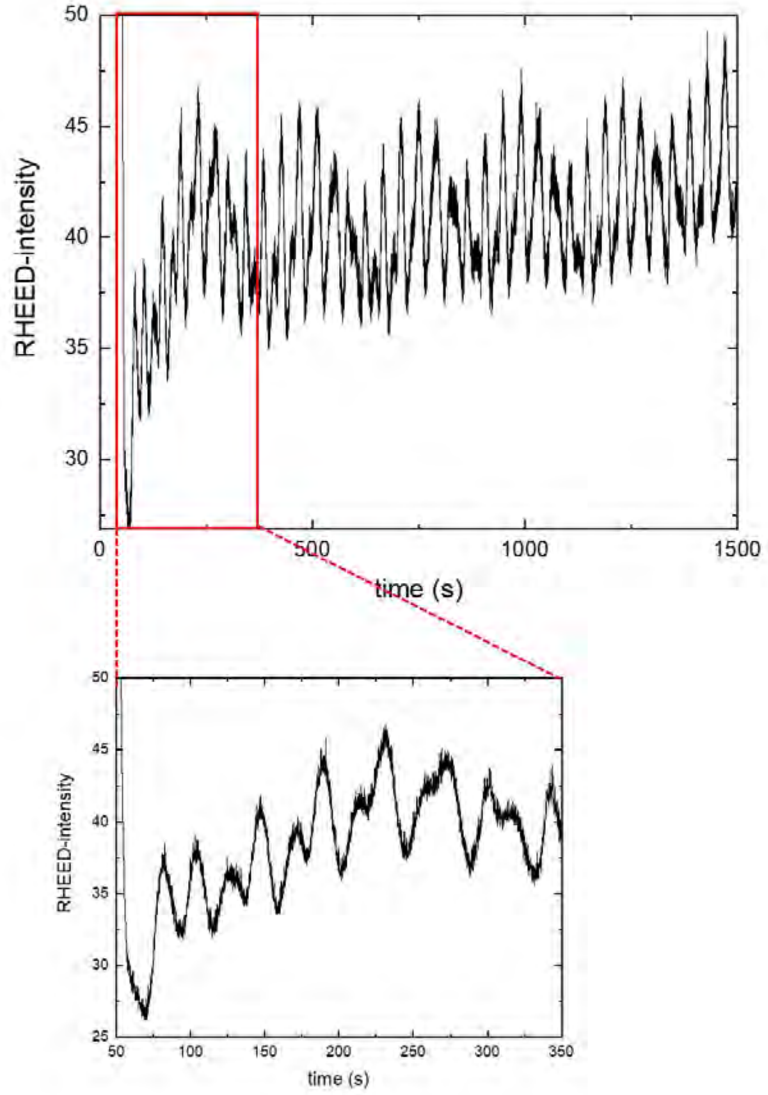

Figure 9.6: RHEED oscillations during the growth of shuttered FePd in sample $F_{\mathrm{mid}}(1)$ at room temperature.

Sample	OMBE Number	Layer	T_S (K)	T_ann (K)	t_ann (s)	deposition method	Δf (cells) or r (EBV)	t_dep (cells) or $\mathrm{d}_\mathrm{Multi1}$ (EBV)	d (nm)	Δd
$\mathrm{F}_\mathrm{high}(1)$	0497	Cr	RT			EBV	r=1.5Å/s	0.2	3	0.5
		Pd	RT	723	1800	cells	Δf_Pd=-1.5 Hz/s	4500 s	59	2
		FePd (cod.)	500			cells cells	Δf_Fe=-0.51 Hz/s Δf_Pd=-1.1 Hz/s	2700 s	54	2
		Pd-cap	500			cells	Δf_Pd=-1.1 Hz/s	235 s	1	0.1
$\mathrm{F}_\mathrm{high}(2)$	0478	Cr	RT			EBV	r=1.5Å/s	0.25	4	0.5
		Pd	RT	723	1800	EBV	r=0.2Å/s	6.0	47	2
		FePd (cod.)	500			EBV EBV	r=0.2Å/s r=0.2Å/s	2.5	38	2
		Pd-cap	500			EBV	r=0.2Å/s	0.25	1.5	0.1
$\mathrm{F}_\mathrm{high}(3)$	0505	Cr	RT			EBV	r=1.5Å/s	0.2	2	0.5
		Pd	RT	723	1800	cells	Δf_Pd=-1.488 Hz/s	4536 s	62	5
		FePd (cod.)	500			cells cells	Δf_Fe=-0.514 Hz/s Δf_Pd=-1.1 Hz/s	2700 s 235 s	55	2
		Pd-cap	500			cells	Δf_Pd= Hz/s		3	0.5
$\mathrm{F}_\mathrm{high}(4)$	0507	Cr	RT			EBV	r=1.5Å/s	0.2	2	1
		Pd	RT	723	1800	cells	Δf_Pd=-0.765 Hz/s	8953 s	65	5
		FePd (cod.)	500			cells cells	Δf_Fe=-0.267 Hz/s Δf_Pd=-0.59 Hz/s	5400 s	54	2
		Pd-cap	500			cells	Δf_Pd=-0.55 Hz/s	470 s	2	0.5

Table 9.1: Growth parameters of Nb/FePd samples and respective layer thicknesses as determined from XRR and TEM.

Sample	OMBE Number	Layer	T_S (K)	T_ann (K)	t_ann (s)	deposition method	Δf (cells) or r (EBV)	t_dep (cells) or $\mathrm{d}_\mathrm{Multi1}$ (EBV)	d (nm)	Δd
$\mathrm{F}_\mathrm{low}(1)$	0512	Cr	RT			EBV	r=1.5Å/s	0.2	1	0.5
		Pd	RT	723	1800	cells	Δf_Pd=-1.23Å/s	5350 s	60	1
		FePd (sh.)	RT			cells cells	Δf_Fe=-0.515Å/s Δf_Pd=-1.17Å/s	19 s·110 19 s·110	39	1
		Pd-cap	RT			cells	Δf_Pd=-1.1 Å/s	200 s	1	0.5
$\mathrm{F}_\mathrm{low}(2)$	0513	Cr	RT			EBV	r=1.5Å/s	0.2	1	0.5
		Pd	RT	723	1800	cells	Δf_Pd=-1.1Å/s	3300 s	62	1
		FePd (sh.)	RT			cells cells	Δf_Fe=-0.49Å/s Δf_Pd=-0.92Å/s	19 s·110 21 s·110	37	1
		Pd-cap	RT			cells	Δf_Pd=-0.92Å/s	200 s	2	0.5
$\mathrm{F}_\mathrm{low}(3)$	0538	Cr	RT			EBV	r=1.5Å/s	0.2	2	0.5
		Pd	RT	723	1800	cells	Δf_Pd=-0.908Å/s	7450 s	56	5
		FePd (sh.)	RT			cells cells	Δf_Fe=-0.922Å/s Δf_Pd=-0.426Å/s	19 s·110 21 s·110	37	5
		no cap								

Table 9.2: Growth parameters of Nb/FePd samples and respective layer thicknesses as determined from XRR and TEM.

Sample	OMBE Number	Layer	T_{S} (K)	T_{ann} (K)	t_{ann} (s)	deposition method	Δf (cells) or r (EBV)	t_{dep} (cells) or d_{Multi1} (EBV)	d (nm)	Δd
$F_{\text{mid}}(1)$	0514	Cr	RT			EBV	r=1.5Å/s	0.2	1	0.5
		Pd	RT	723	1800	cells	Δf_{Pd}=-0.927Å/s	7800 s	69	10
		FePd (sh.)	RT			cells cells	Δf_{Fe}=-0.492Å/s Δf_{Pd}=-0.92Å/s	19 s·110 21 s·110	37	5
		FePd (cod.)	500			cells cells	Δf_{Fe}=-0.416Å/s Δf_{Pd}=-0.89Å/s	1958 s	31	5
		Pd-cap	500			cells	Δf_{Pd}=-0.89Å/s	230 s	2	0.5
$F_{\text{mid}}(2)$	0525	Cr	RT			EBV	r=1.5Å/s	0.2	1	0.5
		Pd	RT	723	1800	cells	Δf_{Pd}=-0.906Å/s	8100 s	70	10
		FePd (sh.)	RT			cells cells	Δf_{Fe}=-0.493Å/s Δf_{Pd}=-0.92Å/s	19 s·110 21 s·110	36	5
		FePd (cod.)	500			cells cells	Δf_{Fe}=-0.422Å/s Δf_{Pd}=-0.92 Å/s	2100 s	34	5
		Pd-cap	500			cells	Δf_{Pd}=-0.92 Å/s	230 s	2	0.5
$F_{\text{mid}}(3)$	0526	Cr	RT			EBV	r=-1.5Å/s	0.2	1	0.5
		Pd	RT	723	1800	cells	Δf_{Pd}=-0.925Å/s	7900 s	63	10
		FePd (sh.)	RT			cells	Δf_{Fe}=-0.492Å/s	19 s·110	36	5
		FePd (cod.)	500			cells cells	Δf_{Pd}=-0.927Å/s Δf_{Fe}=-0.42Å/s	21 s·110 2100 s	34	5
		Nb-cap	RT			cells cells	Δf_{Pd}=-0.93Å/s r=0.7 Å/s	0.2	5	1

Table 9.3: Growth parameters of Nb/FePd samples and respective layer thicknesses as determined from XRR and TEM.

Sample	OMBE Number	Layer	T_S (K)	T_{ann} (K)	t_{ann} (s)	deposition method	Δf (cells) or r (EBV)	t_{dep} (cells) or d_{Multi1} (EBV)	d (nm)	Δd
$SF_{high}(1)$	0550	Cr	RT			EBV	r=1.5Å/s	0.2	1	0.5
		Pd	RT	723	1800	cells	Δf_{Pd}=-0.895Å/s	7550 s	60	10
		FePd (cod.)	670			cells cells	Δf_{Fe}=-0.413Å/s Δf_{Pd}=-0.893Å/s	3100 s	50	5
		Nb	320			EBV	r=1.0Å/s		40	5
		Pd-cap	RT			cells	Δf_{Pd}=-0.88Å/s	200 s	5	2
$SF_{high}(2)$	0622	Cr	RT			EBV	r=1.45Å/s	0.066	1	0.5
		Pd	RT	623	1800	cells	Δf_{Pd}=-0.901Å/s	7840 s	60	10
		FePd (cod.)	670			cells cells	Δf_{Fe}=-0.415Å/s Δf_{Pd}=-0.897Å/s	3090 s	44	5
		Nb	320			EBV	r=0.6-2Å/s		39	5
		Pd-cap	RT			cells	Δf_{Pd}=-0.89Å/s	150 s	2	1
$SF_{low}(1)$	0567	Cr	RT			EBV	r=1.5Å/s	0.2	1	0.5
		Pd	RT	723	1800	cells	Δf_{Pd}=-0.924Å/s	7000 s	53	10
		FePd (sh.)	RT			cells cells	Δf_{Fe}=-0.492Å/s Δf_{Pd}=-0.917Å/s	19 s·110 21 s·110	36	15
		Nb	820			EBV	r=1.0Å/s	d=5.0	32	2
		Cr-cap	RT			EBV	r=1.5Å/s	0.1	2	1
$SF_{mid}(1)$	0537	Cr	RT			EBV	r=1.5Å/s	0.2	1	0.5
		Pd	RT	723	1800	cells	Δf_{Pd}=-0.922Å/s	7300 s	57	10
		FePd (sh.)	RT			cells cells	Δf_{Fe}=-0.494Å/s Δf_{Pd}=-0.915Å/s	19 s·110 21 s·110	(35+35)	5
		FePd (cod.)	500			cells cells	Δf_{Fe}=-0.42Å/s Δf_{Pd}=-0.908Å/s	2150 s		
		Nb	320			EBV	r=1.0Å/s		37	2
		no cap								

Table 9.4: Growth parameters of Nb/FePd samples and respective layer thicknesses as determined from XRR and TEM.

Sample	OMBE Number	Layer	T_S (K)	T_{ann} (K)	t_{ann} (s)	deposition method	Δf (cells) or r (EBV)	t_{dep} (cells) or d_{Multi1} (EBV)	d (nm)	Δd
$SIF_{high}(1)$	0621	Cr	RT			EBV	r=1.5Å/s	d=0.066	1	0.5
		Pd	RT	623	1800	cells	Δf_{Pd}=-0.907Å/s	7800 s	66	5
		FePd (cod.)	670			cells cells	Δf_{Fe}=-0.411Å/s Δf_{Pd}=-0.892Å/s	3100 s	45	5
		MgO	RT			EBV	r=0.75Å/s	1320 s	7.4	0.2
		Nb	320			EBV	r=0.8Å/s	d=6.1	39	1
		Pd-cap	RT			cells	Δf_{Pd}=-0.9Å/s	200 s	2	1
$SIF_{low}(1)$	0643	Cr	RT			EBV	r=1.5Å/s	d=0.1	1	0.5
		Pd	RT	623	1800	cells	Δf_{Pd}=-0.892Å/s	7920 s	60	10
		FePd (sh.)	RT			cells cells	Δf_{Fe}=-0.494Å/s Δf_{Pd}=-0.923Å/s	19 s·110 21 s·110	36.9	0.5
		MgO	RT			EBV	r=1.0Å/s	d=1.13	7.5	0.2
		Nb	320			EBV	r=1.0Å/s	d=5.0	33	1
		Cr-cap	RT			EBV	r=1.5Å/s	d=0.1	2	1

Table 9.5: Growth parameters of Nb/FePd samples and respective layer thicknesses as determined from XRR and TEM.

Sample	OMBE Number	Layer	T_S (K)	T_ann (K)	t_ann (s)	deposition method	Δf (cells) or r (EBV)	t_dep (cells) or $\mathrm{d}_\mathrm{Multi1}$ (EBV)	d (nm)	Δd
S(1)	0541	Cr	RT			EBV	r=1.5Å/s	0.2	1	0.5
		Pd	RT	723	1800	cells	Δf_Pd=-0.907Å/s	7300 s	56	5
		Nb	320			EBV	r=1.0Å/s	5.0	36	5
S(2)	0549	Nb	320			EBV	r=1.0Å/s	6.58	41	1
		Pd-cap	RT			cells	Δf_Pd=-0.81Å/s	280 s	2	0.5
S(3)	0565	Nb	820			EBV	r=1.0Å/s	5.0	28	1
		Cr-cap	RT			EBV	r=1.5Å/s	0.1	1	0.5
S(4)	0585	Nb	820			EBV	r=1.1Å/s	16.0	96	2
		Cr-cap	RT			EBV	r=1.5Å/s	0.1	1	0.5
S(5)	0639	Nb	320			EBV	r=1.0Å/s	5.0	39.4	0.5
		Cr-cap	RT			EBV	r=1.5Å/s	0.1	2	0.4

Table 9.6: Growth parameters of Nb/FePd samples and respective layer thicknesses as determined from XRR and TEM.

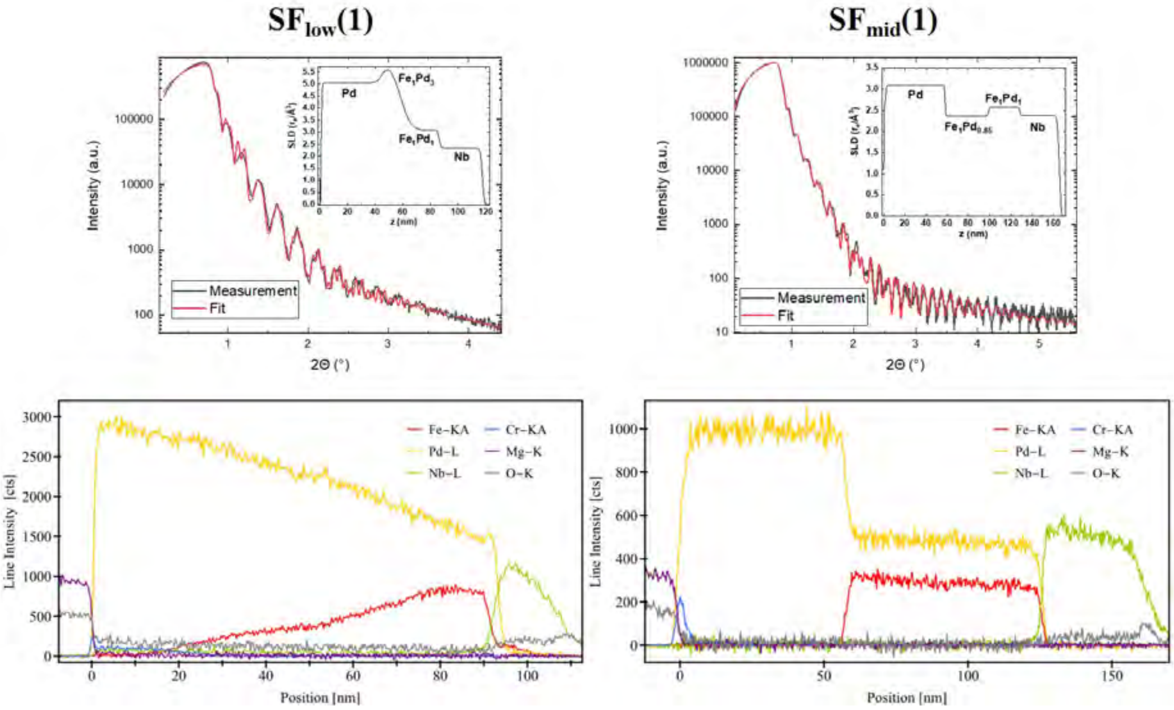

Figure 9.7: XRR measurements and respective fits using GenX of SF$_{low}$(1) and SF$_{mid}$(1) in comparison with the depth-dependent material distribution obtained from STEM-EDX.

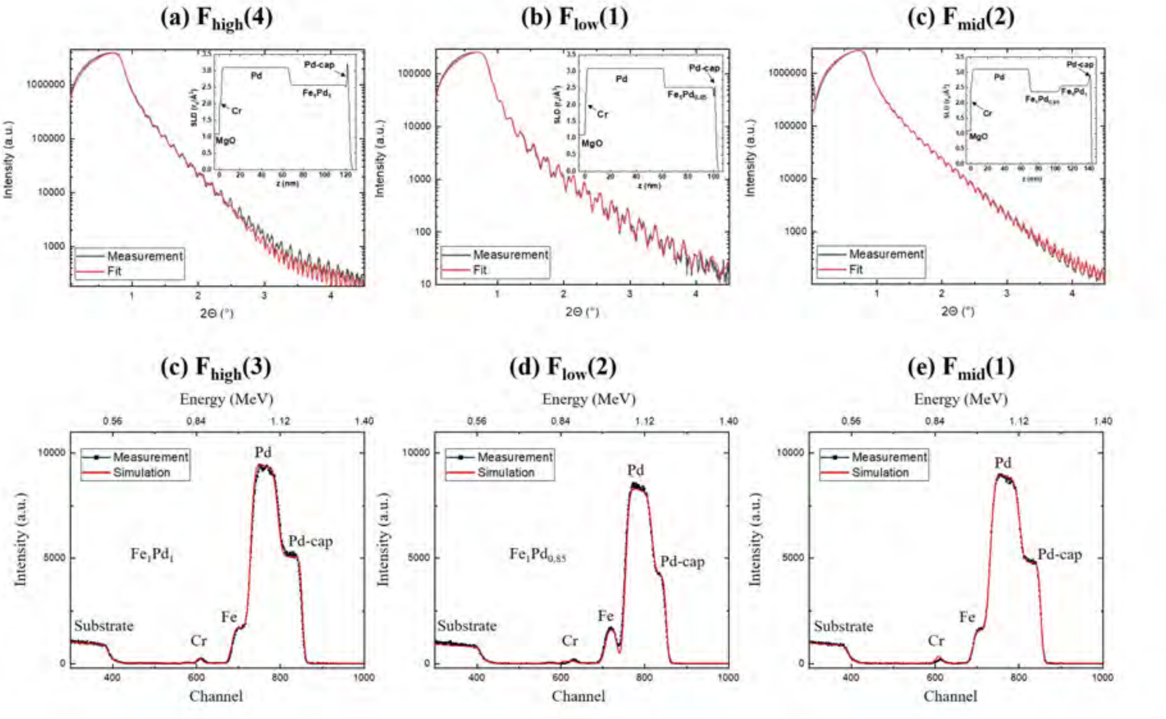

Figure 9.8: XRR and RBS comparison of F$_{high}$-F$_{low}$ and respective fits using GenX and RUMP.

hkl	(001)	(002)
$2\theta\,(^\circ)$	~24.5	~50
$\frac{\sin\theta}{\lambda}\left(\frac{1}{\mathrm{\AA}}\right)$	0.14	0.27
f_{Pd}	39.87	22.37
f_{Fe}	21.05	16.2
Δ_{Pd}	4.2	4.2
Δ_{Fe}	3.4	3.4

Table 9.7: (001) and (002) Bragg reflections of epitaxial FePd and its real and imaginary parts of the atomic scattering amplitudes f_{Fe}, f_{Pd}, Δ_{Fe} and Δ_{Pd}, obtained from [17].

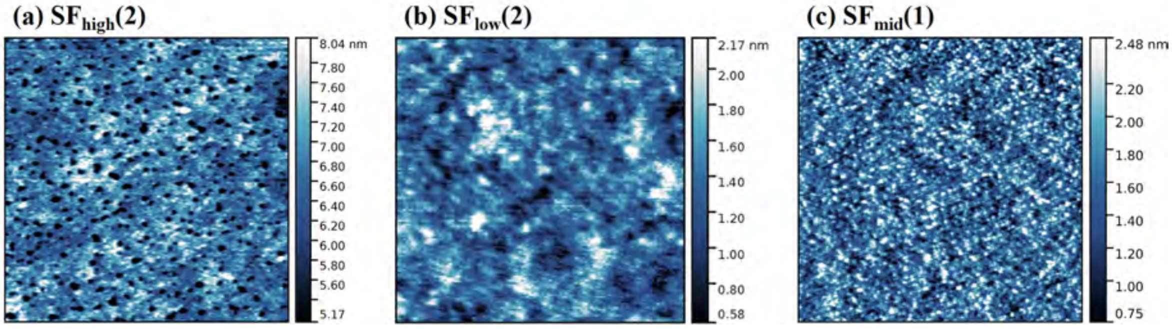
(a) SF$_{high}$(2)
8.04 nm
7.80
7.60
7.40
7.20
7.00
6.80
6.60
6.40
6.20
6.00
5.80
5.60
5.17
(b) SF$_{low}$(2)
2.17 nm
2.00
1.80
1.60
1.40
1.20
1.00
0.80
0.58
(c) SF$_{mid}$(1)
2.48 nm
2.20
2.00
1.80
1.60
1.40
1.20
1.00
0.75

Figure 9.9: 3x3µm AFM images of samples SF$_{\mathrm{high}}$-SF$_{\mathrm{low}}$ at room temperature.

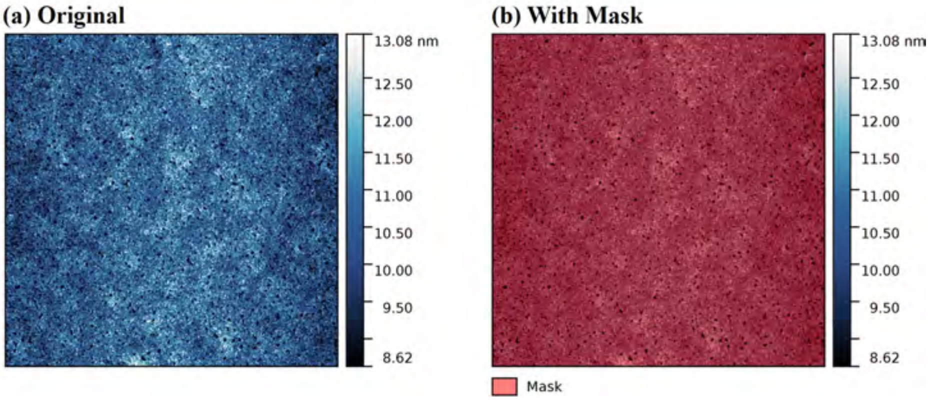
(a) Original
13.08 nm
12.50
12.00
11.50
11.00
10.50
10.00
9.50
8.62
(b) With Mask
13.08 nm
12.50
12.00
11.50
11.00
10.50
10.00
9.50
8.62
Mask

Figure 9.10: (a) 8x8µm AFM image of SIF$_{\mathrm{high}}$(1) displaing deep voids inside the FePd layer. (b) The red area denotes a mask added to the AFM image where the surface height is >60 % above the minimum height level, the voids (black area) obtain a relation to the FePd surface of ~1%.

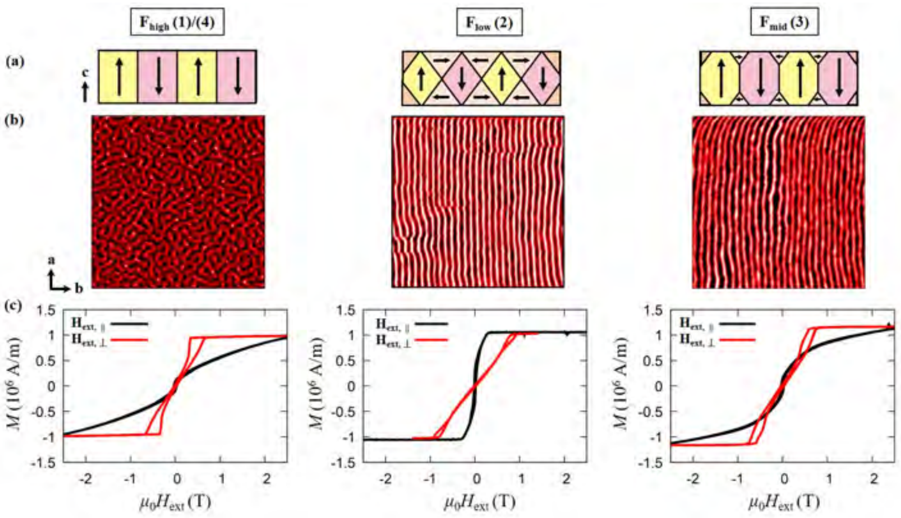

Figure 9.11: (a) Schematic view of the magnetic domain formation inside the FePd layer in direction of the c-axis of L1_0-ordered FePd. (b) (3×3 µm) zero-field MFM measurements in the as-grown states of F$_{\mathrm{high}}$(4), F$_{\mathrm{low}}$(2) and F$_{\mathrm{mid}}$(3). (c) Hysteresis loops of F$_{\mathrm{high}}$(1), F$_{\mathrm{low}}$(2) and F$_{\mathrm{mid}}$(3) measured at 300 K with $H_{\mathrm{ext},||}$ in the surface plane and $H_{\mathrm{ext},\perp}$ perpendicular to the surface plane. All measurements are obtained at 300 K.

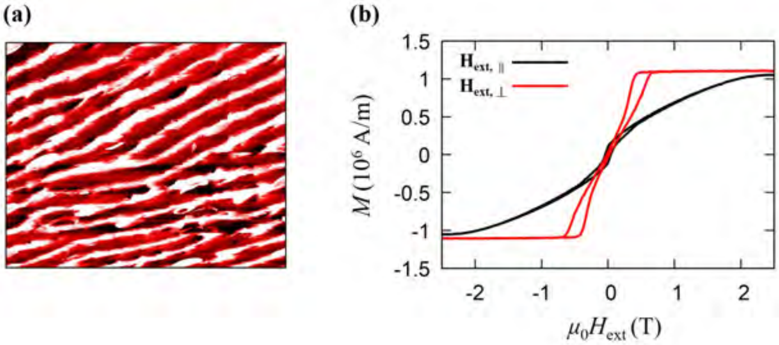

Figure 9.12: (a) 3x3µm MFM image of F$_{\mathrm{high}}$(2) in the as-grown state and (b) hysteresis loops of F$_{\mathrm{high}}$(2) at room temperature.

Sample	Q	$H_{\text{coerc},\perp}$ (mT)	$H_{\text{coerc},\|\|}$ (mT)	M_{S} in (10^6A/m)
$\text{F}_{\text{high}}(1)$	2.17±0.05	24±1	32±1	1.00±0.01
$\text{F}_{\text{high}}(2)$	1.8±0.05	16±1	43±1	1.06±0.01
$\text{F}_{\text{high}}(3)$	2.23±0.04	26±1	23±1	1.01±0.01
$\text{F}_{\text{low}}(1)$	0.7±0.01	16±1	10±2	1.03±0.03
$\text{F}_{\text{low}}(2)$	0.47±0.05	16±1	15±2	1.04±0.06
$\text{F}_{\text{mid}}(1)$	1.4±0.04	35±15	11±5	1.00±0.07
$\text{F}_{\text{mid}}(2)$	1.45±0.03	30±1	27±2	1.05±0.09
$\text{F}_{\text{mid}}(3)$	1.46±0.04	41±6	29±2	1.17±0.09
$\text{SF}_{\text{high}}(1)$	1.56±0.07	23±1	73±7	1.9±0.2
$\text{SF}_{\text{high}}(2)$	2±0.1	6±2	31±1	1.09±0.05
$\text{SIF}_{\text{high}}(1)$	2.1±0.1	7±2	28±1	1.10±0.05
$\text{SF}_{\text{low}}(1)$	0.95±0.02	24±1	13±1	1.10±0.05
$\text{SIF}_{\text{low}}(1)$	0.65±0.01	22±1	17±1	1.18±0.05
$\text{SF}_{\text{mid}}(1)$	1.3±0.02	25±1	22±1	0.94±0.05

Table 9.8: Parameters Q, $H_{\text{coerc},\perp}$, $H_{\text{coerc},||}$, and M_{S} of S/F and S/I/F samples investigated with the SQUID-MPMS.

Value	Description of simulation parameter
0.0	Pix incident polarization (polariser)
0.0	Piy
0.0	Piz
0.0	Pix outgoing polarization (analyser)
0.0	Piy
0.0	Piz
12.8	wavelength (in Angstroem)
0.96	angle of incidence alphai (in deg.)
15.0	layer thickness (in A) Cap Pd
3.985	real part of nuclear scattering length density (in A**-2) *1e6 —
1.d-3	imaginary part of nuclear scattering length density (in A**-2) *1e6 —
0.1	layer thickness (in A) Nb
4.1	real part of nuclear scattering length density (in A**-2) *1e6 —
1.d-3	imaginary part of nuclear scattering length density (in A**-2) *1e6
380.0	layer thickness (in A) FePd
5.5	real part of nuclear scattering length density (in A**-2) *1e6 —
1.d-3	imaginary part of nuclear scattering length density (in A**-2) *1e6
2.8	magnetic scattering length density at saturation (in A**-2) *1e6
470.0	layer thickness (in A) Pd
4.0	real part of nuclear scattering length density (in A**-2) *1e6 —
1.d-3	imaginary part of nuclear scattering length density (in A**-2) *1e6
40.0	layer thickness (in A) Cr
3.116	real part of nuclear scattering length density (in A**-2) *1e6 —
1.d-3	imaginary part of nuclear scattering length density (in A**-2) *1e6
6.0	substrate's real part of nuclear scattering length density (in A**-2) *1e6 —
1.d-4	substrate's Nb" imaginary part of nuclear scattering length density (in A**-2) *1e6
-10.0	ξ_{min}, minimum rotation angle around the z axis [deg.]
11.0	ξ_{max}, maximum rotation angle around the z axis [deg.]
5.0	stepwidth in rotation angle for the powder average [deg.]
220.0	size of the domains along the stripes [nm]
55.0	width of the striped domains [nm]
15.0	ω, disorder parameter [nm]
1	N, number of structural units of the paracrystal
25.0	width of the closure domains at the surfaces [nm]
10.0	depth of the closure domains [nm]
0.1	width of the domain walls [nm]
9.0	rms interfacial roughness amplitude [Angstroem]
500.0	ξ_{corr}, lateral correlation length of interfacial roughness [Angstroem]
0	replication factor of roughness [units of layer thickness]
1.5e-1	cal-ref
1.4e-07	calscat-stripes
7000.0	calscat-rough 5.d8
0.0	min. angle of exit alphaf (in deg.)
2.0	max. angle of exit alphaf (in deg.)
-2.0	min angle thetay (in deg.)
2.0	max. angle thetay (in deg.)
100	number of points in alphaf
100	number of points in thetay
0.15	resolution in alphaf (in deg. - FWHM)
0.15	resolution in thetay (in deg. - FWHM)
100	number of points in alphaf for the resolution-convoluted map
100	number of points in thetay for the resolution-convoluted map

Table 9.9: Parameters used for the GISANS simulation shown in Fig. 5.18 on $\mathrm{F}_{\mathrm{high}}(2)$ at room temperature.

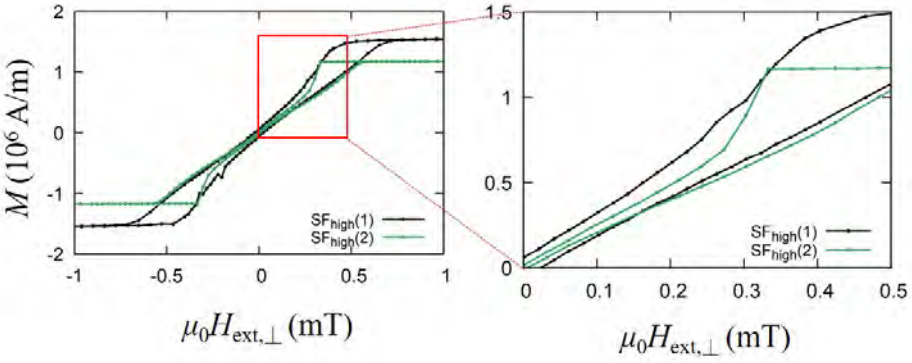

Figure 9.13: Magnetization with respect to an out-of-plane applied field $\mu_0 H_{\mathrm{ext},\perp}$ of $\mathrm{SF_{high}}(1)$ and $\mathrm{SF_{high}}(2)$.

Sample	$T_c(0\,\mathrm{mT})$ (K)	$B^*_{c,\perp}(0\,\mathrm{K})$ (mT)	$\xi_{\mathrm{GL},\|}(0\,\mathrm{K})$ (nm)
$\mathrm{SF_{high}}(2)$	6.958±0.001	3.6±0.03	9.6±0.1
$\mathrm{SF_{low}}(1)$	4.605±0.001	1.2±0.1	17±2
$\mathrm{SF_{mid}}(1)$	6.223±0.001	4±0.2	9.1±0.7
$\mathrm{SIF_{high}}(1)$	8.241±0.001	3.41±0.01	9.82±0.05
S(2)	8.645±0.001	2.51±0.01	11.45±0.07
S(3)	8.457±0.001	1±0.1	18±3

Table 9.10: Superconducting parameters of Nb layers in the S/F samples in comparison with the reference sample $\mathrm{SIF_{high}}(1)$ and the bare Nb layers S(2) and S(3).

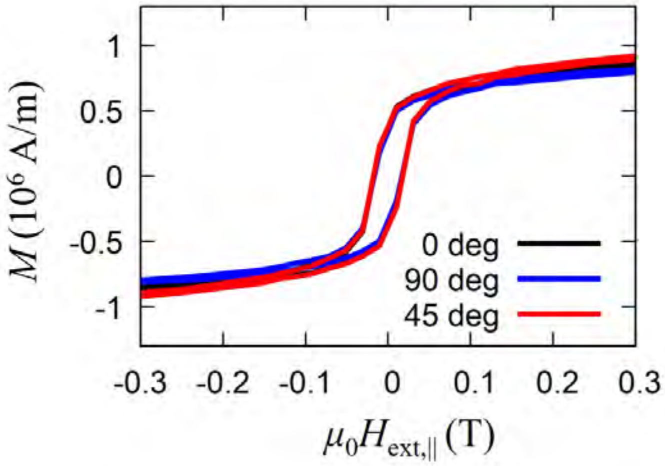

Figure 9.14: Hysteresis loops at 300 K in an in-plane applied field of sample $\mathrm{SF_{low}}(1)$ at various angles between the <100> crystalline axis and the magnetic field. Here, 0° denotes a field applied along <100>.

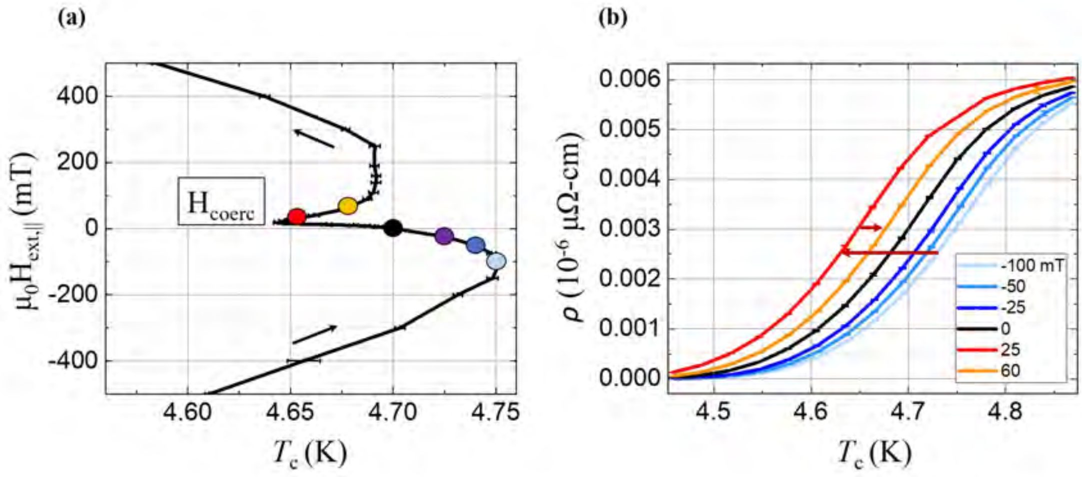

Figure 9.15: (a) Dependence of T_c on the applied field $\mu_0 H_{\mathrm{ext},||}$ of $\mathrm{SF_{low}}(1)$. All data points in (a) are extracted from $\rho(T)$ measurements such as those displayed in (b). Red arrows indicate a transition of T_c first to lower values and subsequently to increasing values for increasing magnetic fields.

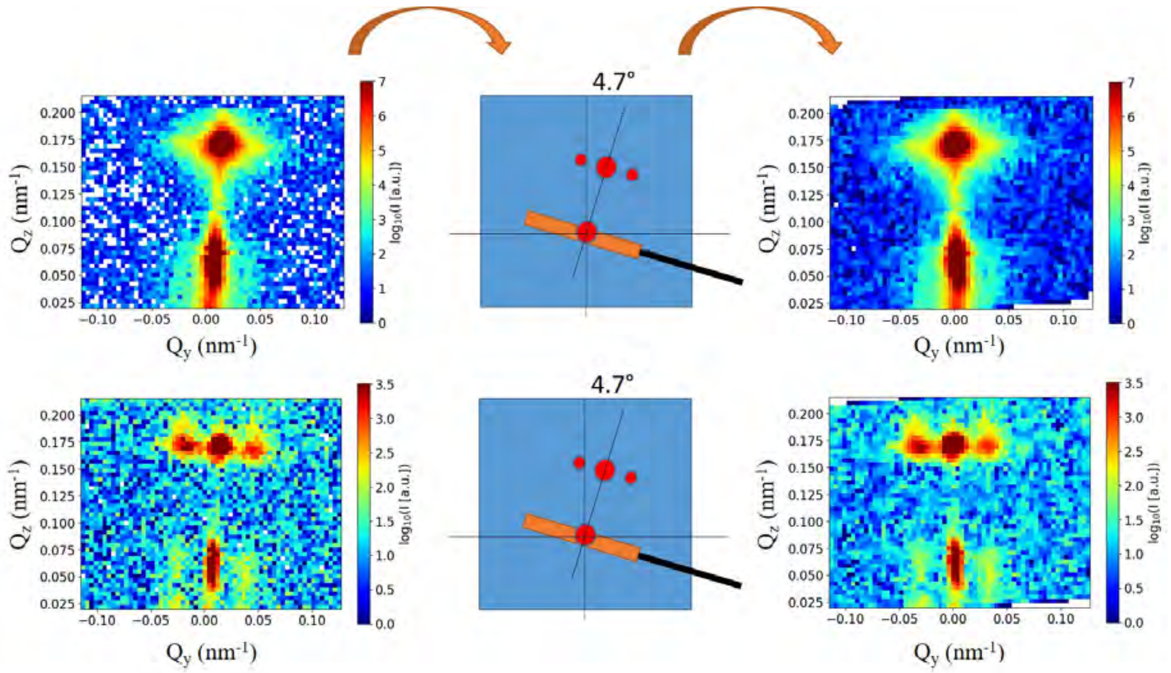

Figure 9.16: Q_y-Q_z-maps of the I^{--} and I^{-+} channels of polarized GISANS at $T_\mathrm{B} = (10.10 \pm 0.02)\,\mathrm{K}$ on $\mathrm{SF_{high}}(2)$ (left) before rotation, and (right) after a rotation of 4.7° due to a slightly tilted GISANS holder as sketched in the middle.

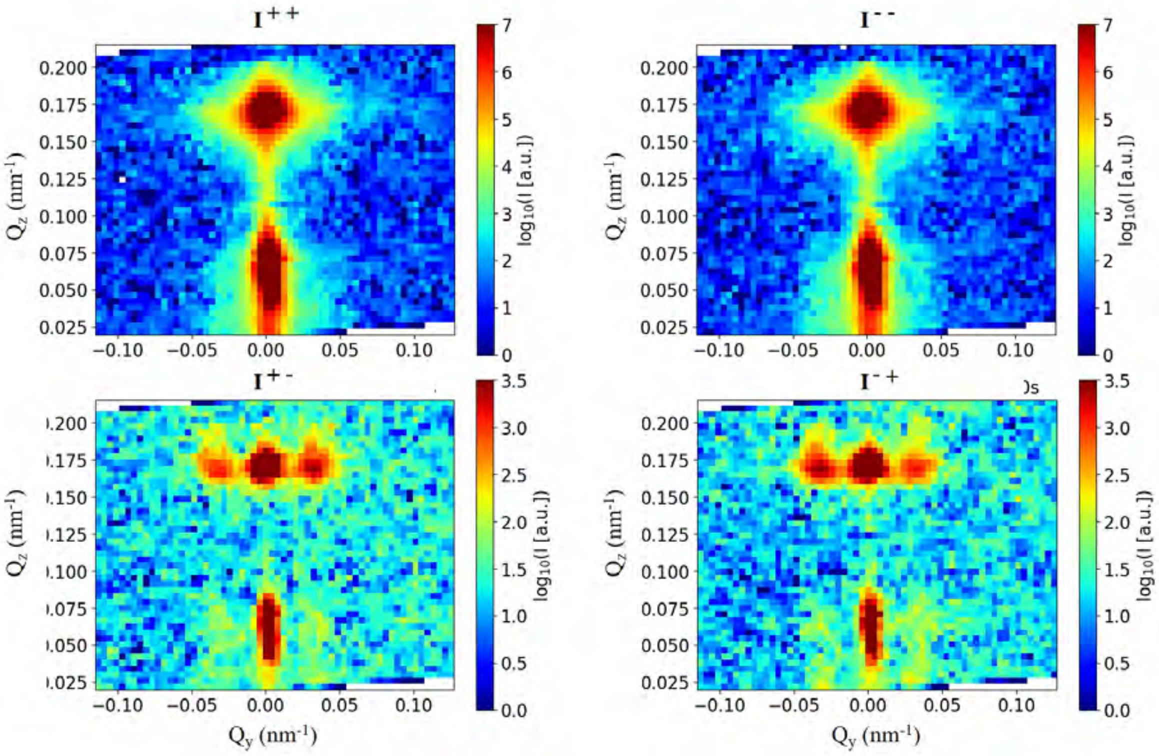

Figure 9.17: Q_y-Q_z-maps of the four different GISANS channels measured at $T_\mathrm{B} = (5.60 \pm 0.02)\,\mathrm{K}$ on $\mathrm{SF}_\mathrm{high}(2)$ after subtraction of a rotation angle of 4.7°.

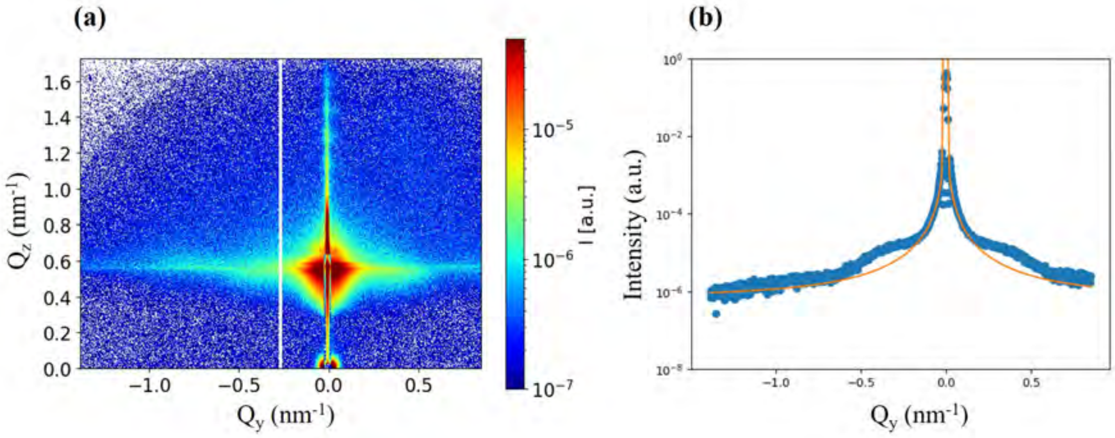

Figure 9.18: (a) Q_y-Q_z-map of GISAXS measured at room temperature on $\mathrm{SF}_\mathrm{high}(2)$ and (b) corresponding $I(Q_y)$ at the specular line.

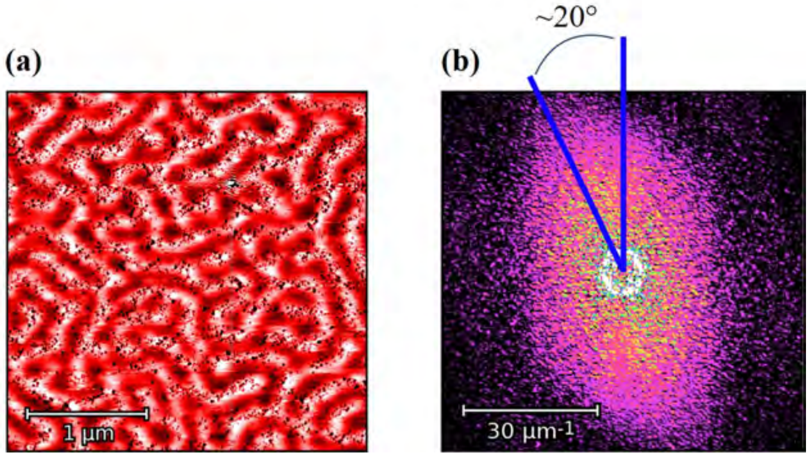

Figure 9.19: (a) 3x3µm MFM image of $SF_{high}(2)$ at room temperature under zero field and (b) 2D-FFT analysis of (a) performed using the software Gwyddion [195]. The dark blue line denotes a preferential direction of magnetic domains visible by a distortion from a circular shape.

Value	Description of simulation parameter
30.0	α, tilt angle of sample surface with respect to the incidence plane (in deg.)
0.0	Pix incident polarization (polariser)
$0.97\cdot \sin\alpha$	Piy
$0.97\cdot \cos\alpha$	Piz
0.0	Pix outgoing polarization (analyser)
$0.988\cdot \sin\alpha$	Piy
$0.988\cdot \cos\alpha$	Piz
8.0	wavelength (in Angstroem)
0.62	angle of incidence alphai (in deg.)
7.0	layer thickness (in A) Cap Pd
3.985	real part of nuclear scattering length density (in A**-2) *1e6 —
1.d-3	imaginary part of nuclear scattering length density (in A**-2) *1e6 —
390.0	layer thickness (in A) Nb
4.1	real part of nuclear scattering length density (in A**-2) *1e6 —
1.d-3	imaginary part of nuclear scattering length density (in A**-2) *1e6
440.0	layer thickness (in A) FePd
5.4	real part of nuclear scattering length density (in A**-2) *1e6 —
1.d-3	imaginary part of nuclear scattering length density (in A**-2) *1e6
3.1	magnetic scattering length density at saturation (in A**-2) *1e6
600.0	layer thickness (in A) Pd
4.0	real part of nuclear scattering length density (in A**-2) *1e6 —
1.d-3	imaginary part of nuclear scattering length density (in A**-2) *1e6
10.0	layer thickness (in A) Cr
3.116	real part of nuclear scattering length density (in A**-2) *1e6 —
1.d-3	imaginary part of nuclear scattering length density (in A**-2) *1e6
6.0	substrate's real part of nuclear scattering length density (in A**-2) *1e6 —
1.d-4	substrate's Nb" imaginary part of nuclear scattering length density (in A**-2) *1e6
-50.0	ξ_{min}, minimum rotation angle around the z axis [deg.]
190.0	ξ_{max}, maximum rotation angle around the z axis [deg.]
5.0	stepwidth in rotation angle for the powder average [deg.]
60.0	size of the domains along the stripes [nm]
96.0	width of the striped domains [nm]
100.0	ω, disorder parameter [nm]
1	N, number of structural units of the paracrystal
0.1	width of the closure domains at the surfaces [nm]
0.1	depth of the closure domains [nm]
10.0	width of the domain walls [nm]
16.0	rms interfacial roughness amplitude [Angstroem]
3000.0	ξ_{corr}, lateral correlation length of interfacial roughness [Angstroem]
0	replication factor of roughness [units of layer thickness]
2.0	cal-ref
2.8e-06	calscat-stripes
10000.0	calscat-rough 5.d8
0.0	min. angle of exit alphaf (in deg.)
1.0	max. angle of exit alphaf (in deg.)
-0.5	min angle thetay (in deg.)
0.5	max. angle thetay (in deg.)
50	number of points in alphaf
50	number of points in thetay
0.09	resolution in alphaf (in deg. - FWHM)
0.09	resolution in thetay (in deg. - FWHM)
50	number of points in alphaf for the resolution-convoluted map
50	number of points in thetay for the resolution-convoluted map

Table 9.11: Parameters used for the GISANS simulation shown in Fig. 7.7 on $\mathrm{SF}_{\mathrm{high}}(2)$ at $T_{\mathrm{B}} = (10.10 \pm 0.02)\,\mathrm{K}$.

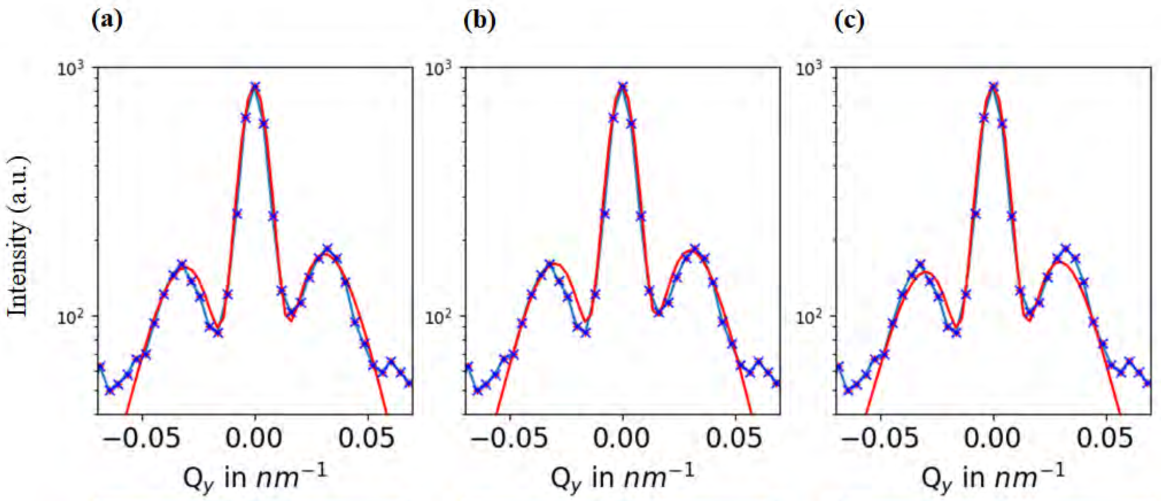

Parameter	Value
$\Delta\xi$	240°
ξ_{av}	70°
D_{domain}	96 nm
w_{DW}	10 nm

Parameter	Value
$\Delta\xi$	240°
ξ_{av}	70°
D_{domain}	100 nm
w_{DW}	10 nm

Parameter	Value
$\Delta\xi$	200°
ξ_{av}	80°
D_{domain}	100 nm
w_{DW}	10 nm

Figure 9.20: $I^{+-}(Q_y)$ of three different simulations with varied $\Delta\xi$, ξ_{av}, and D_{domain} (and constant values for other parameters) in comparison with $I^{+-}(Q_y)$ of $\text{SF}_{\text{high}}(2)$ at $T_{\text{B}} = (10.10 \pm 0.02)\,\text{K}$. (a) Chosen parameter set as given in table 9.11, (b) variation of the domain period D_{domain}, (c) variation of the average rotation angle ξ_{av} and the angular range $\Delta\xi$.

Value	Description of simulation parameter
30.0	α, tilt angle of sample surface with respect to the incidence plane (in deg.)
0.0	Pix incident polarization (polariser)
$0.97\cdot \sin\alpha$	Piy
$0.97\cdot \cos\alpha$	Piz
0.0	Pix outgoing polarization (analyser)
$0.988\cdot \sin\alpha$	Piy
$0.988\cdot \cos\alpha$	Piz
8.0	wavelength (in Angstroem)
0.62	angle of incidence alphai (in deg.)
7.0	layer thickness (in A) Cap Pd
3.985	real part of nuclear scattering length density (in A**-2) *1e6 —
1.d-3	imaginary part of nuclear scattering length density (in A**-2) *1e6 —
390.0	layer thickness (in A) Nb
4.1	real part of nuclear scattering length density (in A**-2) *1e6 —
1.d-3	imaginary part of nuclear scattering length density (in A**-2) *1e6
440.0	layer thickness (in A) FePd
5.4	real part of nuclear scattering length density (in A**-2) *1e6 —
1.d-3	imaginary part of nuclear scattering length density (in A**-2) *1e6
3.1	magnetic scattering length density at saturation (in A**-2) *1e6
600.0	layer thickness (in A) Pd
4.0	real part of nuclear scattering length density (in A**-2) *1e6 —
1.d-3	imaginary part of nuclear scattering length density (in A**-2) *1e6
10.0	layer thickness (in A) Cr
3.116	real part of nuclear scattering length density (in A**-2) *1e6 —
1.d-3	imaginary part of nuclear scattering length density (in A**-2) *1e6
6.0	substrate's real part of nuclear scattering length density (in A**-2) *1e6 —
1.d-4	substrate's Nb" imaginary part of nuclear scattering length density (in A**-2) *1e6
-50.0	ξ_{min}, minimum rotation angle around the z axis [deg.]
190.0	ξ_{max}, maximum rotation angle around the z axis [deg.]
5.0	stepwidth in rotation angle for the powder average [deg.]
60.0	size of the domains along the stripes [nm]
96.0	width of the striped domains [nm]
100.0	ω, disorder parameter [nm]
1	N, number of structural units of the paracrystal
0.1	width of the closure domains at the surfaces [nm]
0.1	depth of the closure domains [nm]
20.0	width of the domain walls [nm]
16.0	rms interfacial roughness amplitude [Angstroem]
3000.0	ξ_{corr}, lateral correlation length of interfacial roughness [Angstroem]
0	replication factor of roughness [units of layer thickness]
2.0	cal-ref
2.8e-06	calscat-stripes
10000.0	calscat-rough 5.d8
0.0	min. angle of exit alphaf (in deg.)
1.0	max. angle of exit alphaf (in deg.)
-0.5	min angle thetay (in deg.)
0.5	max. angle thetay (in deg.)
50	number of points in alphaf
50	number of points in thetay
0.09	resolution in alphaf (in deg. - FWHM)
0.09	resolution in thetay (in deg. - FWHM)
50	number of points in alphaf for the resolution-convoluted map
50	number of points in thetay for the resolution-convoluted map

Table 9.12: Parameters used for the GISANS simulation shown in Fig. 7.8 on $\mathrm{SF}_{\mathrm{high}}(2)$ at $T_{\mathrm{B}} = (5.60 \pm 0.02)\,\mathrm{K}$.

Abbreviations

AES	Auger Electron Spectroscopy
AFM	Atomic Force Microscopy
BCS	Bardeen-, Cooper-, Schrieffer-theory
CS	Complete-Superconductivity
DWBA	Distorted-Wave Born Approximation
DWS	Domain-Wall-Superconductivity
EBV	Electron Beam Evaporator
EDX	Energy-dispersive X-ray Spectroscopy
FFLO	Fulde Ferrel Larkin Ovchinnikov state
FOM	Figure of Merit
GISANS	Grazing-Incidence Small-Angle Neutron Scattering
GL	Ginzburg-Landau theory
HAADF	High-Angle Annular Dark-Field Imaging
LEED	Low-Energy Electron Diffraction
LRPE	Long-Ranged Proximity Effect
LRTC	Longe-Ranged spin-Triplet Components

MBE	Molecular Beam Epitaxy
MFM	Magnetic Force Microscopy
MPMS	Magnetic Properties Measurement System
NSF	Non-Spin-Flip
PID	Proportional-Integral-Derivative
PNR	Polarized Neutron Reflectometry
PMA	Perpendicular Magnetic Anisotropy
PPMS	Physical Properties Measurement System
QMB	Quartz Microbalance
RBS	Rutherford Backscattering Spectrometry
RDS	Reverse-Domain-Superconductivity
RHEED	Reflection High-Energy Electron Diffraction
RSFQ	Rapid Single Flux Quantum
SF	Spin-Flip
S/F	Superconductor/Ferromagnet
SLD	Scattering Length Density
S/N	Superconductor/Normal metal
STEM	Scanning Transmission Electron Microscopy
UHV	Ultra-High-Vacuum
XMCD	X-ray Magnetic Circular Dichroism
XRD	X-ray Diffractometry
XRR	X-ray Reflectometry

Bibliography

[1] J. Linder and J. W. A. Robinson, "Superconducting spintronics," *Nature Physics*, vol. 11, pp. 307–315, Apr 2015.

[2] M. Eschrig, "Spin-polarized supercurrents for spintronics: a review of current progress," *Reports on Progress in Physics*, vol. 78, p. 104501, Sep 2015.

[3] A. M. Kadin, "Duality and fluxonics in superconducting devices," *Journal of Applied Physics*, vol. 68, p. 5741, dec 1990.

[4] J. Y. Gu, C.-Y. You, J. S. Jiang, J. Pearson, Y. B. Bazaliy, and S. D. Bader, "Magnetization-orientation dependence of the superconducting transition temperature in the ferromagnet-superconductor-ferromagnet system: CuNi/Nb/CuNi," *Physical Review Letters*, vol. 89, p. 267001, Dec 2002.

[5] Y. Gu, G. Halász, J. Robinson, and M. Blamire, "Large superconducting spin valve effect and ultrasmall exchange splitting in epitaxial rare-earth-niobium trilayers," *Physical Review Letters*, vol. 115, p. 067201, Aug 2015.

[6] A. I. Buzdin, "Proximity effects in superconductor-ferromagnet heterostructures," *Reviews of Modern Physics*, vol. 77, pp. 935–976, Sep 2005.

[7] Z. Yang, M. Lange, A. Volodin, R. Szymczak, and V. V. Moshchalkov, "Domain-wall superconductivity in superconductor–ferromagnet hybrids," *Nature Materials*, vol. 3, pp. 793–798, Oct 2004.

[8] A. M. Clogston, "Upper limit for the critical field in hard superconductors," *Physical Review Letters*, vol. 9, pp. 266–267, Sep 1962.

[9] B. S. Chandrasekhar, "A note on the maximum critical field of high-field superconductors," *Applied Physics Letters*, vol. 1, pp. 7–8, Sep 1962.

[10] G. Sarma, "On the influence of a uniform exchange field acting on the spins of the conduction electrons in a superconductor," *Journal of Physics and Chemistry of Solids*, vol. 24, pp. 1029–1032, Aug 1963.

[11] K. Maki and T. Tsuneto, “Pauli paramagnetism and superconducting state,” *Progress of Theoretical Physics*, vol. 31, pp. 945–956, Jun 1964.

[12] F. S. Bergeret, A. F. Volkov, and K. B. Efetov, “Josephson current in superconductor-ferromagnet structures with a nonhomogeneous magnetization,” *Physical Review B*, vol. 64, p. 134506, Sep 2001.

[13] S. Blundell, *Magnetism in Condensed Matter.* Oxford University Press, 2001.

[14] R. Gross and A. Marx, *Festkörperphysik.* Oldenbourg Verlag München, 2012.

[15] J. M. D. Coey, *Magnetism and Magnetic Materials.* Cambridge University Press, 2010.

[16] A. Hubert and R. Schäfer, *Magnetic Domains.* Springer-Verlag GmbH, 2008.

[17] V. Gehanno, “Perpendicular magnetic anisotropy of epitaxial thin films of FePd ordered alloys,” Ph.D. dissertation, Université JoSeph-Fourier - Grenoble I, 1997.

[18] D. Navas, C. Redondo, G. A. B. Confalonieri, F. Batallan, A. Devishvili, Ó. Iglesias-Freire, A. Asenjo, C. A. Ross, and B. P. Toperverg, “Domain-wall structure in thin films with perpendicular anisotropy: Magnetic force microscopy and polarized neutron reflectometry study,” *Physical Review B*, vol. 90, p. 054425, Aug 2014.

[19] D. E. Laughlin, K. Srinivasan, M. Tanase, and L. Wang, “Crystallographic aspects of L10 magnetic materials,” *Scripta Materialia*, vol. 53, pp. 383–388, Aug 2005.

[20] G. Beutier, G. van der Laan, K. Chesnel, A. Marty, M. Belakhovsky, S. P. Collins, E. Dudzik, J.-C. Toussaint, and B. Gilles, “Characterization of FePd bilayers and trilayers using soft x-ray resonant magnetic scattering and micromagnetic modeling,” *Physical Review B*, vol. 71, p. 184436, May 2005.

[21] H. A. Duerr, “Chiral magnetic domain structures in ultrathin FePd films,” *Science*, vol. 284, pp. 2166–2168, Jun 1999.

[22] G. van der Laan, K. Chesnel, M. Belakhovsky, A. Marty, F. Livet, S. Collins, E. Dudzik, A. Haznar, and J. Attané, “Magnetic anisotropy of aligned magnetic stripe domains in FePd studied by soft x-ray resonant magnetic scattering, magnetic force microscopy and micromagnetic modeling,” *Superlattices and Microstructures*, vol. 34, pp. 107–126, Jul 2003.

[23] J. Bardeen, L. N. Cooper, and J. R. Schrieffer, “Microscopic theory of superconductivity,” *Physical Review*, vol. 106, pp. 162–164, Apr 1957.

[24] J. Bardeen, L. N. Cooper, and J. R. Schrieffer, “Theory of superconductivity,” *Physical Review*, vol. 108, pp. 1175–1204, Dec 1957.

[25] J. Bardeen and D. Pines, “Electron-phonon interaction in metals,” *Physical Review*, vol. 99, pp. 1140–1150, Aug 1955.

[26] H. Fröhlich, “Interaction of electrons with lattice vibrations,” *Proceedings of the Royal Society of London. Series A. Mathematical and Physical Sciences*, vol. 215, pp. 291–298, Dec 1952.

[27] W. Meissner and R. Ochsenfeld, “Ein neuer Effekt bei Eintritt der Supraleitfähigkeit,” *Die Naturwissenschaften*, vol. 21, pp. 787–788, Nov 1933.

[28] H. K. Onnes, *The Superconductivity of Mercury*, 1911.

[29] M. Tinkham, *Introduction to Superconductivity.* McGraw-Hill College, 1995.

[30] F. London and H. London, “Supraleitung und Diamagnetismus,” *Physica*, vol. 2, pp. 341–354, Jan 1935.

[31] A. B. Pippard, “An experimental and theoretical study of the relation between magnetic field and current in a superconductor,” *Proceedings of the Royal Society of London. Series A. Mathematical and Physical Sciences*, vol. A216, pp. 547–568, Feb 1953.

[32] V. L. Ginzburg and L. D. Landau, “On the Theory of superconductivity,” *Zh. Eksp. Teor. Fiz.*, vol. 20, pp. 1064–1082, 1950.

[33] L. P. Gor‘kov, “Microscopic theory of the Ginzburg-Landau equations in the theory of superconductivity,” *JETP*, vol. 36, Jun 1959.

[34] D. Saint-James, G. Sarma, and E. J. Thomas, *Type* II superconductivity. Oxford, New York, Pergamon Press, 1969, 1969.

[35] A. Abrikosov, “On the Magnetic properties of superconductors of the second group,” *Sov. Phys. JETP*, vol. 5, pp. 1174–1182, 1957.

[36] The NIST Reference on Constants, Units, and Uncertainty, *2018 CODATA Value: magnetic flux quantum*, 2019 (accessed Apr 6, 2020), https://physics.nist.gov/cgi-bin/cuu/Value?eqflxquhs2e.

[37] V. L. Ginzburg, “On the theory of superconductivity,” *Il Nuovo Cimento*, vol. 2, pp. 1234–1250, Dec 1955.

[38] P. G. De Gennes and E. Guyon, “Superconductivity in “normal” metals,” *Physics Letters*, vol. 3, pp. 168–169, Jan 1963.

[39] P. G. De Gennes, “Boundary effects in superconductors,” *Reviews of Modern Physics*, vol. 36, pp. 225–237, Jan 1964.

[40] A. K. Geim, I. V. Grigorieva, S. V. Dubonos, J. G. S. Lok, J. C. Maan, A. E. Filippov, and F. M. Peeters, “Phase transitions in individual sub-micrometre superconductors,” *Nature*, vol. 390, pp. 259–262, Nov 1997.

[41] T. Cren, L. Serrier-Garcia, F. Debontridder, and D. Roditchev, “Vortex fusion and giant vortex states in confined superconducting condensates,” *Physical Review Letters*, vol. 107, p. 097202, Aug 2011.

[42] U. Essmann and H. Träuble, “The direct observation of individual flux lines in type-II superconductors,” *Physics Letters A*, vol. 24, pp. 526–527, May 1967.

[43] A. V. Narlikar, “Oxford handbook of small superconductors,” Oxford, United Kingdom, 2017, edited by A. V. Narlikar.

[44] H. W. Weber, M. Botlo, F. M. Sauerzopf, H. Wiesinger, and U. Klein, “Phase transitions between type-I, type-II/1 and type-II/2 superconductivity,” *Japanese Journal of Applied Physics*, vol. 26, p. 917, Jan 1987.

[45] A. Sirohi, S. Das, P. Adhikary, R. R. Chowdhury, A. Vashist, Y. Singh, S. Gayen, T. Das, and G. Sheet, “Mixed type I and type II superconductivity due to intrinsic electronic inhomogeneities in the type II dirac semimetal $PdTe_2$,” *Journal of Physics: Condensed Matter*, vol. 31, p. 085701, Jan 2019.

[46] C. Rey, *Superconductors in the Power Grid: Materials and Applications.* Woodhead Publishing Series in Energy, 2015.

[47] M. Baert, V. V. Metlushko, R. Jonckheere, V. V. Moshchalkov, and Y. Bruynseraede, “Composite flux-line lattices stabilized in superconducting films by a regular array of artificial defects,” *Physical Review Letters*, vol. 74, pp. 3269–3272, Apr 1995.

[48] L. Civale, A. D. Marwick, T. K. Worthington, M. A. Kirk, J. R. Thompson, L. Krusin-Elbaum, Y. Sun, J. R. Clem, and F. Holtzberg, “Vortex confinement by columnar defects inYBa2cu3o7crystals: Enhanced pinning at high fields and temperatures,” *Physical Review Letters*, vol. 67, pp. 648–651, Jul 1991.

[49] E. V. Blinov, L. S. Vlasenko, Y. A. Kufaev, E. B. Sonin, Y. P. Stepanov, A. K. Tagantsev, and V. G. Fleisher, “Threshold vortex formation and trapping fields in small high-tc superconducting particles,” *J. Exp. Theor. Phys.*, vol. 76, p. 308, 1993.

[50] V. Fleisher, R. Laiho, E. Lähderanta, Y. Stepanov, and K. Traito, “Temperature dependence of the magnetic field penetration depth versus oxygen ordering in submicron YBCO particles,” *Physica C: Superconductivity*, vol. 264, pp. 295–304, Jun 1996.

[51] D. Saint-James and P. G. De Gennes, “Onset of superconductivity in decreasing fields,” *Physics Letters*, vol. 7, pp. 306–308, Dec 1963.

[52] F. E. Harper and M. Tinkham, “The mixed state in superconducting thin films,” *Physical Review*, vol. 172, pp. 441–450, Aug 1968.

[53] M. Schöck, C. Sürgers, and H. v. Löhneysen, "Superconducting and magnetic properties of Nb/$Pd_{1-x}Fe_x$/Nb triple layers," *The European Physical Journal B*, vol. 14, pp. 1–10, Feb 2000.

[54] M. Tinkham, "Effect of fluxoid quantization on transitions of superconducting films," *Physical Review*, vol. 129, pp. 2413–2422, Mar 1963.

[55] I. O. Kulik, "Vortex structure in superconducting films in a parallel field," *JETP*, vol. 25, p. 1085, 1967.

[56] Y. Asada and H. Nosé, "Superconductivity of niobium films," *Journal of the Physical Society of Japan*, vol. 26, pp. 347–354, Feb 1969.

[57] W. E. Lawrence and S. Doniach, in *Proceedings of the 12th International Conference on Low Temperature Physics*, E. Kanda, Ed., Keygaku, Tokyo, 1970, p. 361.

[58] S. T. Ruggiero, T. W. Barbee, and M. R. Beasley, "Superconductivity in quasi-two-dimensional layered composites," *Physical Review Letters*, vol. 45, pp. 1299–1302, Oct 1980.

[59] C. S. L. Chun, G.-G. Zheng, J. L. Vincent, and I. K. Schuller, "Dimensional crossover in superlattice superconductors," *Physical Review B*, vol. 29, pp. 4915–4920, May 1984.

[60] J. Pearl, "Current distribution in superconducting films carrying quantized fluxoids," *Applied Physics Letters*, vol. 5, pp. 65–66, Aug 1964.

[61] A. V. Narlikar, *Superconductors*, Oxford, United Kingdom, 2014, edited by A. V. Narlikar.

[62] C. P. Bean, "Magnetization of hard superconductors," *Physical Review Letters*, vol. 8, pp. 250–253, Mar 1962.

[63] P. W. Anderson and Y. B. Kim, "Hard superconductivity: Theory of the motion of abrikosov flux lines," *Reviews of Modern Physics*, vol. 36, pp. 39–43, Jan 1964.

[64] G. Maksimova, D. Vodolazov, and I. Maksimov, "Magnetization curves and ac susceptibilities in type-II superconductors: geometry-independent similarity and effect of irreversibility mechanisms," *Physica C: Superconductivity*, vol. 356, pp. 67–82, Jul 2001.

[65] E. Altin, D. M. Gokhfeld, S. V. Komogortsev, S. Altin, and M. E. Yakinci, "Hysteresis loops of MgB_2 + Co composite tapes," *Journal of Materials Science: Materials in Electronics*, vol. 24, pp. 1341–1347, Oct 2012.

[66] V. Novotny and P. P. M. Meincke, "Single superconducting energy gap in pure niobium," *Journal of Low Temperature Physics*, vol. 18, pp. 147–157, Jan 1975.

[67] J. A. Thomposn, “Characterization of niobium films and a bulk niobium sample with RRR, SIMS and a SQUID Magnetometer,” *Journal of Undergraduate Research*, vol. 3, pp. 40–42, 2004.

[68] S. C. Mühlbauer, “Vortex lattices in superconducting niobium and skyrmion lattices in chiral MnSi: An investigation by neutron scattering,” Ph.D. dissertation, Technische Universität München, 2009.

[69] J. Halbritter, “On the oxidation and on the superconductivity of niobium,” *Applied Physics A Solids and Surfaces*, vol. 43, pp. 1–28, May 1987.

[70] J. S. Jiang, D. Davidović, D. H. Reich, and C. L. Chien, “Oscillatory superconducting transition temperature in Nb/Gd multilayers,” *Physical Review Letters*, vol. 74, pp. 314–317, Jan 1995.

[71] B. W. Maxfield and W. L. McLean, “Superconducting penetration depth of niobium,” *Physical Review*, vol. 139, pp. A1515–A1522, Aug 1965.

[72] Y. Khaydukov, R. Morari, L. Mustafa, J.-H. Kim, T. Keller, S. Belevski, A. Csik, L. Tagirov, G. Logvenov, A. Sidorenko, and B. Keimer, “Structural, magnetic, and superconducting characterization of the CuNi/Nb bilayers of the S/F type using polarized neutron reflectometry and complementary techniques,” *Journal of Superconductivity and Novel Magnetism*, vol. 28, pp. 1143–1147, Oct 2014.

[73] H. Zhang, J. W. Lynn, C. F. Majkrzak, S. K. Satija, J. H. Kang, and X. D. Wu, “Measurements of magnetic screening lengths in superconducting Nb thin films by polarized neutron reflectometry,” *Physical Review B*, vol. 52, pp. 10 395–10 404, Oct 1995.

[74] A. I. Gubin, K. S. Il’in, S. A. Vitusevich, M. Siegel, and N. Klein, “Dependence of magnetic penetration depth on the thickness of superconducting Nb thin films,” *Physical Review B*, vol. 72, p. 064503, Aug 2005.

[75] A. F. Volkov and K. B. Efetov, “Proximity effect and its enhancement by ferromagnetism in high-temperature superconductor-ferromagnet structures,” *Physical Review Letters*, vol. 102, p. 077002, Feb 2009.

[76] G. Deutscher and P. G. De Gennes, “Proximity effects,” *Superconductivity. Vols. 1 and 2*, pp. 1005–34, Oct 1969.

[77] M. P. Weides, *The Oxford Handbook of Small Superconductors.* Oxford University Press, 2017, ch. Barriers in Josephson Junctions: An Overview, pp. 432–458.

[78] A. F. Andreev, “The thermal conductivity of the intermediate state in superconductors,” *Sov. Phys. JETP*, vol. 19, pp. 1228–1231, Nov 1964.

[79] O. Millo, I. Asulin, A. Sharoni, O. Yuli, and G. Koren, “The superconductor proximity effect in Au-$YBa_2Cu_3O_{7-\delta}$ bilayer films: the role of order parameter anisotropy,” *Microelectronics Journal*, vol. 36, pp. 539–542, Mar 2005.

[80] B. Pannetier and H. Courtois, *Journal of Low Temperature Physics*, vol. 118, pp. 599–615, 2000.

[81] N. R. Werthamer, E. Helfand, and P. C. Hohenberg, "Temperature and purity dependence of the superconducting critical field, H_{c2}. III. Electron spin and spin-orbit effects," *Physical Review*, vol. 147, pp. 295–302, Jul 1966.

[82] G. Fuchs, S.-L. Drechsler, N. Kozlova, M. Bartkowiak, J. E. Hamann-Borrero, G. Behr, K. Nenkov, H.-H. Klauss, H. Maeter, A. Amato, H. Luetkens, A. Kwadrin, R. Khasanov, J. Freudenberger, A. Köhler, M. Knupfer, E. Arushanov, H. Rosner, B. Büchner, and L. Schultz, "Orbital and spin effects for the upper critical field in As-deficient disordered Fe pnictide superconductors," *New Journal of Physics*, vol. 11, p. 075007, Jul 2009.

[83] S. Manalo and U. Klein, "Influence of orbital pair breaking on paramagnetically limited states in clean superconductors," *Physical Review B*, vol. 65, p. 144510, Mar 2002.

[84] M. Eschrig, "Spin-polarized supercurrents for spintronics," *Physics Today*, vol. 64, p. 43, 2011.

[85] R. Wördenweber, V. V. Moshchalkov, S. Bending, and F. Tafuri, *Superconductors at the Nanoscale.* Walter de Gruyter GmbH, 2017.

[86] P. Fulde and R. A. Ferrell, "Superconductivity in a strong spin-exchange field," *Physical Review*, vol. 135, pp. A550–A563, Aug 1964.

[87] A. Larkin and Y. Ovchinnikov, "Nonuniform state of superconductors," *Zh. Eksp. Teor. Fiz.*, vol. 47, pp. 1136–1146, 1964.

[88] J. Stahn, J. Chakhalian, C. Niedermayer, J. Hoppler, T. Gutberlet, J. Voigt, F. Treubel, H.-U. Habermeier, G. Cristiani, B. Keimer, and C. Bernhard, "Magnetic proximity effect in perovskite superconductor/ferromagnet multilayers," *Physical Review B*, vol. 71, p. 140509, Apr 2005.

[89] J. Chakhalian, J. W. Freeland, G. Srajer, J. Strempfer, G. Khaliullin, J. C. Cezar, T. Charlton, R. Dalgliesh, C. Bernhard, G. Cristiani, H.-U. Habermeier, and B. Keimer, "Magnetism at the interface between ferromagnetic and superconducting oxides," *Nature Physics*, vol. 2, pp. 244–248, Apr 2006.

[90] F. S. Bergeret, K. B. Efetov, and A. I. Larkin, "Nonhomogeneous magnetic order in superconductor-ferromagnet multilayers," *Physical Review B*, vol. 62, pp. 11 872–11 878, Nov 2000.

[91] P. W. Anderson and H. Suhl, "Spin alignment in the superconducting state," *Physical Review*, vol. 116, pp. 898–900, Nov 1959.

[92] H. Zabel and S. D. Bader, *Magnetic Heterostructures.* Springer Berlin Heidelberg, 2007.

[93] I. A. Garifullin, D. A. Tikhonov, N. N. Garif'yanov, M. Z. Fattakhov, K. Theis-Bröhl, K. Westerholt, and H. Zabel, "Possible reconstruction of the ferromagnetic state under the influence of superconductivity in epitaxial V/$Pd_{1-x}Fe_x$ bilayers," *Applied Magnetic Resonance*, vol. 22, pp. 439–452, Sep 2002.

[94] E. B. Sonin, "Comment on "Ferromagnetic film on a superconducting substrate"," *Physical Review B*, vol. 66, p. 136501, Oct 2002.

[95] R. Werner, A. Y. Aladyshkin, S. Guénon, J. Fritzsche, I. M. Nefedov, V. V. Moshchalkov, R. Kleiner, and D. Koelle, "Domain-wall and reverse-domain superconducting states of a Pb thin-film bridge on a ferromagnetic $BaFe_{12}O_{19}$ single crystal," *Physical Review B*, vol. 84, p. 020505, Jul 2011.

[96] A. I. Buzdin and A. S. Mel'nikov, "Domain wall superconductivity in ferromagnetic superconductors," *Physical Review B*, vol. 67, p. 020503(R), Jan 2003.

[97] A. Y. Aladyshkin, A. I. Buzdin, A. A. Fraerman, A. S. Mel'nikov, D. A. Ryzhov, and A. V. Sokolov, "Domain-wall superconductivity in hybrid superconductor-ferromagnet structures," *Physical Review B*, vol. 68, p. 184508, Nov 2003.

[98] A. Y. Aladyshkin and V. V. Moshchalkov, "Thin-film superconductor-ferromagnet hybrids: Competition between nucleation of superconductivity at domain walls and domains' centers," *Physical Review B*, vol. 74, p. 064503, Aug 2006.

[99] D. Saint-James, "Angular dependence of the upper critical field of type II superconductors; theory," *Physics Letters*, vol. 16, pp. 218–220, Jun 1965.

[100] Z. Yang, K. Vervaeke, V. V. Moshchalkov, and R. Szymczak, "Modulation of superconductivity by a magnetic template in Nb/$BaFe_{12}O_{19}$ hybrids," *Physical Review B*, vol. 73, p. 224509, Jun 2006.

[101] C. D. Giorgio, F. Bobba, A. M. Cucolo, A. Scarfato, S. A. Moore, G. Karapetrov, D. D'Agostino, V. Novosad, V. Yefremenko, and M. Iavarone, "Observation of superconducting vortex clusters in S/F hybrids," *Scientific Reports*, vol. 6, p. 38557, Dec 2016.

[102] F. Bobba, C. D. Giorgio, A. Scarfato, M. Longobardi, M. Iavarone, S. A. Moore, G. Karapetrov, V. Novosad, V. Yefremenko, and A. M. Cucolo, "Vortex-antivortex coexistence in Nb-based superconductor/ferromagnet heterostructures," *Physical Review B*, vol. 89, p. 214502, Jun 2014.

[103] F. S. Bergeret, A. F. Volkov, and K. B. Efetov, "Long-range proximity effects in superconductor-ferromagnet structures," *Physical Review Letters*, vol. 86, pp. 4096–4099, Apr 2001.

[104] C.-R. Hu, "Midgap surface states as a novel signature for dxa2-xb2-wave superconductivity," *Physical Review Letters*, vol. 72, pp. 1526–1529, Mar 1994.

[105] R. Mélin and S. Peysson, "Crossed andreev reflection at ferromagnetic domain walls," *Physical Review B*, vol. 68, p. 174515, Nov 2003.

[106] F. S. Bergeret, A. F. Volkov, and K. B. Efetov, "Odd triplet superconductivity and related phenomena in superconductor-ferromagnet structures," *Reviews of Modern Physics*, vol. 77, pp. 1321–1373, Nov 2005.

[107] Y. V. Fominov, A. A. Golubov, T. Y. Karminskaya, M. Y. Kupriyanov, R. G. Deminov, and L. R. Tagirov, "Superconducting triplet spin valve," *JETP Letters*, vol. 91, pp. 308–313, Mar 2010.

[108] X. L. Wang, A. D. Bernardo, N. Banerjee, A. Wells, F. S. Bergeret, M. G. Blamire, and J. W. A. Robinson, "Giant triplet proximity effect in superconducting pseudo spin valves with engineered anisotropy," *Physical Review B*, vol. 89, p. 140508, Apr 2014.

[109] N. Banerjee, C. B. Smiet, R. G. J. Smits, A. Ozaeta, F. S. Bergeret, M. G. Blamire, and J. W. A. Robinson, "Evidence for spin selectivity of triplet pairs in superconducting spin valves," *Nature Communications*, vol. 5, p. 3048, Jan 2014.

[110] L. R. Tagirov, "Low-field superconducting spin switch based on a superconductor/ferromagnet multilayer," *Physical Review Letters*, vol. 83, pp. 2058–2061, Sep 1999.

[111] M. D. Lawrence and N. Giordano, "Proximity effects in superconductor-ferromagnet junctions," *Journal of Physics: Condensed Matter*, vol. 11, pp. 1089–1094, Jan 1999.

[112] M. Houzet and A. I. Buzdin, "Long range triplet josephson effect through a ferromagnetic trilayer," *Physical Review B*, vol. 76, p. 060504, Aug 2007.

[113] R. S. Keizer, S. T. B. Goennenwein, T. M. Klapwijk, G. Miao, G. Xiao, and A. Gupta, "A spin triplet supercurrent through the half-metallic ferromagnet CrO2," *Nature*, vol. 439, pp. 825–827, Feb 2006.

[114] T. S. Khaire, M. A. Khasawneh, W. P. Pratt, and N. O. Birge, "Observation of spin-triplet superconductivity in co-based josephson junctions," *Physical Review Letters*, vol. 104, p. 137002, Mar 2010.

[115] Y. Kalcheim, T. Kirzhner, G. Koren, and O. Millo, "Long-range proximity effect in $La_{2/3}Ca_{1/3}MnO_3/(100)YBa_2Cu_3O_{7-\delta}$ ferromagnet/superconductor bilayers: Evidence for induced triplet superconductivity in the ferromagnet," *Physical Review B*, vol. 83, p. 064510, Feb 2011.

[116] V. I. Zdravkov, J. Kehrle, G. Obermeier, D. Lenk, H.-A. K. von Nidda, C. MÃ¼ller, M. Y. Kupriyanov, A. S. Sidorenko, S. Horn, R. Tidecks, and L. R. Tagirov, "Experimental observation of the triplet spin-valve effect in a superconductor-ferromagnet heterostructure," *Physical Review B*, vol. 87, p. 144507, Apr 2013.

[117] A. F. Volkov, Y. V. Fominov, and K. B. Efetov, "Long-range odd triplet superconductivity in superconductor-ferromagnet structures with néel walls," *Physical Review B*, vol. 72, p. 184504, Nov 2005.

[118] J. W. A. Robinson, J. D. S. Witt, and M. G. Blamire, "Controlled injection of spin-triplet supercurrents into a strong ferromagnet," *Science*, vol. 329, pp. 59–61, Jun 2010.

[119] J. W. A. Robinson, G. B. Halász, A. I. Buzdin, and M. G. Blamire, "Enhanced supercurrents in josephson junctions containing nonparallel ferromagnetic domains," *Physical Review Letters*, vol. 104, p. 207001, May 2010.

[120] D. Sprungmann, K. Westerholt, H. Zabel, M. Weides, and H. Kohlstedt, "Evidence for triplet superconductivity in Josephson junctions with barriers of the ferromagnetic Heusler alloy Cu_2MnAl," *Physical Review B*, vol. 82, p. 060505, Aug 2010.

[121] F. S. Bergeret and I. V. Tokatly, "Spin-orbit coupling as a source of long-range triplet proximity effect in superconductor-ferromagnet hybrid structures," *Physical Review B*, vol. 89, Apr 2014.

[122] J. R. Eskilt, M. Amundsen, N. Banerjee, and J. Linder, "Long-ranged triplet supercurrent in a single in-plane ferromagnet with spin-orbit coupled contacts to superconductors," *Physical Review B*, vol. 100, p. 224519, Dec 2019.

[123] M. Eschrig, J. Kopu, J. C. Cuevas, and G. Schön, "Theory of half-metal/superconductor heterostructures," *Physical Review Letters*, vol. 90, p. 137003, Apr 2003.

[124] C. Cohen-Tannoudji, F. Laloe, and B. Diu, *Quantum Mechanics.* New York, NY: Wiley, 1977, vol. 2.

[125] W. Nolting, *Grundkurs Theoretische Physik 5/2: Quantenmechanik - Methoden und Anwendungen.* Springer-Verlag GmbH, 2005.

[126] T. Brückel, *Neutron Scattering Lectures.* Forschungszentrum Jülich GmbH, 2015, vol. 106, ch. 2 - A Neutron Primer, p. 2.8.

[127] W. Nolting, *Grundkurs Theoretische Physik 3.* Springer-Verlag GmbH, 2013.

[128] M. Waschk, "Interference phenomena in $La_{1/3}Sr_{2/3}FeO_3$ / $La_{2/3}Sr_{1/3}MnO_3$ heterostructures and a quest for p-electron magnetism," Ph.D. dissertation, RWTH Aachen University, 2017.

[129] J. Daillant and A. Gibaud, Eds., *X-ray and Neutron Reflectivity.* Springer Berlin Heidelberg, 2009.

[130] T. Chatterji, *Neutron Scattering from Magnetic Materials.* Elsevier, 2006.

[131] E. Kentzinger, *Neutron Scattering Lectures.* Forschungszentrum Jülich GmbH, 2015, vol. 106, ch. 9 - Neutron reflectometry.

[132] E. Kentzinger, U. Rücker, B. Toperverg, F. Ott, and T. Brückel, "Depth-resolved investigation of the lateral magnetic correlations in a gradient nanocrystalline multilayer," *Phys Rev B*, vol. 77, p. 104435, Mar 2008.

[133] L. G. Parratt, "Surface studies of solids by total reflection of x-rays," *Physical Review*, vol. 95, pp. 359–369, Jul 1954.

[134] M. Björck and G. Andersson, "GenX: an extensible x-ray reflectivity refinement program utilizing differential evolution," *Journal of Applied Crystallography*, vol. 40, pp. 1174–1178, Nov 2007.

[135] C. Fermon, F. Ott, B. Gilles, A. Marty, A. Menelle, Y. Samson, G. Legoff, and G. Francinet, "Towards a 3D magnetometry by neutron reflectometry," *Physica B: Condensed Matter*, vol. 267-268, pp. 162–167, Jun 1999.

[136] L. I. Schiff, *Quantum mechanics*, M. Hill, Ed., 1949.

[137] U. Rücker, *Neutron Scattering Lectures.* Forschungszentrum Jülich GmbH, 2015, vol. 106, ch. 10 - Magnetic Nanostructures.

[138] C. Fermon, "Neutron reflectometry with polarization analysis: A theory and a new spectrometer," *Physica B: Condensed Matter*, vol. 213-214, pp. 910–913, Aug 1995.

[139] M. Pannetier, F. Ott, C. Fermon, and Y. Samson, "Surface diffraction on magnetic nanostructures in thin films using grazing incidence SANS," *Physica B: Condensed Matter*, vol. 335, pp. 54–58, Jul 2003.

[140] J.-Y. Chauleau, W. Legrand, N. Reyren, D. Maccariello, S. Collin, H. Popescu, K. Bouzehouane, V. Cros, N. Jaouen, and A. Fert, "Chirality in magnetic multilayers probed by the symmetry and the amplitude of dichroism in x-ray resonant magnetic scattering," *Physical Review Letters*, vol. 120, p. 037202, Jan 2018.

[141] Jülich Centre for Neutron Science, "GALAXI: Gallium anode low-angle x-ray instrument," *Journal of large-scale research facilities JLSRF*, vol. 2, Mar 2016.

[142] B. P. Toperverg, "Polarized neutron reflectometry of magnetic nanostructures," *The Physics of Metals and Metallography*, vol. 116, pp. 1337–1375, dec 2015.

[143] P. M. D. Wolff, "R. Hosemann und S. N. Bagchi: direct analysis of diffraction by matter," *Berichte der Bunsengesellschaft für physikalische Chemie*, vol. 67, pp. 134–135, jan 1963.

[144] R. Lazzari, "IsGISAXS: a program for grazing-incidence small-angle x-ray scattering analysis of supported islands," *Journal of Applied Crystallography*, vol. 35, pp. 406–421, Jul 2002.

[145] D. Korolkov, P. Busch, L. Willner, E. Kentzinger, U. Rücker, A. Paul, H. Frielinghaus, and T. Brückel, "Analysis of randomly oriented structures by grazing-incidence small-angle neutron scattering," *Journal of Applied Crystallography*, vol. 45, pp. 245–254, Mar 2012.

[146] C. Kittel, "Theory of the structure of ferromagnetic domains in films and small particles," *Physical Review*, vol. 70, pp. 965–971, Dec 1946.

[147] M. A. Herman and H. Sitter, *Molecular Beam Epitaxy.* Springer Berlin Heidelberg, 2013.

[148] A. Förster, *Fundamentals of Nanoelectronics*, 2003, ch. C2 - Layer Deposition I: Physical Vapor Deposition.

[149] K. L. Chopra, "Thin film phenomena," New York, 1969.

[150] V. Gehanno, A. Marty, B. Gilles, and Y. Samson, "Magnetic domains in epitaxial ordered FePd(001) thin films with perpendicular magnetic anisotropy," *Physical Review B*, vol. 55, pp. 12 552–12 555, May 1997.

[151] G. Sauerbrey, "Verwendung von Schwingquarzen zur Wägung dünner Schichten und zur Mikrowägung," Zeitschrift für Physik, vol. 155, pp. 206–222, Apr 1959.

[152] D. B. Williams and C. B. Carter, *Transmission Electron Microscopy.* Springer-Verlag New York Inc., 2009.

[153] J. Haeni, C. Theis, and D. Schlom, *Journal of Electroceramics*, vol. 4, pp. 385–391, 2000.

[154] I. Lüth, *Festkörperphysik.* Springer Berlin Heidelberg, 2009.

[155] B. Fultz and J. Howe, *Transmission Electron Microscopy and Diffractometry of Materials.* Springer-Verlag GmbH, 2012.

[156] Ernst Ruska-Centre for Microscopy and Spectroscopy with Electrons (ER-C) et al., "FEI Titan G2 80-200 CREWLEY," *Journal of large-scale research facilities JLSRF*, vol. 2, A43, Feb 2016.

[157] Ernst Ruska-Centre for Microscopy and Spectroscopy with Electrons (ER-C) et al., "FEI Titan G3 50-300 PICO," *Journal of large-scale research facilities JLSRF*, vol. 1, Nov 2015.

[158] H. Lüth, *Solid Surfaces, Interfaces and Thin Films.* Springer International Publishing, 2015.

[159] L. R. Doolittle, "Algorithms for the rapid simulation of Rutherford backscattering spectra," *Nuclear Instruments and Methods in Physics Research Section B: Beam Interactions with Materials and Atoms*, vol. 9, pp. 344–351, Jun 1985.

[160] Agilent Technologies, Inc. 2007, "Agilent technologies 5400 scanning probe microscope - user's guide," Tech. Rep., 2007.

[161] J. E. Jones, "On the determination of molecular fields. —II. from the equation of state of a gas," *Proceedings of the Royal Society of London. Series A, Containing Papers of a Mathematical and Physical Character*, vol. 106, pp. 463–477, Oct 1924.

[162] M. McElfresh, "Fundamentals of magnetism and magnetic measurements featuring Quantum Design's Magnetic Property Measurement System," Quantum Design, 1994.

[163] F. M. Smits, "Measurement of sheet resistivities with the four-point probe," *Bell System Technical Journal*, vol. 37, pp. 711–718, May 1958.

[164] V. Pipich and Z. Fu, "KWS-3: Very small angle scattering diffractometer with focusing mirror," *Journal of large-scale research facilities JLSRF*, vol. 1, Aug 2015.

[165] E. Kentzinger, L. Dohmen, B. Alefeld, U. Rücker, J. Stellbrink, A. Ioffe, D. Richter, and T. Brückel, "KWS-3, the new focusing-mirror ultra small-angle neutron scattering instrument and reflectometer at jülich," *Physica B: Condensed Matter*, vol. 350, pp. E779–E781, Jul 2004.

[166] W. Chen, S. Watson, H. Burrall, K. Krycka, and J. A. Borchers, "NIST Center for neutron research - CHRNS VSANS."

[167] K. Krycka, R. Booth, J. Borchers, W. Chen, C. Conlon, T. Gentile, C. Hogg, Y. Ijiri, M. Laver, B. Maranville, S. Majetich, J. Rhyne, and S. Watson, "Resolving 3d magnetism in nanoparticles using polarization analyzed SANS," *Physica B: Condensed Matter*, vol. 404, pp. 2561–2564, Sep 2009.

[168] K. Momma and F. Izumi, "Vesta: a three-dimensional visualization system for electronic and structural analysis." *Journal of Applied Crystallography*, vol. 41, pp. 653–658, Jun 2008.

[169] T. Ichitsubo and K. Tanaka, "Single-crystal elastic constants of disordered and ordered FePd," *Journal of Applied Physics*, vol. 96, pp. 6220–6223, Dec 2004.

[170] P. Aitchison, J. Chapman, V. Gehanno, I. Weir, M. Scheinfein, S. McVitie, and A. Marty, "High resolution measurement and modelling of magnetic domain structures in epitaxial FePd(001) L10 films with perpendicular magnetisation," *Journal of Magnetism and Magnetic Materials*, vol. 223, pp. 138–146, Jan 2001.

[171] V. Gehanno, R. Hoffmann, Y. Samson, A. Marty, and S. Auffret, "In plane to out of plane magnetic reorientation transition in partially ordered FePd thin films," *The European Physical Journal B*, vol. 10, pp. 457–464, Aug 1999.

[172] F. Virot, L. Favre, R. Hayn, and M. D. Kuz'min, "Theory of magnetic domains in uniaxial thin films," *Journal of Physics D: Applied Physics*, vol. 45, p. 405003, Sep 2012.

[173] D. Ravelosona, A. Cebollada, F. Briones, C. Diaz-Paniagua, M. A. Hidalgo, and F. Batallan, "Domain-wall scattering in epitaxial FePd ordered alloy films with perpendicular magnetic anisotropy," *Physical Review B*, vol. 59, pp. 4322–4326, Feb 1999.

[174] T. E. Hutchinson, "Epitaxial growth on MgO of niobium films investigated by electron microscopy," *Journal of Applied Physics*, vol. 36, pp. 270–273, Jan 1965.

[175] B. L. Henke, E. M. Gullikson, and J. C. Davis, "X-ray interactions: photoabsorption, scattering, transmission, and reflection at E=50-30000 eV, Z=1-92," *Atomic Data and Nuclear Data Tables*, vol. 54, pp. 181–342, Jul. 1993.

[176] B. E. Warren, *X-ray Diffraction: by B. E. Warren.* Addison-Wesley Pub. Co, 1969.

[177] D. Halley, Y. Samson, A. Marty, C. Beigné, and B. Gilles, "Surface morphology and chemical ordering in FePd/Pd(001) thin layers," *Surface Science*, vol. 481, pp. 25–32, Jun 2001.

[178] D. Halley, Y. Samson, A. Marty, P. Bayle-Guillemaud, C. Beigné, B. Gilles, and J. E. Mazille, "Anomaly of strain relaxation in thin ordered FePd layers," *Physical Review B*, vol. 65, p. 205408, May 2002.

[179] J. R. Skuza, C. Clavero, K. Yang, B. Wincheski, and R. A. Lukaszew, "Microstructural, magnetic anisotropy, and magnetic domain structure correlations in epitaxial FePd thin films with perpendicular magnetic anisotropy," *IEEE Transactions on Magnetics*, vol. 46, pp. 1886–1889, Jun 2010.

[180] O. Durand, J. Childress, P. Galtier, R. Bisaro, and A. Schuhl, "Origin of the uniaxial magnetic anisotropy in fe films grown by molecular beam epitaxy," *Journal of Magnetism and Magnetic Materials*, vol. 145, pp. 111–117, Mar 1995.

[181] W. Weber, C. H. Back, A. Bischof, C. Würsch, and R. Allenspach, "Morphology-induced oscillations of the magnetic anisotropy in ultrathin co films," *Physical Review Letters*, vol. 76, pp. 1940–1943, Mar 1996.

[182] A. Stellhorn, A. Sarkar, E. Kentzinger, J. Barthel, A. D. Bernardo, S. Nandi, P. Zakalek, J. Schubert, and T. Brückel, "Tailoring superconducting states in superconductor-ferromagnet hybrids," *New Journal of Physics*, vol. 22, p. 093001, Sep 2020.

[183] A. Stellhorn, A. Sarkar, E. Kentzinger, M. Waschk, P. Schöffmann, S. Schröder, G. Abuladze, Z. Fu, V. Pipich, and T. Brückel, "Control of the stripe domain pattern in L10-ordered FePd thin films," *Journal of Magnetism and Magnetic Materials*, vol. 476, pp. 483–486, Apr 2019.

[184] S. V. Grigoriev, Y. O. Chetverikov, D. Lott, and A. Schreyer, "Field induced chirality in the helix structure of Dy/Y multilayer films and experimental evidence for dzyaloshinskii-moriya interaction on the interfaces," *Physical Review Letters*, vol. 100, p. 197203, May 2008.

[185] S. V. Maleyev, "Investigation of spin chirality by polarized neutrons," *Physical Review Letters*, vol. 75, pp. 4682–4685, Dec 1995.

[186] H. W. Weber, E. Seidl, C. Laa, E. Schachinger, M. Prohammer, A. Junod, and D. Eckert, "Anisotropy effects in superconducting niobium," *Physical Review B*, vol. 44, pp. 7585–7600, Oct 1991.

[187] S. K. Sinha, E. B. Sirota, S. Garoff, and H. B. Stanley, "X-ray and neutron scattering from rough surfaces," *Physical Review B*, vol. 38, pp. 2297–2311, Aug 1988.

[188] S. Komori, A. D. Bernardo, A. Buzdin, M. Blamire, and J. Robinson, "Magnetic exchange fields and domain wall superconductivity at an all-oxide superconductor-ferromagnet insulator interface," *Physical Review Letters*, vol. 121, p. 077003, aug 2018.

[189] A. D. Bernardo, S. Komori, G. Livanas, G. Divitini, P. Gentile, M. Cuoco, and J. W. A. Robinson, "Nodal superconducting exchange coupling," *Nature Materials*, vol. 18, pp. 1194–1200, sep 2019.

[190] U. Welp, W. K. Kwok, G. W. Crabtree, K. G. Vandervoort, and J. Z. Liu, "Magnetic measurements of the upper critical field ofYBa2cu3o7-δsingle crystals," *Physical Review Letters*, vol. 62, pp. 1908–1911, apr 1989.

[191] M. Faley, "Epitaxial oxide heterostructures for ultimate high-tc quantum interferometers," in *Applications of High-Tc Superconductivity.* InTech, Jun 2011.

[192] N. Plakida, *High-Temperature Cuprate Superconductors.* Springer Berlin Heidelberg, 2010.

[193] V. Peña, Z. Sefrioui, D. Arias, C. Leon, J. Santamaria, M. Varela, S. J. Pennycook, and J. L. Martinez, "Coupling of superconductors through a half-metallic ferromagnet: Evidence for a long-range proximity effect," *Physical Review B*, vol. 69, p. 224502, Jun 2004.

[194] T. Golod, A. Rydh, V. M. Krasnov, I. Marozau, M. A. Uribe-Laverde, D. K. Satapathy, T. Wagner, and C. Bernhard, "High bias anomaly in $YBa_2Cu_3O_{7-x}/LaMnO_{3+\delta}/YBa_2Cu_3O_{7-x}$superconductor/ferromagnetic insulator/superconductor junctions: Evidence for a long-range superconducting proximity effect through the conduction band of a ferromagnetic insulator," *Physical Review B*, vol. 87, p. 134520, Apr 2013.

[195] D. Nečas and P. Klapetek, "Gwyddion: an open-source software for SPM data analysis," *Open Physics*, vol. 10, pp. 181–188, Jan 2012.

Thesis-related publications

A. Stellhorn, A. Sarkar, E. Kentzinger, J. Barthel, A. D. Bernardo, S. Nandi, P. Zakalek, J. Schubert, and T. Brückel, „Tailoring superconducting states in superconductor-ferromagnet hybrids,“ *New Journal of Physics*, vol. 22, p. 093001, Sep 2020.

A. Stellhorn, A. Sarkar, E. Kentzinger, M. Waschk, P. Schöffmann, S. Schröder, G. Abuladze, Z. Fu, V. Pipich, and T. Brückel, „Control of the stripe domain pattern in L10-ordered FePd thin fims,“ *Journal of Magnetism and Magnetic Materials*, vol. 476, pp. 483-486, Apr 2019.

List of Figures

2.1 Density of states $D(E)$ for a metallic ferromagnet with majority spin up and minority spin down bands filled up to the Fermi energy E_F. 6
2.2 Sketch of a thin film with magnetic domains in out-of-plane direction, separated by Bloch domain walls and with closure domains at the sample surfaces. 9
2.3 (a,b) Micromagnetic simulation for FePd layers with 40 nm thickness and (a) Q=0.35 and (b) Q=1.5, taken from [22]. (c) Bubble and band domain growth in a perpendicular recording medium (Co with 20 at% Cr) of 622 nm thickness, taken from [16]. 10
2.4 Attractive phonon interaction vs. repulsive Coulomb interaction of a spin-singlet Cooper pair. 12
2.5 Superconductor (blue) to insulator (grey) interface with spatially varying Cooper pair density $n_\mathrm{S}(x)$ and the superconducting parameters $\xi_\mathrm{GL}(x)$ and $\lambda_\mathrm{L}(x)$ in an applied magnetic field $\mu_0 H_\mathrm{ext}(x)$. 16
2.6 Shubnikov phase of a type-II bulk superconductor, inspired from [43]. (a) Radial distribution of the Cooper pair density n_S (blue), the magnetic field B inside the vortices (green), and the supercurrent density J_S enclosing the magnetic field (orange). (b) Top view on a triangular vortex lattice (same color code). 17
2.7 Spatial variation of $\psi(x)$ for surface superconductivity in a parallel magnetic field $B_\mathrm{c2}<\mu_0 H_\mathrm{ext}<B_\mathrm{c3}$ at a superconductor to vacuum interface. 19
2.8 Magnetization with respect to external magnetic field for a perfect undefected bulk type-II superconductor with critical fields B_c1 and B_c2. 22

2.9 Magnetic hysteresis for superconductors including irreversibility mechanisms and bulk pinning (KA-model), taken from [64]. (1) Narrow thin film (i.e., $W < \lambda_{\mathrm{L}}^2/d$ and $d < \lambda_{\mathrm{L}}$) with $H^* = \frac{8\pi j_{\mathrm{p}} \lambda_{\mathrm{L}}^2}{cW}$, and (2) wide thick film with $H^* = \frac{2\pi j_{\mathrm{p}} W}{c}$, with the depinning current density j_{p} and the velocity of light c. The magnetization is given in units of $\frac{j_{\mathrm{p}} W}{8c}$. Note (i) the plot of negative magnetization and (ii) the definition of values in cgs-units. 23

2.10 Magnetic hysteresis of bulk Nb adapted from [67]. 24

2.11 Parallel critical field $B_{\mathrm{c2},||}(t)$ measured for Nb thin films, taken from [53]. Arrows indicate the temperature t^* below which surface superconductivity comes into play due to a decrease of ξ_{GL} with decreasing temperature, details can be taken from the main text. Solid and dashed lines show the square-root and linear behavior above and below t^*, respectively. . 25

2.12 Thickness dependence of (a) T_{c} and the residual resistivity ρ_0 and (b) $\lambda_{\mathrm{L}}(0)$ at zero temperature for Nb thin films, taken from [74]. 26

2.13 S(blue)/N(orange) heterostructure with (a) the order parameter $\psi(x)$ at the interface and the penetration length ξ_{N} of Cooper pairs into N and (b) a schematic sketch of the Andreev reflection. A Cooper pair inside S penetrates in form of quasiparticles with opposite spin and momentum ("electron-like" and "hole-like" quasiparticles) into N and vice versa. Additionally plotted are the density of states $D_{\mathrm{S}}(E)$ inside the superconductor and $D_{\mathrm{N}}(E)$ inside the normal metal, the up and down spin-bands of the normal metal, and the Fermi energy E_{F}. 27

2.14 Pair breaking effects in spin-singlet Cooper pair components. The orbital pair breaking (left) leads to a circulation of both electrons via the Lorentz force and destroys the Cooper pair above B_{c2}. The Pauli pair breaking (right) leads to an alignment of the spins in a Cooper pair and thus destroys spin-singlet components of Cooper pairs. 28

2.15 S/F interface with Andreev reflection of the two spins of the Cooper pair into different energy bands (red for spin down and white for spin up bands) of the F layer with a resutling difference in energy of $2E_{\mathrm{ex}}$. . . . 29

2.16 Comparison of S/N and S/F_{hom} proximity effects with a homogeneous magnetization inside F_{hom}. (a) $\psi(x)$ of the spin-singlet components decays monotonically over x inside N. Inside S/F_{hom}, the shift of energy bands for up and down spin orientation leads to an oscillation in $\psi(x)$ and a phase shift for the spin-singlet (black line) and spin-triplet (grey line) components with $S_z = 0$. (b) Dependence of T_{c} on the thickness of the proximity coupled layer. In S/N, T_{c} decreases monotonically with increasing d_{N}, whereas in S/F_{hom}, T_{c} oscillates with increasing d_{F}. Figure (b) is inspired from [85]. 30

2.17 Sketch of the inverse proximity effect on the magnetization: the homogeneous magnetization orientation of the F layer can cause spin-singlet Cooper pairs with a spin up electron inside F and a spin down electron inside S. This leads to a reduced magnetization at the interface of the F layer and a reverse magnetization induced at the interface of the S layer. 31

2.18 Schematic representation of an S/F system with S being a paramagnetic metal above T_{c}. Domain-Wall-Superconductivity (DWS) nucleates in zero applied field (top) and Reverse-Domain-Superconductivity (RDS) nucleates in an applied field perpendicular to the sample surface (bottom). Blue color denotes superconducting nucleation inside S, whereas yellow and red represent a normal conducting state of F and S in different orientations of magnetization. In the RDS state, in the direction of applied field the superconductor is in the paramagnetic state with stray fields penetrating from the F layer. On top of magnetic domains in reverse direction to the applied field, superconductivity nucleates near T_{c}. If $2\xi_{\mathrm{GL}} < D_{\mathrm{domain}}$, isolated superconductivity is possible. 33

2.19 The transformation of the phase transition line $T_{\mathrm{c}}(H_{\mathrm{ext}})$ with increasing thickness d_{S} of the superconducting film: $d_{\mathrm{S}} \to 0$ (red), $d_{\mathrm{S}} = 180\,\mathring{A}$ (green), $d_{\mathrm{S}} = 400\,\mathring{A}$ (blue), $d_{\mathrm{S}} = 1000\,\mathring{A}$ (magenta), and $d_{\mathrm{S}} = 2000\,\mathring{A}$ (black). The dashed line is the reference dependence for M_{S}=0, adapted from [98]. 35

2.20 Low-temperature MFM measurement of the vortex formation in a Nb/Py heterostructure below T_{c} and acquired in a field of 19 Oe of the MFM-tip, i.e. perpendicular to the sample surface, taken from [101]. 36

2.21 Comparison of the penetration of Cooper pair components into a homogeneous ferromagnet (top) and an inhomogeneous ferromagnet (bottom) inside a S/F heterostructure. Black lines denote spin-singlet components, grey spin-triplet components with $S_\mathrm{z}=0$ and red spin-triplet components with $S_\mathrm{z}=\pm1$. At the S/F$_\mathrm{inhom}$ interface, the magnetization rotation leads to a formation of spin-triplet components with $S_z=\pm1$ and large coherence length. 38

2.22 F (red)/S (blue)/F (red) structure with homogeneous magnetization inside the F layers and a critical temperature T_c^P for a parallel magnetization configuration and T_c^AP for an antiparallel magnetization configuration. If the device is operated at $T_\mathrm{c}^\mathrm{P} < T_\mathrm{op} < T_\mathrm{c}^\mathrm{AP}$, it can be switched from normal to superconducting resistance state by switching the two ferromagnets in parallel or antiparallel configuration in an external magnetic field. 39

2.23 S (blue)/F1 (light red)/F2 (dark red) structure. (a) non-collinear magnetization configuration, where additionaly to the short ranged $(\uparrow\downarrow - \downarrow\uparrow)$ and $(\uparrow\downarrow + \downarrow\uparrow)$ components also the long ranged $(\uparrow\uparrow)$ and $(\downarrow\downarrow)$ components appear. Black lines denote spin-singlet components, grey spin-triplet components with $S_\mathrm{z}=0$ and red spin-triplet components with $S_\mathrm{z}=\pm1$. (b) antiparallel magnetization configuration, and (c) parallel magnetization configuration, with only short ranged Cooper pair penetration. 40

2.24 (a) Dependence of the critical temperature T_c on the magnetic field for different relative magnetization orientations of the F1 and F2 layers, marked in dark and light red. The thin blue layer between F1 and F2 denotes a normal conducting interlayer to independently switch the magnetization inside the two F layers. (b) Resistance measurements with respect to an external field H at constant temperature for the sample shown in (a). Figure taken from [116]. 41

3.1 Scattering of the incident wave (i) at a point-like scatterer with V being the δ-function and the scattered wave in direction $\vec{r}$ and (ii) after multiple scattering within a finite sample volume with scattering directions $\vec{r}\,'$ inside the sample. 45

3.2 Ewald sphere of radius $|\vec{k}| = |\vec{k}\,'|$. Scattering can only occur at reciprocal lattice points which fall on the Ewald sphere. Adapted from [128]. . . . 46

3.3 Overview on the measurement configurations for specular and GISANS reflecometry methods: For specular reflectometry, specularly scattered signals at $\theta = \theta_i = \theta_f$ are measured as function of θ, whereas in GISANS configuration at fixed θ_i the $Q_y - Q_z$-map is measured on a 2D detector. 49
3.4 Thin film sample with lateral domains of different density ρ_i and/or magnetic moments $\vec{m}_i$, and a layered structure denoted with light blue lines. The coherence volume of the incoming beam spreads over $L{=}(L_x, L_y, L_z)$. 50
3.5 Measurement setup for specular reflection: the outgoing beam is scattered in an angle $\theta_f = \theta_i$ resulting in an out-of-plane oriented $Q = Q_z$, and refracted in direction θ_r. Red color denotes the sample and blue color the detector. 51
3.6 (a) Measurement setup for off-specular reflection where Q_x and Q_z are probed. (b) Measurement setup for GISANS where Q_y and Q_z are probed. On the detector, the GISANS line and specular line are drawn in red. 53
3.7 Penetration depth of the neutron beam Λ into Nickel as function of the incident angle α_i at a neutron wavelength of 6 Å. 54
3.8 (a) Non-perturbed scattering potential $V_{0,l}$ of a homogeneous sample and (b) pertubation potential $V_l(\vec{s})$ of a sample with lateral inhomogeneous structural or magnetic density. 55
3.9 (a) Side-view of one unit with one up- and one down-oriented domain of FePd with high PMA and a domain width of D_domain. (b) Top-view of three not correlated units with various in-plane rotation angles ξ and a mean correlation length L_x. Inspired by [145]. 60
3.10 3x3 μm measurements of the surface domain pattern of (a) FePd with high PMA and (b) FePd with low PMA. Yellow rectangular boxes mark two units of aligned domains in both images. 60

4.1 Three growth modes in heteroepitaxial deposition: (a) Layer-by-layer growth, (b) island-growth due to low binding of adatoms to the substrate surface, and (c) mixed layer-by-layer and island-growth. Taken from [128]. 63
4.2 Setup of the OMBE system: (a) overview on the Load Lock, the Buffer line (including LEED and AES measurement setups), the transfer rod to move samples to the deposition chamber, and the main chamber. (b) Side view on the main chamber with the vacuum system and the effusion cells and electron beam evaporators at the bottom, and the upper part of the OMBE system as described in the text. Based on [128]. 64

4.3 RHEED measurement setup and scattering intensities for reflection on a perfect surface and bulk crystal structure, forming sharp spots on the RHEED screen due to scattering at 1D reciprocal lattice rods. Taken from [128]. 66
4.4 RHEED patterns of (a) a smooth MgO substrate after annealing, sharp Kikuchi lines denote a flat surface and high crystalline order, (b) an FePd layer with elongated RHEED intensities and smeared-out Kikuchi lines which accounts for some crystalline imperfections or terraces on the surface and (c) an Nb layer with a rough surface and island growth, visible in the multiple, smeared-out and point-like scattering features without any visible Kikuchi lines. 67
4.5 LEED measurement setup: The electron beam impinges on the sample surface in an angle of 90° and is reflected and accelerated towards the LEED screen by an accelerator grid. Taken from [128]. 68
4.6 LEED images of (a) an $L1_0$-ordered FePd lattice with an in-plane rectangular lattice and (b) an in-plane disordered lattice of a Nb layer. 68
4.7 Instrument Setup of the D8 Reflectometer and Diffractometer with the X-ray tube (left), the sample stage (middle) and the detector (right), taken from [128]. 69
4.8 Detector arrangement for Bright-Field, Dark-Field, and High-Angle Annular Dark-Field measurements in STEM [152]. The path of scattered and detected electrons after transition through the sample is depicted in red. 70
4.9 Measurement principle of AFM (a) and the respective force-distance potential with regions ”C” (contact), ”NC” (non-contact), and ”FO” (free oscillation). The influence on the tip’s resonance frequency and phase by stray fields of a domain structured sample is schematically given in (c). 73
4.10 Schematic instrument setup of the rf-SQUID and the sample environment: the sample is mounted in a straw and placed between pick-up coils to transfer the induced voltage to the rf-SQUID. Taken from [128]. 74
4.11 Instrument setup of GALAXI, taken from [141]. 75
4.12 Instrument setup of KWS-3, taken from [164]. 76
4.13 Instrument setup of vSANS, taken from [167]. 76

4.14 vSANS sample holder with two sample stages and the temperature sensor B mounted in between the sample positions for a precise temperature monitoring. 77

5.1 Layered structure of $L1_0$-phase materials with different atoms depicted by different colors. The black lines connect the tP2 unit cell with lattice parameters $a = b \neq c$, whereas the tP4 unit cell is shifted to the tP2 cell by an in-plane rotation of 45° (drawn with VESTA [168]). 80
5.2 Critical thickness d_c with respect to $Q = \frac{K_\mathrm{u}}{K_\mathrm{sh}}$ for uniaxial thin films, Figure adapted from Virot et al. [172]. The area above the dashed line denotes thicknesses and Q values leading to strong PMA, whereas between the dashed and solid lines a weak PMA is evolved. Below the solid line, no PMA occurs in the thin film. 82
5.3 Sample growth procedure: first, bare F and S layers are grown to determine suitable growth processes for high, low and medium PMA in the F layer, and layer thicknesses as well as substrate temperatures of the S-layer which determines $T_\mathrm{c}(d)$. In a second step, S/F samples are investigated and compared with S/I/F samples. 83
5.4 Heterostructure of (a) S/F samples with an EDX-STEM measurement of SF_mid and (b) S/I/F samples with a bright-field STEM measurement of $\mathrm{SIF}_\mathrm{high}$. In the schematically drawn layer stacks, violet color denotes Mg of the MgO layer, yellow color Pd, red color Fe, and green color Nb. 85
5.5 Growth mode (bottom) and expected domain formation (top) of FePd layers with high, low, and medium PMA, as well as their layer thicknesses. F_mid consists of two FePd layers with first low and second high PMA, which together yield a magnetic formation with intermediate PMA. Different colors and arrows denote the magnetic domains and their orientation, respectively. 86
5.6 RHEED measurements taken at room temperature after the growth of the FePd layers (top) and the Nb layers (bottom) of samples $\mathrm{SF}_\mathrm{high}(2)$, $\mathrm{SF}_\mathrm{low}(1)$, and $\mathrm{SF}_\mathrm{mid}(1)$. 87
5.7 LEED measurements taken after the growth of FePd (top) of the F samples and after Nb (bottom) of the S/F samples with high, low, and medium PMA. 88

5.8 RHEED (top) and LEED (bottom) of S(2) and S(3) grown at different substrate temperatures T_{s}. The RHEED images show an island growth at T_{s}=320 K and an ordered out-of-plane growth with surface reconstructions at T_{s}=820 K. In LEED, no in-plane structural order is observed in both cases. 88

5.9 X-ray reflectometry measurements of $\mathrm{F_{high}}(4)$, $\mathrm{F_{low}}(1)$ and $\mathrm{F_{mid}}(2)$ with respective fits regarding the layer thicknesses and values given in tables 9.1-9.6. The insets show the SLD as function of depth inside the sample. FePd with 1:1 and 1:0.85 composition exhibits different SLD values. . 91

5.10 (a) XRR measurement and fit regarding the same thicknesses and compositions of $\mathrm{SIF_{high}}(1)$ as taken for the RBS simulation shown in (b), all values are listed in table 9.5. From the RBS measurement, a oxygen content of ∼20% was revealed in the Nb layer, leading to a reduced SLD of Nb within the XRR fit. 92

5.11 (a) FePd(001) and FePd(002) peaks of XRD measurements regarding samples $\mathrm{F_{high}}(4)$, $\mathrm{F_{low}}(2)$ and $\mathrm{F_{mid}}(3)$. The relation of integrated intensities from the (001) to the (002) reflection is proportional to the long-range order parameter S shown in table (b). All values of S are less than 1, for example resulting from plane defects inside the FePd layer of $\mathrm{SF_{mid}}(1)$ as marked by red arrows in (c). 94

5.12 (a) 3x3μm AFM measurement of sample $\mathrm{F_{high}}(4)$, (b) $\mathrm{F_{low}}(2)$ (with 2.5x3μm) and $\mathrm{F_{mid}}(2)$ (3x3μm). (d) Plane defects along (111) in a thin film FePd layer of strong PMA can cause surface terraces visible in sample $\mathrm{F_{high}}$ in (a), Figure inspired from [17]. 95

5.13 3x3μm AFM measurements of sample $\mathrm{F_{high}}(4)$ in the as-grown state with a flat surface (a) and after three weeks of sample aging with islands of ∼20 nm height (b). 95

5.14 Void formation in $\mathrm{SIF_{high}}(1)$: (a) HAADF-STEM measurement with side view on the Nb/MgO/FePd/Pd/Cr/MgO heterostructure, (b) HAADF-STEM EDX measurement where the FePd void is filled with MgO and Nb and (c) top-view on the void-formation given by a 3x3μm sized AFM measurement. 96

5.15 From left to right: $\mathrm{SF_{high}}(2)$, $\mathrm{SF_{low}}(1)$, and $\mathrm{SF_{mid}}(1)$, respectively. (a) Schematic view of the magnetic domain formation inside the FePd layer and the toplayer of Nb in direction of the c-axis of $\mathrm{L1_0}$-ordered FePd. (b) (3×3 µm) zero-field MFM measurements in the as-grown state of $\mathrm{SF_{high}}(2)$ and $\mathrm{SF_{mid}}(1)$ and after demagnetization of $\mathrm{SF_{low}}(1)$. (c) Hysteresis loops measured at 300 K with $H_{\mathrm{ext},||}$ in the surface plane and $H_{\mathrm{ext},\perp}$ perpendicular to the surface plane, adapted from [182]. All measurements are obtained at 300 K. 99
5.16 3x3µm MFM measurements of $\mathrm{F_{low}}(3)$ after application of (a) 0 mT, (b) 700mT in an out-of-plane applied external field and (c) after in-plane oscillating demagnetization, adapted from [183]. 100
5.17 (a) Schematic sample alignment with the magnetic stripes aligned along x to probe the domain structure with finite periodicity in y-direction and (b) aligned along y with infinite periodicity in y-direction. (c,b) Respective Q_y-Q_z-maps of the GISANS measurements shown in (a) and (b), at an incident angle of $\alpha_\mathrm{i} = 0.96°$ and a direct beam located at $Q_y = Q_z = 0\,\mathrm{nm}^{-1}$. The blue horizontal line denotes the GISANS line at $Q_z = 0.165\,\mathrm{nm}^{-1}$, which at the critical angle of total reflection corresponds to the Yoneda line. 101
5.18 (a) Q_y-Q_z-map of the room-temperature GISANS measurement on FePd. (b) Corresponding simulated Q_y-Q_z-map. (c) $I(Q_y)$ at the GISANS line with a small integration range of Q_z for the measurement (blue data points) and the simulation (red line). (d) Schematics of the shape and sizes of the simulated domain structure inside the FePd layer of the simulated layer stack given in table 9.9, including closure domains with in-plane magnetic moments and out-of-plane oriented magnetic domains. 103

6.1 (a) $M(H_{\mathrm{ext},\perp})$ of $\mathrm{SF_{high}}(2)$ measured at various temperatures indicated by the legend. (b) Hysteresis loops of S(5) with corresponding Nb thickness to $\mathrm{SF_{high}}(2)$ (d_{Nb}=39 nm, see tables 9.1-9.6). 109
6.2 $M(H_{\mathrm{ext},\perp})$ of $\mathrm{SF_{high}}(2)$, $\mathrm{SF_{low}}(1)$ and $\mathrm{SF_{mid}}(1)$ measured below and above T_c in an out-of-plane applied magnetic field, adapted from the supplementary information in [182]. 109
6.3 (a) $M(H_{\mathrm{ext},\perp})$ of $\mathrm{SF_{high}}(2)$ and its comparison sample $\mathrm{SIF_{high}}(1)$ at $T = 300\,\mathrm{K} > T_\mathrm{c}$ and (b) at $T = 5.6\,\mathrm{K} < T_\mathrm{c}$. 110

6.4 $\rho(T)$ measurements in a constant out-of-plane applied field, for $\mathrm{SF_{high}}(1)$ (a) and S(1) (b). (c) $\rho(H_{\mathrm{ext},\perp})$ at constant temperature for $\mathrm{SF_{high}}(1)$ (c) and for S(1) (d). 112
6.5 Schematic view on a DWS, RDS, and CS formation at different $\rho(H_{\mathrm{ext},\perp})$ (left) and $\rho(T)$ (right). 113
6.6 (a,b) $\rho(T)$ in a constant out-of-plane applied field, for $\mathrm{SF_{high}}(2)$ and $\mathrm{SIF_{high}}(1)$, respectively. (c) $\rho(H_{\mathrm{ext},\perp})$ at constant temperature for $\mathrm{SF_{high}}(2)$ and for the reference sample $\mathrm{SIF_{high}}(1)$ (d). 115
6.7 (a) $H_{\mathrm{ext},\perp}(T_{\mathrm{c}})$ as obtained from $\rho(T)$ measurements shown in (b). Blue arrows mark the direction of change in T_{c} for increasing applied fields. . 116
6.8 (a) Stray fields B_{d} in c-direction of the FePd crystallographic axes in a distance z=40 nm of the FePd layer in $\mathrm{SF_{high}}(2)$ with infinitely thin domain walls as shown in (b). D_{domain} denotes the thickness of FePd lateral domains and d_{FePd} the thickness of the FePd layer. 117
6.9 From left to right: S/F Samples with high, low, and medium PMA, respectively. (a) Schematic view of the domain formation inside the FePd layer in direction of the c-axis of L10-ordered FePd. (b) $\rho(T)$ in constant out-of-plane applied field. (c) $\rho(H_{\mathrm{ext},\perp})$ at constant temperature. 119
6.10 (a) External magnetic field $H_{\mathrm{ext},\perp}$ applied out-of-plane to the sample surface with respect to the reduced temperature $T_{\mathrm{c}}(H_{\mathrm{ext},\perp})/T_{\mathrm{c}}(0)$, obtained from $\rho(T)$ measurements. (b) Square of $H_{\mathrm{ext},\perp}$ with respect to $T_{\mathrm{c}}(H_{\mathrm{ext},\perp})/T_{\mathrm{c}}(0)$ as shown in (a). Black lines denote linear fits to the data points. 121
6.11 $\rho(H_{\mathrm{ext},||})$ at constant temperature for (a) $\mathrm{SF_{low}}(1)$ and (b) for the reference sample $\mathrm{SIF_{low}}(1)$. 124
6.12 (a) Schematic sketch of the penetration of Cooper pair components from S into an inhomogeneous F layer. Black lines denote spin-singlet components, grey spin-triplet components with $S_{\mathrm{z}} = 0$ and red spin-triplet components with $S_{\mathrm{z}} = \pm 1$. (b) Critical temperature T_{c} and (c) resistance R with respect to an external magnetic field H, taken from Zdravkov et al. [116]. 125
6.13 $H_{\mathrm{ext},||}(T_{\mathrm{c}})$ of $\mathrm{SF_{low}}$ (left), all data points are measured after saturation of the sample in a negative magnetic field. The corresponding hysteresis loop (right) is measured in both field sweep direcitons at $T = 3.5\,\mathrm{K}$, adapted from [182]. 126

6.14 $\rho(H_{\mathrm{ext},||})$ at various external magnetic field angles with respect to the sample surface: 0° denotes a magnetic field applied parallel to the <100> axis and 90° a magnetic field applied along the <001> axis (i.e. perpendicular to the sample surface). All measurements are obtained at $T = 4.5\,\mathrm{K}$. 127
6.15 From left to right: S/F Samples with high, low, and medium PMA, respectively. (Top) Schematic view of the domain formation inside the FePd layer in direction of the c-axis of L10-ordered FePd. (Bottom) $\rho(H_{\mathrm{ext},||})$ at constant temperature. 128

7.1 (a) Q_y-Q_z-map of $\mathrm{SF}_{\mathrm{high}}(1)$ at $T = 8.3\,\mathrm{K}$, above the superconducting critical temperature. (b) Integrated intensities I_{spec} and I_{GIS} over the areas displayed by black and red boxes in (a), respectively, and with dependence on temperature. The grey vertical line denotes $T_{\mathrm{c}} = (7.247 \pm 0.001)\,\mathrm{K}$ of $\mathrm{SF}_{\mathrm{high}}(1)$ at $0\,\mathrm{mT}$. 132
7.2 Sketch of DWS, RDS and CS formation in $\mathrm{SF}_{\mathrm{high}}(1)$ and the corresponding temperature dependences of ρ, M and I_{spec}. 133
7.3 Q_y-Q_z-maps of the four different GISANS channels measured at $T_{\mathrm{B}} = (10.10 \pm 0.02)\,\mathrm{K}$ on $\mathrm{SF}_{\mathrm{high}}(2)$ including a rotation angle of 4.7°. 135
7.4 $I(Q_y)$ near the GISANS line at $Q_z = 0.17\mathrm{nm}^{-1}$ a temperature of 5.6 K (left) and 10.10 K (right). 136
7.5 Sketch of the domain structure and Bloch domain wall chirality in the model used for the DWBA simulations of GISANS on $\mathrm{SF}_{\mathrm{high}}(2)$. Displayed is one structural unit including two half up and one full down oriented magnetic domain as well as two Bloch domain walls. The red arrow denotes the direction of the beam polarization which is tilted by 4.7° with respect to $\vec{z}$ (rotation around the x-axis). 137
7.6 vSANS instrument setup and polarization direction in each compound as side-view, and a front-view on the inner part of the electromagnet including the pole-shoes, the cryoshield with the sample holder inside, and the exit of the neutron beam guide. 140
7.7 (Left) Measured Q_y-Q_z-maps, (middle) simulated Q_y-Q_z-maps, and (right) $I(Q_y)$ near the GISANS line of both Q_y-Q_z-maps for all four GISANS channels at $T_{\mathrm{B}} = (10.10 \pm 0.02)\,\mathrm{K}$. 142
7.8 (Left) Measured Q_y-Q_z-maps, (middle) simulated Q_y-Q_z-maps, and (right) $I(Q_y)$ near the GISANS line of both Q_y-Q_z-maps for all four GISANS channels at $T_{\mathrm{B}} = (5.60 \pm 0.02)\,\mathrm{K}$. 145

7.9 Sketch of the increase in domain wall width w_{DW} and constant domain period D_{domain} with decreasing temperature. Light blue color denotes the paramagnetic state of Nb, whereas dark blue denotes the superconducting state. 146

8.1 $M(H_{\mathrm{ext},\perp})$ of (a) $\mathrm{SF}_{\mathrm{high}}(1)$ and its comparison sample $\mathrm{SIF}_{\mathrm{high}}(1)$ at $T = 4\,\mathrm{K}$ and (b) S(2) and $\mathrm{SIF}_{\mathrm{high}}(1)$ at $T = 3\,\mathrm{K}$. The Nb layers of all displayed samples exhibit similar layer thicknesses. 152

8.2 Trilayer structure enforcing an epitaxial growth of both the lower and upper FePd layers by the bottom template (here Pd). 153

9.1 (Left) $\mathrm{L1_0}$-ordered phase with an atomic monolayer growth of the two materials in the compound. (Right) HAADF-STEM measurement of the Nb/FePd interface in $\mathrm{SF}_{\mathrm{mid}}(1)$ with an overlay of the tP4 unit cell of $\mathrm{L1_0}$-ordered FePd with Fe and Pd marked as red and yellow dots. In the HAADF-STEM image, the in-plane <011> crystalline direction of the FePd tP2 unit cell as shown on the right is displayed, which corresponds to the <100> direction of the tP4 unit cell. 155

9.2 (a) EDX line-profile through the depth of the heterostructure of $\mathrm{SF}_{\mathrm{low}}(1)$, showing a diffusion of Fe deep into the Pd layer. Only the first 20 nm of the Pd layer are free of Fe which can be seen in the HAADF-STEM images in 9.4. Also a high oxygen content of ∼25% in comparison to the Nb content is revealed in the Nb layer. (b) EDX line-profile in out-of-plane direction at the Nb/FePd interface shows a monolayer-by-monolayer growth of $\mathrm{L1_0}$-ordered FePd. (c) The EDX line-profile through the depth of the heterostructure of $\mathrm{SF}_{\mathrm{mid}}(1)$. In contrast to $\mathrm{SF}_{\mathrm{low}}(1)$, the Pd and FePd layers obtain sharp interfaces and only little interdiffusion between each layer of the heterostructure. The oxygen content inside Nb amounts to ∼10% in comparison to Nb. Colors are indicated in the legend. 156

9.3 Sample stack of S/F samples (left) and HAADF-STEM measurements of $\mathrm{SF_{mid}}(1)$ (middle). The measurements reveal an epitaxial growth of Pd and FePd. The Nb layer acquires an out-of-plane order but in the in-plane direction, the structural order is missing which leads to lines in the STEM measurement. STEM EDX-elemental maps are shown on the right and prove the existence of (i) a thin Cr layer between MgO and Pd, (ii) the monolayer structure of the $\mathrm{L1_0}$-ordered FePd phase, and (iii) that the atomic diffusion at the Nb/FePd interface is limited to a few monolayers. Colors are indicated in the legend. 157

9.4 Sample stack of S/F samples (left) and HAADF-STEM measurements of $\mathrm{SF_{low}}(1)$ (middle). The high substrate temperature of $\mathrm{SF_{high}}$ with $T_\mathrm{s} = 820\,\mathrm{K}$ has lead to an interdiffusion of the FePd and Pd layers. Nearly defect-free Pd is grown in the vicinity of MgO which subsequently mixes with Pd; forming first a $\mathrm{Fe}_x\mathrm{Pd}_{1-x}$ layer with a small amount of Fe; and in a second step a $\mathrm{Fe_1Pd_3}$ layer, which can be revealed by the STEM-EDX elemental map on the right. Near the FePd/Nb interface, the $\mathrm{L1_0}$-ordered phase of $\mathrm{Fe_1Pd_1}$ is established. Colors are indicated in the legend. . . . 158

9.5 Sample stack of S/I/F samples (left) and STEM measurements of $\mathrm{SIF_{high}}(1)$ (right). Different to the HAADF-STEM measurements, here the sample was not thinned by FIB preparation as much as samples $\mathrm{SF_{mid}}(1)$ and $\mathrm{SF_{low}}(1)$. The epitaxy cannot be proven here due to the high sample thickness. Still it can be seen that the FePd and Nb layers are well separated by a thin MgO interlayer. Some structural defects are present also in the annealed MgO substrate. 159

9.6 RHEED oscillations during the growth of shuttered FePd in sample $\mathrm{F_{mid}}(1)$ at room temperature. 160

9.7 XRR measurements and respective fits using GenX of $\mathrm{SF_{low}}(1)$ and $\mathrm{SF_{mid}}(1)$ in comparison with the depth-dependent material distribution obtained from STEM-EDX. 167

9.8 XRR and RBS comparison of $\mathrm{F_{high}}$-$\mathrm{F_{low}}$ and respective fits using GenX and RUMP. 167

9.9 3x3µm AFM images of samples $\mathrm{SF_{high}}$-$\mathrm{SF_{low}}$ at room temperature. . . . 168

9.10 (a) 8x8µm AFM image of $\mathrm{SIF_{high}}(1)$ displaing deep voids inside the FePd layer. (b) The red area denotes a mask added to the AFM image where the surface height is >60 % above the minimum height level, the voids (black area) obtain a relation to the FePd surface of ∼1%. 168

9.11 (a) Schematic view of the magnetic domain formation inside the FePd layer in direction of the c-axis of $L1_0$-ordered FePd. (b) (3×3 µm) zero-field MFM measurements in the as-grown states of $F_{high}(4)$, $F_{low}(2)$ and $F_{mid}(3)$. (c) Hysteresis loops of $F_{high}(1)$, $F_{low}(2)$ and $F_{mid}(3)$ measured at 300 K with $H_{ext,||}$ in the surface plane and $H_{ext,\perp}$ perpendicular to the surface plane. All measurements are obtained at 300 K. 169

9.12 (a) 3x3µm MFM image of $F_{high}(2)$ in the as-grown state and (b) hysteresis loops of $F_{high}(2)$ at room temperature. 169

9.13 Magnetization with respect to an out-of-plane applied field $\mu_0 H_{ext,\perp}$ of $SF_{high}(1)$ and $SF_{high}(2)$. 172

9.14 Hysteresis loops at 300 K in an in-plane applied field of sample $SF_{low}(1)$ at various angles between the <100> crystalline axis and the magnetic field. Here, 0° denotes a field applied along <100>. 172

9.15 (a) Dependence of T_c on the applied field $\mu_0 H_{ext,||}$ of $SF_{low}(1)$. All data points in (a) are extracted from $\rho(T)$ measurements such as those displayed in (b). Red arrows indicate a transition of T_c first to lower values and subsequently to increasing values for increasing magnetic fields. 173

9.16 Q_y-Q_z-maps of the I^{--} and I^{-+} channels of polarized GISANS at $T_B = (10.10 \pm 0.02)$ K on $SF_{high}(2)$ (left) before rotation, and (right) after a rotation of 4.7° due to a slightly tilted GISANS holder as sketched in the middle. 173

9.17 Q_y-Q_z-maps of the four different GISANS channels measured at $T_B = (5.60 \pm 0.02)$ K on $SF_{high}(2)$ after subtraction of a rotation angle of 4.7°. 174

9.18 (a) Q_y-Q_z-map of GISAXS measured at room temperature on $SF_{high}(2)$ and (b) corresponding $I(Q_y)$ at the specular line. 174

9.19 (a) 3x3µm MFM image of $SF_{high}(2)$ at room temperature under zero field and (b) 2D-FFT analysis of (a) performed using the software Gwyddion [195]. The dark blue line denotes a preferential direction of magnetic domains visible by a distortion from a circular shape. 175

9.20 $I^{+-}(Q_y)$ of three different simulations with varied $\Delta\xi$, ξ_{av}, and D_{domain} (and constant values for other parameters) in comparison with $I^{+-}(Q_y)$ of $SF_{high}(2)$ at $T_B = (10.10 \pm 0.02)$ K. (a) Chosen parameter set as given in table 9.11, (b) variation of the domain period D_{domain}, (c) variation of the average rotation angle ξ_{av} and the angular range $\Delta\xi$. 177

List of Tables

2.1 Spin wavefunctions, total spins and spin projection on the z-axis, S_z, of superconducting two-electron systems. 12
2.2 Literature values of superconducting parameters for pure bulk Nb. . . . 24
2.3 Literature values of thin film Nb [53] at $T = 0$. $B_{c2,\perp}$ and $B_{c2,||}$ were calculated from the coherence lengths. 25

3.1 Comparison af advantages and disadvantages of GISANS and soft XMCD. 58

5.1 Lattice parameters in (Å) of the tP2 and tP4 unit cells of $L1_0$-ordered FePd and the respective atomically disordered fcc phase [169]. 80
5.2 Comparison of magnetic and structural properties of all F samples with high, medium, and low anisotropy. Domain thicknesses w and the magnetic patterning are taken from MFM measurements in the as grown state of the samples. 97

6.1 Fit parameters for a model of stray field-generated DWS by [97] on $T_c(H_{ext})$ of sample $SF_{high}(2)$. 116
6.2 Comparison of $H^*_{ext,\perp}$ obtained from Fig. 6.10 and of $H_{ext,\perp}$ at which the hysteresis loops shown in Fig. 5.15(c) close. 121
6.3 Bloch domain wall width w_{DW}, domain width D_{domain} and Nb layer thickness d_{Nb} of samples comprising different PMA in comparison with their respective reference bare S films. By these parameters, the mean free path l_{mfp}, the GL-coherence length $\xi_{GL,||}(T_c)$ and the Pearl penetration depth $\Lambda(0\,K)$ are calculated. 122

9.1 Growth parameters of Nb/FePd samples and respective layer thicknesses as determined from XRR and TEM. 161

9.2 Growth parameters of Nb/FePd samples and respective layer thicknesses as determined from XRR and TEM. 162
9.3 Growth parameters of Nb/FePd samples and respective layer thicknesses as determined from XRR and TEM. 163
9.4 Growth parameters of Nb/FePd samples and respective layer thicknesses as determined from XRR and TEM. 164
9.5 Growth parameters of Nb/FePd samples and respective layer thicknesses as determined from XRR and TEM. 165
9.6 Growth parameters of Nb/FePd samples and respective layer thicknesses as determined from XRR and TEM. 166
9.7 (001) and (002) Bragg reflections of epitaxial FePd and its real and imaginary parts of the atomic scattering amplitudes f_{Fe}, f_{Pd}, Δ_{Fe} and Δ_{Pd}, obtained from [17]. 168
9.8 Parameters Q, $H_{\mathrm{coerc},\perp}$, $H_{\mathrm{coerc},||}$, and M_{S} of S/F and S/I/F samples investigated with the SQUID-MPMS. 170
9.9 Parameters used for the GISANS simulation shown in Fig. 5.18 on $\mathrm{F}_{\mathrm{high}}(2)$ at room temperature. 171
9.10 Superconducting parameters of Nb layers in the S/F samples in comparison with the reference sample $\mathrm{SIF}_{\mathrm{high}}(1)$ and the bare Nb layers S(2) and S(3). 172
9.11 Parameters used for the GISANS simulation shown in Fig. 7.7 on $\mathrm{SF}_{\mathrm{high}}(2)$ at $T_{\mathrm{B}} = (10.10 \pm 0.02)\,\mathrm{K}$. 176
9.12 Parameters used for the GISANS simulation shown in Fig. 7.8 on $\mathrm{SF}_{\mathrm{high}}(2)$ at $T_{\mathrm{B}} = (5.60 \pm 0.02)\,\mathrm{K}$. 178

List of Symbols

$\vec{S}_i$	Spin orientation of an electron on site i
$\mu_0\vec{H}_{\text{ext}}$	External applied magnetic field
$\mathcal{H}$	Hamiltonian
$J_{i,j}$	Exchange constant between the i^{th} and j^{th} electrons
g	g-value of electrons
μ_B	Bohr magneton
B_{mf}	Molecular field
T_{Curie}	Curie temperature
$D(E)$	Density of states
E_{F}	Fermi energy
U	Coulomb energy
E_{ex}	Exchange interaction energy
E_{Zeeman}	Zeeman energy
E_{ma}	Magnetic anisotropy energy
E_{d}	Demagnetizing energy
E_{a}	Magnetocrystalline anisotropy energy
$\vec{M}$	Magnetization
K	Anisotropy constant
K_{u}	Uniaxial magnetocrystalline anisotropy constant
K_{sh}	Shape anisotropy constant
H_{sat}	Saturation field along the hard axis
M_{S}	Saturation magnetization
$\vec{H}_{\text{d}}$	Demagnetizing field
$\mathcal{N}$	Shape-related demagnetizing tensor
σ_{DW}	Bloch domain wall per unit area
w_{DW}	Bloch domain wall width
D_{domain}	Magnetic domain period
$\Omega_p(\vec{q})$	Plasma frequency
$E_{\vec{k}}$	Energy of electron with wave vector $\vec{k}$
$\vec{\sigma}$	Spin orientation
S	Total spin
S_{z}	Spin projection on the z-axis
$\xi_{\vec{k}}$	Kinetic single-electron energy within the BCS theory
$\Delta_{\vec{k}}$	Superconducting energy gap
ξ_0	Static coherence length of Cooper pairs
λ_{L}	London penetration depth
B_{c}	Critical field of superconductivity

μ_0	Vacuum permeability
v_{F}	Fermi velocity
n_{S}	Density of Cooper pairs
F	Free energy
ψ	Wave function
$\mathbf{A}$	Vector potential
$\xi_{\mathrm{GL}}(T)$	Temperature dependent Ginzburg-Landau coherence length of Cooper pairs
ξ_{S}	Coherence length of a bulk superconductor
κ	Ginzburg–Landau parameter
B_{c1}	Lower critical field value of a type-II superconductor
B_{c2}	Upper critical field value of a type-II superconductor
B_{c3}	Critical field for surface superconductivity
B_{c}^*	Highest critical field value
Φ_0	Magnetic flux quantum
J_{S}	Cooper pair current density
ρ_0	Residual resistance
l	Mean free path of electrons
Λ	Pearl penetration depth
χ	Suszeptibility
c	Speed of light
ξ_{N}	Cooper pair penetration depth inside a normal metal N
ξ_{F}	Cooper pair penetration depth inside a ferromagnet F
D_{N}	Diffusion constant of a normal metal N
D_{F}	Diffusion constant of a ferromagnet F
k_{B}	Boltzmann constant
$D_{\mathrm{S}}(E)$	Density of states of a superconductor
$\Delta T_{\mathrm{c}}^{\mathrm{orb}}$	Shift of critical temperature due to orbital influence
E_{min}	Energy eigenvalue of the Ginzburg-Landau equation
$f_k(\theta, \varphi)$	Scattering amplitude
$\vec{Q}$	Scattering vector
$\vec{P}$	Polarization vector
γ	Surface energy
ξ_{av}	Average rotation angle of simulated domain units
$\Delta\xi$	Angular range of simulated domain units

Acknowledgements

This work would not have been possible without the guidance and advice of many people during the time of my thesis. I want to specially thank:

Prof. Dr. Thomas Brückel for giving me this interesting topic and the working place at JCNS-2, for profound discussions, your supervision and immense support, and for reviewing my thesis. It is a pleasure to work in your research group with its lively atmosphere.

Prof. Dr. Matthias Wuttig for reviewing my thesis and for the possibility to present my work to your group.

Dr. Emmanuel Kentzinger and Dr. Anirban Sarkar for your great advice, your patience in teaching me, the lively discussions, and for your ideas regarding this project. You have managed giving me freedom to decide the project directions and to guide me where I needed your experience. In particular I want to thank you both for your honesty and friendship and for this wonderful time.

The OMBE-team: Patrick Schöffmann, Tanvi Bhatnagar-Schöffmann, Dr. Markus Waschk, Dr. Sonja Schröder, Dr. Sabine Pütter, Dr. Connie Bednarski-Meinke and Mai Hussein for guidance, great support in the initial stages of sample growth, your patience to improve my English language and most notably for your companionship and friendship. This team is more than only a working team, and I am happy to be part of it.

Prof. Dr. Angelo di Bernardo for your great support in data interpretation, for new ideas and profound help particularly for the thesis-related paper publication.

PD Dr. Oleg Petracic and Dr. Shibabrata Nandi for support in questions regarding magnetism and superconductivity.

Dr. Ulrich Rücker for helpful discussions concerning X-ray and neutron scattering and for support at GALAXI.

Dr. Vitaliy Pipich and Dr. Baohu Wu for your considerable support in performing the GISANS measurements at MLZ. At this point I also want to thank **Dr. Sebastian**

Mühlbauer, Dr. Kirill Zhernenkov, Dr. Alexandros Koutsioumpas and Dr. Amir Syed Mohd for the assistance during neutron beamtimes.

The scientists and technicians from NIST, Gaithersburg, and particularly **Dr. Kathryn Krycka** for your enormous effort to make our beamtime at NIST a huge success.

Dr. Juri Barthel for performing TEM measurements and for your patience while explaining and showing me the techniques of sample handling and data analysis of TEM, and to **Dr. Jürgen Schubert** for performing RBS measurements and for your help in analysing them.

Berthold Schmitz, Frank Gossen and Micha Hölzle for immense and friendly assistance with technical issues.

Mathias Strothmann for the construction of the GISANS sample holder for the measurements at NIST, for all the support and for encouragement. Also I thank both **Dr. Paul Zakalek and Mathias Strothmann** for your assistance with using Python.

Marc-André Rose for the introduction and help at the bonding machine from PGI-7. Many thanks for the permission to use it constantly during my thesis time. **All my colleagues:** for the amazing working atmosphere, fruitfull discussions, great dinner evenings, for involving me into your traditions and life, and for more than 3 fantastic years in which you never have left me alone when I needed your help.

My family and friends for your humour and companionship and the motivation you always give me, and **my grandaunt and grandma** for good mood with good food.

Most of all I want to thank **my parents**: for supporting and listening to me whenever I needed an advice and for encouraging me to explore the fascinating world of natural sciences. I love you with all my heart.

Without all of you, a completion of this thesis would not have been possible.

Declaration

I hereby declare under oath that the submitted doctoral dissertation has been written solely by me without any outside assistance, information other than provided sources or aids have not been used and those used have been fully documented. The dissertation here present is identical to the electronically transmitted text document.

Ich erkläre an Eides statt, dass ich die vorliegende Dissertation selbstständig und ohne fremde Hilfe verfasst, andere als die angegebenen Quellen und Hilfsmittel nicht benutzt bzw. die wörtlich oder sinngemäss entnommenen Stellen als solche kenntlich gemacht habe. Die vorliegende Dissertation ist mit dem elektronisch übermittelten Textdokument identisch.

Aachen, den 28.03.2021 Annika Stellhorn